Electrochemical control of oxygen stoichiometry and materials properties in ion-gel-gated cobaltite thin films

A DISSERTATION
SUBMITTED TO THE FACULTY OF THE
UNIVERSITY OF MINNESOTA
BY

William M. Postiglione

IN PARTIAL FULFILLMENT OF THE REQUIREMENTS
FOR THE DEGREE OF
DOCTOR OF PHILOSOPHY

Advisor: Chris Leighton

December 2023

Acknowledgements

It's hard for me to believe I have come to this point. 10 years ago, attaining a PhD was something I never thought I could accomplish, and frankly, without the kindness and support of the many extraordinary people in my life and those I met along the way, it would not have been possible. It is therefore my great pleasure to write this section, and to put into words the deep appreciation I have felt for all those who helped me along this journey. I will be forever grateful.

My first, and biggest thanks, of course goes to my advisor Chris Leighton. I first met Chris when I was an undergraduate in 2010, and although I thought at the time he was a rather strict professor, he was a great teacher, very approachable, and always extremely helpful. Fast forward to my return to graduate school to pursue a Master's degree, and the decision to join the Leighton group could not have been easier. Since then, throughout my time in the Lab, from my Masters continuing to my PhD research, Chris has been a model advisor, providing me opportunities, supporting and pushing me when I needed it, and fostering my growth as a researcher and a person. While reminiscing, I also want to thank two greatly important people who helped facilitate entry into my graduate career: Prof. Russ Holmes and Julie Prince. Without the support of Chris and Julie, and approval from Russ, I would likely not have committed to grad school or to a PhD. I also want to thank Ryan Haislmaier, a then post-doc in the Jalan group, who gave me the initial idea to pursue a PhD after my Masters. It was just something he mentioned in passing, but his confidence and genuine support in that moment led to the path I am on today. This leads me to perhaps the most impactful person in my growth over these past years: Koustav Ganguly. Working under him during my Master's research served as my introduction to the Leighton Lab, and to graduate research in general. His tutelage was invaluable, it helped me find my self-confidence, and I learned first-hand the dedication and attention to detail it takes to be a research scientist.

Of course, other former / current PhD students and Post-docs in the Leighton group were also highly positive influences on me, and to whom I owe many thanks: Mike Manno, Jeff Walter, Shameek Bose, Bryan Voigt, Justin Watts, Eric McCalla, Joe Batley, Sami El-

Khatib, Vipul Chaturvedi, John Dewey, Helin Wang, Ben Kaiser, Yi Zhang, Justin Ramberger, Bhaskar Das, Jierui Liang, Nileena Nandakumaran, Yu Tao, Yeon Lee, Moumita Maiti, and Kei Heltemes. In particular, I want to thank Jeff Walter, whose guidance, teaching, and training were invaluable in making the research in this thesis a success; Vipul Chaturvedi, who I worked most closely with during my PhD, and was always a reliable resource, research partner, and friend (especially during many long nights at the beamline!); and John Dewey, who I worked most closely with toward the end of my PhD, but was nevertheless a great influence on me providing a role model for professionalism. I would be remiss to not also mention here all the outstanding undergraduate students that I had the pleasure of working with, and who directly contributed to the work in this thesis and/or helped make my research more productive and enjoyable: Hudson Shih, William Moore, Andrew Jacobson, Joseph Gotchnik, Lindsey Borgeson, Margaret Brown, Caroline Korostynski, Fred Tutt, and Lucca Figari.

A great part of my research also involved PhD students and Post-docs from other research groups in CEM, and other departments at the University of Minnesota, to whom I am very grateful. In Prof. Bharat Jalan's group: Abhinav Prakash, Tianqi Wang, Bill Nunn, Tristan Truttman, Jin Yue, Laxman Thoutam, Anil Rajapitamahuni, and Anusha Manjeshwar. In Prof. Andre Mkhoyan's group: Hwanhui Yun and Supriya Ghosh. In Prof. Martin Greven's group (PHYS): Sajna Hameed, Biqiong Yu, Nikolaos Biniskos, and Wojciech Tabis. In Prof. Vivian Ferry's group: Rohan Chakraborty, and in Prof. Xiaojia Wang's group (Mech. E.): Yingying Zhang.

The University of Minnesota has had an incredible impact on my life, and that of my family's. I want to especially acknowledge some of the terrific people I had the pleasure of working with and learning from through the many different University resources. First, I want to thank all the CEMS departmental staff at Amundson Hall, and especially Julie Prince, Teresa Bredahl, Danny Williams, Ann Tran, Chrstine Fruzyna, and Ted Butler. Next, the scientific staff at the Characterization Facility: Javier Garcia Barriocanal, Guichuan Yu, and Greg Haugstad. And finally, the staff at the Minnesota Nano Center (MNC), Institute of Rock Magnetism (IRM), Polymer Characterization Facility, and CSE Machine shop: Lage Von Dissen, Peter Solheid, Prof. David Giles, and Ron Bystrom /

Peter Ness, respectively. I am also grateful to have had the opportunity to perform several exciting (and highly successful!) experiments at US National Laboratories, and to work with the wonderful staff and scientists there: Zhan Zhang and Hua Zhou at the Advanced Photon Source at Argonne National Lab, and Adam Aczel at the High-Flux Isotope Reactor at Oak Ridge National Lab.

Finally, I want to thank my friends and family, especially my parents Pamela and James Postiglione, for their unconditional love and support. Pursuit of this degree has been the hardest undertaking of my life, and I want to acknowledge the cost they bore in it; in time, missed events, emotion, stress, and comfort food occasionally needed to pull me away from my work! I want to dedicate this work to my late grandfather Robert Omoth, and to my late uncle Gary Postiglione.

Abstract

Wide-ranging control of materials properties using applied voltages represents a longstanding goal in physics and technology, particularly for low-power applications. To this end, substantial interest has developed around electric-double-layer transistors (EDLTs) based on functional materials. More recently, *electrochemical* EDLTs, where ions such as O^{2-}, H^{+}, Li^{+}, *etc*., are driven into / out of a channel material *via* voltage, have proven capable of offering unique benefits (including non-volatility) for a variety of novel applications. Cobaltites, such as $SrCoO_{3-\delta}$ (SCO) have recently emerged as an archetypal example of electrochemical control of materials properties in electrolyte-gate devices. This is accomplished by voltage-driven redox cycling between two distinct phases: fully oxygenated perovskite (P) ($\delta \approx 0$) and oxygen-vacancy-ordered brownmillerite (BM) ($\delta = 0.5$). To date, SCO has received the most attention in this regard, despite significant issues with air stability in the P phase, and few alternatives have been considered. Additionally, critical issues of voltage hysteresis and fundamental limits on reversibility and cycling endurance remain unaddressed.

To address this, using EDLTs based on epitaxial $La_{1-x}Sr_xCoO_{3-\delta}$ (LSCO) thin films, we first investigate the electrochemical reduction that is known to occur at positive gate voltages (V_g) in such systems, establishing that the P → BM transformation occurs in LSCO over a wide doping range. Importantly, both the P and BM phase of $x = 0.5$ LSCO are robustly air stable, and the electrochemical reduction behavior was found to be voltage-tunable with both doping and strain. We then leverage this voltage-tuned P → BM transformation to demonstrate large property modulations in electronic transport, magnetism, thermal transport, and optical properties, achieving similar or greater ranges of control than in SCO. Next, to explore the reversibility of the transformation, we performed detailed analysis of V_g hysteresis loops, revealing a wealth of new mechanistic findings, including asymmetric transformations due to differing oxygen diffusivities in the P *vs*. the BM phase, non-monotonic transformation rates due to the first-order nature of the P-BM transformation, and limits on reversibility due to first-cycle structural degradation. Additionally, using minor hysteresis loops, we demonstrate the first rational design of an optimal V_g cycle, leading to state-of-the-art cycling of electronic and magnetic properties, encompassing $>10^5$ transport ON/OFF ratios at room temperature, reversible and non-volatile metal-insulator-metal and ferromagnet-nonferromagnet-ferromagnet cycling, all at ultrathin 10-unit-cell thickness. Finally, to further investigate the magnetic properties of the BM nonferromagnet "OFF" state, we performed neutron diffraction experiments, finding the first direct evidence of antiferromagnetic order in BM-SCO films and identifying weak ferromagnetism in $x = 0.5$ BM-LSCO. These findings thus significantly advance the understanding of voltage-induced P ↔ BM transformations in cobaltite films

and pave the way for future work establishing the ultimate cycling frequency and endurance in such electrolyte-gated devices.

Table of Contents

List of figures

Chapter 1

Chapter 6

Appendix E

List of tables

List of symbols

Bolded symbols represent a vector object

Symbols listed in alphabetical order

A	Amplitude (vibrating sample magnetometer)
a_0	Bohr radius
a, a_{op}, c	Out-of-plane Lattice parameter (in thin films)
a_c	Cubic unit cell lattice parameter
a_{pc}	Pseudocubic lattice parameter
a, b, c,	General unit cell lattice parameters
a_{BM}, b_{BM}, c_{BM}	Brownmillerite lattice parameters
C	Coupling constant (vibrating sample magnetometer)
C	Volumetric heat capacity (time-domain thermoreflectance)
C_p	Heat capacity at constant pressure
D	Diffusivity
D_O	Diffusivity of oxygen
$D_{O,chem.}$	Chemical diffusivity of oxygen
D_{Vo}	Diffusivity of oxygen vacancies
d_{hkl}	Interplanar spacing for (hkl) plane
e	Elementary charge
e^-	Electron
E-field	Electric field
E_{Vo}	Oxygen vacancy formation energy
f	Anisotropy factor (van der Pauw)
f	Frequency (vibrating sample magnetometer)
f_P, f_{BM}	Phase fraction of perovskite and brownmillerite, respectively
G	Interfacial thermal conductance
h	Plank's constant
h^+	Hole
H	Applied magnetic field
H_c	Coercive field or "Coercivity"
hkl, HKL	Miller indices
I	Intensity
I_{SD}	Source-drain current
I_g	Gate current

J_H	Hund's coupling energy
k	Imaginary part of the refractive index
K	Magnetic anisotropy energy
l_d	Diffusion length
L	Lorenz number
$\underline{L}$	Ligand hole
Ln	Lanthanide
M	Magnetization
m	Magnetic moment
m^*	Electron effective mass
M_s	Saturation magnetization
n	Oxygen vacancy ordering index, *i.e.*, $ABO_{(3n-1)/n}$
n	Real part of the refractive index
n_{CT}	Electrochemical charge transfer
n, n_{2D}, n_s, n_{3D}	Charge carrier density (2D, sheet, 3D, respectively)
n_K	Kiessig fringe index (Kiessig fringe t determination method)
n_V	Ratio of oxygen vacancy concentration to lattice oxygen concentration
P	Pressure (usually used to express vacuum level)
P_{Ar}	Argon partial pressure
P_{O_2}	Oxygen partial pressure
$\boldsymbol{Q}$	Scattering vector
$Q_{x,y}$	In-plane component of scattering vector $\boldsymbol{Q}$
Q_z	Out-of-plane component of scattering vector $\boldsymbol{Q}$
r_p, r_s	Reflectance coefficients for parallel and perpendicularly polarized light, respectively
R_1, R_2, R, R_{4T}	Resistance (Van der Pauw)
$(RA)_{contact}$	Resistance-area product of electrical contact
R_{AH}	Anomalous Hall coefficient
R_H	Hall coefficient
R_{Hall}	Hall resistance
R_s	Sheet resistance
R_{SD}	Source-drain resistance
R_x, R_y	Diffractometer tilt angles
r_A, r_B, r_O	Ionic radii of A, B, O in perovskite ABO_3
S	Spin angular momentum

T	Temperature
t	Film thickness
T_c	Critical temperature for superconductivity
T_C	Curie temperature
T_N	Néel temperature
t^*	Dead layer thickness
U	Hubbard "U" electron-coulomb repulsion energy
V_O	Oxygen vacancy
V_{Co}, $\overline{V}_{Co}$	Mean Cobalt valence (nominal Co Valence)
V_{Coil}	'Pick-up' coil voltage (vibrating sample magnetometer)
V_g	Gate voltage
V_{SD}	Source-drain voltage
V_{th}	Threshold voltage
x	Perovskite A-site chemical substitution, *i.e.*, $A_{1-x}A'_xBO_3$
y	Perovskite B-site chemical substitution, *i.e.*, $AB_{1-y}B'_yO_3$
Z	Atomic number
z	Film depth
Γ	Goldschmidt tolerance factor
Δ	Phase difference (spectroscopic ellipsometry)
Δ_{CF}	Crystal field energy
Δ_{CT}	Charge-transfer gap energy
ΔH_{Do}	Activation enthalpy for diffusion of oxygen
ΔH_m	Activation enthalpy of migration
ΔH_{Vo}	Enthalpy of formation of an oxygen vacancy
$\Delta\omega$	'Offset' angle, *i.e.*, deviation from specular condition
ΔR	Gate-induced resistance change
$(\Delta R)_{gate}$	Gate-induced resistance change after 30 minutes at a particular gate voltage
$(\Delta R)_{irrev.}$, $(\Delta R)_{nv}$	Change in resistance between initial and final states
$\Delta\rho$	Difference in resistivity
$\Delta\rho_{//}$	Magnetoresistivity with current parallel to applied magnetic field
$\Delta\rho_{\perp}$	Magnetoresistivity with current perpendicular to applied magnetic field
δ	Oxygen non-stoichiometry in $ABO_{3-\delta}$
ε_{xx}, ε_{yy}	In-plane strains
ε_{zz}	Out-of-plane strain

κ	Dielectric constant
θ	Receiving angle (½ of X-ray diffraction 2θ)
θ_c	Critical angle (GIXR)
θ_{nL}	Angle of n_L^{th} Laue fringe maxima
θ_{nK}	Angle of n_K^{th} Kiessig fringe maxima
Λ	Scherrer length (Scherrer formula and in X-ray diffraction analysis)
Λ, [Λ_r, Λ_z]	Thermal conductivity [Thermal conductivity in cylindrical coordinates, r (radial), and z (depth)] (time-domain thermoreflectance
Λ_{el}	Electronic contribution to thermal conductivity
Λ_{lat}	Lattice contribution to thermal conductivity
Λ_{tot}	Total thermal conductivity
λ	Wavelength
λ_{TF}	Thomas-Fermi screening length
μ_0	Permeability of free space
μ_B	Bohr magneton
ρ, ρ_{xx}	Electrical resistivity
ρ_0	Residual resistivity
ρ_{xy}	Transverse resistivity
ρ	Complex reflectance ratio
σ	Electrical conductivity
σ_{AH}	Anomalous Hall conductivity
σ_{xy}	Transverse conductivity
σ_{RMS}	Root-mean-square roughness
τ	Time
φ	Diffractometer sample plane rotation angle
χ	Magnetic susceptibility
ω	Incident angle (X-ray diffraction)
tan(Ψ)	Amplitude ratio (spectroscopic ellipsometry)

List of acronyms

Acronyms listed in alphabetical order

1D, 2D, 3D	One dimensional, two dimensional, three dimensional
2DEG	Two-dimensional electron gas
AE	Alkaline earth
AF	Antiferromagnetic/antiferromagnetism
AFM	Atomic force microscopy
AMR	Anisotropic magnetoresistance
APS	Advanced Photon Source
BM	Brownmillerite
BM-LSCO	$La_{1-x}Sr_xCoO_{2.5}$
BM-SCO	$SrCoO_{2.5}$
CMR	Colossal magnetoresistance
DC	Direct current
DFT	Density functional theory
EDL	Electric double layer
EDLT	Electric-double-layer transistor
EELS	Electron energy-loss spectroscopy
EMIM	1-ethyl-3-methlyimidazolium
F	Ferromagnetic/ferromagnetism
FET	Field-effect transistor
FIE-TAX	Fixed-incident-energy triple-axis
FTIR	Fourier transform infrared spectroscopy
FWHM	Full-width at half-maximum
GKA	Goodenough-Kanamori-Anderson rules
GIXR	Grazing-incidence X-ray reflectometry
GKMD	Green-Kubo molecular dynamics (thermal simulations)
GST	$Ge_xSb_yTe_z$
HAADF	High-angle annular dark field
hBN	Hexagonal boron nitride
HFIR	High-Flux Isotope Reactor
HRXRD	High-resolution X-ray diffraction
HS	High spin
IL	Ionic liquid

IS	Intermediate spin
IS1	Incident slit 1
LAO	$LaAlO_3$
LCO	$LaCoO_3$
LLS	Length limiting slit
LS	Low spin
LSAT	$(LaAlO_3)_{0.3}(Sr_2AlTaO_6)_{0.7}$
LSCO	$La_{1-x}Sr_xCoO_{3-\delta}$
MBE	Molecular beam epitaxy
MD	Molecular dynamics (thermal simulations)
MEMS	Microelectromechanical systems
MEPS	Magnetoelectronic phase separation
MIEC	Mixed ion electron conductor
MIT	Metal-insulator transition
MOSFET	Metal-oxide-semiconductor field-effect transistor
MPMS	Magnetic Property Measurement System
ND	Neutron diffraction
NPD	Neutron powder diffraction
NEMD	Non-equilibrium dynamics (thermal simulations)
OER	Oxygen evolution reaction
ORNL	Oak Ridge National Laboratory
P	Perovskite
PB	Parallel beam
PLD	Pulsed laser deposition
PMA	Perpendicular magnetic anisotropy
PNR	Polarized neutron reflectometry
PPMS	Physical Property Measurement System
PVD	Physical vapor deposition
P(VDF-HFP)	Poly(vinylidene-hexafluoropropylene)
PXRD	Powder X-ray diffraction
RC	Rocking curve
RE	Rare earth
RF	Radiofrequency
r.l.u.	Reciprocal lattice unit(s)
RMS	Root-mean-square

R-P	Ruddlesden-Popper
RS1, RS2	Receiving slit 1
RSM	Reciprocal space map
RSO	Reciprocating sample option
RTA	Rapid thermal anneal
SAM	Self assembled monolayer
SC	Superconductivity/superconducting
SCO	$SrCoO_{3-\delta}$
SE	Spectroscopic ellipsometry
SLAO	$SrLaAlO_4$
SNR	Signal-to-noise ratio
SOFC	Solid oxide fuel cell
SP	Spectrophotometry
SQUID	Superconducting quantum interference device
SSVT	Single stage variable temperature
STEM	Scanning transmission electron microscopy
STO	$SrTiO_3$
SXRD	Synchrotron X-ray diffraction
TEM	Transmission electron microscopy
TFSI	Bis(trifluoromethylsulfonyl)imide
TM	Transition metal
u.c.	Unit cell(s)
VDP	Van der Pauw
VSM	Vibrating sample magnetometer
VERITAS	Versatile, intense triple-axis spectrometer
WAXRD	Wide-angle X-ray diffraction
XAS	X-ray absorption spectroscopy
XMCD	X-ray magnetic circular dichroism
XRD	X-ray diffraction
YBCO	$YBa_2Cu_3O_{7-\delta}$
YSZ	Yyttria stabilized zirconia

Chapter 1: Introduction and Background

Collecting, storing, transferring, and analyzing vast quantities of data are now integral parts of almost every aspect of the global economy. As demand for computing hardware continues to rise, the issue of energy and power consumption is gaining attention. Historically, data storage and computation energy efficiency has been a relatively small design concern, especially when compared to high-energy-consuming sectors like manufacturing and transportation. However, this landscape is changing, as continual operation of the world's tech infrastructure now makes up a significant fraction of the global energy usage, and is expected to continue to grow rapidly [1]. Considering the urgent need for energy conservation, especially during the ongoing transition toward green energy, this raises interesting new challenges for the materials science and engineering communities.

Much of the modern data storage technology employs so-called 'volatile' memory, where a continuous power supply is needed to store and retrieve information. However, more recent technologies, based on storing information as magnetic elements, such as magnetoresistive random access memory, have been gaining significant traction [2]. While storing information as non-volatile magnetic elements is certainly promising in terms of energy efficiency, efficient means of switching (*i.e.*, writing) is still an active area of research [1]. Voltage control of materials properties represents a longstanding goal in science and engineering and is one particularly promising route to achieving high energy efficiency in computing, *i.e.*, to control non-volatile magnetic elements using an applied voltage, rather than a current which produces heat. The primary goal of this thesis is to explore electrolyte gating of perovskite cobaltites, and specifically their electrochemical functionality, as a novel means to realize voltage-induced modulation of various materials properties, including magnetism, electrical resistivity, thermal conductivity, and optical properties for a variety of potential low-power applications.

The focus of this opening chapter is to review basic concepts and summarize the relevant literature to provide context for the research presented in the later chapters. First, the general physics and chemistry of perovskite oxides and thin films will be introduced. I

will then narrow the focus to one particularly important family of perovskite oxides: the cobaltites, starting first with $LaCoO_3$, then moving to the general La/Sr cobaltite system, $La_{1-x}Sr_xCoO_{3-\delta}$, and finally $SrCoO_{3-\delta}$. In the latter, an emphasis will be placed on oxygen non-stoichiometry, vacancy ordering, and phase transformations. Next, I will introduce the concept of electrolyte gating through the lens of the broader field-effect-based voltage-control of material properties, but eventually narrowing the scope to the more novel concept of *electrochemical* gating. Finally, I will conclude by briefly reviewing the literature on electrolyte gating of cobaltite thin films, focusing on the advantages and applicability of the electrochemical approach.

1.1 Perovskite oxides

Recent decades have seen an extraordinary rise in the number of research publications centered around the broad class of materials known as perovskites [3]. These materials have drawn interest for a wide range of critical applications, including in catalysis [4], solar cells [5], solid oxide fuel cells (SOFCs) [6], high critical temperature (T_c) superconductors [7], and more. Perovskite oxides, in particular, are of high interest, not only for the above applications, providing promise for the next generation of electronic devices, but also for the study of fundamental science [8]. Indeed, a growing number of important technologies already incorporate perovskite oxides, such as piezoelectric actuators [9], microwave telecommunications [10], and non-volatile ferroelectric random access memory [11]. The versatility of the perovskites lies largely in their chemical diversity within a common structural framework, allowing material synthesis combinations that push the imagination. The following sections broadly cover the basic structure, chemistry, and fundamental physics of perovskite oxides.

1.1.1 Crystal structure of perovskites

Perovskite oxides have the general formula ABO_3, where ‘A’ and ‘B’ represent different metal elements. They are therefore metal-oxides and represent a specific class of the more general ‘complex’ oxides (oxides with multiple metal elements). The ideal cubic crystal structure of a perovskite oxide is shown in Fig. 1.1(a), where the A-site metal cations sit on the corners of the unit cell, the B-site metal cations occupy the center of the

cell, and the anions (O^{2-} in this case) are located on the 6 face centers. The fundamental structural unit of the perovskite structure is the BO_6 octahedron, as shown in the center of the cell in Fig. 1.1(a). The crystal structure of a perovskite can also be viewed as an interconnected network of corner-sharing BO_6 octahedral units, in the manner shown in Fig. 1.1(b). This representation is useful when considering deviations from the ideal cubic cell of Fig. 1.1(a). Indeed, perovskites need not be cubic, and depending on the relative sizes of the ionic constituents the octahedral units can 'distort', *i.e.*, rotate about different crystallographic axes. An example of this is shown schematically in Fig. 1.1(c), where rotations of the octahedral units result in a lowering of the crystal symmetry from left (no rotation, *i.e.*, cubic), to middle (one axis of ration, tetragonal), to right (two axes of rotation, orthorhombic). Such tilting of the octahedra occurs when the ionic radii are not ideal to form the cubic structure. In other words, the atoms can more efficiently fill space by octahedral tilting, thus lowering the symmetry.

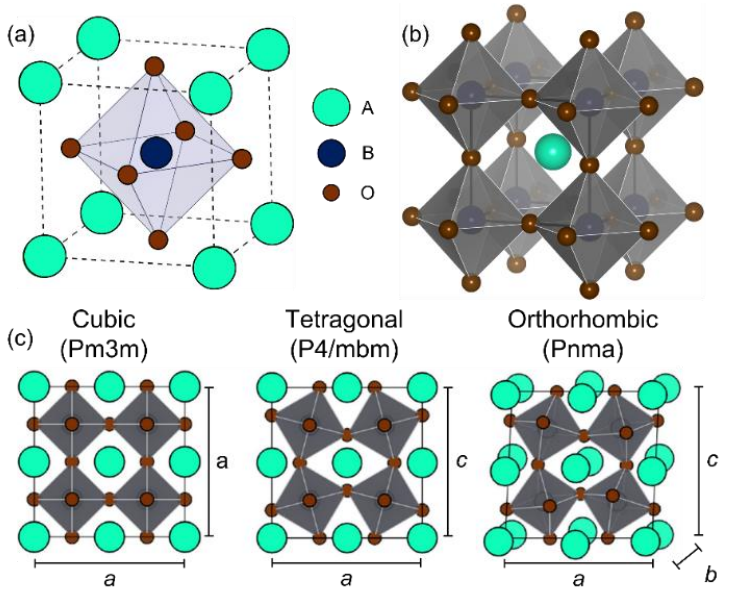

Figure 1.1: (a) The crystal structure of the general ABO_3 perovskite oxide in a cubic unit cell. (b) An alternate way of viewing the ABO_3 perovskite as a network of corner-sharing BO_6 octahedra. (c) Schematic representations of example tilt patterns which deviate from the cubic symmetry.

A useful tool for predicting the symmetry of a perovskite is the Goldschmidt tolerance factor (Γ), shown below in Eq 1.1 (for O^{2-} as the anion):

$$\Gamma = \frac{r_A + r_O}{\sqrt{2}(r_B + r_O)}, \tag{1.1}$$

where r_A, r_B, and r_O, represent the ionic radii of the A-site, B-site, and O^{2-}, respectively. This factor is based entirely on geometric arguments, it is simply the ratio of the lattice parameter from either O-B-O or A-O-A constructions, where $\Gamma = 1$ describes a cube. Cubic perovskites (space group $Pm\bar{3}m$) tend for form for $0.9 < \Gamma < 1$ [3,12]. When $\Gamma > 1$, hexagonal (with some face-sharing octahedra) or tetragonal symmetries (with ferroelectric properties) are favored, and when $0.7 < \Gamma < 0.9$, rhombohedral, tetragonal, or orthorhombic symmetries arise depending on the specific tilt patterns [13]. Below $\Gamma \approx 0.7$, trigonal 'ilmenite' structures are formed [12]. In some cases, the energy differences between different tilt patterns and symmetries in perovskite oxides are quite small, such that structural transitions can be driven as a function of temperature. An illustrative example of this is the ferroelectric perovskite $BaTiO_3$. At room temperature, $BaTiO_3$ has a $\Gamma \approx 1.1$ leading to tetragonal symmetry. However, $BaTiO_3$ undergoes structural transitions on both warming (tetragonal → cubic at 393 K) and cooling (tetragonal → orthorhombic at 273 K, and orthorhombic → rhombohedral at 183 K) [14]. The relative ease with which BO_6 octahedra can distort due to external parameters such as temperature, pressure, *etc*., is one of the most fascinating and useful functionalities of the perovskites, as such effects can lead to significant changes in material properties.

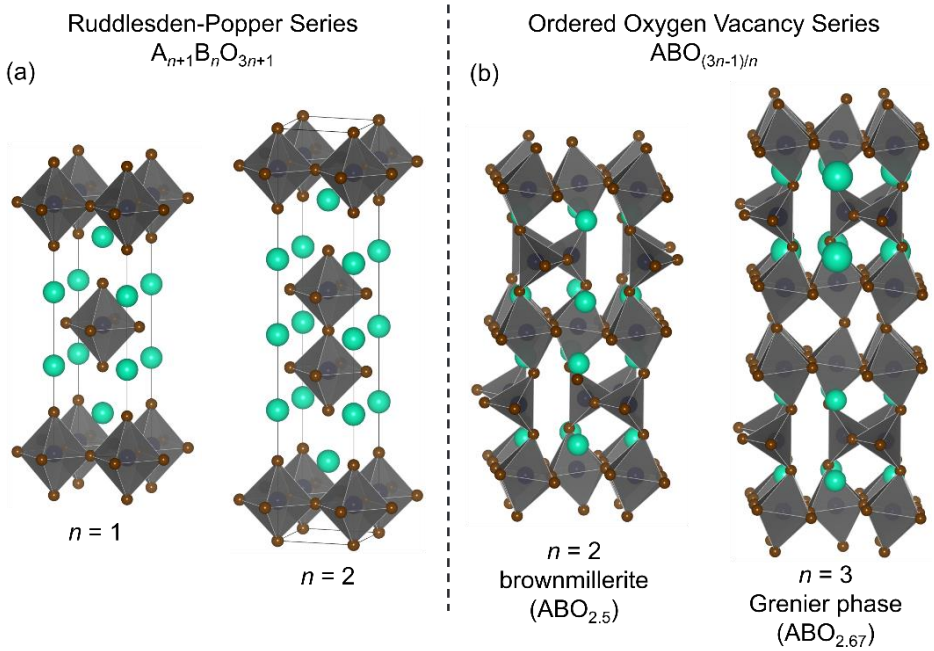

Figure 1.2: (a) The Ruddlesden-Popper series of $A_{n+1}B_nO_{3n+1}$ layered perovskites, showing the n = 1 (left) and n = 2 (right) crystal structures. (b) Example of the oxygen-deficient perovskite series $ABO_{(3n-1)/n}$, for n = 2 (brownmillerite, right), and n = 3 (Grenier phase, left).

In addition to the ABO_3 perovskites, there are myriad perovskite-related structures that are also of great scientific / technological importance. Such compounds can be formed by deviation from the ideal 1:1:3 stoichiometry. Two important examples of this are shown in Fig. 1.2. In Fig. 1.2(a), the Ruddlesden-Popper (R-P) series of so-called 'layered perovskites' is shown, where the structure $A_{n+1}B_nO_{3n+1}$ is related to the perovskite by insertion of an additional rock-salt A-O layer, *i.e.*, a stacking fault. The specific layering sequence then determines the stoichiometry, n = 1 leads to compounds of the 2:1:4 stoichiometry, n = 2 leads to 3:2:7, and so forth, until eventually $n \rightarrow \infty$ recovers the perovskite 1:1:3. The R-P series of cuprates [15] and ruthenates [16] are particularly important compounds in the study of superconductivity.

Fig. 1.2(b) shows another important defect series of perovskites, this time by varying *oxygen* stoichiometry. In general, perovskites can accommodate a variety of low-formation-energy point defects, the most common being the oxygen vacancy (V_O). By removing an oxygen atom from any of the structures in Fig. 1, it is easy to see how the interconnecting BO_6 octahedra may be interrupted, resulting in other B-O polyhedral, *e.g.*, tetrahedra or square pyramids. Randomly spatially distributed V_O play a role in the materials properties of perovskite oxides, and at high enough concentration V_O can also spatially *order*, altering the crystal structure. One such series of V_O-ordered oxygen-deficient perovskites is described by the formula $ABO_{(3n-1)/n}$ and is shown in Fig. 1.2(b). Like the R-P phases above, these V_O-ordered phases also form a layered structure along one crystallographic axis. In the case of n = 2, also known as brownmillerite $ABO_{2.5}$ (or $A_2B_2O_5$), the structure consists of alternating layers of BO_6 octahedra and BO_4 tetrahedra, as shown on the left of Fig. 1.2(b). Increasing n then corresponds to increasing the number of BO_6 layers between BO_4 layers. The n = 3 $ABO_{2.67}$, or 'Grenier' phase, is shown on the right in Fig. 1.2(b). Analogous to the R-P series, the perfectly stoichiometric ABO_3 phase is recovered at $n = \infty$. Historically, oxygen deficient perovskites have primarily been of interest for ionic transport applications and for catalysis [17]. However, more recently, the ability to topotactically transform (by altering oxygen stoichiometry) between a perovskite ($n = \infty$) and brownmillerite (n = 2) has generated significant promise for a variety of

potential applications. This transformation is of prime importance to this thesis and will be discussed in detail in later sections.

1.1.2 Basic chemistry and physics

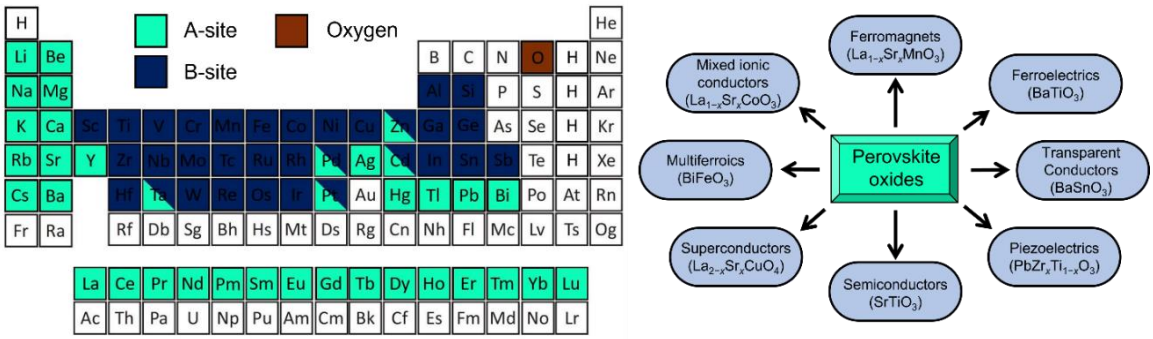

Figure 1.3: (a) The periodic table showing the known A- and B-site elements in perovskite oxides. (b) A thematic illustration of the diverse range of functional properties of perovskites oxides.

With a basic understanding of the structure of perovskites in hand, we now move on to the general chemistry and physics that govern their fascinating properties. In terms of chemistry, the A- and B-site cations of perovskite oxides tend to come from different areas of the periodic table. In the most basic consideration of charge balance, the sum of the valence on the A- and B-site cations must compensate the –6 total charge of the three O^{2-} anions per unit cell. This can be accomplished by different combinations of A and B, either +1/+5 (*e.g.*, $KTaO_3$), +2/+4 (*e.g.*, $SrTiO_3$), or +3/+3 (*e.g.*, $LaAlO_3$). The ionic radius of the O^{2-} anion necessitates that the A-site cation be larger than the B-site. As a result, A-site elements are primarily alkali, alkaline earth, and rare earth (RE) elements, whereas the B-site cations typically consist of transition metals (TM). Fig. 1.3(a) shows the common perovskite oxide elements on the periodic table, and what site they typically occupy in the structure. In addition to size, important chemical differences also exist between the cation sites. The A-site elements tend to have closed-shell electronic structures, and thus have little orbital overlap with surrounding oxygen anions. The B-sites elements, on the other hand, consist mainly of TMs, where the partially filled *d*-orbitals overlap significantly with O 2*p* orbitals. It is these interactions that largely define the electronic and magnetic properties of perovskites. As can be clearly seen from Fig. 1.3(a), perovskite oxides are incredibly chemically diverse, with nearly all the metallic elements known to form in the perovskite structure. This enormous chemical diversity, within a similar structural

framework, gives rise to an extraordinary range of materials properties, including high-temperature superconductivity [7,18], ferro / antiferromagnetism [19,20], ferroelectricity [14,21], multiferroicity [22,23], colossal magnetoresistance [19,20,24], transparent conductivity [25], and more [26]. Fig. 1.3(b) highlights the diverse functional properties of some of the more well-known perovskite and perovskite-related oxides.

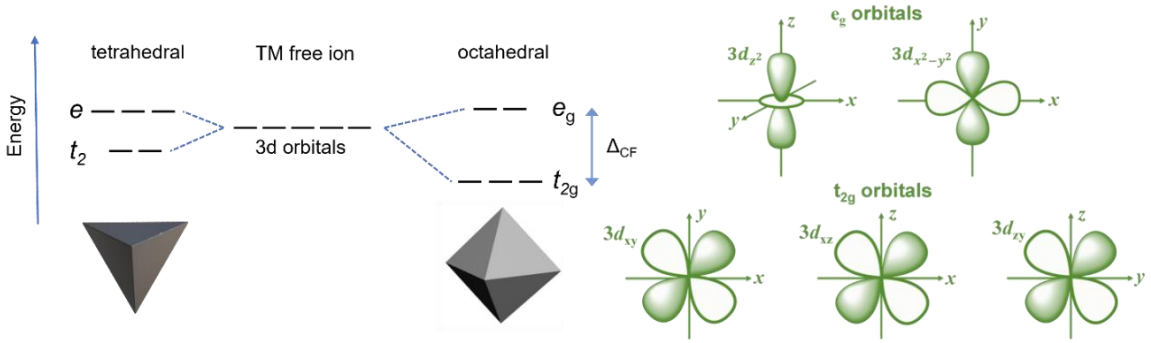

Figure 1.4: A schematic diagram of the concept of crystal field theory in perovskites, where TM *d*-orbitals are split into e_g and t_{2g} *via* interaction with the oxygen anion ligand field 2*p*-orbitals. e_g orbitals share the axes of the surrounding O 2*p* orbitals, raising their energy, while the t_{2g} orbitals are off-axis and thus lower in energy (adapted from Ref. [27])

As mentioned above, the *d*-orbitals of the B-site cation play the dominant role in determining the electronic and magnetic properties of a perovskite. Fig. 1.4 shows the splitting of the 3*d* orbitals of a free TM ion into tetrahedral (left) and octahedral (right) anion ligand fields. Interactions between the TM 3*d* orbitals and the surrounding O 2*p* orbitals break the degeneracy of the 3*d* states, splitting them into so-called t_{2g} and e_g levels. For cubic symmetry, the $3d_{z^2}$ and the $3d_{x^2-y^2}$ orbitals share the axes of the ligand field, and thus increasing in energy (becoming e_g states), whereas the $3d_{xy}$, $3d_{xz}$, and $3d_{zy}$ are lowered in energy (becoming t_{2g}). Analogous arguments can be made to explain the splitting in tetrahedral fields. This concept is known as crystal field splitting, and the energy between e_g and t_{2g} states is thus the crystal field energy, Δ_{CF}. Electronic filling of these split orbitals depends on the energy balance between Δ_{CF} and the intra-atomic electron-electron exchange coupling known as Hund's exchange energy (J_H), which favors unpaired electrons. In addition, further lifting of orbital degeneracy can be accomplished by structural distortion of the octahedra, favoring certain orbital energies over others. Known as Jahn-Teller distortions, these effects are spontaneous in certain bulk perovskites but are

also common in thin films, where strain effects imparted from a substrate can significantly alter material properties in thin films compared to their bulk equivalents.

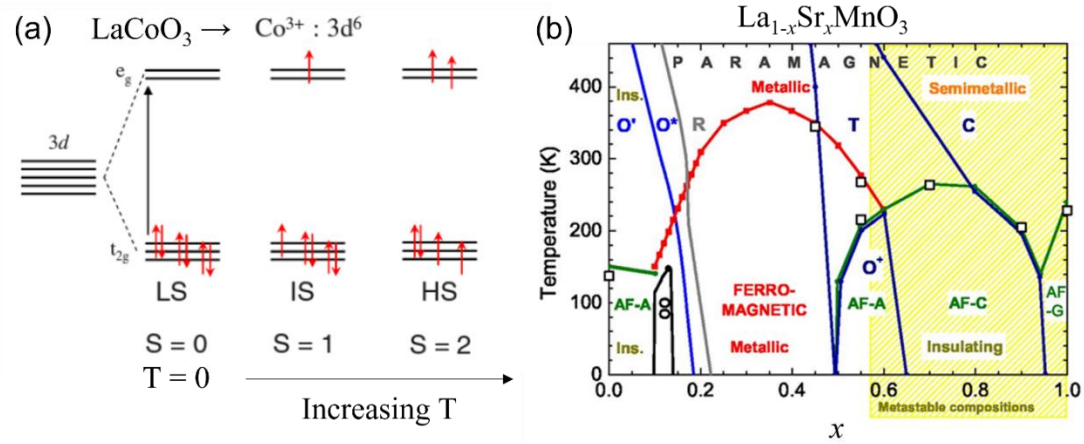

Figure 1.5: (a) Orbital filling in $LaCoO_3$ as a function of T. $LaCoO_3$ is a diamagnet ($S = 0$) in its ground state, but due to the small energy difference between Δ_{CF} and J_H finite-spin states are populated at temperatures above ~30 K [28]. (b) The phase diagram of $La_{1-x}Sr_xMnO_3$ as an example of 'hole doping', where many different electronic and magnetic phases appear at different T and x [29]. AF: Antiferromagnetic (AF-A: A-type, AF-C: C-type, AF-G: G-type), O: orthorhombic, R: rhombohedral, T: tetragonal, C: cubic.

For perovskites with small spin-orbit coupling, *i.e.*, with low atomic number (Z) TMs, the electronic and magnetic properties are predominantly determined by the energy splitting of the B-site 3*d* orbitals and the subsequent electronic occupancy. The choice of B-site element is thus the most important factor, as Δ_{CF} and J_H are determined by this. However, the A-site cations are also important but in a more indirect way. Besides their size-based geometric impact on the structure / symmetry, they can also influence the valence state, and thus the orbital filling, of the B-site cation. The A-site cations typically have only one stable valence state, while many TMs have multiple valence states close in energy. This can be exploited by 'designing' a perovskite such that the choice of A-site cations can be used to tailor the structure, valence, and thus electronic filling and properties. Illustrative examples include the $La_{1-x}Sr_xMnO_{3-\delta}$ and $La_{1-x}Sr_xCoO_{3-\delta}$ systems, where La^{3+} and Sr^{2+} form a solid solution (*i.e.*, randomly spatially distributed). The Sr content, x, then determines the valence state of the Mn / Co *via* 'hole doping' according to the formula $V_{Mn/Co} = 3 + x - 2\delta$. By charge balance, varying the Sr content in such systems effectively controls the valence of the Mn / Co, the orbital filling, and consequently the electronic and magnetic properties. In $LaCoO_3$, for example, Δ_{CF} and J_H are similar in magnitude, with

Δ_{CF} being slightly larger, resulting in a diamagnetic low-spin (LS) ground state (*i.e.*, at 0 K). However, at higher temperatures, Δ_{CF} is overcome by thermal energy and intermediate spin (IS) and high spin (HS) Co populations begin to appear [28], as shown schematically in Fig. 1.5(a). In $La_{1-x}Sr_xMnO_3$, hole doping leads to in a variety of different electronic and magnetic (and structural) phases, producing the rich *x vs.* temperature (*T*) phase diagram shown in Fig. 1.5(b) [29].

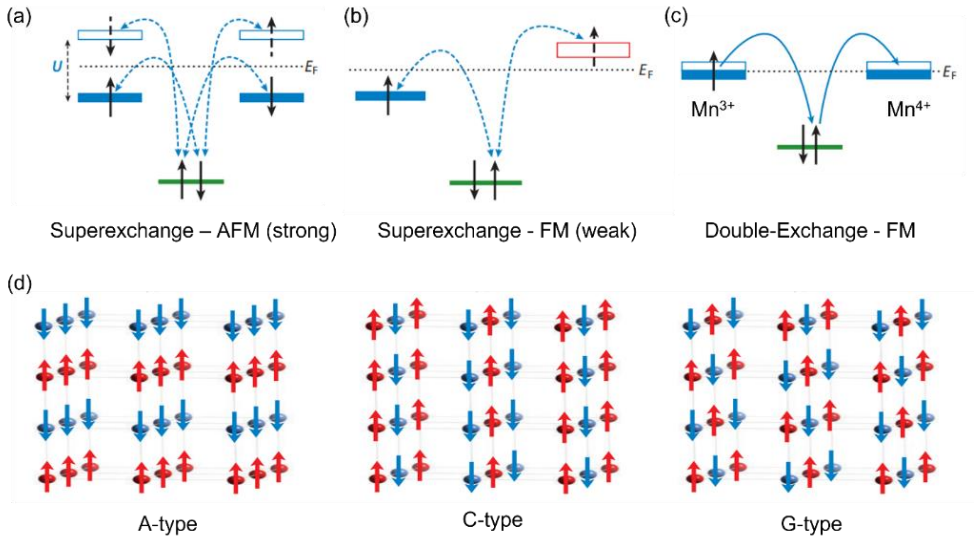

Figure 1.6: (a) AF superexchange interaction between two half-filled orbitals, (b) superexchange F interaction between one half-filled and one empty orbital, and (c) double-exchange involving movement of itinerant electrons from a Mn^{3+} to a Mn^{4+}, and *vice versa*, *e.g.*, in $La_{0.7}Sr_{0.3}MnO_3$. (d) 3 common types of AF order in perovskites oxides. Adapted from Ref. [30].

Moving to magnetic properties, unlike purely metallic systems, in perovskite oxides magnetic exchange interactions take place through interconnecting O bridges, *i.e.*, across B-O-B bonds. The widely adopted theory to explain / predict the magnetic properties in perovskites is known as the Goodenough-Kanamori-Anderson (GKA) rules [31]. The GKA rules describe the exchange mechanisms through B-O-B bonds, and thus can be used to predict the magnetic interactions as either ferromagnetic (F) or antiferromagnetic (AF). The magnetic exchange interaction through the B-O-B bonds of an insulating perovskite is known as 'superexchange'. This interaction involves virtual 'hops' of an electron between *d*-orbitals of two neighboring B-site cations and the 2*p*-orbitals of the abridging O. The energy landscape of the orbitals, their structural relationship with each other (*i.e.*, the B-O-B bond angle), and their electronic filling then determines whether the magnetic exchange will be F or AF. AF is predicted when the interaction is between two half-filled orbitals,

while F is favored if the interaction is between half-filled and empty orbitals (for bond angles close to 180°). Schematic examples of these two cases are shown in Fig. 1.6(a) and (b). Depending on the exact structure and chemistry, AF order can manifest in perovskites in different ordering patterns, some examples of these are shown in Fig. 1.6(d). Note that, A-, C-, and G-type AF ordering are all present in different parts of the $La_{1-x}Sr_xMnO_3$ phase diagram of Fig. 1.5(b). In superexchange materials, AF order is more commonly observed, and in general the AF interactions are strong, often resulting in high Néel temperatures (T_N), whereas the F case is less common and weaker [30,32]. However, strong B-O-B F exchange interactions also exist, known as 'double-exchange'. Double-exchange differs from superexchange in that it requires *mobile* electrons. These itinerant electrons can then move in a series of orbital transfers between B-site cations; interacting with B-site core spins and leading to an overall strong F order [31]. This process is shown schematically in Fig. 1.6(c). As unsubstituted ABO_3 perovskites tend to be insulators (or semiconductors), achieving mobile electrons (or holes) often involves 'doping', *i.e.*, chemical substitution of the A-site, as described above. Sr-doped $La_{1-x}Sr_xMnO_3$ again provides an illustrative example, where Sr^{2+} doping on La^{3+} sites introduces holes (h^+) to the system, increasing conductivity and leading to the double-exchange-mediated F-metallic ground state shown in Fig. 1.5(b) for ~$0.2 < x <$ ~0.6 [29].

1.1.3 Thin films and heterostructures

While the relatively simple examples described above are helpful in explaining basic principles of perovskite oxides, real-world perovskite material systems can quickly become much more complicated. For example, as the symmetry is lowered, defects are introduced, and/or dimensional constraints / interface effects come into play. To make functional devices for applications many of these must be considered / reconciled. Of prime importance in this regard are thin films, or more generally 'heterostructures', which are now ubiquitous in modern electronic devices. The primary difference between material properties of thin films and those of their bulk counterparts, is the role of the interface with the substrate. This interface, along with the specific growth mode / microstructure, largely determines the structure and thus the properties of the film. With proper choice of substrate materials and growth conditions, highly perfect single-crystalline films can be produced.

Deposition of such films is known as epitaxy. Single crystal substrates are often used to produce epitaxial films, in which the film's crystallographic orientation is set by registry with the substrate interface. When the lattice size of the film material is mismatched with that of the substrate, the film can be made to grow in a 'strained' state, *i.e.*, stretched or compressed in the plane of the interface to maintain perfect registry with the substrate. Fig. 1.7(a) and (b) show schematic examples of the impact of strain on epitaxial perovskite films for the cases of in-plane compression (a) and tension (b). The resulting distortion of the film lattice can lead to different orbital degeneracy / filling, in some cases giving thin films starkly different properties compared to their bulk forms. $LaCoO_3$ is a well-documented example of this phenomenon. Its bulk ground state is diamagnetic but when grown on substrates imparting tensile strain films of $LaCoO_3$ become F at low T [33].

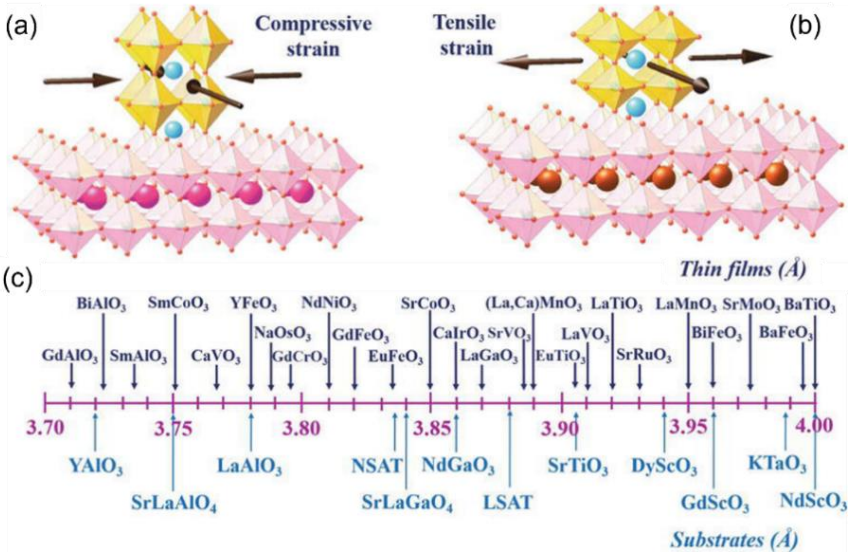

Figure 1.7: Schematic examples of the effect of epitaxial strain on a perovskite for in-plane compression (a) and in-plane tensile strain (b). (c) Scale of the relative sizes (expressed in terms of pseudocubic lattice parameter in Å) of some perovskite oxides, for commercial substrates (bottom row, light blue) and selected materials of interest (top row, dark purple). Adapted from Ref. [34].

Epitaxial strain imparted from a substrate can thus be used to *tune* the material properties in thin films, and in perovskite oxides this has become somewhat a field of its own [26,34]. Significant advances in thin film deposition techniques, combined with the growing availability of high-quality single-crystal substrates has helped fuel the ever-growing interest in epitaxial perovskite oxide films and heterostructures [3,26]. Fig. 1.7(c) shows the range of cubic (or pseudocubic) lattice parameter sizes for some common perovskite oxide substrate (bottom) and film (top) materials. The size mismatch between

the lattice parameter of the film and the substrate determines the strain imparted to the film according to the relation: $(a_{film} - a_{sub.})/a_{sub.}$, where a_{film} and a_{sub} refer to the film and substrate lattice parameter, respectively. Coherent, *i.e.*, fully strained or 'pseudomorphic' films of perovskite oxides can generally accommodate mismatches of up to ~±2%.

The importance of films and heterostructures to device design in applications cannot be overstated. Thin film heterostructures provide an elegant route to combining multiple functionalities into a single device structure, *e.g.*, a patterned 'stack' of multiple thin films. Fig. 1.8(a) shows an illustration capturing this idea, where layers of different chemistries of perovskites are combined into a specifically designed stack. Beyond the obvious need for films in functional devices, oxide heterostructures also represent an exciting area to explore new physics. The physics of material interfaces lies at the intersection of lattice, charge, spin, and orbital degrees of freedom, providing a wealth of possibilities to explore [35–37]. This concept is shown schematically in Fig. 1.8(b), where a heterogenous perovskite interface can take on properties which are not present in either bulk form. To provide just one example, the interface between insulating $LaAlO_3$ and semiconducting $SrTiO_3$, two well-studied perovskite oxides, forms a highly conductive two-dimensional electron gas or 2DEG [38]. In addition to single interfaces, the above concepts can also be extended to form 'superlattices, which are artificial materials consisting of repeated atomic-scale layering of two or more materials. Superlattices thus leverage the unique interactions at heterogenous interfaces to explore new materials physics and properties [26,36].

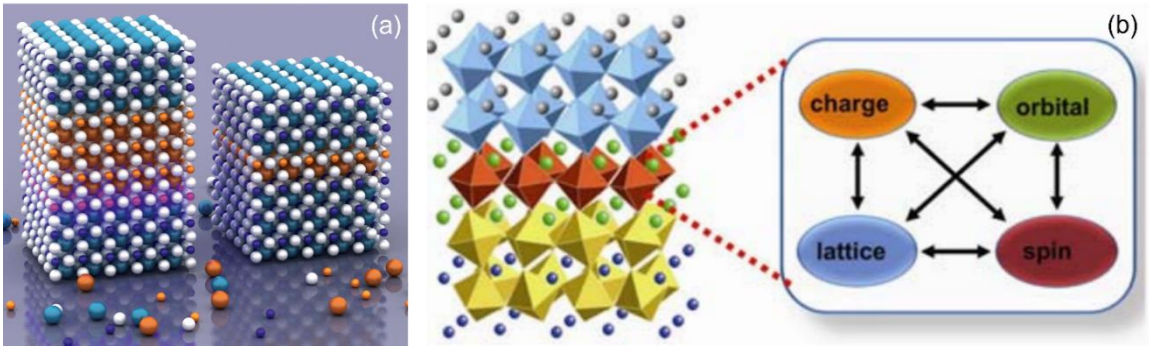

Figure 1.8: (a) Illustration of a perovskite oxide heterostructure made of constituent "building blocks" to achieve a functional heterointerface (pink layer in left block) [39]. (b) Conceptual schematic highlighting the physical interactions (charge, orbital, lattice, and spin degrees of freedom) at perovskite heterointerfaces that can give rise to unique properties [35].

1.2 La- and Sr-based perovskite cobaltites

La^{3+} and Sr^{2+} cations have similar ionic radii but differ in charge by one *e*. Therefore, alloying (also sometimes referred to as 'doping') Sr^{2+} for La^{3+} in perovskites does not greatly perturb the structure, nor induce A-site cation ordering. Such chemical substitution can be used to effectively tune the valence and thus orbital filling on the B-site TM, leading to a range of interesting and useful properties. The $La_{1-x}Sr_xCoO_{3-\delta}$ system is one of the most widely studied such systems, largely owing to the unique magnetic properties of Co. This section serves to introduce the basics materials physics across the phase diagram of $La_{1-x}Sr_xCoO_{3-\delta}$, with especial focus on the impact of oxygen non-stoichiometry (δ) that comes into play at higher *x*.

1.2.1 $LaCoO_3$ bulk and thin films

The $x = 0$ parent compound of $La_{1-x}Sr_xCoO_{3-\delta}$ (LSCO), $LaCoO_{3-\delta}$ (LCO), is historically one of the most well-studied cobaltites due to its unique spin state transitions [40–45]. In bulk LCO, $\Gamma \approx 0.88$ resulting in rhombohedral symmetry (space group $R\bar{3}c$). Its crystal structure features slight distortion from the ideal cubic, with Co-O-Co bond angles of ~164° [46] and pseudocubic lattice parameter ~3.81 Å [47,48]. Additionally, oxygen non-stoichiometry (δ) in LCO is typically very small due to the relative stability of the Co^{3+} valence state. In terms of properties, LCO is a diamagnetic $3d^6$ ($t_{2g}^6 e_g^0$) insulator in its ground state (at $T = 0$). However, as mentioned in Section 1.1.2 the magnetic ground state evolves to paramagnetic on warming, with finite Co spin states, IS ($t_{2g}^5 e_g^1$) and/or HS ($t_{2g}^4 e_g^2$), appearing above ~30 K. The system remains electrically insulating until high *T*, where a second spin state transition is accompanied by a broad insulator-to-metal transition at ~500 K (see Fig. 1.10(a)). The nature of this metal-insulator transition (MIT) remains a subject of active research.

Also alluded to earlier, LCO additionally provides one of the most well-known examples of ground state differences between bulk and thin films, where LCO films grown under tensile strain are ferromagnetic [33,47–51]. More recent studies also revealed a majority carrier inversion depending on the sign of the strain [48]. The exact origins of these effects remain subject to some controversy but one contributing factor is undoubtedly

the presence of (ordered) V_O in LCO films [47,48,50,51]. V_O, which are positive doubly charged point defects, generally expand the lattice of perovskite oxides, and preferential ordering can thus serve to alleviate epitaxial strain in thin films [52–54]. Fig. 1.9(a) and (b) show examples of this effect for films of $LaCoO_{3-\delta}$ grown on $LaAlO_3$ (LAO) (a) and $SrTiO_3$ (STO) (b) substrates from cross-sectional scanning transmission electron microcopy (STEM) images. The dark stripes indicate rows of ordered V_O perpendicular to the interface for STO (tensile strain) and parallel for LAO (compressive strain) [47].

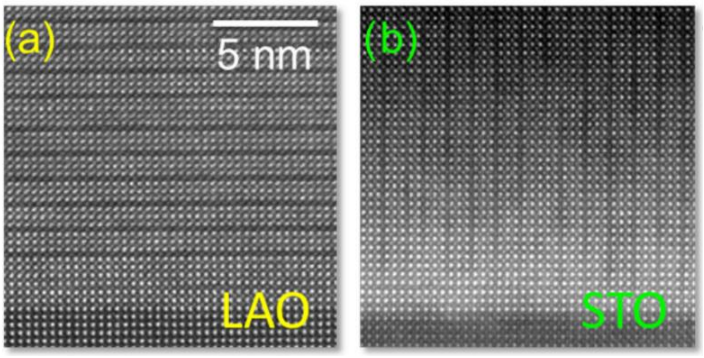

Figure 1.9: High-resolution STEM images of the film / substrate interface of $LaCoO_{3-\delta}$ thin films on $LaAlO_3$ (LAO) (a) and $SrTiO_3$ (STO) (b) substrates. LAO provides in-plane compressive strain, causing expansion of the film out-of-plane, while STO provides in-plane tensile strain. The dark stripes in the images correspond to V_O-ordered planes. Adapted from Ref. [47].

1.2.2 Sr doping of $LaCoO_3$: $La_{1-x}Sr_xCoO_{3-\delta}$ at low x

When trivalent La^{3+} are substituted by divalent Sr^{2+} in the LCO lattice they introduce h^+, which then leads to unpaired electrons on Co and additional thus magnetic interactions. At very low x ($0 < x < 0.04$), the unpaired electrons on isolated Co sites lead to exotic magnetic phenomena known as spin-state polarons [41,55–57]. In essence, the finite spin of a central isolated Co then induces spin in its neighbors, resulting in seven-site magnetic polarons that can exhibit very high spin [41,55–57]. As x further increases, these polarons begin to interact and form 'clusters' of small F (metallic) regions in an otherwise paramagnetic insulating matrix. The formation of such mixed phase states is commonly referred to as magneto-electronic phase separation (MEPS). These clusters, and their overall volume fraction, grow as x further increases, eventually reaching percolation around $x \approx 0.18$ producing a long-range F state [58–61]. Finally, further Sr doping leads to the elimination of MEPS, resulting in a uniform F metallic state for $x > 0.22$ [61,62]. The electrical resistivity (ρ) *vs.* T of LSCO of various x ($0 \leq x \leq 0.3$) is shown in Fig. 1.10(a).

The *x vs*. *T* magneto-electric phase diagram (from $0 \leq x \leq 0.5$) is then shown in Fig. 1.10(b), along with schematic illustrations of the percolative transition with increasing *x* (right side) [63]. In totality, hole doping of LCO with Sr (LSCO) drives a transition from diamagnetic insulator to ferromagnetic metal.

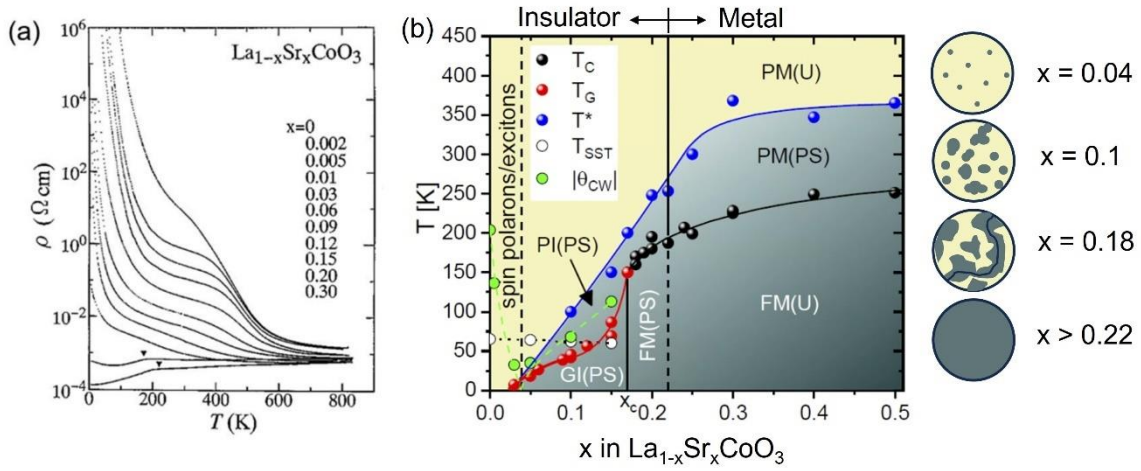

Figure 1.10: (a) Resistivity (ρ) *vs*. temperature (*T*) for various Sr doping levels (*x*) in bulk $La_{1-x}Sr_xCoO_{3-\delta}$ [43]. (b) The phase diagram of $La_{1-x}Sr_xCoO_3$ for $0 \leq x \leq 0.5$, showing the magnetic regions (teal) and paramagnetic regions (yellow). I = insulator, M = metal, G = glassy ferromagnet, P = paramagnetic, F = ferromagnetic, PS = phase separated, and U = uniform. The various magnetic transitions *vs. T* are indicated by the colored points, x_c denotes percolation threshold, and the solid / dashed vertical line at ~0.22 indicates the MIT. Adapted from Ref. [63].

In addition to the above described magnetic and electronic phase transitions with *x*, LSCO also undergoes a relatively subtle structural change on Sr doping. Substitution of La^{3+} with the slightly larger Sr^{2+} ion reduces the rhombohedral distortion of LCO, increasing Γ and thus the Co-O-Co bond angles towards 180° until a transition to cubic takes place at $x \approx 0.5$ [46,59,64,65]. The cubic structure at $x = 0.5$ has a lattice parameter ~3.836 Å [52]. The structure then remains cubic all the way to the terminal (nominally stoichiometric) parent compound at $x = 1$, $SrCoO_{3-\delta}$ (SCO).

1.2.3 $La_{1-x}Sr_xCoO_{3-\delta}$ at high x and oxygen non-stoichiometry δ

It should be noted that the phase diagram of Fig. 1.10(b) is only plotted to $x = 0.5$. This is primarily due to the difficulty in fabricating high-*x* LSCO samples with ideal oxygen stoichiometry ($\delta \approx 0$). As mentioned above, increasing Sr content in LSCO serves to increase the effective Co valence, but only up to a point. Due to the instability of the Co^{4+} valence state, at high *x* LSCO spontaneously forms V_O defects. These V_O then act as

electron donors according to defect reaction: $O_O^x \rightarrow V_O^{\cdot\cdot} + 2e'$ (in Kroger-Vink notation). The electrons (e^-) donated by V_O then compensate Sr-doped h^+ lowering the Co valence. This phenomenon was originally documented in early work by Jonker and Van Santen in 1953 [66]. Fig. 1.11(a) shows the Co valence as a function of x for samples annealed in air at 1200 °C (reproduced from Ref. [66]). The percentage of Co^{4+} was determined by dissolution in acid and subsequent titration measurements; the Co valence is then simply 3 + (Co^{4+}%/100%). From Fig. 1.11(a), the Co valence clearly begins to deviate from the nominal Sr-doped value, *i.e.*, 3 + x (dashed line), around $x \approx 0.4$, and by $x = 0.8$ the cobalt valence is trending back down toward ~3. At high x, δ (red points, right axis) is thus trending up toward 0.5, where brownmillerite (BM) is the most stable form at $x = 1$ (*i.e.*, $SrCoO_{2.5}$). Another way to understand this effect is in terms of the thermodynamics of V_O formation as shown in Fig. 1.11(b), where the enthalpy of formation of an V_O (ΔH_{Vo}) is plotted as a function of x. From the figure, ΔH_{Vo} decreases significantly with x, reaching its lowest at $x = 1$ (but is still very low, less than 1 eV even at $x \approx 0.5$) [104,150]. The kinetics of oxygen diffusion in LSCO also strongly depend on x; the diffusivity of oxygen / V_O increasing significantly with x [105]. The tendency of high x LSCO (and related cobaltites / ferrites) to accommodate high δ and fast oxygen transport are primary drivers for the study of these compounds in applications, such as oxygen evolution reaction (OER) catalysis, SOFCs, and mixed ion electron conductors (MIECs) [67,69–71].

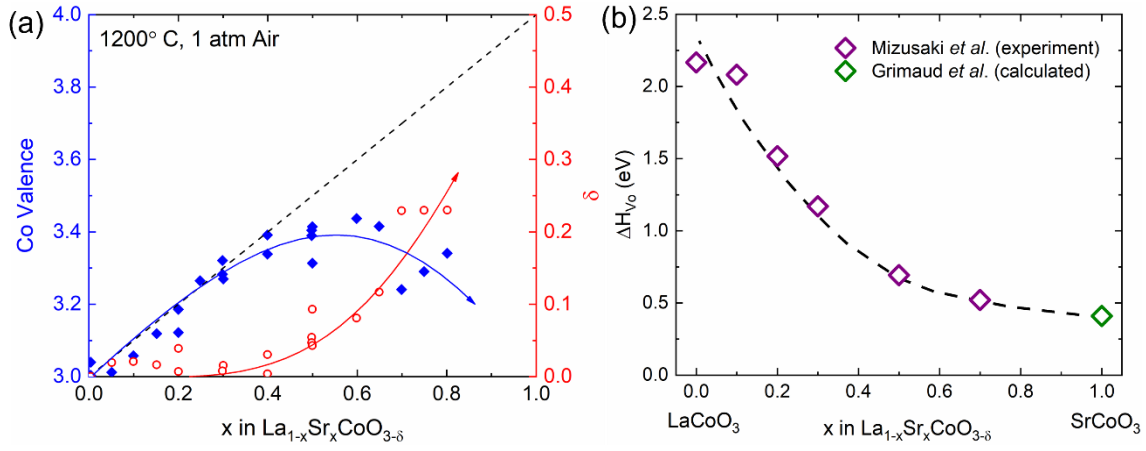

Figure 1.11: (a) Co valence in LSCO as a function of the nominal Sr level, x, after 1200 °C thermal treatment in air (adapted from [66]). The red points (right-hand axis) were calculated from the blue points using the relation: $V_{Co} = x - 2\delta$, to show the increasing oxygen deficiency at high x. (b) Experimental (purple) and theoretical (green) results taken from the literature [67,68] for the enthalpy of formation of an oxygen vacancy (ΔH_{Vo}) in LSCO as a function of x. Note the much lower energy cost to form V_O at high x.

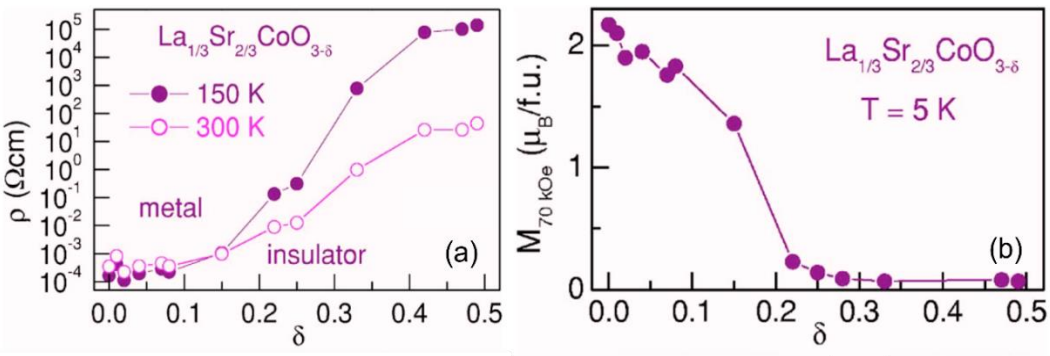

Figure 1.12: (a) resistivity (ρ) *vs*. oxygen non-stoichiometry (δ) in bulk $La_{0.33}Sr_{0.67}CoO_{3-\delta}$. Open points represent 300-K ρ, while solid points represent 150-K ρ. (b) 70 kOe magnetization ($M_{70\ kOe}$) *vs*. δ, at 5 K, for the same samples as in (a). These results outline the metal → insulator and F → weak F transitions as δ is increased. Adapted from Ref. [72].

In terms of V_O-ordered structures, the LSCO family is less well studied than the x = 1 parent compound SCO, which is discussed in the following section. However, trends in ΔH_{Vo} with x, for example, point toward similar oxygen deficiency and V_O ordering characteristics. Ramesh *et al*. reported brownmillerite-like structures in ammonia-reduced bulk x = 0.5 and x = 0 [73]. While, Van Doorn and Burggraaf observed a phase separation between full-oxygen-stoichiometric regions and regions of a V_O-ordered $a_c \times a_c \times 2a_c$ superstructure in $La_{0.3}Sr_{0.7}CoO_{3-\delta}$ [64]. In 2006, Kolesnik *et al*. used a variety of thermal treatments to systematically explore the properties in oxygen deficient LSCO, from the starting point of x = 0.67 [72]. As shown in Fig. 1.12(a), a MIT was observed at $\delta \approx 0.15$, near the boundary with the cubic phase. At higher δ, the starting perovskite structure transitioned to an intermediate tetragonal phase corresponding to $\delta = 0.25$. This intermediate phase was related to the cubic perovskite by the relationship: $a_t = 2a_c$, and $c_t = 4a_c$, and was thus dubbed '224'. This phase was determined to be a G-type AF by neutron powder diffraction (NPD), with T_N above room temperature (~360 K). Finally, the structure transformed to phase-pure BM by $\delta \approx 0.5$, which was indexed to the orthorhombic space group *Icmm* (with CoO_4 tetrahedral chains running along the [010] direction). Both the 224 and BM phases were found to exhibit weak F signals, with Curie temperatures (T_C) of ~220 K and ~120 K, respectively, and saturation magnetization (M_s) ~0.1 μ_B/Co for both phases. Fig. 1.12(b) shows the reported high-field magnetization (*M)* of each sample as a function of δ. Note that the high-field *M* in Fig. 1.12(b) never drops below ~0.1 μ_B/Co, even at δ = 0.5. In the case of the 224 phase, the authors attributed the weak F state to a non-collinear,

i.e., 'canted', AF structure. The magnetic structure of the BM was not probed by NPD, but a large, negative Curie-Weiss temperature was determined from magnetometry indicating dominating AF interactions.

1.2.4 $SrCoO_{3-\delta}$ and its oxygen-vacancy-ordered derivatives: $0 < \delta < 0.5$

Strontium cobaltite, $SrCoO_{3-\delta}$ (SCO), is an archetypal oxygen-deficient perovskite. Sometimes referred to in the literature as $SrCoO_x$, the structure of SCO can accommodate a very wide range of oxygen deficiency ($0 < \delta < 0.7$) and has been studied since the 1950s [74]. Early work on SCO reported that high oxygen stoichiometry samples, *i.e.*, samples with $\delta \approx 0$, are difficult to fabricate and spontaneously reduce in ambient [75–77]. Indeed, only recently have SCO single crystals of near full oxygen stoichiometry ($\delta \approx 0.05$) been synthesized, requiring extremely high oxygen pressures and the presence of strong chemical oxidizers [78]. The stoichiometric perovskite SCO (P-SCO) forms a cubic crystal structure (a = 3.83 Å) and is a F metal, with low-T resistivity as low as ~40 μΩ cm, $T_C \approx$ 305 K, and $M_s \approx 2.5\ \mu_B$/Co [78,79]. The origins of the F metallic ground state of P-SCO are thought to originate from its small (or even negative) charge-transfer gap (Δ_{CT}) and subsequent 'self-doping' [76,80–84]. The concept of a negative Δ_{CT} is shown schematically in the orbital bonding energy diagrams of Fig. 1.13, where panel (a) shows the typical charge transfer ($\Delta_{CT} > 0$) crystal field splitting and (b) shows the case when Δ_{CT} is negative. When the 2*p* orbitals of the O^{2-} ligand field lie close in energy to the 3*d* orbitals of Co, their hybridization leads to states where 2*p* orbitals of oxygen can contribute to conduction. In a band diagram picture, this constitutes the Fermi level dropping into the O 2*p*-dominated valence band. From an ionic perspective, the Co valence in P-SCO may not take the nominal 4+ but rather a combination of 3+ and a hole (h^+) tied to the oxygen (*i.e.*, O^- rather than O^{2-}), which is referred to as a 'ligand hole' ($\underline{L}$). When the other energies of the system are considered, this leads to a likely magnetic ground state of $3d^6\underline{L}$ ($t_{2g}^4 e_g^2$) intermediate spin (IS), although this is still a matter of debate [78,79,81,83–85].

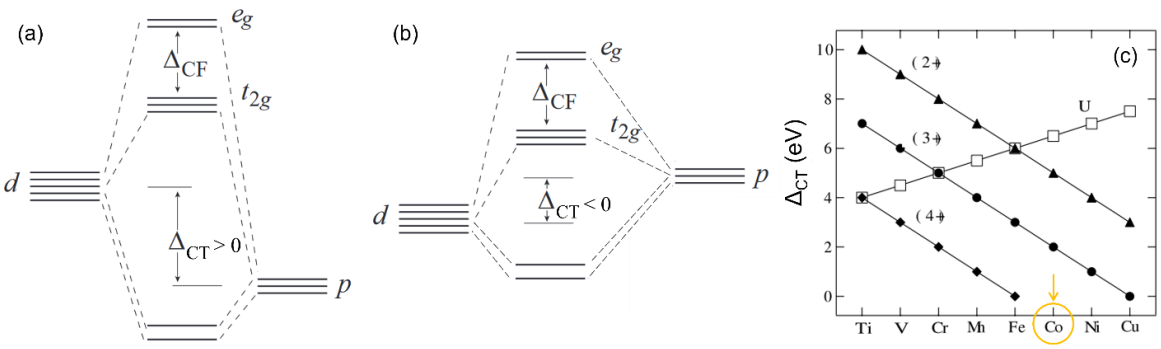

Figure 1.13: (a) and (b) show crystal field theory energy diagrams illustrating the influence of the charge transfer gap (Δ_{CT}) on the hybridized TM 3d - O 2p orbitals (adapted from Ref. [31]). (a) shows $\Delta_{CT} > 0$, whereas (b) shows $\Delta_{CT} < 0$. (c) Δ_{CT} for different 3*d* TMs at different nominal valence. The Hubbard "*U*" representing the strength of on-site e^--e^- repulsion is also shown for reference. Adapted from Ref. [80].

As shown in Fig. 1.13(c), low or negative Δ_{CT} oxides feature heavy 3*d* TMs with high valence [80,86]. This situation not only leads to the self- (hole) doping, and thus metallic F properties outlined above, but also influences the thermodynamic stability of the crystal. Like in high *x* LSCO, in SCO it becomes more energetically favorable to form V_O point defects rather than to form Co^{4+} (or $Co^{3+}\underline{L}$) in the octahedral crystal field. In general, the energy associated with V_O formation is very low in high-valence cobaltites [87]. As shown above in Fig. 1.11(b) ΔH_{Vo} in P-SCO has been calculated to be as low as 0.4 eV [67].

Not only does P-SCO feature very low ΔH_{Vo} and prefers high oxygen deficiency under ambient conditions, it also boasts among the highest values of 300-K oxygen diffusivity (D_O) known in perovskites, with 300-K $D_O \approx 10^{-11}$ cm^2 s^{-1} [17,69,75,88]. In general, oxygen diffusion in perovskites proceeds *via* a vacancy migration mechanism (interstitial diffusion is kinetically unfavorable due to Coulombic effects and size constraints) and can be expressed by the following equation [89]:

$$D_O = D_{Vo}\frac{[V_O]}{[O]} \approx D_{Vo} n_V, \tag{1.3}$$

where $[V_O]$ and $[O]$ are the respective concentrations of V_O and O lattice sites and n_V is their approximate ratio. In stoichiometric perovskites ($\delta \approx 0$), $n_V << 1$, making D_{Vo} many times greater than D_O. In oxygen deficient perovskites, however, n_V can be as high as ~ 0.1 making oxygen much more mobile. Eq. 1.3 corresponds to the case of concentration-gradient diffusion only. However, oftentimes there is also a chemical potential gradient as

well. This situation is termed 'chemical diffusion' and in the case of electronic conductors (*i.e.*, $D_{e^-} >> D_{Vo}$), in which electroneutrality is maintained by $e' = \frac{1}{2} V_O^{\cdot\cdot}$, the expression for D_O can be simplified to the following [89]:

$$D_{O,chem} = 3D_{Vo} \,. \tag{1.4}$$

Note that Eq. 1.4 corresponds to the special case where the activation enthalpy for diffusion is equal to the migration barrier enthalpy (ΔH_m) [89]. In either case, the critical value to understand oxygen mobility in these systems is the diffusivity of an oxygen vacancy, D_{Vo}.

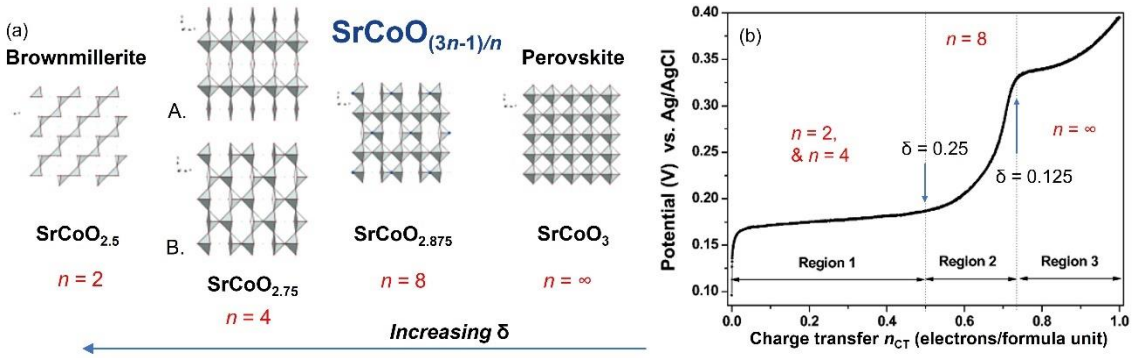

Figure 1.14: (a) V_O-ordered structures of $SrCoO_{(3n-1)/n}$ as a function of n, from $n = 2$ to $n = \infty$ (left to right) in one experimental study on bulk SCO (adapted from Ref. [90]). The progression from left to right shows the sequential alteration of a fully CoO_4 tetrahedral plane ($n = 2$, brownmillerite, left) as it is oxidized and eventually transformed to the fully CoO_6 octahedral perovskite (right). (b) shows the electrochemical potential of an electrochemical cell *vs.* charge transfer (n_{CT}) describing the oxidation of $SrCoO_{2.5}$ [where $n_{CT} = 1 - 2\delta$ (as in $SrCoO_{3-\delta}$)]. The different V_O-ordered phases (designated by red "n = ") are shown for different regions of the charge transfer curve [90].

In stoichiometric perovskites, V_O form as dilute non-interacting point defects, *i.e.*, $n_V << 1$. However, as n_V increases, the average V_O-V_O distance decreases. For example, at a δ value of 0.1, the average distance between V_O becomes ~1 nm. At these concentrations, interactions between V_O can lead to local V_O-ordering and eventually long-range V_O-ordered superstructures. In fact, in bulk SCO, the n = 2, 3, 4, 5, 6, 7, and 8, members of the oxygen deficient series $ABO_{(3n-1)/n}$ have been observed [77,90–92]. Fig. 1.14(a) shows the progression of different V_O-ordered crystal structures in SCO as a function of δ, as observed from *in situ* neutron powder diffraction (NPD) experiments involving electrochemical oxidation of a starting BM $SrCoO_{2.5}$ sample [77,90]. Note that in Fig. 1.14(a) only one plane of polyhedra is shown to more clearly track the changes from $n = 2$ (fully tetrahedral CoO_4, left) to $n = \infty$ (fully octahedral CoO_6, right). Note also, the two

distinct polymorphs of the $n = 4$ phase, marked "A" and "B". The authors point to a possible mixture of both "A" and "B" to explain a lack of long range V_O order in their oxidized $SrCoO_{2.75}$ sample [90]. Fig. 1.14(b) shows the electrochemical charge transfer (n_{CT}) as a function of cell potential during the oxidation reaction, where the various n structural phases (as determined by NPD) are marked in each region.

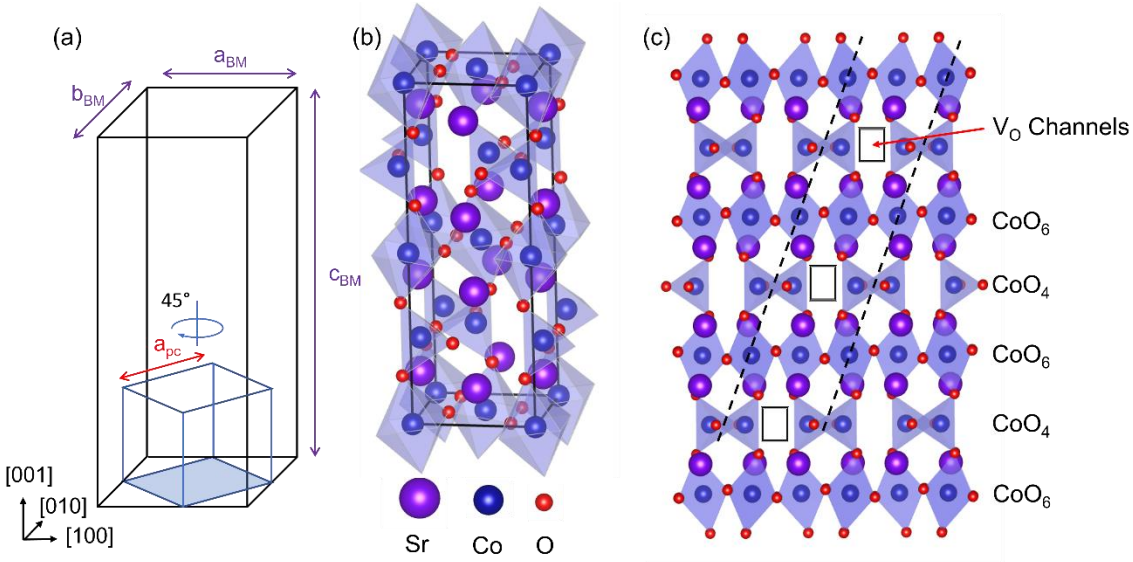

Figure 1.15: (a) The relationship between the orthorhombic unit cell of brownmillerite (BM) $SrCoO_{2.5}$ (black box) and its pseudocubic cell (blue box). (b),(c) Alternate representations of the BM-SCO structure. (b) shows a typical 3D-projected perspective, while (c) is looking down the $[1\bar{1}0]$ direction to more clearly illustrate the V_O channels (black boxes) and stacking sequence of the octahedra / tetrahedral layers.

Of the $SrCoO_{3(n-1)/1}$ homologues, $n = 2$, or BM $SrCoO_{2.5}$ (BM-SCO), is by far the most well studied. The brownmillerite structure, introduced in Section 1.1.1, consists of alternating layers of CoO_6 and CoO_4. Additionally, in BM-SCO, the tilt patterns produce a slightly orthorhombic symmetry with $a_{BM} = 5.470$, $b_{BM} = 5.574$, $c_{BM} = 15.875$ Å (space group I*ma*2) [93]. The symmetry of BM-SCO is related to the pseudocubic perovskite unit cell by a 45° rotation in the *ab* plane and a quadrupling of the *c*-axis lattice parameter. This relationship is shown schematically in Fig. 1.15(a). The pseudocubic lattice parameter, a_{pc}, can thus be expressed by the following relations: $a_{pc} = (a_{BM} + b_{BM})/2\sqrt{2}$ *or* $a_{pc} = c_{BM}/4$. Fig. 1.15(b),(c) then show the BM-SCO structure from other perspectives, panel (c) highlighting the alternating CoO_6-CoO_4-CoO_6 stacking and the 'V_O channels' that run in the $[1\bar{1}0]$ crystallographic direction. These channels run parallel to the tetrahedral chains and provide low-energy-barrier interstitial sites for fast ion diffusion [94]. Interestingly,

however, the diffusion of oxygen in BM is slower than in P. Although ΔH_m, is thought to be similar between P- and BM-SCO (0.5 *vs.* 0.6 eV, respectively), the latter has significant anisotropy [94,95]. Indeed, the BM strongly favors diffusion along the 1D V_O channels, while the P exhibits nearly isotropic 3D diffusion [94]. Except in the special case where the direction of diffusion is coincident with the V_O channels, this lower dimensionality for diffusion thus *guarantees* a slower overall oxygen diffusivity for BM compared with P, which has been noted experimentally [17,75,77,96].

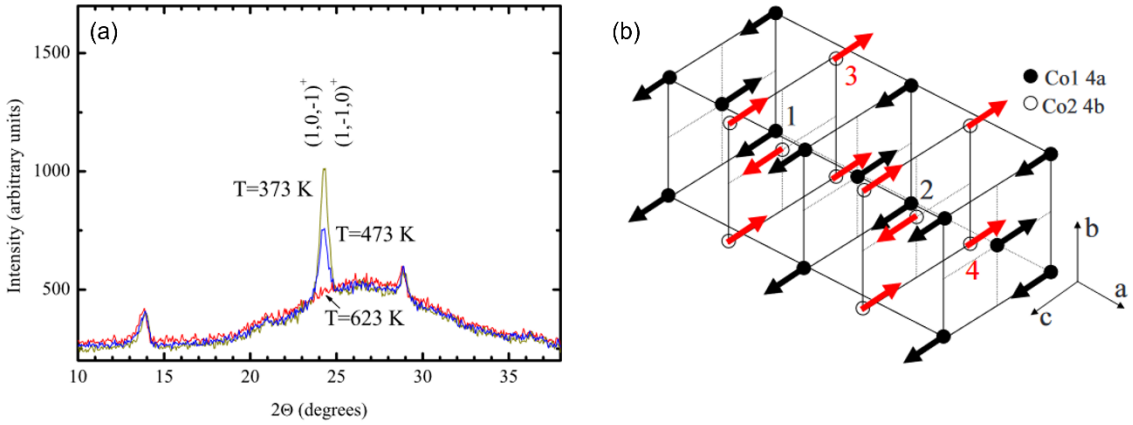

Figure 1.16: (a) Neutron powder diffraction of brownmillerite (BM) $SrCoO_{2.5}$ around the most intense magnetic doublet peak [$(1,0,-1)^+$ and $(1,-1,0)^+$]. This peak is characteristic of G-type antiferromagnetic order and thus disappears above the Néel temperature (~540 K) [93]. (b) Schematic diagram of the magnetic ordering in BM-$SrCoO_{2.5}$. For clarity, only Co sites are shown. Note the long axis of the structure is in the "*a*" direction. Adapted from Ref. [93].

BM-SCO is a charge-transfer insulator, owing to its small Δ_{CT} and relatively high e^--e^- repulsion (or Hubbard "*U*"), with a band gap of ~0.4 - 2.1 eV [97–99]. According to the GKA rules, BM-SCO is expected to have strong AF ordering mediated by superexchange through its near-180° Co-O-Co bonds. The AF order of BM-SCO was first characterized *via* NPD by Takeda *et al*., and later Grenier *et al*., who both found G-type AF with $T_N \approx 550$ - 570 K [100–102]. A later report by Muńoz *et al*. found $T_N \approx 540$ K with moments on the two distinct Co sites of ~3 μ_B/Co [93,100,103]. Additionally, the ground state electronic structure was determined to be Co^{2+} $3d^7\underline{L}$, by density functional theory (DFT) calculations, with both the octahedrally and tetrahedrally coordinated Co in HS, *i.e*., $S = 3/2$ [93]. The findings from the latter study are summarized in Fig. 1.16(a) and (b). In panel (a), NPD results show the magnetic doublet peak (labeled $(1,0,-1)^+$, $(1,-1,0)^+$) consistent with a G-type AF ordering and its disappearance at $T = 623$ K (above T_N). In

panel (b), a schematic of the G-type AF ordering on the Co sites is shown. As a final note on the magnetic properties of SCO, only one study has so far sought to experimentally investigate the magnetic properties as a function of δ. In their study, Xie *et al*. found evidence of magnetic phase separation between of $n = 4$ and $n = 8$ $SrCoO_{3(n-1)/1}$ (*i.e*., $\delta = 0.25$ and $\delta = 0.125$, respectively), and noted that F persists down to at least $\delta = 0.25$ [104].

1.2.5 $La_{1-x}Sr_xCoO_{3-\delta}$ and $SrCoO_{3-\delta}$ thin films

While the previous sections describe the properties of bulk LSCO, significant differences arise in properties of thin films, which are the focus of this thesis. Therefore, the following subsections serve to provide an overview of the strain, oxygen non-stoichiometry effects, and associated materials properties found in LSCO thin films.

1.2.5.1 Strain and oxygen-vacancy-ordering in perovskite films

The concept of strain-induced V_O-ordering was introduced in Section 1.2.1, with the example of LCO films forming oxygen deficient planes either parallel or perpendicular to the substrate interface depending on the sign of the strain (see Fig. 1.9). One likely explanation for this phenomenon is as an epitaxial-strain-relaxation mechanism, *i.e*., V_O-ordered planes expanding the lattice in the orthogonal direction, reducing strain energy at a lower energy cost than forming other defects, *e.g*., dislocations [53,54]. In LSCO, the V_O concentration and specific ordering pattern/periodicity is determined by the sign of the strain, the strain magnitude, and x (the Sr doping). The film properties are then a combination of the nominally stoichiometric ($\delta = 0$) bulk properties and the perturbations caused by the combined effects of the V_O, V_O-ordering, and strain. In LCO films, compressive *vs.* tensile strain causes a majority carrier inversion and 100-fold difference in 300-K ρ [48]. In $x = 0.5$ LSCO, V_O ordering is similar to LCO but with different periodicity. Comparing Fig. 1.17(a) to Fig. 1.9(b), one can see that the spacing between the dark stripes is 1 unit cell ($n = 2$) for $x = 0.5$, while for $x = 0$ it is 1.5 unit cells ($n = 3$). Fig. 1.17(b) then shows the V_O ordering in LSCO on (110)-type substrates, showing V_O-ordered planes running at 45° angles to the interface. While the STEM images of Fig. 1.17(a),(b) show the $n = 2$ periodicity, $\delta \neq 0.5$ as in BM. In fact, in a 45-nm $x = 0.5$ LSCO film on STO, δ was estimated to be ~0.13, based on comparison with bulk electron energy loss

spectroscopy (EELS) O K-edge spectra [105]. Using this method, O concentration was also tracked as function of depth (Fig. 1.17(c)), finding the largest δ in the bottom ~10 nm of the film [105]. This causes a 'dead layer' effect (shown schematically in Fig. 1.17(d)), where the higher V_O concentration near the substrate interface depletes local hole doping, reducing the 'effective' x (*i.e.*, $x_{eff} = x - 2\delta$) and driving the low thickness region toward the insulating / MEPS state [105].

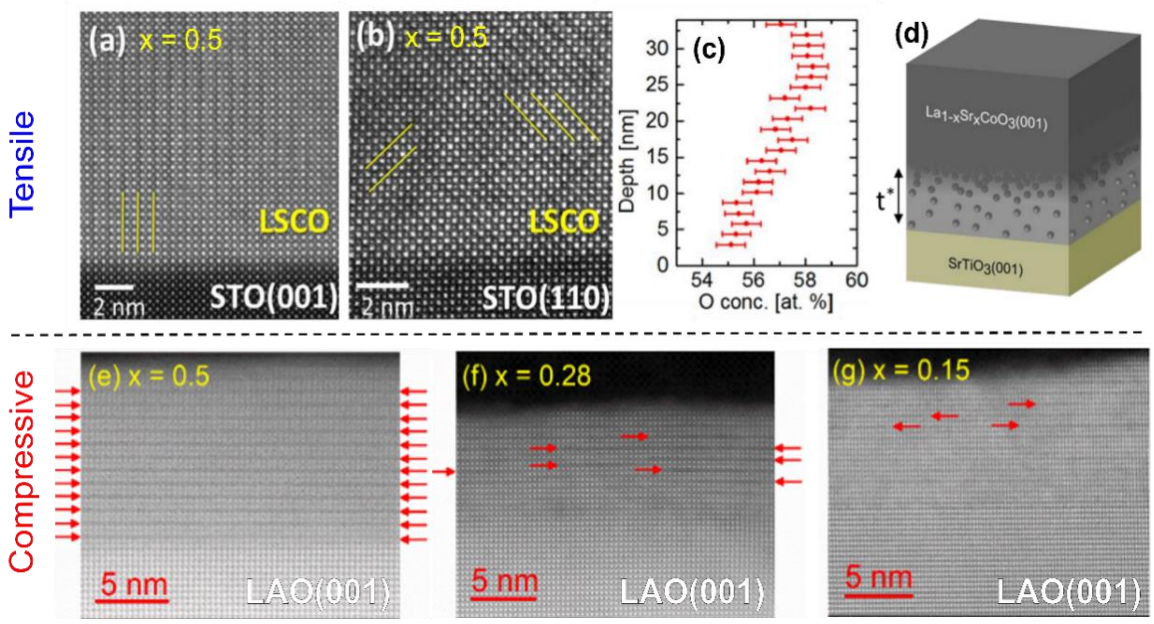

Figure 1.17: (a),(b) High resolution STEM images of the film/substrate for x = 0.5 LSCO films on STO(001)(a) and STO(110)(b). The (001) orientation leads to vertical V_O-ordered planes (marked by yellow lines), while the (110) orientation leads to 45° ordering [52]. (c) O-concentration (determined from comparison of O K-edge EELS spectra to bulk data) as a function of depth in a STO/LSCO film, showing significantly less O near the interface with the substrate [105]. (d) Schematic representation of the 'dead layer' effect in LSCO films, where V_O near the interface deplete holes, reducing the effective doping level and causing local MEPS below a critical thickness, t^* [106]. (e)-(g) STEM images of compressively strained LSCO films on LAO(001) for x = 0.5 (e), 0.28 (f), and 0.15 (g) [107]. The V_O planes are indicated by red arrows.

The effect of varying x is shown next in Fig. 1.17(e)-(g), this time for films under compression on LAO [107]. For x = 0.5, clear n = 2 periodicity is observed throughout the film. As x is decreased to 0.28, this periodicity remains ~2 but the distributions are clearly less homogenous, as evidenced by the varying intensity of the O-deficient planes. At x = 0.15 this inhomogeneity becomes even more pronounced. And finally, at x = 0 (Fig. 1.9(a)), the average periodicity increases to ~3, indicating an overall lowering of V_O concentration.

The trends in Fig. 1.17(e)-(g) are likely due to the combination of higher ΔH_{Vo} and lower strain at low x.

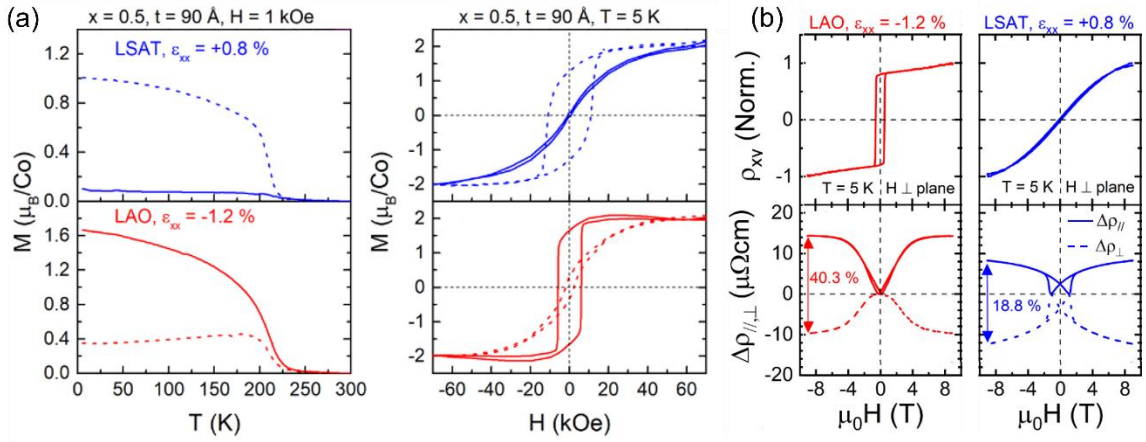

Figure 1.18: (a) *M vs*. *T* (left) and *M vs*. *H* (right) for x = 0.5 LSCO films under tensile strain (LSAT: blue, top) and compressive strain (LAO: red, bottom), showing the clear preference for *M* out-of-plane for films on LAO [107]. (b)-top panels, transverse resistivity (ρ_{xy}) *vs*. out-of-plane magnetic field ($\mu_0 H$), (b)-bottom panels, $\Delta\rho$ *vs*. in-plane $\mu_0 H$ for current parallel (solid lines) and perpendicular (dashed lines) to the field direction. All data were taken at 5 K on x = 0.5 LSCO films on LAO (red) and LSAT (blue) substrates. The epitaxial strain, ε_{xx}, is shown above the top panels for the two substrates. The bottom panels in (b) highlight the extraordinary AMR present in both samples (marked by red and blue arrows, respectively) [108].

The impact of varying V_O concentration / ordering on the observed properties in LSCO films is well-characterized [52,105–109]. The sign and magnitude of the strain, as well as the substrate orientation, influence the dead layer thickness, t^* (Fig 1.17(d)), and thus the film properties at any given t. For example, x = 0.5 LSCO films under compression, *e.g.*, on LAO (–1.2%) and $SrLaAlO_4$ (–2.1%), exhibit lower resistivity and higher T_C [107,109]. Compressively strained films also exhibit perpendicular magnetic anisotropy (PMA), with large anisotropy energy, $K > 5 \times 10^6$ erg/cm^3, for films on LAO where V_O-ordered planes running parallel to the substrate interface are thought to stabilize the out-of-plane magnetization [107]. Fig. 1.18(a) compares the in-plane and out-of-plane $M(T)$ and $M(H)$ for 9-nm-thick LSCO films under both tension on $(LaAlO_3)_{0.3}(Sr_2TaAlO_6)_{0.7}$ (LSAT) and compression on LAO, showing a clear preference for *M* out-of-plane (solid lines) for the latter. Finally, V_O ordering is also thought to give rise to the recently observed giant anisotropic magnetoresistance (AMR) in LSCO films [108]. Fig. 1.18(b) shows the transverse resistivity (ρ_{xy}) *vs*. out-of-plane H and magnetoresisitivty ($\Delta\rho$) *vs* in-plane H [with current parallel (//) and perpendicular ($\perp$) to H] for LSCO films on LAO and LSAT,

where AMR values of 20 - 40 % at 5 K are among the largest reported for any ferromagnetic conductor [108]. In this case, the sign of the strain appears less important, the phenomenon likely originating from symmetry lowering due to long-range V_O-ordered superstructure formation [108].

Moving to x = 1 (SCO), the properties of thin films are also well-studied [79,97,110–120]. However, highly oxygenated P-SCO films (low δ) are notoriously difficult to achieve [116,118,120]. Therefore, growth of BM-SCO films and subsequent oxidation to P is often the preferred route [79,97,111–120]. P-SCO films grown on substrates with small strain magnitude are opaque, metallic, and F, with ρ and M highly dependent on the precise oxygen stoichiometry [79,97,110–116,118,119]. In fully stoichiometric P-SCO films on moderately tensile-strained LSAT substrates, ρ reaches ~40 μΩ cm, even lower than bulk single crystals [79]. While under large tensile stain on $DyScO_3$ substrates (+3.0%), a rare robust F ($M_s \approx 1.6$ μB/Co) insulating ground state was observed [118]. Similar to x = 0.5 P-LSCO, compressively strained P-SCO films grown on LAO were found to exhibit PMA, again with high K, ~10^6 erg/cm^3 [116]. Substrate induced strain effects also significantly impact the formation and mobility of V_O in SCO films [120]. Hu *et al*. showed that the BM → P transition T in high-pressure O_2 atmosphere and the P → BM transition T in vacuum, both strongly depend on the strain state of the film, with high strain magnitudes (both tensile and compressive) destabilizing the P phase [120]. Interestingly, P-SCO seems to be unusually stable on STO, which exhibits a significant tensile strain with respect to the P (+1.8%) but is essentially lattice matched to the BM [132,134]. In terms of V_O-ordering, similar trends to those outlined in Fig. 1.17 have been observed in SCO films, particularly for δ = 0.5 BM [121–123].

1.2.5.2 Brownmillerite films and the P-BM transformation

Thin films of LSCO have also been studied in the V_O-ordered BM phase, particularly at x = 1, where BM is significantly more stable than P. In recent years, many research groups have demonstrated growth of high-quality BM-SCO films on a variety of perovskite oxide substrates using primarily pulsed laser deposition [97,112–114,117,118,120–136] (PLD) but also molecular beam epitaxy (MBE) [137,138]. Such

films have been shown to be electrically insulating, non-F, and optically transparent. In addition, BM films at other x in LSCO have also been studied, but their preparation is fundamentally different from $x = 1$. For $x < 1$, films are typically deposited in the P phase and subsequently reduced to the BM phase. This can be done by vacuum annealing [139–141] but has also been reported *via* the deposition of an oxygen-gettering capping layer, *e.g.*, Gd [142,143]. BM-LSCO films have thus been synthesized and characterized for $x = 0$ [139,140] and $x = 0.33$ [141–143]. Meanwhile, $\delta = 0.33$, *i.e.*, the $n = 3$ Grenier phase, has only been observed in $x = 0$ films [139,140].

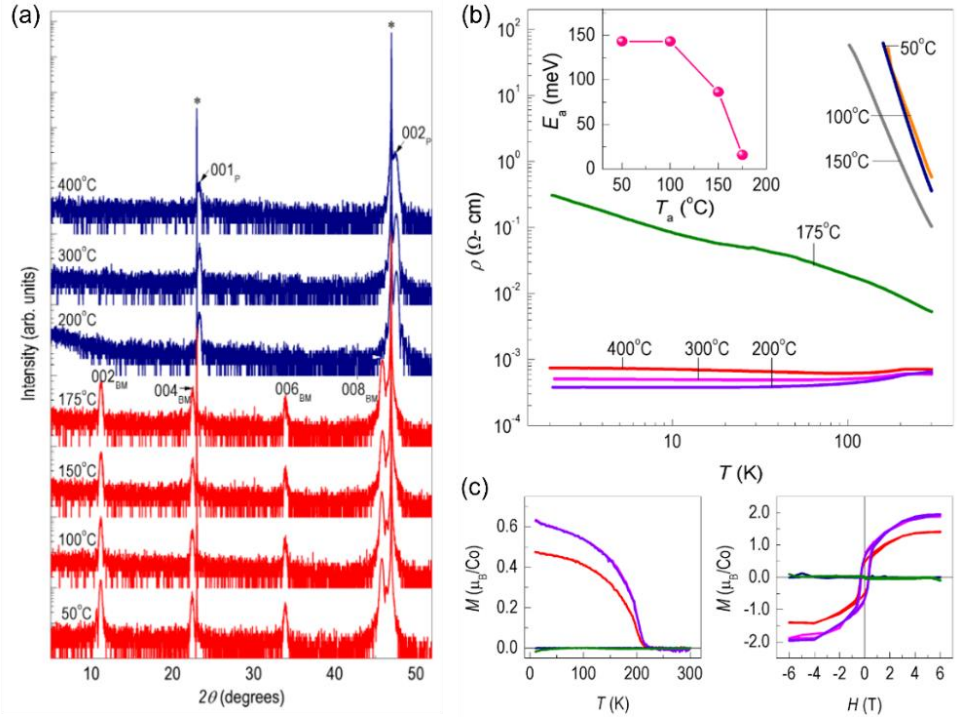

Figure 1.19: (a) X-ray diffraction $\theta/2\theta$ scans of BM-SCO films on LSAT substrates at different anneal temperatures (T) in pure O_2 (500 Torr). The T's are marked along the left side of the figure, and peak indexes are marked for the uppermost red (BM) and blue (P) datasets. (b) resistivity (ρ) *vs*. T, both on $\log_{10}$ scales. The inset shows the Arrhenius-like activation energy (E_a) from linear fits to the high-ρ insulting film data (upper right). (c) magnetization (M) *vs*. T (left) and M *vs*. applied field (H) (right) for the same films color-coded to match (b). Adapted from Ref. [114].

Considering the tendency for LSCO films to form ordered V_O, and even BM, and the clear sensitivity of LSCO material properties to δ, a recent focus has developed around redox cycling of LSCO films. In 2013, Jeen *et al*. showed that BM-SCO thin films could be transformed to a highly oxygenated P phase by thermal oxidation, *i.e.*, annealing in high pressure O_2 [112,113]. Fig. 1.19(a) shows X-ray diffraction (XRD) patterns of BM-SCO thin films annealed at different temperatures in 500 Torr O_2 for 5 minutes [114]. From the

figure, between 175 - 200 °C the structure of the film clearly changes from BM (red) to P (blue). At this *T*, the (002) and (006) film peaks disappear, and the primary perovskite peaks ((001) and (002)) appear upshifted in angle, indicative of the volume contraction upon transformation to P. Fig. 1.19(b) and (c) then show the electronic transport and magnetic property changes, respectively, that occur with increasing O_2 anneal *T*. In Fig. 1.19(b), a MIT can be seen at ~175 °C, and in Fig. 1.19(c) a non-F - F transition is seen near the same temperature, corresponding to an oxygen stoichiometry of ~2.75 [114]. The above demonstration of wide-range electronic and magnetic property modulation *via* topotactic transition in a single film, immediately generated significant research interest around SCO. Many other studies have since confirmed the facile nature of the P-BM transformation in SCO films using various techniques, including thermal treatments [114,118,120,141], chemical oxidizers [119,120,136], electrochemical cells [127], and both solid [117,128–130] and liquid [79,97,122,124–126,131–134] electrolyte gating. As discussed in the following sections, P-BM transformations triggered by gating (*i.e.*, voltage-induced) are particularly attractive for applications.

1.3 Electrolyte gating

As mentioned above, voltage control over materials properties is highly appealing for applications. In this section, I will review the basic concept of the field-effect transistor. I will then introduce the relatively new, but exciting, field of electrolyte gating, covering the basics operating principles of the electric-double-layer transistor. Finally, I will provide a brief review the recent literature on electrolyte gating in cobaltites and conclude by highlighting the advantages and potential applications of electrochemical transistors.

1.3.1 Property modulation and control by external voltage

Designing functional devices based on perovskite oxides for potential applications requires harnessing their exotic properties in a controllable manner, either passively by design considerations, *e.g.*, chemical doping or interface design, or actively by applying an external stimulus as needed, such as temperature, pressure (strain), electronic and/or magnetic fields, photon flux, *etc.* Due to its practical simplicity and energy efficiency, use of an applied voltage to control material properties has been a longstanding goal in science

and engineering. By far the most well-known example of this is the field-effect transistor or "FET". In a FET, a voltage is applied to a gate electrode that then acts on a semiconducting channel to induce or deplete charge carriers, thereby changing the resistance of the device by orders of magnitude. Fig. 1.20(a) shows the basic structure and operating principle of the metal-oxide-semiconductor FET (MOSFET), a transformational device at the heart of the technological boom of the latter half of the 20th century. A key parameter in a field-effect device is the electrostatic screening length which quantifies the depth over which the gate-induced field is felt. This length is often approximated by the semiclassical Thomas-Fermi length (λ_{TF}):

$$\lambda_{TF}^2 = \left(\frac{\pi}{6}\right)^{1/3} \frac{\kappa a_0}{4n^{1/3}m^*} , \qquad (1.2)$$

where κ is the dielectric constant of the material, a_0 the Bohr radius, n the 3D carrier concentration, and m^* the electron effective mass. In semiconductors, where n can be quite small, λ_{TF} reaches appreciable lengths of several nm, allowing relatively thick accumulation / depletion regions in FETs. In metals, $n > 10^{22}$ cm^{-3} (with low κ), making them effectively impervious to the field effect ($\lambda_{TF} << 1$ Å). Functional oxides provide a middle ground in terms of n (typically ~10^{19} - 10^{22} cm^{-3}) and typically higher κ, allowing λ_{TF} of a few unit cells, large enough to make functional devices [144,145].

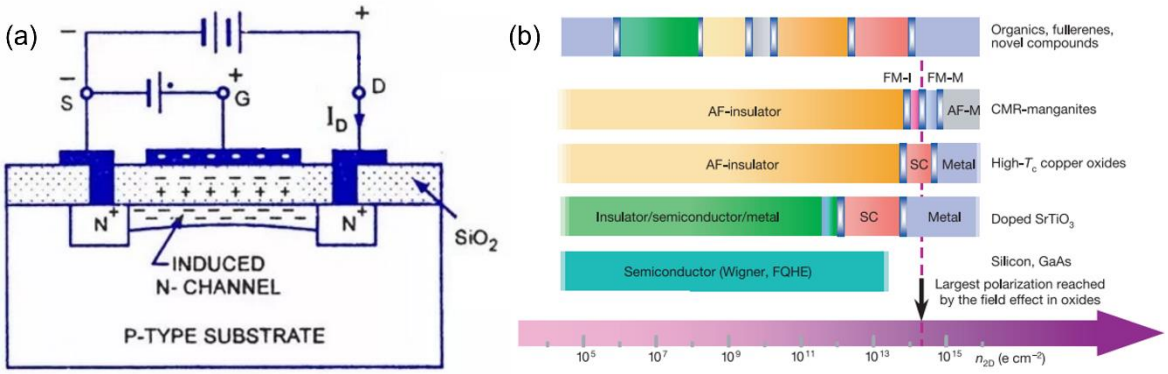

Figure 1.20: (a) Schematic diagram showing the "*npn*" Si/SiO_2 MOSFET operating in accumulation mode [146]. A positive gate voltage induces electrons in the *p*-type channel forming a conductive bridge between the *n*-type electrodes (labelled N^+), thus turning the transistor to the "ON" state. (b) 1D phase diagrams *vs.* areal charge carrier density (n_{2D}) of various materials. In perovskite oxides (middle 3 bars), very large n_{2D} is needed to cross phase boundaries between different electronic/magnetic ground states. SC = superconductor, FM-I = ferromagnetic insulator, FM-M = ferromagnetic metal, AF-M = antiferromagnetic metal. Adapted from Ref. [144].

However, extending the principles of the field effect to modulate the exotic functional properties of complex oxides remains a challenge [144,145]. Practical limitations on fabricating low-defect FET structures aside, inducing electronic phase transitions in highly correlated electronic systems, such as perovskite oxides, requires extremely large modulations of 2D carrier density (n_{2D}). While n_{2D} modulations in Si-based MOSFETs only reach ~10^{13} cm^{-2}, $n_{2D} \approx 10^{14}$ - 10^{15} cm^{-2} are needed to manipulate electronic/magnetic phases in many perovskite oxides systems, *e.g.*, in colossal magnetoresistance (CMR) manganites (like $La_{1-x}Sr_xMnO_3$) and high-T_c superconducting cuprates [43,144,145] (Fig. 1.20(b)). Techniques to increase the n_{2D} modulation above 10^{13} cm^{-2} in field-effect devices include using high-κ and/or ferroelectric perovskites as gate dielectrics [144,145], or replacing the solid-oxide dielectric with an electrolyte. The latter idea will be explained in-depth in the following section.

A promising alternative mechanism to the electrostatic FETs described above is to utilize voltage-induced electrochemistry, *i.e.*, altering materials properties through ionic motion. The concept of 'ionotronics' involves electrochemical intercalation / deintercalation of ions, *e.g.*, H^+, Li^+, O^{2-}, *etc.*, into / out of a channel material to reversibly modulate its properties [147–154]. This mechanism is central to the field of energy storage technology, such as Li-ion batteries and SOFCs, but has also recently been demonstrated as a means to control magnetic properties of various materials, leading to the term 'magnetoionics' [148–154]. Interestingly, the concept of electrolyte-based FETs holds promise for *both* electrostatic- and electrochemistry-driven device function.

1.3.2 The electric-double-layer transistor

As discussed above, the limitations of traditional metal-oxide FETs have driven the search for improved field-effect device structures to control properties in functional oxides. One promising alternative to solid-oxide dielectric gating, known as electrolyte gating has enjoyed much recent success, and has rapidly been extended to many different materials systems [147–149]. Essentially, by replacing the solid-oxide gate dielectric with an electrolyte, that is, a liquid (or solid) containing mobile ions, application of a gate voltage (V_g) induces the accumulation of ions at the gate and channel interfaces. Provided that the

ions cannot penetrate these surfaces, this leads to the formation of electric double layers (EDLs), where one side of an EDL consists of a layer of ions from the electrolyte and the other side consists of electrons or holes accumulated near the interface to balance charge. This process is shown schematically in Fig. 1.21(a) for a positive V_g. The advantage of this technique lies in the small length scale defining the EDL. The EDL can be thought of as an effective nanometer-scale capacitor, leading to extremely large specific capacitances, ~10 - 100 μF [147,148,155,156], and n_{2D} modulations up to 10^{15} cm^{-2} [156]. The unprecedented n_{2D} modulation of EDL transistors (EDLTs) combined with the relative ease to fabricate electrolyte-based devices, has led to a rapid expansion of the field with many successful demonstrations in complex oxides, organic semiconductors, and 2D materials [147–150,152–156].

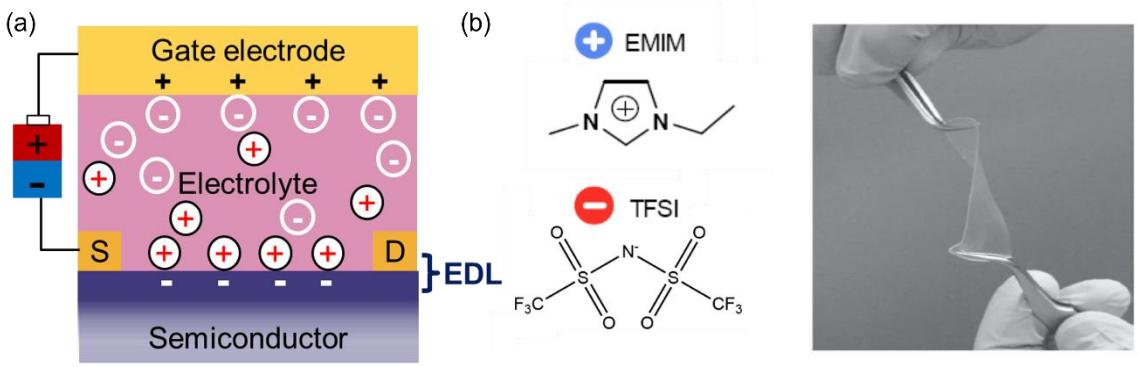

Figure 1.21: (a) Schematic representation of an electrolyte-gated transistor. Under the effect of a positive voltage applied between the source and gate electrodes, mobile ions of the electrolyte accumulate at the interface of the channel (labelled "Semiconductor" in this example) inducing an electric double layer (EDL) at the interface. (b) Chemical representation of the ions in the ionic liquid 1-ethyl-3-methylimidazolium bis(trifluoromethylsulfonyl)imide (EMIM-TFSI). (c) Photo of an "ion-gel" composed of an ionic liquid contained in a polymer matrix, forming a rubbery solid and highlighting the ease of handling [157].

In EDLTs, the optimal choice of electrolyte is extremely important. Ions must be sufficiently mobile and in high enough concentration to form the EDL, but also need to be stable (*i.e.*, resistant to adverse chemical reaction) and impermeable to the channel (although penetration of the ions is desirable in some materials, such as polymer semiconductors [147]). An exceptional choice of electrolytes for EDLTs are ionic liquids (ILs). ILs are molten salts often composed of irregularly shaped organic ions that feature very low melting T, sometimes well below 300 K. These materials are solvent-less (allowing for extremely large charge densities), have high ionic mobility [147,148,158],

negligible vapor-pressure [147,148,159], and possess wide electrochemical stability windows [158,160], making them useful for gating applications over relatively wide voltage ranges. Further, ILs are easily adaptable into the solid state in the form of ionic gels. Ionic gels (or ion gels) essentially encapsulate the ions of an IL within a polymer matrix, maintaining high ionic conductivity but in the form of a rubbery solid [157,161–164]. By carefully selecting the combination of polymer and IL, high charge density and high ionic mobility can be maintained, with the added versatility and convenience of working in the solid state [157,161–164]. Fig. 1.21(b) shows an example of a commonly used IL electrolyte (left), and its ion gel equivalent (right), showcasing its convenient "cut and stick" handling [157].

Ionic-liquid- and ion-gel-based EDLTs have enjoyed much early success in modulating the properties of complex oxide materials [148,149]. Some particularly notable examples include inducing superconductivity (SC) from an insulating state in $SrTiO_3$ [165], discovery of SC in $KTaO_3$ [166], observation of high-T_c SC in single-unit-cell-thick $La_{2-x}Sr_xCuO_4$ films [167], control of the T-dependent MIT in VO_2 [168], control of F over a 150 K window in $La_{1-x}Sr_xCoO_{3-\delta}$ [169], as well as MITs in various oxide semiconductors [170–173]. However, after many early successes, questions soon arose about the true nature of the gating mechanisms. It was soon discovered that the simple electrostatic picture of Fig. 1.21(a) was not strictly true for many electrolyte-gated materials, and that electrochemical effects (often involving O^{2-} or H^+) were in fact the dominant mechanism in many cases [97,117,148,149,174–177].

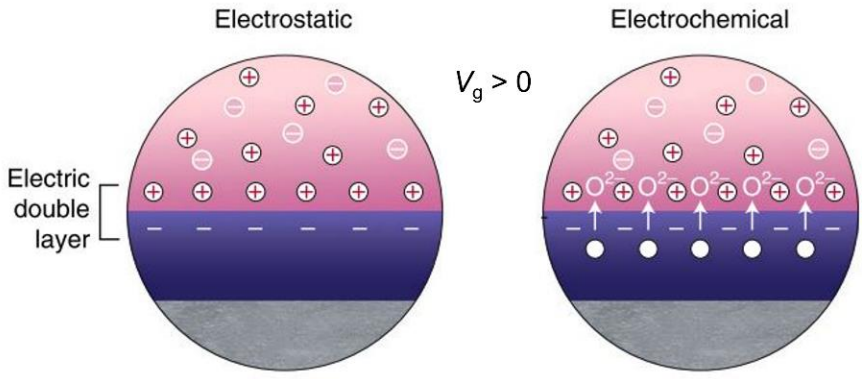

Figure 1.22: Schematic diagrams illustrating the modes of operation of an electric double-layer EDLT. These diagrams show close-ups of the EDL interface for both electrostatic (left) and electrochemical (right) operation of an oxide-based EDLT at positive V_g. Adapted from Ref. [149].

The electrolyte gating community soon realized that in many cases EDLTs could operate in either electrostatic *or* electrochemical modes, with both mechanisms providing benefits and drawbacks. In the simple electrostatic picture of Fig. 1.21(a) and Fig. 1.22 (left side) the EDL produces a large specific capacitance, and thus a large electric field (*E*-field) at the interface. This *E*-field can be so large in fact, that it can induce local electrochemical reactions, leading to modification of the channel material's stoichiometry. An illustrative example is provided in the case of oxide EDLTs, where, under the effect of the EDL-induced *E*-field, oxygen anions from the lattice are pulled out of the channel oxide material, leaving behind V_O [149,174,176]. Fig. 1.22 (right), shows a schematic of this scenario, where (under positive V_g) the EDL is composed of cations at the interface and electrons accumulated in the channel, leading to favorable conditions for reduction electrochemistry. In a similar vein, when small positively charged ions, *e.g.*, H^+, are present in the electrolyte, they can also be intercalated into the channel [97,117,177,178]. In the opposite situation, *i.e.*, $V_g < 0$, negatively charged species (*e.g.*, O^{2-}) would be injected and positively charges species would be removed [97,117,149,174]. In the next section, a detailed review of recent literature of electrolyte gating of $La_{1-x}Sr_xCoO_{3-\delta}$ serves to map the electrostatic *and* electrochemical modes in a single material.

1.3.3 Ion gel gating of $La_{1-x}Sr_xCoO_{3-\delta}$ thin films

Electrolyte gating of the cobaltite LSCO has been thoroughly investigated in recent years using ion-gel electrolytes [169,176,179,180]. In 2016, Walter *et al*. expounded the V_g-dependence and underlying gating mechanisms in $x = 0.5$ LSCO, *i.e.*, electrostatic *vs*. electrochemical [179]. Some of the findings from that study are reproduced in Fig. 1.23(a)-(d). Fig. 1.23(a) summarizes the procedure used to distinguish electrochemical *vs*. electrostatic electrolyte-gate response in 10 unit-cell-thick (~4 nm) ion-gel-gated LSCO films. In this process, a gate voltage was applied, and the response of the device resistance was measured *vs*. time. In this experiment V_g was applied in steps, with 30 minutes at each V_g, followed by an additional 30-minute period at $V_g = 0$ V. Such long times were chosen to ensure sufficient time for EDL charging/discharging. The measured channel resistances were then used to calculate $(\Delta R)_{gate}$ and $(\Delta R)_{irrev.}$ (see Fig. 1.23(a)), where $(\Delta R)_{gate}$ represents the gate effect (*i.e.*, the V_g-induced resistance change) and $(\Delta R)_{irrev.}$ is a measure

of the 'irreversibility' (or nonvolatility) of the V_g-induced changes. The findings are summarized in Fig. 1.23(b), where the V_g dependence of the gating spans three distinct regimes. The electrostatically controlled range corresponds to regime II in Fig. 1.23(b), ~ $-2 < V_g < 0$ V, where accumulation of holes in the top few unit cells of the film lowers the device resistance, leading to a small negative $(\Delta R)_{gate}$. This is accompanied by negligible irreversibility ($(\Delta R)_{irrev.} \approx 0$), indicating an entirely electrostatic response. On the other hand, at $V_g > 0$ (regime III) even a small voltage induces large changes in $(\Delta R)_{gate}$ and $(\Delta R)_{irrev.}$, indicating a non-volatile *electrochemical* change had taken place. In regime I of Fig. 1.23(b), another interesting effect was observed, in which small irreversibility occurs on top of electrostatic changes ($V_g <$ ~-3.5 V). This was understood to be the result of overoxidation of the Co valence near the EDL (large h^+ accumulation → high V_{Co}), leading to instability and thus spontaneous electrochemistry, *i.e.*, V_O formation, upon returning to 0 V. Importantly, the above work thus revealed both electrostatic- ($V_g < 0$) and electrochemistry-dominated ($V_g > 0$) electrolyte-gate response in a single EDLT.

In a subsequent study, Walter *et al*. built upon this understanding to great effect, utilizing purely electrostatic gating to demonstrate control over F in LSCO films over a 150 K window [169]. To do this, ultrathin films of $x = 0.5$ LSCO (6 unit cells) were grown intentionally below their t^* to yield an initially insulating / MEPS film state, close to the percolative transition (see Section 1.2.5.1) [169,181]. Then, *via* electrostatic h^+ doping at negative V_g, a F-metallic state was induced demonstrating the power of electrostatic electrolyte gating in this system. The primary results of this work are shown in Fig. 1.24, where the electrostatic gating at increasingly larger $V_g < 0$ magnitude is seen to induce a MIT transition (panel (a)), while simultaneously turning on F up to $T_C \approx 150$ K (panel (b)) and opening a F hysteresis loop at low T (panel (c)).

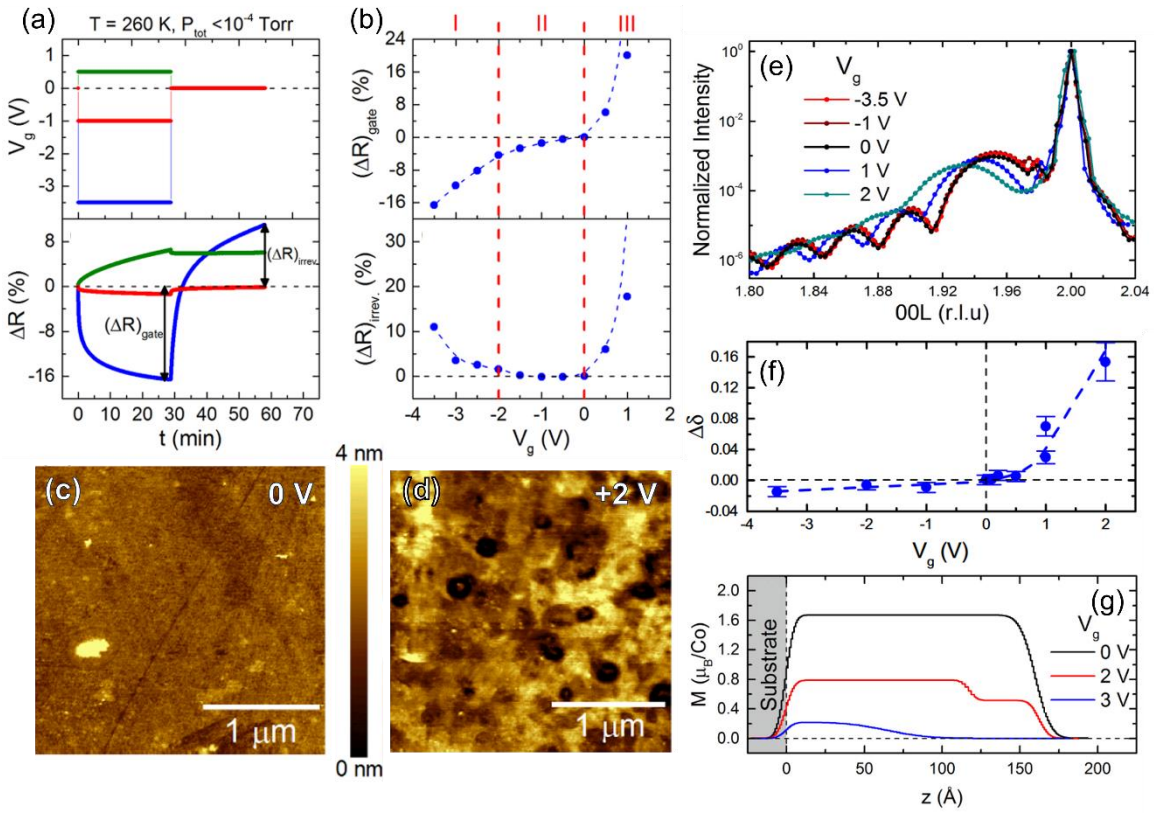

Figure 1.23: (a) Graphical definitions of the values $(\Delta R)_{gate}$ and $(\Delta R)_{irrev.}$ determined for stepped-voltage ion-gel-gating experiments on 10-unit-cell-thick x = 0.5 LSCO films on LAO [179]. (b) plots of $(\Delta R)_{gate}$ and $(\Delta R)_{irrev.}$ *vs*. gate voltage (V_g), showing the different regimes (I, II, and III) of the gate response. (c),(d) Atomic force microscopy (AFM) images of ungated (0 V, (c)) and +2 V-gated (d) LSCO films surfaces [179]. (e) *Operando* SXRD for an LSCO film on LAO as a function of V_g. The downshift in the film (002) peak position with increasing positive V_g indicates expansion of the lattice due to V_O formation. (f) Δδ (or the change in δ) *vs*., V_g for the same film as in (e). (g) Depth (z) profile of M determined by PNR fitting, showing the uniform reduction in M with z for an LSCO film after ion-gel-gating to large positive V_g [176].

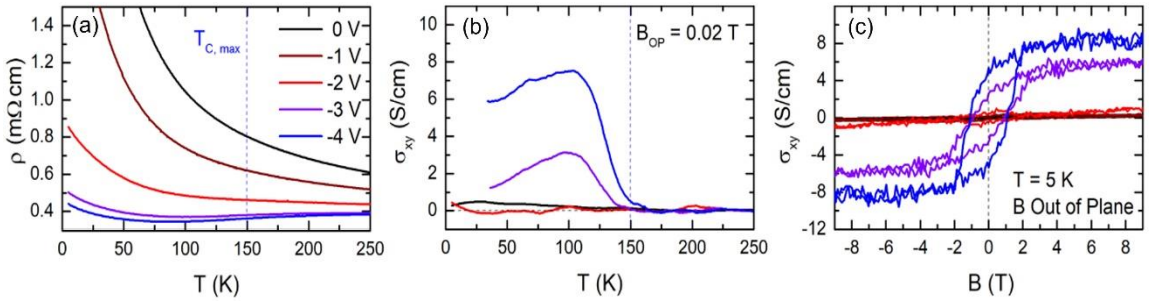

Figure 1.24: (a) Zero-magnetic-field resistivity (ρ) *vs*. temperature (T), (b) transverse conductivity (σ_{xy}) *vs*. T, and (c) σ_{xy} *vs*. out-of-plane magnetic flux density (B) for a 6-unit cell-thick, x = 0.5 LSCO thin film on LAO(001). The various colored curves correspond to the measurements taken during *in situ* electrostatic ion-gel-gating at different gate voltages (see legend in (a)) [169].

Returning to the electrochemical response, strong evidence has been presented to definitively establish V_O formation as the mechanism responsible for the above observations at $V_g > 0$ [176,179,180]. In hole-doped LSCO V_O formation compensates h^+ increasing resistivity, which is consistent with the rapid increase of $(\Delta R)_{gate}$ and $(\Delta R)_{irrev.}$ at $V_g > 0$ in Fig. 1.23(b). Additionally, the effects at $V_g > 0$ were suppressed when the gating was performed under high O_2 pressure [179]. The role of V_O formation was further confirmed by *operando* X-ray absorption spectroscopy / X-ray magnetic circular dichroism (XAS/XMCD) through observation of decreased V_{Co} [180]. In a subsequent study, *operando* synchrotron X-ray diffraction (SXRD) was performed on similarly gated $x = 0.5$ LAO/LSCO films [176]. Fig. 1.23(d) shows *operando* SXRD scans of the LSCO film and substrate (002)-peak region after increasingly positive V_g, showing a downshift in the film peak position along the out-of-plane direction (L), indicating an expansion of the lattice, again consistent with V_O formation. This result was then used in combination with bulk thermogravimetric analysis (TGA) to estimate the change in δ ($\Delta\delta$), finding $\Delta\delta \approx 0.16$ after +2 V (Fig. 1.23(f)). Finally, Polarized neutron reflectometry (PNR), a powerful probe of magnetism in thin films, was used to generate a model of the depth (z)-dependent M (Fig. 1.23(g)), where suppression of M is evident throughout the depth of the film after gating at large positive V_g. This indicates that not only are V_O formed at the interface during gating but that they also migrate through the entire depth of the film.

Considering electrochemical effects beside V_O formation, Walter *et al.* also characterized film surface morphology using atomic force microscopy (AFM) before and after ion gel gating to different V_g. These results are shown in Fig. 1.23(c) and (d). In panel (c), simply applying the ion gel (but not applying any voltage) does not significantly disturb the atomically smooth surface of the as-deposited film. However, after application of +2 V, the surface roughens significantly (Fig. 1.23(d)) and shows evidence of etch pit formation. The surface changes at +2 V were attributed to ion-gel-gate-induced acid etching, likely caused by the splitting of dissolved H_2O in the gel and the subsequent accumulation of H^+ ions at the interface (increasing local pH) [179].

1.3.4 Electrostatic vs. electrochemical response in EDLTs

The electrolyte gating studies of LSCO outlined above provide a useful case study to aid in understanding the principles which govern electrostatic *vs.* electrochemical response in EDLTs. Recently, a strong case has been made that the diffusivity of the lowest-energy anion defect (V_O in the case of oxides) is the dominant factor in predicting electrostatic *vs*. electrochemical response [153]. While many oxides feature relatively low energy for V_O formation, the diffusivity of such defects varies widely [153]. For example, in $BaSnO_3$, $D_{Vo} \approx 10^{-26}$ cm^2 s^{-1} at room T [182] (likely related to the large ionic radii of Ba^{2+} and Sn^{4+}), and electrolyte gating of this material has been shown to be entirely electrostatic [183]. On the other hand, cobaltites, such as LSCO and SCO, feature radically lower 300-K D_{Vo}, roughly 10^{-11} - 10^{-13} cm^2 s^{-1} [75], and readily exhibit electrochemistry on electrolyte gating, even at small $V_g > 0$ [176,179]. This is despite the fact that V_O are known to form readily in both systems [153]. The differences in electrolyte gating response can then be rationalized by the following: While V_O may form in both materials, in $BaSnO_3$, they are effectively immobile after formation, playing a minimal role, while in LSCO they are sufficiently mobile to proliferate through the bulk, thus dominating the observed response. This theory also applies well to electrolyte gating in sulfides, where a similar dichotomy in sulfur vacancy diffusivity (D_{Vs}) between NiS_2 and FeS_2 leads to electrostatic response in the latter (low D_{Vs}) and electrochemical response in the former (high D_{Vs}) [184,185]. In light of the above, due to their outstandingly high D_{Vo} among perovskite oxides, cobaltites appear to be excellent materials candidates for use in electrochemical EDLTs.

1.3.5 Voltage-induced perovskite-brownmillerite transformations in $SrCoO_{3-\delta}$

In addition to the electrolyte gating of $x = 0.5$ LSCO films outlined above, $x = 1$ SCO films have also been heavily investigated by electrolyte gating, albeit *via* entirely electrochemical operation. As discussed above, the low ΔH_{Vo} and exceptionally high D_{Vo} in SCO makes it well-suited for use in electrochemical EDLTs. Further, the stark differences in material properties between P and BM forms of SCO makes the prospect for dynamically switching between the two phases extremely enticing. Toward that end, many

recent studies have focused on reversibly inducing the P ↔ BM transformations in SCO films by application of a gate voltage, finding much success, particularly using electrolyte gating techniques [79,97,117,122,124–134].

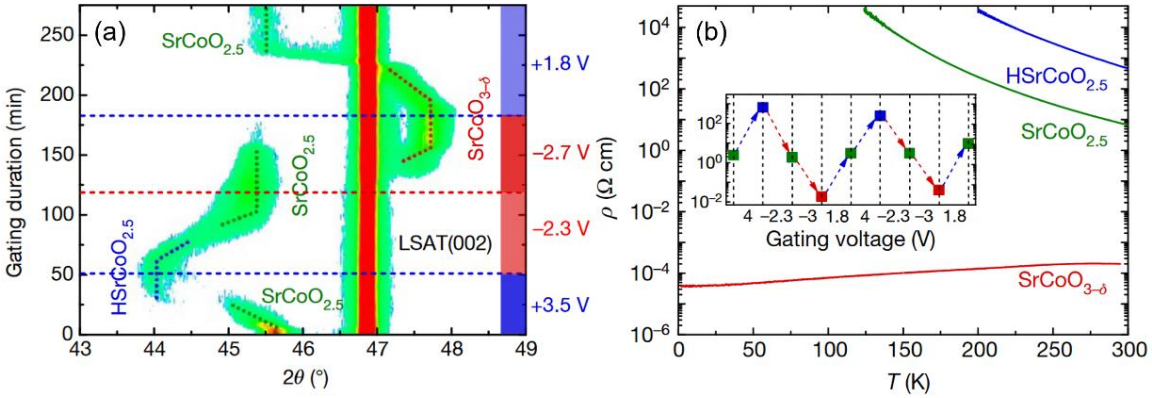

Figure 1.25: (a) *In situ* intensity *vs.* 2θ X-ray diffraction (XRD) scans for an as-grown $SrCoO_{2.5}$ film during an IL gating experiment. Individual XRD line scans were taken at different times (*y*-axis, left) during the experiment and overlaid to create a raster-image contour plot. The thick red line represents the LSAT (002) substrate peak. The various phases and gate voltages (right axis) are labelled. (b) resistivity (ρ) *vs.* temperature (*T*) for different film phases: $SrCoO_{3-\delta}$ (red), $SrCoO_{2.5}$ (green), and $HSrCoO_{2.5}$ (blue). The 300-K ρ over several gate voltage cycles is shown in the inset. Adapted from Ref. [97].

The pioneering work regarding voltage control of the P-BM transformation in SCO thin films was presented by Q. Lu *et al.* in 2016. By growing SCO films on top of the well-known solid-state oxygen conductor Yttria-stabilized zirconia (YSZ), a voltage applied at high temperature was used to drive oxygen in and out of the film, toggling between P and BM phases [129,130]. In 2017, N. Lu *et al.* demonstrated a similar concept, instead using IL gating at 300 K. Fig. 1.25(a) shows one of the more remarkable results from their work, in which the structure of the film was tracked *in situ* by XRD. Fig. 1.25(a) shows a raster-image of XRD patterns *vs.* time (*y*-axis), resulting in a contour map tracking the structural phase transformations during an IL-gating experiment. At the bottom of the figure, the as-grown film peak (BM $SrCoO_{2.5}$) appears at ~45.6°. A V_g of +3.5 V was first applied (blue, right axis), whereupon the film transformed to a previously unknown hydrogen-intercalated phase, $HSrCoO_{2.5}$, indicated by the downshift of the film peak to ~44°. Upon reversing the V_g polarity, *i.e.*, V_g = –2.3 V and then –2.7 V, the film was driven back to BM $SrCoO_{2.5}$, and eventually oxidized all the way to P-$SrCoO_{3-\delta}$, thus constituting a "tri-state" phase transition. Such tri-state transitions were demonstrated in SCO films grown on various substrates and at various film thickness. The P-BM transformation was shown to

take place on the order of minutes, with strong dependencies on the thickness (faster transformation in for thinner films) and strain state (faster transformation for compressively strained films) [97].

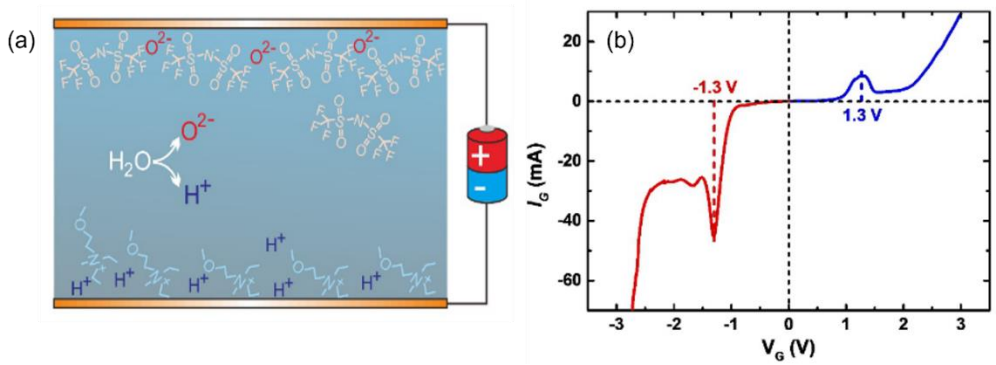

Figure 1.26: (a) Schematic illustration of the hydrolysis of H_2O dissolved in EMIM-TFSI ionic liquid (IL) during application of a voltage. (b) Gate current (I_G) *vs*. gate voltage (V_G) showing the relatively small but visible peaks that indicate the hydrolysis of water within the IL at ~± 1.3 V, close to that expected for standard hydrolysis reaction. Adapted from Ref. [97].

The basic principles of electrochemical IL gating of SCO follow the mechanisms laid out in Section 1.3.2. It is important to note the H^+ and O^{2-} species in the IL are thought to original from hydrolysis of dissolved H_2O [97,149,153,154]. Fig. 1.26(a) shows this process schematically for H_2O dissolved in EMIM-TFSI, and Fig. 1.26(b) shows experimental evidence of the hydrolysis reaction from peaks evident in the gate current during IL gating experiments. It was also found that dissolved H_2O is essentially always present in ILs, even after rigorous drying treatments or gating under vacuum. Moreover, only trace amounts of H_2O are needed to fully oxidize / hydrogenate nm-scale thin films.

In terms of electronic transport, Fig. 1.25(b) shows representative ρ *vs*. *T* data measured for the films gated to each of the three phases: $HSrCoO_{2.5}$, BM-$SrCoO_{2.5}$, and P-$SrCoO_{3-\delta}$, highlighting the MIT and > 10^4 modulation of 300-K ρ between P and BM phases. The inset of Fig. 1.25(b) also demonstrates the reversibility of the gate-induced transformation by showing the 300-K ρ as a function of V_g over several full cycles. In addition to the above demonstrated control over structure and electronic transport, N. Lu *et al*. also presented evidence of the opening of a F hysteresis loop in the case of P-SCO (and a weakly F signal in $HSrCoO_{2.5}$), as well as significant changes in optical transmission / absorption spectra between the three film phases.

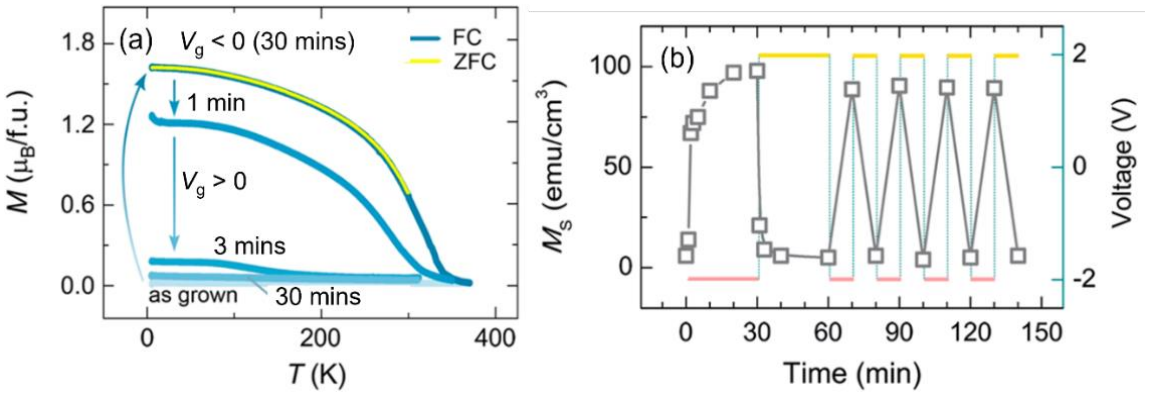

Figure 1.27: (a) *Ex situ* magnetization (*M*) *vs*. temperature (*T*) of a 60-nm-thick film of $SrCo_{0.5}Fe_{0.5}O_{3-\delta}$ after different IL gating treatments, *i.e*., gate voltages (V_g) and times, measured in 13 kOe field. (b) Saturation magnetization (M_s) *vs*. time for a similar IL-gated film as in (a) as determined from high-field *M* at 300 K. The pink horizontal lines correspond to application of –2 V (oxidation), whereas the horizontal yellow lines correspond to application of +2 V (reduction). Adapted from Ref. [124].

Since the above-described work of Q. Lu *et al*. and N. Lu *et al*., many other studies have since confirmed their results and further advanced the understanding of electrochemical gating in SCO and LSCO films [79,117,122,124–128,131–134,176,180,186]. These include research using a variety of *in situ* or *operando* probes, including XRD / SXRD [124,125,127,132,176], transmission electron microscopy (TEM) [131], XAS / XMCD [180], (AFM) [133], and PNR [176]. Remarkably, Cui *et al*. were able to image the P ↔ BM phase transformation in real time using IL gating and *in situ* TEM, observing a highly anisotropic BM → P phase front that moves ~30-times faster laterally than through the depth of the film [131]. In another study by Miao *et al*., the apparent anisotropy of oxygen transport in BM-SCO was further evidenced by a relatively faster change in conductivity under negative V_g in the [110] direction *vs*. the [100], presumably due to faster diffusion facilitated by {110}-family V_O channels in BM (see Fig. 1.15(c)) [94,126]. The important concept of switching F 'on' and 'off' was also recently extended to above room *T* in IL-gated SCO EDLTs [124]. By alloying $SrCoO_{3-\delta}$ and $SrFeO_{3-\delta}$ to increase T_C, Ning *et al*. demonstrated ON/OFF switching of F above 300 K. Fig. 1.27(a) shows *M vs*. *T* magnetometry data for an IL-gated film of $SrCo_{0.5}Fe_{0.5}O_{3-\delta}$ after various gating treatments. The as-grown BM film showed no F signature, as expected, but upon gating at $V_g < 0$ (*i.e*., oxidation) for 30 minutes, robust F signal was observed, with $T_C \approx 340$ K. Subsequently applying $V_g > 0$ then resulted in relatively more rapid reduction

back to the non-F BM state. As in the inset of Fig. 1.25(b), this process was also shown to be reversible over several cycles. Fig. 1.27(b) shows M_s (measured from 300-K *M vs. H* loops) of a similar $SrCo_{0.5}Fe_{0.5}O_{3-\delta}$ film as a function of time spanning several voltage cycles (V_g shown on right axis), highlighting the repeatability of the voltage control of F.

In addition to the remarkable control over electronic and magnetic properties, IL-gating induced P-BM transformations in SCO films have also been used to demonstrate wide modulations of optical properties [97], and thermal conductivity [117]. The "tri-state" transitions outlined above allow modulation of thermal conductivity by a factor of ~10 [117]. The P-BM phase transition in IL-gated SCO has also recently been extended to heterostructures [134,186]. By growing BM-SCO atop a F $La_{0.67}Sr_{0.33}MnO_{3-\delta}$ underlayer and using IL-gating to switch the BM-SCO to P, Song *et al*. demonstrated reversible switching of the magnetic easy axis direction of the film stack [134]. More recently, V_g-control of V_O ordering direction in BM-SCO, has been shown using IL gating. Han *et al*. showed that as-grown horizontally V_O-ordered BM-SCO films could be switched to form *vertical* V_O-ordering, by cycling from BM → P → BM *via* IL gating [132]. This is shown in the STEM images of Fig. 1.28. Kinetic differences likely drive this effect; however, the detailed mechanisms are not yet understood. Regardless, the capability to control V_O-ordering direction in films holds promise for device functionality [132].

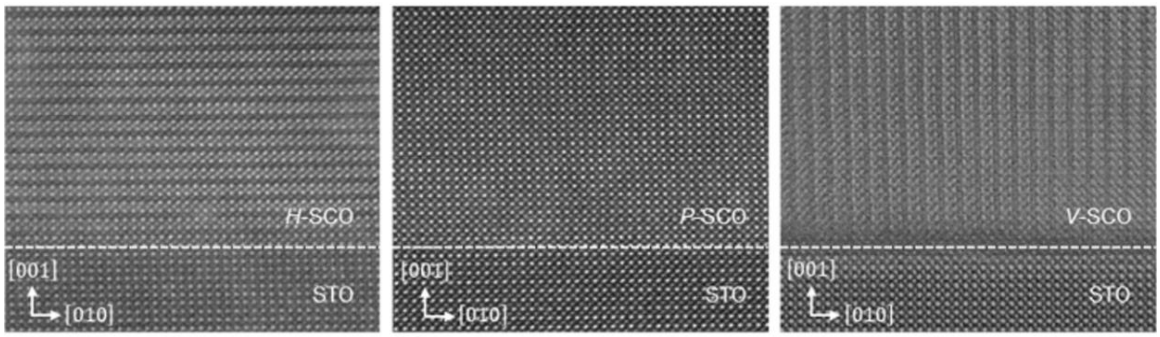

Figure 1.28: Cross-sectional high-resolution HAADF-STEM images of the film/substrate interface of representative STO/$SrCoO_{3-\delta}$ films. The left panel shows as-grown horizontally ordered BM-SCO (H-SCO). The middle panel shows perovskite SCO (P-SCO) after negative-V_g IL-gating (oxidation). And the right panel shows vertically ordered BM-SCO (V-SCO) after positive V_g IL-gating (reduction) of P-SCO. The interface with the substrate is marked by the white dashed horizontal line. The dark stripes in the images indicated the V_O-ordered Co-O tetrahedral planes characteristic of the BM structure. These stripes run horizontal in the left image but are switched to vertical in the right, after cyclic IL gating was applied. Adapted from Ref. [132].

1.3.6 Advantages of electrochemical transistors and potential applications

Although perhaps initially viewed as a side-effect of intended electrostatic gating, electrochemically driven EDLTs (sometimes referred to as electrochemical transistors) have made rapid progress [97,117,124,131,132,149,154] and continue to attracted prime interest. They are appealing over their electrostatic counterparts for a variety of reasons. Perhaps most importantly, electrochemical transistors are inherently non-volatile, meaning the changes induced upon application of V_g remain after the voltage is switched off, a highly desirable feature for energy efficiency. Another benefit of the electrochemical gating mechanism is that, unlike traditional field-effect devices, it is not limited by screening. This allows much larger volumes to be gated, also of critical importance in applications. Finally, it is notable that the widest reported ranges of property modulations in EDLTs have been achieved using electrochemical mechanisms [149,154], owing to extreme sensitivity of materials properties to chemistry / stoichiometry.

One potential limitation of electrochemical EDLTs, however, is their speed. While electrostatic EDLTs are fundamentally limited by the EDL formation time, they have already been shown capable of MHz speed operation [187]. Electrochemical EDLTs, on the other hand, depend on *both* the time scales of EDL formation and diffusion of the relevant species into / out of the channel, the slower of the two being rate limiting. This could limit the ultimate application space for electrochemical EDLTs. Although, it should be noted that many potential applications do not necessarily require high switching speeds, in some cases kHz ranges, and even down to ~1 Hz, *e.g.*, in photonics, may suffice [149].

Some exciting potential applications for electrochemical transistors include magnetoionics for low power switchable magnets [150,152,188,189], novel computing applications, such as neuromorphic and stochastic computing [148,152,188], tunable photonics [148,149], and thermoelectric switches [117,148]. Magnetoionics, in particular, represent a range of useful applications for switchable magnetic elements, with the central benefit of drastically lower energy consumption [150,152,188,189]. Many magnetic applications feature magnets which are switched *via* applied magnetic fields (sometimes *T*-assisted) or spin currents (for spin-transfer torque applications), both of which have high

energy costs [1]. By instead using ionic motion, a relatively small voltage (and thus current) can be used to manipulate magnetic properties. Magnetoionic function has potential to be useful in data storage, computing, microelectromechanical systems (MEMS), and sensors / actuators [150,152,188,189].

In terms of computing, one particularly exciting potential application is to use electrochemical EDLTs as artificial neurons / synapses in neuromorphic computing architectures [190,191]. Traditional von Neumann computing architectures rely on physically separated processing and memory storage units. In contrast, in a neuromorphic computer, both processing and memory operations are performed simultaneously. Inspired by characteristics of the human brain, neuromorphic computing thus offers a number of advantages, such as increased computation and energy efficiency, stochasticity (*i.e.*, an ability to handle randomness), and inherent scalability, making it ideal for artificial intelligence and machine learning applications [192]. Electrochemical transistor devices represent one possible route to realize artificial neural networks, perovskite cobaltites, such as $SrCoO_{3-\delta}$ and $La_{1-x}Sr_xCoO_{3-\delta}$, representing intriguing candidate materials. As outlined in the preceding sections, cobaltites feature desirable electronic and magnetic properties, extreme sensitivity to oxygen stoichiometry (δ), and a high mobility of oxygen at 300 K. Such characteristics make cobaltites prime candidates for ultra-low-power synaptic devices in artificial neural networks [125,126,193–195].

1.4 Motivation and outline

Despite numerous high-impact studies and demonstrations of promising novel functionality, oxide EDLTs, as a technology, are still in their very early stages (especially so for electrochemically driven EDLTs). Perovskite cobaltites are clearly promising materials for such applications owing to a propensity for oxygen-deficiency and fast V_O diffusion rates, providing a route to oxygen-ion control of various material properties. In this regard, SCO has recently come to the fore as an outstanding candidate material. However, SCO also presents challenges due to its tendency to spontaneously reduce from the P state. This raises concerns about its long-term retention of properties, and few alternate materials have so far been explored for similar applicability. In addition, there

remain many open questions regarding the mechanistic details and V_g-dependence of the P ↔ BM transformation and reversibility in cobaltites, not to mention ultimate limitations in terms of speed and cycling endurance. This thesis therefore aims to further the understanding of electrochemical gating in cobaltites by focusing on ion-gel gating of the LSCO family, and particularly x = 0.5 LSCO, a promising air-stable alternative to SCO, with the following specific goals:

1. *Investigating the P → BM transformation in ion-gel-gated LSCO thin films and its doping- and strain-dependence*

So far, the topotactic P-BM transformation has been demonstrated *via* electrolyte gating almost exclusively in SCO, with few alternatives having been investigated. The LSCO family of compounds presents a promising, air-stable base for such an investigation. The extensive work outlined in Section 1.3.3 additionally provides a robust starting point for further study of the electrochemical operation of LSCO EDLT devices. Primary open questions from the above work include whether the gated LSCO forms a BM structure at high positive V_g (as in SCO), and what affects composition (*i.e.*, Sr doping) and strain may have on the observed electrochemical response. Motivated by this, Chapter 3 focuses on the electrolyte-gate-induced electrochemical reduction of LSCO thin films by ion-gel-gating, with particular focus on identifying and characterizing the P → BM structural transformation. To investigate the generality of the P → BM transformation in LSCO, and to gain insight into the parameters that drive it, these effects are studied across the majority of the LSCO phase diagram ($0 \leq x \leq 0.7$) and over a wide range of epitaxial strains (–2.1% to +1.5%).

2. *Characterizing thermal and optical property modulations in V_g-induced P-BM transformations*

While the P → BM transformation and its composition and strain dependence in LSCO are expounded in Chapter 3, the primary focus was on the associated structural, electronic, and magnetic property changes. Meanwhile, the thermal and optical property changes were less well characterized, despite the potential for significant modulation of both based on prior work and literature studies at x = 1. To address this, in Chapter 4 the

thermal transport and optical property changes associated with the P → BM transformation in LSCO are characterized in detail in two parallel studies. In the first, thermal conductivity of ion-gel-gated LSCO films is quantified by time-domain thermoreflectance (TDTR), an all-optical probe of thermal transport, as a function of V_g entirely at $x = 0.5$. And in the second, spectroscopic ellipsometry and optical transmittance measurements are combined to determine the complex refractive index over a broad range of wavelengths for nearly the entire phase diagram in both gated and ungated LSCO films. Led by my colleagues, these studies had the expressed goal of exploring the potential of ion-gel-gated LSCO for thermal switching and photonic applications, respectively.

3. *Understanding the hysteresis and reversibility of the voltage-driven P-BM transformation in ultrathin LSCO*

As discussed above, the P-BM transformation in cobaltites is of prime interest for applications. However, much of the existing literature on electrolyte gating in cobaltites has focused on the *end states*, *i.e.*, either fully P or fully BM, while less has been done to investigate the details of the transformation. Even in Chapters 3 and 4, the focus is primarily on property modulations specific to the P → BM process in LSCO, and relatively less on the *reversibility* of the transformation. Moreover, full hysteresis loops of essential quantities, such as ρ, lattice parameter, *etc*., an important base for frequency-dependent measurements, are rarely reported. This omission is glaring, as full understanding of the hysteretic phenomena associated with the V_g-induced P ↔ BM transformation is essential to the realization of high-endurance devices. In Chapter 5, we address these concerns by studying detailed source-drain current *vs*. V_g hysteresis loops of the P ↔ BM transformation in LSCO films in combination with complementary structural characterization *via operando* SXRD. Using both major and minor hysteresis loop analyses, we seek to gain mechanistic understanding of the V_g-dependence of the transformation, in both the forward *and* reverse direction, and to identify potential limitations to 1st-cycle reversibility. Additionally, by working entirely with ultrathin (10-unit-cell-thick) films, we aim to provide further insight into the ultimate capabilities of such systems, where high-frequency applications necessitate exploration of the very-thin-film limit.

4. *Probing the magnetic order in brownmillerite SCO and LSCO thin films via neutron diffraction*

A primary feature driving interest in the P ↔ BM transformations in SCO thin films is the potential for F ↔ AF switching functionality. However, due in part to the difficulty in probing AF order, particularly in thin films, direct evidence of such a transition is lacking in the literature. In fact, the magnetic order in BM-SCO thin films has yet to be proven unambiguously, many film studies simply presume the magnetic properties in BM-SCO films are comparable to the bulk. This is problematic, however, as significant differences in magnetic properties between film and bulk states are well known in cobaltites [33]. In addition, the magnetic order of the BM phase in other compositions of LSCO, *i.e.*, away from $x = 1$, is generally unknown in both films and bulk. Considering the growing interest in these compounds for voltage-cycling applications, understanding of the magnetic properties in both P ("ON") and BM ("OFF") states is important. To address this, in Chapter 6, we directly probe the magnetic structure in $x = 1$ BM-SCO and $x = 0.5$ BM-LSCO films using neutron diffraction. Complementary structural characterization and magnetometry measurements are then used to further characterize both compositions (in thin films and bulk), and to generate a magnetic phase diagram *vs.* δ for $x = 0.5$ LSCO films.

Chapter 2: Experimental Methods

In this chapter I will outline the experimental techniques and procedures that were used to conduct the research presented in this thesis. To begin, I introduce the specialized film deposition technique known as high-pressure-oxygen sputtering, which was used to make *all* the experimental samples studied in this thesis. Next, I will discuss the primary structural characterization methods using X-ray diffraction (XRD), followed by the techniques used for measuring electronic, magnetic, thermal, and optical properties. To conclude the chapter, I will detail the procedures used in more specialized experiments, specifically the fabrication of LSCO film EDLT devices and ion gel gating, *operando* synchrotron XRD, and neutron diffraction.

2.1 High-pressure-oxygen sputtering of $La_{1-x}Sr_xCoO_{3-\delta}$ thin films

Physical vapor deposition (PVD) is a common form of film deposition, where a source material is volatilized to the gas phase and subsequently deposited onto a substrate. The most common type of PVD is known as 'sputtering'. In this process, a large voltage (100's of volts) is applied between an anode and cathode (target) in the presence of a low pressure of gas (often Ar). At a critical voltage, electrons are ripped from the gas molecules generating a plasma. The ions of the plasma, under the effect of the *E*-field, accelerate into the target causing ballistic collisions at the surface. These collisions eject material from the target at the molecular level, forming a vapor of the target material elements that emanates from the bombarded surface. This vapor can then be used to deposit, or 'grow', thin films of the target material on a substrate. Sputtering is a commonly employed deposition technique in industrial applications due to its relatively low cost and scalability [196]. Under optimized growth conditions, *e.g.*, *T*, pressure, power, substrate, *etc*., deposited films grow as single-crystalline layers with a common orientation. The practice of depositing such films is known as epitaxy. Recent decades have seen spectacular advances in the epitaxy of oxide thin films using vacuum deposition techniques such as PLD, MBE, and hybrid MBE [26,197,198]. However, not all oxide materials are good candidates for high-vacuum deposition, such as LSCO, where achieving full oxygen stoichiometry is challenging due to inherently low pressures of O_2 (P_{O_2}) and high temperatures needed for

growth. Moreover, implementation of these methods is relatively complex, costly, and may pose challenges for high-throughput processing compared to sputtering.

While sputtering has some advantages, sputter deposition of epitaxial perovskite oxides presents its own challenges [199]. To sputter oxide films, O_2 partial pressures are introduced during sputtering to increase the oxygen uptake of the film. This is known as *reactive* sputtering. O_2 plasma can be problematic, however, as O^{2-} anions are produced and move in the opposite direction to other ions in the plasma, *i.e.*, bombarding the growing film rather than the target, this is known as 're-sputtering'. This phenomenon is known to cause damage to films and can lead to large cation non-stoichiometry / inhomogeneity [199–201]. Effects of re-sputtering can be mitigated by lowering P_{O_2}, increasing P_{Ar}, or by moving the substrate 'off-axis' from the target. However, these solutions are not ideal for oxide films due to poor oxygenation in the former, and lower deposition rates in the latter, both requiring optimized post-deposition thermal treatments. To address these issues, a novel method of oxygen reactive sputtering was developed in the late 1980s, when U. Poppe and colleagues at Forschungzenstrum Jülich pioneered a method of high-P_{O_2} sputtering to deposit films of the perovskite-related high-T_c superconductor $YBa_2Cu_3O_{7-\delta}$ (YBCO) [202]. By using pure O_2, with no other gases, and drastically increasing P_{O_2} by orders of magnitude over traditional reactive sputtering (~3 Torr *vs.* 10's of mTorr), the energy of anions was reduced enough to render re-sputtering issues negligible while simultaneously increasing the oxygenation of the film, and allowing for workable on-axis deposition rates [203]. Since its original success with films of YBCO [202,204], high-P_{O_2} sputtering has been used to deposit high-quality epitaxial films of a variety of other perovskite (and perovskite-related) oxides including other superconducting cuprates and heterostructures [205,206], manganites [207–209], cobaltites [48,107,108,169,210], $SrTiO_3$ [208,209,211], and $BnSnO_3$ [183,212,213]. High-P_{O_2} DC sputtering was used to deposit all the film samples studied in this thesis. The methodology was adapted/developed from prior work in the case of P-LSCO [107–109,169,179], and was newly developed for BM-SCO.

2.1.1 Preparation of polycrystalline sputtering targets

Sputter deposition requires bulk sputtering targets to provide the material that will eventually form the film, and the 'quality', *i.e.*, stoichiometry and elemental purity, of the target directly influences that of the resultant films. For metals and some common oxides, sputtering targets are commercially available. However, in general, for complex oxides this is not yet the case. Therefore, in this work, bulk sputtering targets were produced in-house using solid-state reactions and standard powder processing techniques.

For $0 \leq x \leq 0.7$ LSCO, the same target synthesis procedure was followed. First, stoichiometric amounts of high purity (>99.9%) powders of La_2O_3, $SrCO_3$, and Co_3O_4, were weighed and mixed in air using mortar and pestle, and subsequently reacted to form the perovskite according to the solid-state reaction: $(1\text{-}x)/2\ La_2O_3\ (s) + x\ SrCO_3\ (s) + 1/3\ Co_3O_4\ (s) + (13 - 9x)/12\ O_2\ (g)$(in air) $\rightarrow La_{1-x}Sr_xCoO_3\ (s) + CO_2\ (g) \uparrow$. This reaction consisted of a thermal treatment of 1000 °C for 24 hours in air (~5 °C min^{-1} warming / cooling rates). Note that the La_2O_3 powder, due to its significant hygroscopicity [214], was hot-weighed (at >100 °C) prior to mixing, immediately following a drying treatment (1000 °C, 24 hrs, air). After the first reaction, the powder was re-ground and reacted a second time using the same thermal treatment. This process was repeated until the resulting powder was deemed phase-pure by powder XRD (PXRD), usually taking 2 - 3 reaction steps. The phase-pure perovskite powder was then mixed with a small volume fraction (~1%) of binding agent (polyvinyl alcohol) and cold-pressed into the form of a 2" diameter target (~3 mm thick for 20 - 25 g of powder), using steel dies and an automated uniaxial single-action hydraulic press, under a pressure of 40,000 psi. These "green bodies" were then sintered at 1200 °C in ~0.2 scfh of flowing O_2 (~1 atm) to form the final polycrystalline targets used for sputtering. Slow ramping rates of 0.5 - 1 °C min^{-1} were used during the sintering, to minimize the risk of thermal-stress-induced crack formation. Note that, for each sputtering target, a nominally equivalent pellet was made (0.5" diameter, ~2 - 3 mm thick). These pellets were used for PXRD and magnetometry to confirm phase purity and magnetic properties of the target.

For SCO sputtering targets, a similar procedure to the above was followed, but with some notable exceptions: (1) the reaction steps were carried out at slightly higher temperature (1050 °C), and (2) the sintering was performed at lower temperature, 1100 °C, due to the significantly lower melting *T* of SCO. Note that the equilibrium composition of 1:1 $SrCoO_x$ at room temperature consists of a mixture of hexagonal $Sr_6Co_5O_{15}$ and precipitated Co_3O_4 [215–217]. As a result, the polycrystalline sputtering targets used for deposition of BM-SCO films were *not* phase-pure, but nevertheless contained ~1:1 Sr/Co ratio. Another benefit of sputtering is that simply using a cation stoichiometric target, and not necessarily a phase pure one, can still produce phase-pure films.

After sintering, the targets were prepared for mounting into the sputtering chamber. This was done by bonding the targets to a Cu backing plate using In metal. First, one face of the target was lightly sanded and then 'painted' with a thin layer of liquid In to wet the surface and provide good electrical contact. Next, the Cu backing plate was heated to above the melting point of In (157 °C), and a small 'puddle' of In was spread uniformly over the plate and subsequently cooled. Then, with both the target and plate near room *T*, the target was placed on the center of the plate (In-painted-side down), and the plate was again heated to melt the In. Finally, with the In still liquid, weights were added atop the target and it was cooled back to room *T*.

As a final note on polycrystalline target preparation, the choice of DC sputtering over radiofrequency (RF) sputtering warrants some discussion. Generally, DC sputtering can be used when the target material has sufficiently low resistivity to avoid charge buildup. The 'cutoff' for this is not well defined, however, and depends on the target and deposition system. The benefits of DC over RF (which is necessarily used for insulators), *e.g.*, much faster deposition rate, convenience of mounting, *etc.*, made exploring this limit worthwhile in our system. Typical values of "front-to-back" resistance of metallic cobaltite sputtering targets, *e.g.*, $x = 0.5$ LSCO, were of the order of 100 Ω or less. However, for LCO (nominally insulating) and SCO (two-phase) this number was much greater, ~5 - 20 kΩ and 2 - 5 kΩ, respectively. These materials were nonetheless successfully sputtered using a DC plasma, although, the longevity of the targets was significantly less, possibly due to charging and / or thermal-stress-induced cracking.

2.1.2 High-pressure-oxygen sputtering

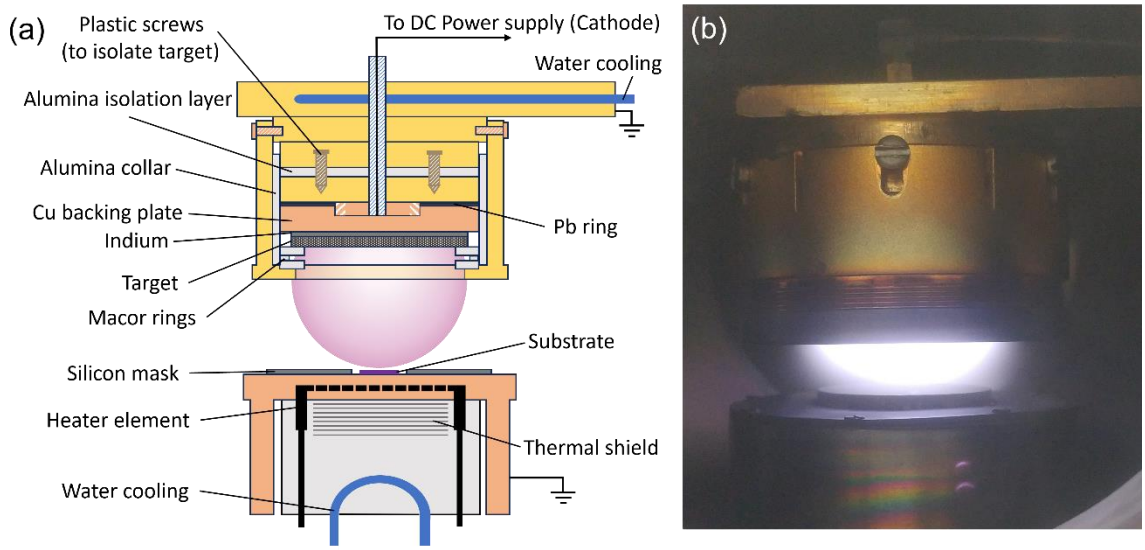

Figure 2.1: (a) Schematic diagram of the Forschungzenstrum Jülich-designed high-pressure-oxygen sputtering system used in this work to grow epitaxial thin films of LSCO and SCO. The major design features are indicated. (b) An example photo of a thin film deposition in progress, showing an active oxygen plasma directly over the substrate / heater stage.

High-pressure-oxygen sputtering was used to deposit epitaxial films of LSCO and SCO on single-crystal perovskite-oxide substrates. The sputtering chamber contained 3 'guns' capable of holding different sputtering targets with complementary power supplies, one DC, one RF, and one that can be switched between DC and RF. The sputtering targets were loaded into the guns by attaching the Cu backing plate to the gun arm's fixture, consisting of a threaded mate. Once attached, the sputtering targets were 'upside-down' and away from the substrate heater. A schematic of the critical components of the sputtering system is shown in Fig. 2.1(a). During downtime, a dedicated turbomolecular pump kept the chamber at its base pressure ($< 1 \times 10^{-6}$ Torr). While sputtering, a feedback-loop system consisting of a pressure gauge, flow control valve, and controller was used to regulate the flow of high purity O_2 gas (99.998%) from a supply cylinder to maintain a setpoint pressure. The same turbomolecular pump was also used to maintain O_2 flow during sputtering through a high-impedance bypass line. After a stable flow of O_2 was established, such that P_{O_2} was ~0.45 Torr, a 600 V/300 mA DC power supply (Heinzinger PNC 600-300) was used to ignite an oxygen plasma beneath the target. This was done by setting the DC current setpoint to 18 mA and slowly raising the voltage until the plasma ignited

(typically 450 - 500 V). At these high voltages, electrons are ripped from the O_2 gas molecules, creating cations that are then accelerating into the target, which is electrically mated to the power supply cathode and isolated from the ground (see Fig. 2.1(a)). Once lit, the plasma was sustained by the DC current setpoint of the power supply. The plasma was spatially confined to the inner diameter (~1.5") of the 2" target by a series of insulating Macor rings seated on the surface of the target. An outer Cu shield and ring-cap assembly (fixed to the gun arm) held the rings in place when upside down in the chamber. Note that these insulating rings were routinely inspected and cleaned (or replaced), due to the high conductivity of the sputtered LSCO. During long sputtering times, these rings would build up a layer of sputtered material that eventually formed shorts to the ground, causing the plasma to arc. Such arcing negatively impacted film properties (*e.g.*, increasing film roughness) and damaged the sputtering targets.

After installation, new targets were 'pre-sputtered' *via* 8 - 24 hours of continuous sputtering (until reaching a stable voltage), to remove surface layers and expose the bulk of the target for optimal film stoichiometry. Single-crystal (001)-oriented perovskite oxide substrates (MTI Corp.) were placed directly on top of the substrate heater (see Fig. 2.1(a)) and annealed at 900 °C for 15 - 30 minutes under 0.45 - 1.5 Torr of flowing O_2, to remove any organic contaminants and prepare the surface for film deposition. After this anneal and sufficient pre-sputtering time, the substrates were then cooled to the growth temperature and the plasma power / P_{O_2} were ramped to the growth conditions. The substrate heater functioned by joule-heating of a metallic meander 'element' made of a specialized oxidation-resistant steel alloy, KAF (Kanthal® AF), a proprietary alloy of the type Fe-Cr-Al, where the alloying element Al is critical in building up an oxidation-resistant surface layer upon repeated high-T cycling in oxidative conditions. The heater was rated for 1000 °C and isolated from its mounting fixture by Al_2O_3 thermal insulators and radiation shielding. Both the heater mounting fixture and the back of the target arm were water cooled (~20 °C) (see Fig. 2.1(a)).

Table 2.1

Material	T (°C)	I (mA)	P_{O_2} (Torr)	"z" (mm)	Growth rate (Å min^{-1})	Cooling
$LaCoO_3$	700	200	1.5	102 – 106	15 – 20	600 Torr O_2
$La_{1-x}Sr_xCoO_{3-\delta}$ ($0.1 < x < 0.7$)	600	175 – 200	1.4 – 1.7	103 – 107	15 – 22	600 Torr O_2
$SrCoO_{2.5}$	700 - 750	100 – 200	1.5	108 – 111	10 – 20	1.5 Torr O_2

Table 2.1 shows the optimized growth conditions used in this study for the growth of LSCO and SCO thin films. After an additional pre-sputter of ~15 - 30 min at the conditions shown in Table 2.1, growths were initiated by moving the arm such that the gun with the lit plasma came to rest directly over the substrate heater (as shown in Fig. 2.1(a)). The target-to-substrate distance was fixed during deposition, but adjusted beforehand, to typically ~1 - 2 cm. This distance has a constant offset relationship to the value '*z*' in Table 2.1, *i.e.*, $z - C$ = target-to-substrate distance. C varied slightly based on the target thickness and specific electrical isolation but was ~90 mm. Fig. 2.1(b) shows an example photo of the oxygen plasma during deposition of an LSCO thin film. After the intended growth time, the arm was moved back, the DC current was ramped to zero, the chamber was flooded with O_2 (600 Torr), and the heater was switched off. Note that BM-SCO films were cooled *without* post-deposition O_2 flooding but were instead cooled in 1.5 Torr O_2. The optimal sputtering conditions of Table 2.1 (T, P_{O_2}, '*z*', DC current / power, growth rate), were established, for the most part, in prior work on high-P_{O_2} sputtered LSCO films [48,107–109,169], except in the case of SCO, where only 1 prior report on high-P_{O_2} (RF) sputtering was available [218]. For BM-SCO, the growth optimization process consisted of systematically varying growth and cooling conditions, while prioritizing peak intensity, phase purity, lattice parameter, and surface / interface roughness as determined from the X-ray characterization described in the following section.

2.2 Thin film structural characterization *via* X-ray scattering

X-ray scattering techniques have been used to characterize the structure of crystalline solids for over a century. High-resolution X-ray diffraction (HRXRD), rocking curve analysis, and reciprocal space mapping are complementary techniques, which are particularly well suited for characterization of epitaxial thin films. Each of these are

introduced in the following subsections, followed by the related technique of grazing-incidence X-ray reflectometry (GIXR).

2.2.1 High-resolution X-ray diffraction

Structural characterization of epitaxial films can be likened to that of single crystals, as an ideal film is in perfect registry with the substrate. Therefore, for epitaxial films on single-crystal substrates, high angular resolution is needed to quantitatively characterize the film structure. In general, HRXRD implies the use of more X-ray beam optics *vs.* other XRD techniques, sacrificing intensity for higher angular resolution. Depending on the needs of a particular sample, however, either more intensity (and potentially higher signal-to-noise ratio (SNR)) *or* higher resolution may be more desirable.

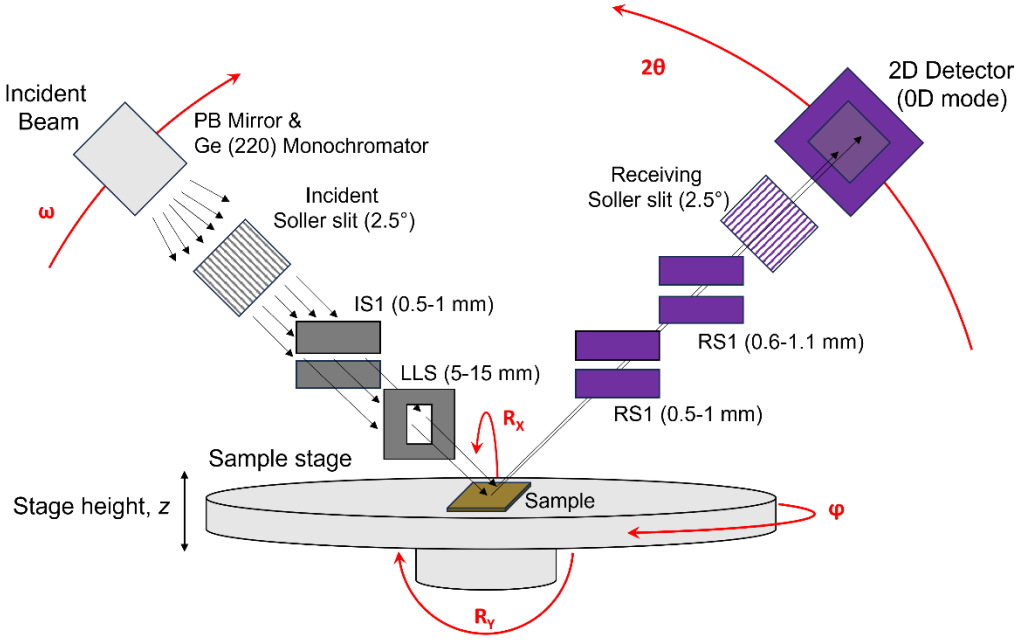

Figure 2.2: Schematic diagram of the Rigaku SmartLab XE high-resolution X-ray diffractometer with all the optics used in this thesis. The various beam optics are marked with their respective setting ranges. The relevant rotation axes are marked by red arrows.

In this work, HRXRD was performed on LSCO and SCO thin films using a Rigaku SmartLab XE diffractometer equipped with a Cu anode, W filament X-ray source. All HRXRD scans were taken using a parallel beam (PB) geometry (vertical divergence ~0.01°), and a Ge (220) single-crystal two-bounce monochromator, allowing only Cu $K_{\alpha 1}$ radiation (λ = 1.5406 Å). For specular scans, incident and receiving 2.5° Soller slits were used to limit horizontal beam divergence, while asymmetric scans used only the incident

2.5° Soller slit (to increase intensity). The diffractometer was also equipped with computer-controlled incident and receiving vertical slits. These were varied depending on the intensity *vs.* resolution needs of each sample (mostly determined by the thickness of the film), but were typically as follows: incident slit 1 (IS1) = 0.5 - 1 mm, receiving slit 1 (RS1) = 0.5 - 1 mm, and receiving slit 2 (RS2) = 0.6 - 1.1 mm. A length-limiting slit (LLS) on the incident beam was also used to control the lateral beam footprint, roughly translating to the lateral size of the film, *e.g.*, 5 × 5 mm^2 → 5 mm LLS, 10 × 10 mm^2 → 10 mm LLS. The above optics are shown schematically in Fig. 2.2, along with the angles of rotation of the diffractometer: R_x, R_y, and ϕ, representing the sample stage's rotation angles, and ω and 2θ the source and detector angles, respectively.

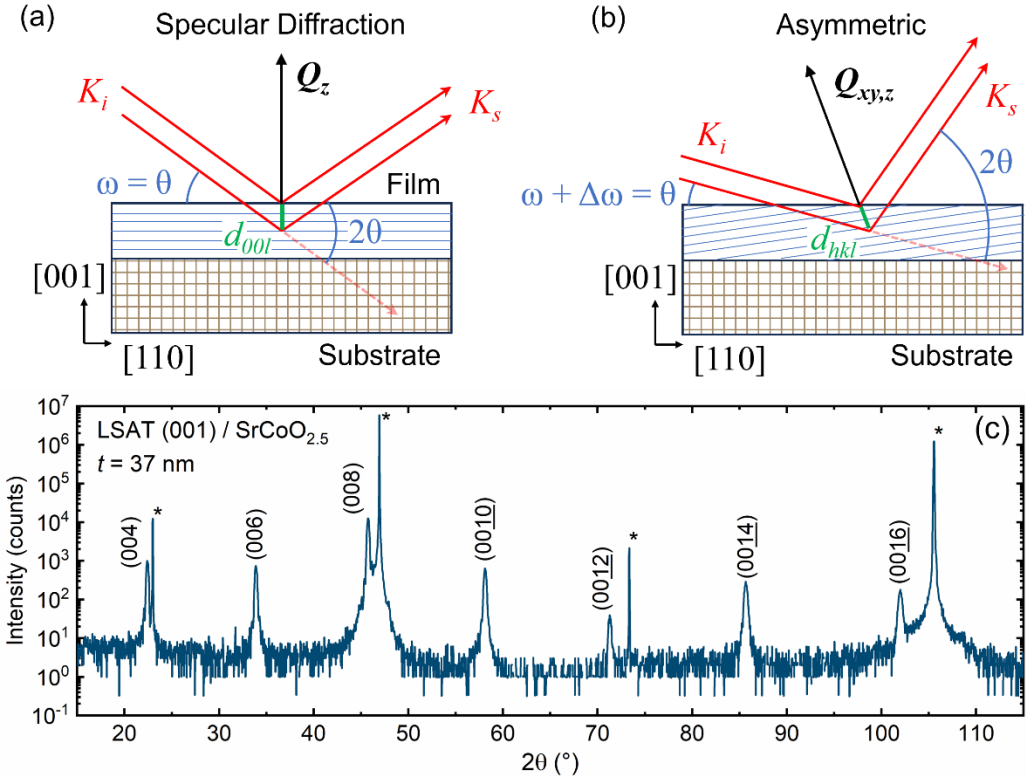

Figure 2.3: (a) and (b) are schematic illustrations which highlight the differences between specular and asymmetric diffraction modes in thin films. (c) An example of a wide-range HRXRD 2θ-ω coupled scan in specular mode for a 37-nm-thik BM-SCO film on LSAT(001) showing all the 00*l*-type peaks. The substrate 00*l* peaks are marked by asterisks.

In epitaxial thin films, the direction normal to the substrate surface is known, and interplanar spacing in this direction can be probed directly using the so-called 'specular' condition, *i.e.*, ω = ½ 2θ. In this thesis, only (001)-oriented substrates were used, and

therefore specular XRD scans probed the *c*-direction in the crystal, *i.e.*, the film surface-normal direction. First, the samples were affixed flat to the sample stage with double-sided tape in the center of the beam spot. Then the height of the sample was adjusted such that the surface corresponds to the mid-point of the X-ray beam. Next the beam was aligned to the surface of the sample using a series of alternating ω and R_x (tilt) scans at low 2θ (typically 0.5 - 0.75°). Once the beam was aligned to the surface it was more easily aligned to the substrate crystallographic directions. Ideally, the relationship of the sample surface should exactly translate to its crystallographic orientation, in practice, however, miscut angles cause deviations from the ideal and must be corrected for. Therefore, to align the scattering vector perfectly with the substrate's [001] direction, the (002) Bragg peak was found, and its intensity optimized (in ω and R_x), resulting in an offset in ω such that the (002) peak position meets the specular condition. This is shown schematically in Fig. 2.3(a), where $\boldsymbol{Q}$, the scattering vector, is shown to be parallel with the substrate [001] direction. Fig. 2.3(c) then shows an example of a wide-range 2θ-ω coupled scan of a 37-nm-thick BM-SCO film on LSAT(001), where only the film/substrate 00*l* reflections can be seen. Such scans immediately provide quantitative insight into the film structure, such as the out-of-plane lattice parameter, *c*, and the 'Scherrer' length, Λ, from the following equations, respectively:

$$c = \frac{1}{2}\lambda l \sin\theta \qquad (2.1) \qquad \text{and} \qquad \Lambda = \frac{0.9\lambda}{w\cos\theta}\,. \qquad (2.2)$$

Eqs. 2.1 and 2.2 represent Bragg's law (solved for *c* from 00*l*-type planes) and the standard Scherrer equation, respectively, where λ is the wavelength of X-ray radiation, *l* is the miller index of the 00*l* plane of interest, and *w* is the width of the peak in 2θ (expressed in radians), usually the full-width-at-half-maximum (FWHM). Peak broadening, in a high-resolution system, is primarily due to finite crystallite size and microstrain. Thus, the ratio Λ/t is a measure of film crystalline quality, where a perfectly crystalline microstrain-free film would produce diffraction peaks of widths corresponding to $\Lambda/t = 1$. Film thickness, *t*, was also extracted from 2θ-ω coupled scans using the 2θ spacing of the finite size oscillation fringes about the film peak reflections (when observed). This process is outlined in detail in Section 2.2.3.

2.2.2 *Rocking curves and reciprocal space maps*

In addition to the specular coupled scans described above, *asymmetric* HRXRD can also be extremely powerful in characterizing thin film structure. Fig. 2.3(a) and (b) show schematic diagrams illustrating the differences between the special case of specular diffraction (panel (a)) and the more general asymmetric condition (panel (b)). In specular diffraction, because $\boldsymbol{Q}$ has no *x*- or *y*-component, no information about the film structure other than in the *z*-direction can be deduced. However, deviating from the specular condition, *i.e.*, $\omega + \Delta\omega = \theta$, immediately gives information about the film's in-plane structure. The simplest form of this is attained by simply 'rocking' the sample about the specular condition, *i.e.*, scanning ω at a particular 2θ position. Such scans are routine in triple-axis diffractometers and are known as rocking curves (RCs). The width of the film peak RC provides information about the 'mosaicity' of the sample: the broader the RC peak, the less coherent those planes are within the sample (*i.e.*, higher mosaic spread). An ideal epitaxial film will have a RC FWHM mirroring that of the substrate, and it is common for RC FWHM values to be used as a measuring stick for film crystalline perfection.

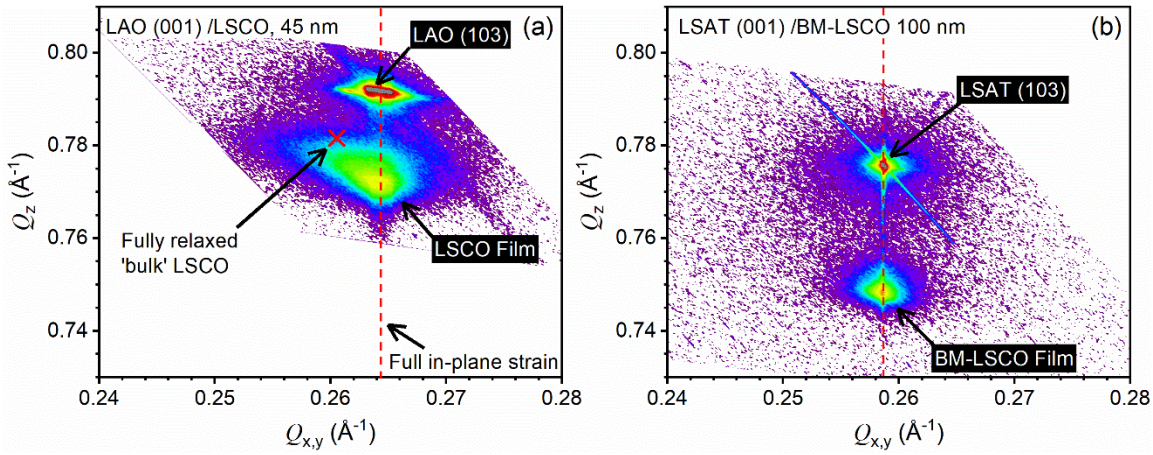

Figure 2.4: Examples of HRXRD RSMs of LSCO thin films. (a) RSM of a 45-nm-thick LSCO *x* = 0.5 film on LAO(001) (–1.2% strain) around the (103) peak. The nominal bulk value of LSCO *x* = 0.5 is shown on the map as a red "×". The film peak intensity is shown to lie partly 'off-line' from the pseudomorphic in-plane lattice constant of the substrate (red dashed vertical line) toward the bulk position, indicating partial strain relaxation. (b) RSM of a 100-nm-thick BM-LSCO *x* = 0.5 film on LSAT(001) (–0.3% strain) showing essentially no strain relaxation.

More information on the in-plane film structure can be extracted by generating reciprocal space maps (RSMs). When moving from 00*l*-type to any other general *hkl*, such

planes will intersect the film substrate interface, as shown in Fig. 2.3(b), and therefore can reveal information about the film's in-plane structure. In perovskites, the asymmetric reflection with the highest structure factor is the (103) and its equivalents. These peaks are therefore commonly mapped in reciprocal space to characterize the in-plane structure of epitaxial perovskite films. Fig. 2.4 shows two examples of (103) peak RSMs of LSCO films: in (a) a partly relaxed 45-nm P film on LAO, and in (b) a fully strained (or pseudomorphic) 100-nm BM film on LSAT. RSMs are generated by performing 2θ-ω coupled scans at a range of different starting values of Δω, essentially forming a raster image of diffracted intensity over a region of reciprocal space. However, in the Rigaku Smartlab XE used in this work, this process is sped up considerably by employing the functionality of a 2D detector. Normally, this detector operates in "0D" mode (no spatial consideration of detected counts), but when collecting RSM images the detector is operated in "1D" mode, where for each ω the detector differentiates the signal for different 2θ. This Δω *vs.* 2θ *vs.* intensity image is then converted to scattering vector components Q_x (or Q_y) and Q_z, or equivalently, into reciprocal lattice units (r.l.u.), *h*, *k*, and *l*, generating a contour map of reciprocal space. The following equations are used to convert between these coordinate systems [219]:

$$Q_z = \frac{2\pi}{\lambda}[\sin(2\theta - \omega) + \sin(\omega)], \tag{2.3}$$

$$Q_{x,y} = \frac{2\pi}{\lambda}[\cos(2\theta - \omega) - \cos(\omega)], \tag{2.4}$$

where Q_z and $Q_{x,y}$ have units of Å^{-1}, and can be converted to r.l.u. by multiplying by the substrate lattice constant. Equivalently, the lattice parameters of the film, in both the out-of-plane and in-plane directions, can easily be calculated from the Q_z and $Q_{x,y}$ peak position, as $c = 3/Q_z$, and $a,b = 1/Q_{x,y}$. In general, RSMs can provide a wealth of information in thin films and heterostructures [220], however, for epitaxial films, RSMs are perhaps most useful as probes of a film's strain state (*i.e.*, whether fully strained, or partly to fully relaxed). Epitaxy implies registry of an overlying film with the crystal symmetry of the substrate at the interface, requiring that the film takes on a specific in-plane lattice constants set by the relationship to the substrate lattice. This results in RSM film reflections which lie on the same $Q_{x,y}$ line as the substrate (see vertical red dashed lines in Fig. 2.4). It should

be noted that Q_x and Q_y can only be considered equivalent when the substrate's in-plane lattice parameters are equal. When this is not the case, it indicates some form of defects in the film that allow for the relaxation of in-plane strain. Fig. 2.4 provides an illustrative example, where in panel (a), a P-LSCO film under –1.2% strain on LAO begins to relax at a thickness of 45 nm, while in panel (b), a 100-nm-thick BM-LSCO film on LSAT (~-0.3 %) remains fully strained.

2.2.3 Grazing-incidence X-ray reflectometry and determination of film thickness

The previous subsections described XRD techniques at relatively large 2θ and are sometimes referred to as wide-angle XRD (WAXRD). GIXR, on the other hand, focuses on X-rays' interaction with matter at very low (grazing) incidence angles, making it a highly surface sensitive technique. GIXR is thus extremely important in characterization of thin films, where interference patterns of reflected X-rays can be fit to extract useful information such as the surface roughness, film thickness, depth dependent density, *etc*. GIXR was used in this thesis primarily to determine film thicknesses, and as a *qualitative* measure of film roughness during optimization of growth parameters. The same Rigaku Smartlab XE instrument was used for GIXR measurements, but with slightly different optics, and much tighter vertical slits. For GIXR, a LLS of 2 mm was used, with IS, RS1, and RS2 set to 0.05 - 0.25, 0.2, and 0.3 mm, respectively.

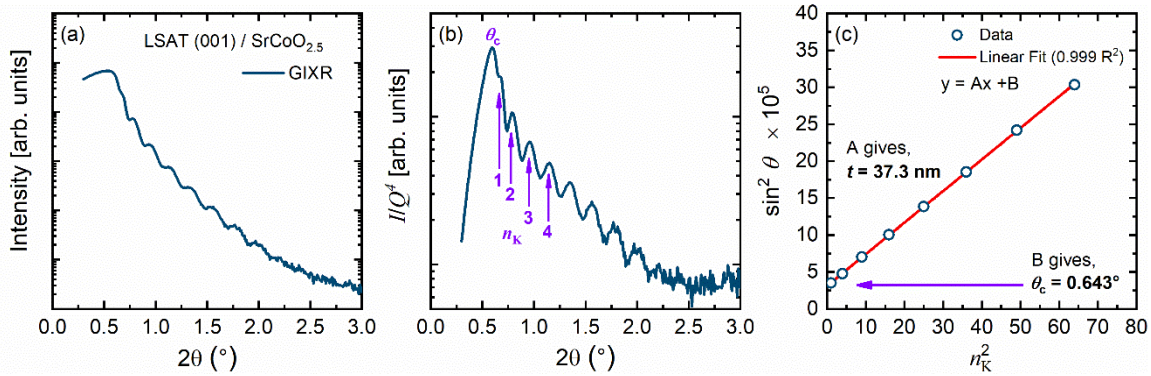

Figure 2.5: (a) Specular GIXR of a the same $SrCoO_{2.5}$ film on LSAT(001) as in Fig. 2.3(c). (b) the same data as in (a) but re-plotted after normalizing by the Fresnel decay, Q^{-4} (where $Q = Q_z = 4\pi\sin\theta/\lambda$), as is common [219]. (c) $\sin^2\theta_{n_K}$ *vs.* n_K^2 where θ_{n_K} are the maxima of the Kiessig fringes indexed by n_K (marked by purple arrows in). The linear fit to the data (red solid line) was used to calculate the film thickness, t, and critical angle, θ_c, as in Eq. 2.5.

Fig. 2.5(a) shows the GIXR 2θ-ω coupled scan, in specular mode, for the same BM-SCO film as shown in Fig. 2.3(c). The oscillations (known as Kiessig fringes) in the reflected intensity, which are overlaid on the overall Q_z^{-4} Fresnel decay behavior, are due to the interference of X-rays reflected from the film/air interface with those reflected from the substrate/film interface. The 2θ period between successive fringes depends on the film thickness according to the Kiessig formula [219]:

$$\sin^2\theta_{n_K} - \sin^2\theta_c = \frac{\lambda^2}{4t^2} n_K^2, \tag{2.5}$$

where n_K is the Kiessig fringe integer index, θ_{n_K} is the angle corresponding to the maxima of the n_K^{th} fringe, and θ_c is the critical angle for total internal reflection. Fig. 2.5(b) shows the same data as in panel (a) but with the *y*-axis normalized by the Fresnel decay, *i.e.*, I / Q_z^{-4}, where $Q_z = 4\pi\sin\theta/\lambda$. This is commonly done to more easily inspect the fringe shape and amplitude [219]. Fig. 2.5(c) then shows a plot of $\sin^2\theta_{n_K}$ *vs.* n_K^2. Film thickness (t) was determined from the slope of a linear fit to the points in Fig. 2.5(c). An analogous treatment can also be used to extract t from finite-thickness oscillations about film reflections in WAXRD scans (so-called Laue fringes) using the following equation:

$$\sin\theta_{n_L} = \frac{\lambda}{2t} n_L, \tag{2.6}$$

where n_L and θ_{n_L} correspond to the Laue fringe integer index and corresponding θ value, respectively. Film thickness was determined by an average of both methods when fringes were observed from both. When fringes from GIXR were not observed, *e.g.*, due to high surface roughness, the Laue fringe t was used instead. And in rare cases, *e.g.*, very thick films >100 nm, where fringes were not resolvable by either method, the t was simply estimated from previously established deposition rates and times.

2.3 Measurement of thin film electronic and magnetic properties

2.3.1 Electronic transport and magneto-transport

Electronic properties of LSCO and SCO thin films were characterized using the four-terminal van der Pauw method, which is commonly employed for measuring the

resistivity of thin films. Van der Pauw (VDP) first pioneered this approach for determining sheet resistance and resistivity in 1958, where four electrical contacts (two current leads and two voltage leads) are used to eliminate the wire- and contact-resistances from the measurement [221]. There are four requirements for an accurate VDP measurement of an arbitrarily shaped sample: (1) the sample is uniform in thickness, (2) it is homogenous and isotropic with no holes / cracks, (3) the contacts are on the circumference, and (4) the contact area makes up < 10% of the sample area [221]. The relevant equations are:

$$\exp\left(\frac{-\pi R_1}{R_s}\right)+\exp\left(\frac{-\pi R_1}{R_s}\right)=1\,, \quad (2.7) \qquad \rho = R_s t\,, \quad (2.8)$$

$$\rho=\frac{\pi t}{\ln 2}\left(\frac{R_1+R_2}{2}\right)f\,, \quad (2.9) \quad \text{and} \quad \cosh\left(\frac{\left[\frac{R_1}{R_2}-1\right]}{\left[\frac{R_1}{R_2}+1\right]}\frac{\ln 2}{f}\right)=\frac{1}{2}\exp\left(\frac{\ln 2}{f}\right), \quad (2.10)$$

where R_1 and R_2 are the two orthogonal four-terminal resistances in the VDP geometry, R_s is the sheet resistance (in Ω sq^{-1}), t is the film thickness, and f is the anisotropy factor, which depends on the ratio (R_1/R_2), where $R_1 \leq R_2$.

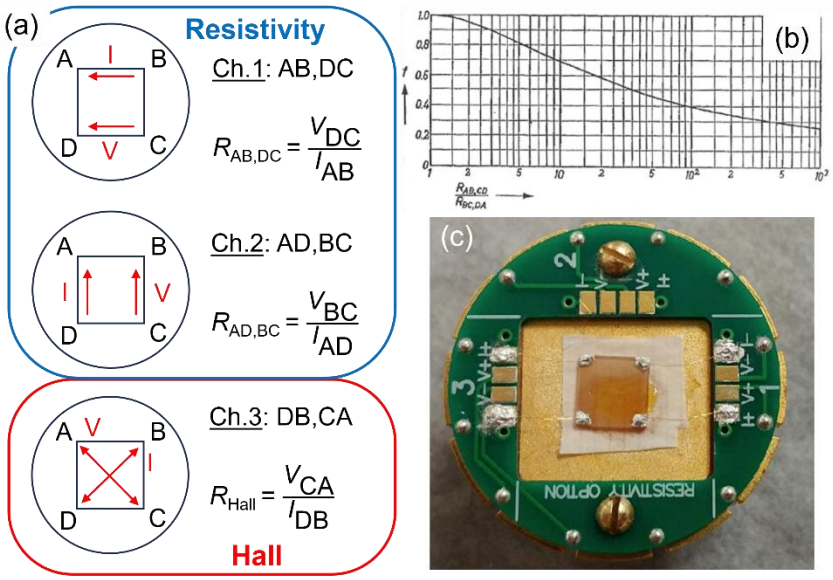

Figure 2.6: (a) Schematic diagrams of the two VDP four-terminal resistance channels (Ch. 1 and 2, top, blue) and the Hall channel (Ch. 3, bottom, red). (b) Anisotropy factor, *f*, *vs.* anisotropy of VDP resistance (R_1/R_2) [221]. (c) Photo of an example 5 × 5 mm^2 film wired and mounted onto a PPMS puck. (Magnetic field is applied out-of-plane.)

Fig. 2.6(a) shows the two orthogonal VDP channels R_1 and R_2 schematically (blue) and how they are calculated using Ohm's law. Calculating ρ using Eqs. 2.7 and 2.8 is

equivalent to using 2.9 and 2.10, however, the latter is often more convenient, as f has been solved numerically and tabulated as a function of R_1/R_2, as shown in Fig. 2.6(b), such that the simpler Eq. 2.9 can be used directly. In this thesis, the measured anisotropy was rarely above 2, resulting in $f \approx 1$ from Fig. 2.6(b). Fig. 2.6(c) shows a photograph of a prototypical film sample mounted on a puck and wired using 4 corner contacts of In solder and fine Au wire. The pads on the outside of the puck lead to pins on the bottom (not shown) which then complete a circuit to the measurement instrument(s).

The third resistance channel shown in Fig. 2.6(a) (red, bottom) is used to measure the so-called Hall resistance (R_{Hall}). Hall effect measurements are used to characterize the dependence of electronic properties on the applied magnetic field, sometimes referred to as *magneto*-transport. Due to the Lorentz force, electrons passed in a diagonal current across the sample will be directed ±90° when acted on by a magnetic field directed out-of-plane. This change will then be reflected in the measured R_{Hall} *via* the 'ordinary' hall effect, $R_{\mathrm{Hall}} = R_{\mathrm{H}}\mu_0 H$, where μ_0 is the vacuum permeability and R_{H} is the Hall coefficient. For diffusive transport where one dominant carrier type is present $R_{\mathrm{H}} = 1/en_{\mathrm{s}}$, where e is the elementary charge and n_{s} is the 2D 'sheet' carrier concentration. By multiplying by t, one can express the Hall resistivity, ρ_{xy} (*i.e.*, $R_{\mathrm{Hall}} \times t = \rho_{xy}$). In semiconductors, $R_{\mathrm{Hall}}(H)$ can be used to determine the type of the majority carrier, their concentration, and their mobility (in combination with R_{s}). In F materials however, another term must be added, modifying the above Hall equation to [222]:

$$\rho_{xy} = R_{\mathrm{H}}\mu_0 H + R_{\mathrm{AH}}\mu_0 M, \tag{2.11}$$

where the 1st term on the right-hand-side is the ordinary Hall term, while the 2nd term is the 'anomalous' Hall term (R_{AH} is the anomalous Hall coefficient). In highly hole-doped F oxides, like LSCO, R_{H} is small (being inversely proportional to n_{s}, with holes as the dominant carrier type), whereas R_{AH} can be quite large [179,223] allowing the 2nd term to dominate (*i.e.*, $\rho_{xy} \approx R_{\mathrm{AH}}\mu_0 M$). Thus, in such materials, measuring R_{Hall} can be used to effectively probe M. Using the fact that $R_{\mathrm{AH}} \propto \sigma_{\mathrm{AH}}$ (where σ_{AH} is the anomalous Hall conductivity), and the definition of σ_{xy} (from tensor notation), we have [179]:

$$\sigma_{xy}^2 = \rho_{xy}/\rho_{xx}^2 \propto \sigma_{\mathrm{AH}} M\,, \tag{2.12}$$

where σ_{xy} is the transverse conductivity. Using Eq. 2.12, the four-terminal resistance measurements described above can then be used to generate plots of $\sigma_{xy}(T)$, and $\sigma_{xy}(H)$, which are directly proportional to $M(T)$ and $M(H)$. Note that R_{AH} (and thus σ_{AH}) is independent of M but has T dependence, which must be considered when interpreting results, *e.g.*, $\sigma_{xy}(T)$. This electronic-transport-based approach to probing magnetism can be highly beneficial in thin films, where traditional magnetometry can be challenging due to the extremely low mass of the films and difficulty separating the magnetic signal of the film from that of the substrate.

In this thesis, four-terminal resistance measurements of LSCO and SCO thin film samples were performed using the above described VDP method, using either: (1) direct current measurements from a Keithley 2400 source-measure unit (sometimes in combinations with a Keithley 2000/2002 multimeter), or (2) a quasi-AC measurement system incorporated within the measurement bridge of the Quantum Design Physical Property Measurement System (PPMS). *T*- and *H*-dependent measurements were performed in the PPMS Evercool-II liquid-He-cooled cryostat, between 2 - 400 K in maximum applied magnetic fields of ±90 kOe. The films were electrically contacted by either In solder as shown in Fig. 2.6(c) or using sputtered metal contacts comprised of ~5 nm Mg / 400 nm Pt deposited in a vacuum chamber through a hard (steel) mask. The latter contacts were used exclusively for all ion-gel-gated EDLT film devices (see Section 2.5). The role of the Mg 'adhesion' layer was critical to providing Ohmic contact behavior, especially at low-*T*. In all measurements, *I vs*. *V* curves were recorded at representative *T* (and *H*), to ensure ohmic contacts and to avoid Joule-heating by selection of appropriate probe currents. Finally, when performing DC-measurements, both positive and negative currents were applied to account for thermoelectric voltages and other effects.

2.3.2 Magnetometry

Direct measurements of the magnetization of LSCO and SCO films and bulk samples were performed using several magnetometers: (1) vibrating sample magnetometers (VSMs) using both a PPMS Evercool-II (PPMS-VSM)(in both standard and oven-mode) and a Lakeshore 8600 single-stage variable temperature VSM (SSVT-

VSM), (2) a superconducting quantum interference device (SQUID) equipped VSM (or SQUID-VSM) using a Quantum Design Magnetic Property Measurement System 3 (MPMS-3), and (3) a reciprocating-sample-option (RSO) SQUID using a Quantum Design MPMS-*XL*. Bulk samples and BM-LSCO and BM-SCO films were measured in the VSM-based systems, while ion-gel-gated films were measured in the MPMS-*XL*. Table 2.2 lists the different magnetometers used in this work and summarizes some of their technical specifications.

Table 2.2

Magnetometer	T-range	Sensitivity	Max. Field
PPMS-VSM(standard)	2-400 K	10^{-6} emu	±9 T
PPMS-VSM(oven)	300-1000 K	~10^{-5} emu	±9 T
Lakeshore SSVT-VSM	77-950K	10^{-6} emu	~±2 T
MPMS-XL RSO-SQUID	2-400 K	10^{-8} emu	±7 T
MPMS-3 SQUID-VSM	2-400 K	<10^{-8} emu	±7 T

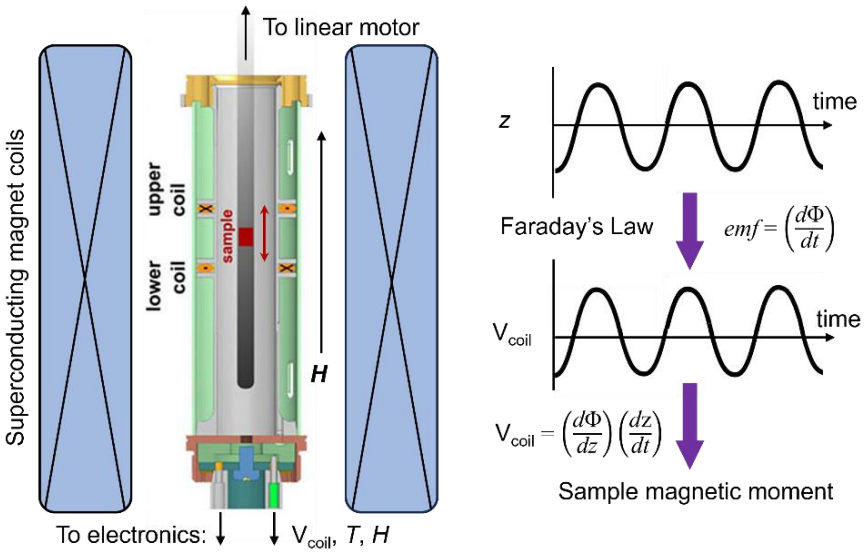

Figure 2.7: Schematic depiction of the vibrating sample magnetometer (VSM) option of the Quantum Design PPMS (adapted from Ref. [224]). The left-side shows the PPMS coil-set puck inserted into the cryostat inside a superconducting magnet, with the sample stick vibrated in the center by a linear motor (not shown). The right-side shows the principle of the conversion of measured *V* to magnetic moment.

As primarily VSMs were used in this work, a brief introduction to their working principle and the design of the PPMS VSM option is warranted. From Faraday's law of

electromagnetic induction, by moving a magnetic sample near a loop of wire, a voltage will be induced in the wire proportional to the change in magnetic flux through the loop. In a VSM, by comparing the oscillations of sample position with the resulting voltage induced oscillations in the so-called 'pickup coils'(V_{coil}), a magnetic moment can be calculated using the following equation [225]:

$$V_{coil} = 2\pi f C m A \sin(2\pi f \tau), \tag{2.13}$$

where m is the DC magnetic moment, A is the amplitude of the oscillation, f, is the frequency, τ is time, and C is a coupling constant. In the PPMS VSM option this is accomplished by driving a sample stick in an oscillatory fashion using a linear motor through a set of pickup coils. An analogous oscillatory V_{coil} reading is then recorded, and the moment is calculated for a given averaging time. (Note that this conversion makes use of an initial calibration to a sample with a known magnetic moment). Meanwhile, the sample T is maintained (between 2 K to 400 K) by concerted liquid-He cooling and Joule heating *via* an exchange gas of low pressure He (~20 Torr). The applied magnetic field (applied along the direction of oscillation) is set by charging/discharging a superconducting magnet coil, that is kept below its superconducting T_c by a bath of liquid He. Fig. 2.7 shows this setup specifically for the PPMS VSM option (left), along with a schematic of the above-described principle of operation (right). During magnetometry measurements in the PPMS VSM, the oscillation (vibration) frequency, amplitude, and averaging time were set to 40 Hz, 2.5 mm, and 10 seconds, respectively. Initial sample centering was accomplished by lowering the sample through the pickup coils while oscillating, and automatically fitting the measured curve to the flat region of maximal m. For accurate centering, a moderate field (500 - 2500 Oe) was sometimes applied to increase the detected m. After sample centering, 'touchdown' operations were performed at 30 K intervals to adjust the sample center position to account for thermal expansion differences between the cryostat and sample stick. 5 × 5 mm^2 film samples were mounted using GE-7031 varnish to the center of a 4 mm wide quartz paddle. Bulk polycrystalline samples were first powdered and then mounted using mating polypropylene capsules snapped in place within a brass half-tube.

SQUID magnetometers are the most sensitive probes of magnetization, owing to their ability to measure magnetic flux quanta using superconductor-insulator-superconductor devices known as Josephson junctions. SQUID magnetometers can measure magnetic moments < 10^{-8} emu. For this reason, they are particularly advantageous, if not essential, in characterizing the magnetic properties of samples of very small mass (like thin films). Even higher sensitivity / precision can be achieved by combining the working principles of a SQUID with that of a VSM, *e.g.*, by replacing the pickup coils in Fig. 2.7 with SQUID loops (as in the MPMS-3 SQUID-VSM). SQUID based magnetometers were utilized in this work to measure the magnetic properties of the lowest moment samples, including ion-gel-gated LSCO film devices and BM-LSCO/SCO film and bulk samples.

Measurement of very small magnetic moments presents challenges in the form of contamination by magnetic impurities which can significantly impact magnetometry measurements involving signals below ~10^{-4} emu [226]. Therefore, great care was taken to avoid magnetic contamination of the samples in these studies. In thin films, another challenge to reliable magnetometry measurements is accounting for the magnetic signal from the substrate. While the oxide substrates used in this work have relatively low susceptibility their macroscopic nature puts their diamagnetic / paramagnetic m on par with (or larger than) that of the film, particularly at low T and in high H. In addition, magnetic impurities are always present in such crystals from their fabrication processes, so two nominally identical substrates may not have exactly the same $M(T)$ / $M(H)$ characteristics. Nevertheless, relevant substrate background subtraction methodologies have been developed [106,227,228], and these were adopted in the treatment of magnetometry data in this thesis, as appropriate.

2.4 Optical probes of thermal transport and refractive indices

The following sections describe the optical techniques used by my colleagues in our collaborative work to characterize the thermal and optical properties of ion-gel-gated LSCO thin films. While I did not perform the following experiments, the results generated

from them are critically important to the analyses and discussions presented in Chapter 4. Therefore, basic introductions to the working principles of each is worthwhile.

2.4.1 Time-domain thermoreflectance

Measurement of the thermal conductivity of LSCO thin films was performed using time-domain thermoreflectance (TDTR). TDTR is an ultrafast-laser based pump-probe technique. It is entirely optical and 'non-contact', making it compatible with many materials systems (including thin films and heterostructures) and sample environments [229,230]. In addition, the ultrafast technique (10^{-15} - 10^{-9} s) makes it suitable for studying different energy carriers such as electrons, phonons, and magnons [229,230]. Fig. 2.8 shows the basic principles of TDTR and procedure for measuring the thermal conductivity in a thin film sample. In panel (a), a laser pulse is shown moving from the source (upper left) to the sample, it is split along the way into a 'pump' and 'probe' beam, that are related by a time delay. The pump beam strikes the sample in high frequency pulses, locally heating it, while the probe beam is reflected off the sample surface, and the change in reflectance of the sample is used to calculate T [231]. The probe beam tracks the T-decay on cooling, and by modelling the time dependence, using a diffusion equation, the thermal conductivity (Λ) can be extracted [232,233]:

$$\frac{\Lambda_r}{r}\frac{\partial}{\partial r}\left(r\frac{\partial T}{\partial r}\right)+\Lambda_z\left(\frac{\partial^2 T}{\partial z^2}\right)=C\frac{\partial T}{\partial t}. \tag{2.14}$$

Eq. 2.14 is the governing equation, based on Fourier's law of heat conduction in, where Λ_z and Λ_r are directionally dependent thermal conductivities (in cylindrical coordinates: r, and z, due to the symmetry of laser heating), and C is the volumetric heat capacity. Eq. 2.14 can be solved by converting to the frequency domain, given the ultrafast periodic heating of the pump pulses and proper boundary conditions [232,233]. The ratio of thermoreflectance signals (read as voltages) as a function of time delay between pump and

probe beams is then fit to the diffusion model solution (*i.e.*, modelling the *T*-response in the frequency domain) to determine Λ [229,232,233].

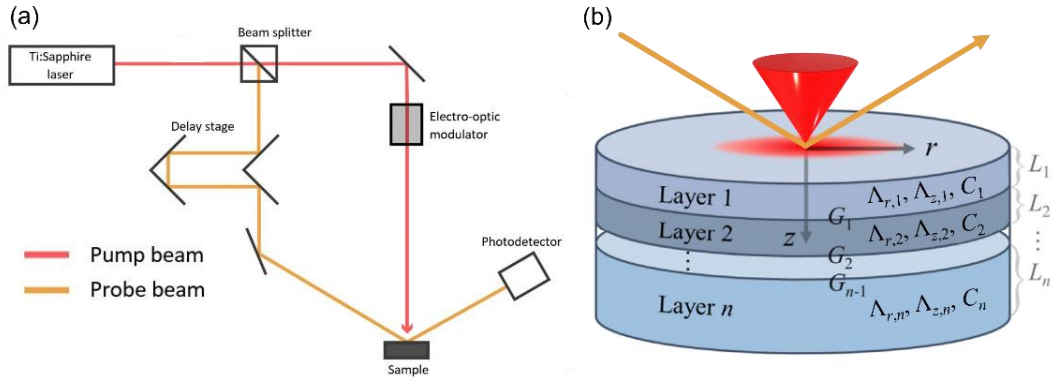

Figure 2.8: Schematic representation of the operating principles of TDTR and measurement of thermal conductivity (Λ). (a) Pump-probe beam optical laser set-up (adapted from Ref. [234]). (b) Cylindrical coordinate representation of a sample of arbitrarily numbered (*n*) layer stacking, showing the necessary input parameters to model the thermal diffusion equation: $\Lambda_{r,n}$ and $\Lambda_{z,n}$, are thermal conductivities in *r* and *z* directions, respectively, C_n, are volumetric heat capacities, and G_n are the interfacial thermal conductances. Adapted from Ref. [232].

The situation becomes more complicated when multiple layers are involved, requiring input parameters for each layer and each heterointerface to produce an accurate fit. This concept is shown schematically in Fig. 2.8(b), where each of *n* layers in the stack has their own values for $\Lambda_{r,n}$, $\Lambda_{z,n}$, and C_n, and each of *n* interfaces their own interfacial thermal conductance (G_n). Additionally, TDTR often requires the use of an optically opaque top transducer layer to both absorb the probe beam and provide sufficient reflectance. Metals with high thermoreflectance coefficients, such as Al or Pt, are commonly used as transducers for TDTR [229]. Finally, varying frequency of the pump beam can add a depth-dependent sensitivity, by varying the time for heat transfer to occur between pulses [229]. In this work, a pump-beam wavelength of 783 nm was used along with 70 nm Pt transducer layers. Pt was specifically chosen to avoid gettering of O from the LSCO film (see Section 4.1.1). The pulse durations were ~100 fs and modulated to between 1.5 and 19 MHz. Additional specific experimental details of the TDTR technique used here will be discussed in Chapter 4 and can also be found in the work of my colleague Yingying Zhang [235].

2.4.2 Spectroscopic ellipsometry

Ellipsometry is a widely used optical characterization technique and is particularly useful for thin films, where it is commonly used to determine thickness, roughness, and electronic and optical properties [236]. Its operating principle involves reflection (or transmission) of a *polarized* light beam from (or through) a sample and measuring the change in polarization due to the interaction with the sample. The reflected beam passes through another polarizer, called an analyzer, before reaching the detector, so that the degree of polarization of the reflected beam can be measured with respect to the incident beam (as a function of the analyzer angle). This parameter is called the complex reflectance ratio, ρ, and is defined as,

$$\rho = \frac{r_p}{r_s} = \tan(\Psi)e^{i\Delta}, \tag{2.15}$$

where r_p and r_s are reflectance coefficients for parallel and perpendicularly polarized light (with respect to the plane of incidence), respectively, $\tan(\Psi)$ is the amplitude ratio, and Δ the phase difference. These two quantities, Ψ and Δ, can then be mathematically fit to theoretical models based on Fresnel's equations to indirectly determine the properties of the sample. In the case of solving for refractive indices of a thin film, this involves evaluating an appropriate model using known quantities where appropriate, such as the film thickness and the optical characteristics of the substrate.

In this work, optical characterization of ion-gel-gated LSCO films was performed using spectroscopic ellipsometry (SE) (350 - 1100 nm) with complementary spectrophotometry (SP) (350 - 2500 nm) and Fourier transform infrared spectroscopy (FTIR) (2500 - 5000 nm). The objective was to determine the real (n) and imaginary (k) parts of the refractive index of the films over a wide spectral range (350 - 5000 nm), from the visible to the near-infrared. To do this, transmittance spectra were first taken with unpolarized light at normal incidence using SP and FTIR (over different ranges) for both the bare substrates and subtrate/films samples. These spectra were then incorporated into a Kramers-Kronig-consistent refractive index model of the film and substrate, and fit, along with the results from SE, to produce broad-spectrum models of n and k of the films (See Section 4.2.1 for more measurement details).

2.5 EDLT device fabrication, ion gel synthesis, and gating experiments

The design and fabrication of LSCO-film EDLT devices for ion-gel gating experiments was based on the procedures developed in prior work [106,169,179]. Therefore, the details in this section will be given in brief to highlight the most important aspects as they relate to the research presented in Chapters 3, 4, and 5. Side-gate EDLT devices were fabricated in a four-step process, as shown schematically in Fig. 2.9:

(1) The as-deposited film was mounted into a fixture with a steel mask affixed over the top of the film covering the channel and contact electrode 'legs' but exposing the rest of the film surface. An Ar-ion milling sequence was used to remove the film material in all but the covered features. An IntlVac Ion mill was used with a beam voltage of 300 V, a current of 125 mA, an accelerating voltage of 36 V, and an incident angle of 85° (with stage rotation), producing an approximate etch rate of 2 - 3 nm min^{-1}. Various milling times were used based on the film *t*, ranging from 5 mins to 20 min.

(2) The ion-milled pattered film was then mounted in a similar fashion to step (1) but with a different steel mask, and Mg (5 nm) / Pt (40 - 50 nm) electrode pads and gate pads were sputtered at room *T* on the exposed areas of the film and substrate as in Fig. 2.9(c). The large overlap of the Mg/Pt contacts on the film electrode legs was intentional to provide more robust electrical contact. In other words, by increasing the area for a given resistance-area-product contact ($(RA)_{contact}$) material, we were able to reduce the contact resistance for our transport measurements.

(3) After sputtering of the gate and electrode / contact pads, the devices were then annealed to increase the adhesion of the contacts to the film. Such anneals were performed using a rapid thermal annealer (RTA) at 450 °C for 5 minutes in flowing O_2 (to prevent film reduction). The RTA step was critical in achieving low resistance contact to the film by lowering $(RA)_{contact}$. When no annealing was performed contact resistance was prohibitively high and exhibited non-ohmic behavior.

(4) The final step to complete the EDLT device was to laminate the gate pads, film channel, and electrodes with the ion gel electrolyte, as shown in Fig. 2.9(d) using a "cut and stick" method (see Fig. 1.21(c)) [157].

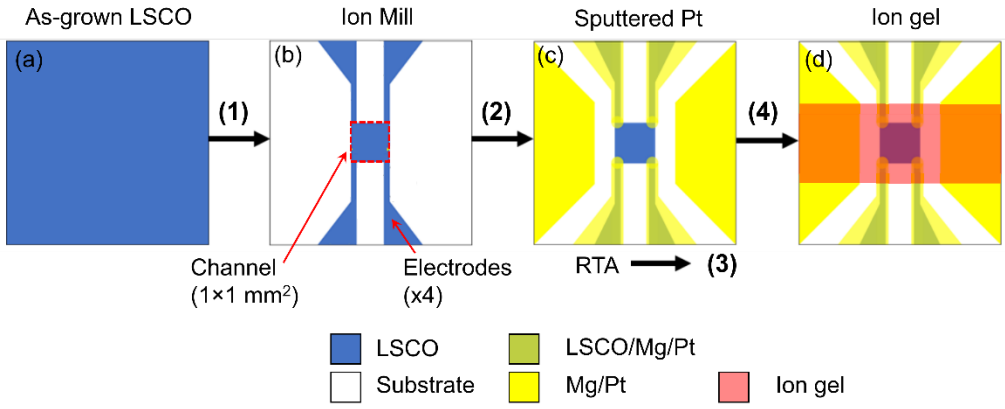

Figure 2.9: Schematic of the fabrication process for 5 × 5 mm^2 LSCO film EDLT ion-gel devices, adapted from Ref. [106]. (a) As-deposited film, (b) Ion-milled pattern with central 1 × 1 mm^2 channel and four electrode legs, (c) Mg (5 nm) / Pt (40 nm) sputtered contact electrodes and gate pads (followed by RTA), and (d) lamination of overlying ion gel onto side-gated EDLT.

Note, the above EDLT device geometry was used for electronic transport and TDTR measurements, while alternative geometries with larger channel areas (1.75 × 2 mm^2 to 4 × 3.5 mm^2), were used for *operando* SXRD, HRXRD, and magnetometry. The side-gate geometry was chosen over more traditional top-gate geometries primarily for its convenience, but with added benefits of lower gate 'leakage' currents and improved access to *operando* probes (such as that described in the next section) [176,180]. All the device geometries used identical fabrication steps, simply employing different steel masks and/or starting substrate sizes *e.g.*, either 5 × 5 mm^2 or 10 × 10 mm^2. The gate-to-channel-area ratio, a critical design consideration in electrolyte gate devices [237], was designed to be ~10 in 1 × 1 mm^2 channel devices (as in Fig. 2.9), and ~4 in all other devices.

The ion gels used in this work were prepared from 1:8:4 solutions (by mass) of polymer, solvent (acetone), and ionic liquid, respectively. The polymer employed in this work was a copolymer of vinylidene fluoride and hexafluoropropylene, P(VDF-HFP), and the ionic liquid was 1-ethyl-3-methylimidazolium bis(trifluoromethylsulfonyl)imide (EMIM-TFSI). The gel solution was spin-coated onto glass wafers and subsequently dried at ~70 °C for ~24 hours under vacuum. To complete the EDLT devices, as in step (4) above, ion gels were cut into rectangular shapes of ~3 × 5 mm^2 with a razor and laminated

directly onto the device, in open air, using fine tipped tweezers. Immediately after placing the gel, the sample environment was pumped to < 10^{-5} Torr in a PPMS cryostat. Gate voltage (V_g) was applied at 300 K using a Keithley 2400 between the gate pads and one of the four electrodes. *In situ* four-terminal resistance (one VDP channel) measurements were collected by applying an alternating source-drain voltage (V_{SD}) of ±0.1 - 0.2 V between 2 electrodes and measuring a source-drain current (I_{SD}), while an induced voltage was measured between the opposite 2 electrodes.

2.6 *Operando* synchrotron X-ray diffraction

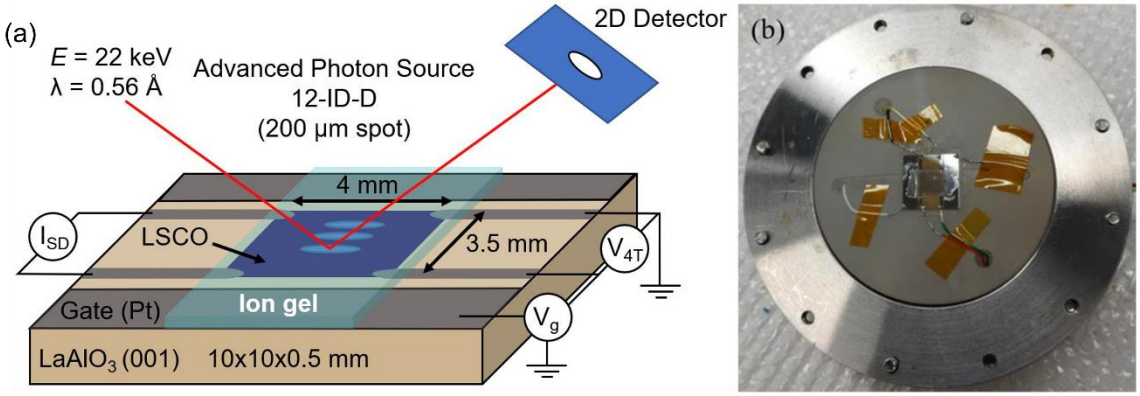

Figure 2.10: (a) Schematic of experimental device setup for *operando* SXRD experiments at the 12-ID-D beamline of the APS at Argonne National Lab, showing the $LaAlO_3$ substrate, LSCO channel, ion gel, Pt gate and film electrode contact pads, incoming / outgoing synchrotron X-ray beam, source-drain current (I_{SD}), measured voltage for four-terminal measurements (V_{4T}), and gate voltage (V_g). (b) Photo of the actual device experimental device, complete with ion gel and wiring on the sample stage immediately before mounting into the beamline instrument goniometer.

Operando SXRD measurements were conducted at the 12-ID-D beamline of the Advanced Photon Source (APS) at Argonne National Laboratory, mirroring procedures developed in prior work [176,183]. These experiments were conceptually similar to the specular WAXRD described in Section 2.2.1, with 2 major differences: First, the measurement took place concurrently, or *in operando*, with ion-gel gating experiments, and second, the probe radiation consisted of synchrotron-supplied hard (*i.e.*, high-energy) X-rays. Synchrotron sources provide beam brilliance (and thus diffracted intensity) many orders of magnitude beyond what is possible in standard metal-anode X-ray tube sources [238]. In addition, the ability to alter the energy and focus the beam has enabled transformational measurement approaches to a wide variety of scientific disciplines [238]. In this work, the primary benefits of synchrotron radiation were the high intensity,

providing robust SNRs even for ultrathin (< 10 u.c.) films, and the high energy (> 20 keV = < 0.6 Å) that allowed the beam to penetrate the macroscopically thick (10's of μm) ion-gel gate dielectric during *operando* experiments. (Note that the latter was also a primary reason for the use of side-gated device geometries). Fig. 2.10(a) shows a schematic representation of the *operando* SXRD gating experiments performed in this thesis, where devices with 4 × 3.5 mm^2 channels were used to provide a larger area. This larger area was crucial as the high intensity of the beam caused damage to the gel / film structure after prolonged beam exposure [176], meaning that, to explore the impact of the gating (*i.e.*, take scans at different V_g) no two scans were taken at the same spot on the channel. This idea is shown in Fig. 2.10(a) as light-blue ovals on the film channel area meant to indicate previously probed areas. Prior to the application of the ion gel, the film channel area was 'mapped' using the diffracted intensity of the film (002) peak as a metric to identify the *x* and *y* coordinates (in the film plane) of prospective spots. SXRD was performed at 150 K, partly to mitigate the aforementioned beam damage effects, but also to freeze the ions in the gel in place for the duration of the scan. Thus, the experimental procedure was as follows: (1) apply V_g, (2) cool to 150 K, (3) perform SXRD scan, (4) warm to ~300 K, (5) apply next V_g, and repeat, for subsequent V_g. Fig. 2.10(b) shows an example of one LSCO EDLT device for *operando* SXRD before the entire pictured assembly was mounted onto the instrument goniometer. The sample atmosphere during the experiments was flowing N_2 from a liquid nitrogen cryocooler system, which was also used to accomplish the sample *T* control. The 12-ID-D beamline experiments utilized a five-circle Huber goniometer and scattered X-rays were collected *via* a Pilatus II 100K 2D pixeled area detector. 1D scans, *i.e.*, 2θ *vs.* intensity, were then generated by integration of carefully selected areas of the 2D detector images. Background subtraction was accomplished using a beamline-developed Matlab program, accounting for instrument and geometrical uncertainties, as well as point-by-point subtraction of 'background' intensity (defined by integration of specified areas of the detector images). The beam energy and lateral footprint sizes were 20 - 22 keV and 200 - 300 μm (perpendicular to the plane of incidence), respectively.

2.7 Neutron diffraction

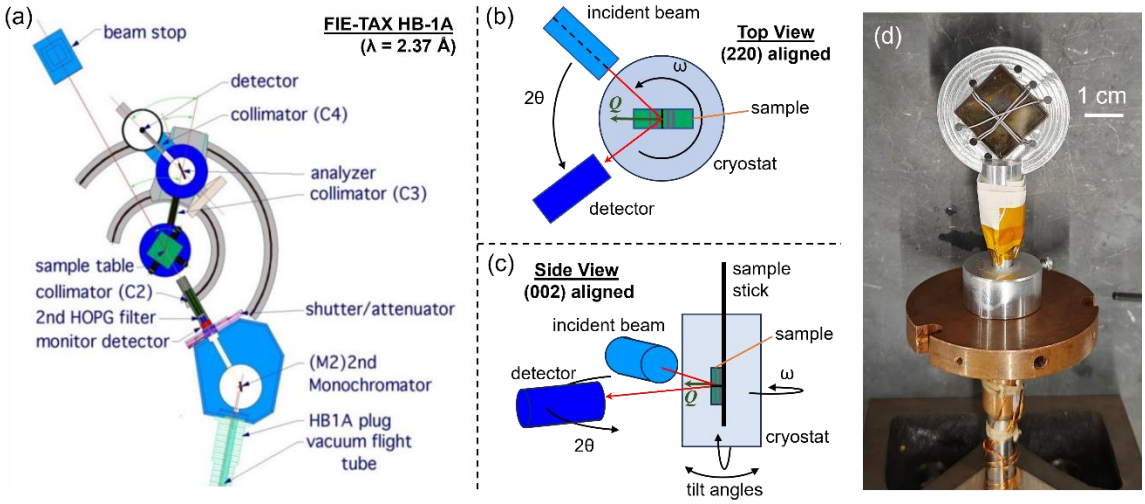

Figure 2.11: (a) Schematic diagram of the FIE-TAX instrument at beamline HB-1A of the High Flux Isotope Reactor (HFIR) at Oak Ridge National Laboratory, showing the triple-axis beam optics and goniometer setup (adapted from Ref. [239]). (b) and (c) show schematics of top-down and side-views of the neutron diffraction experiments depicting the alignments specific to the (220) 'in-plane' (b), and (002) 'out-of-plane' (c), substrate peak. (d) Photo of a stack of six 50-nm-thick BM-SCO films on LSAT(001) 20 × 20 mm^2 substrates wired to Al an plate and mounted at the bottom of the cryostat sample stick.

Diffraction experiments employing neutron beams have several significant advantages over their X-ray-based counterparts. While X-rays scatter primarily from electrons, neutrons scatter primarily from the nuclei. This is because neutrons are neutral particles, which interact strictly *via* extremely short-range nuclear forces [240,241]. This leads to several fundamental differences between X-ray and neutron scattering in experiments. For example, X-rays scatter more strongly from high-Z elements owing to their higher scattering form factors, and thus differentiating elements of similar Z (or detecting elements of low Z) can be difficult. On the other hand, neutron scattering lengths are more varied, allowing better detection of low-Z elements, and higher compositional sensitivity overall. Another consequence of neutrons having no charge is that they are much more penetrating than X-rays, allowing them to probe much larger volumes. Lastly, and importantly, neutrons are particles with intrinsic spin (S = ½) and are therefore sensitive to the magnetic moments of unpaired electrons (magnetically scattered neutrons are thus $\boldsymbol{Q}$-dependent, unlike nuclear-scattered neutrons). The magnetic sensitivity of neutrons makes them ideal for probing the magnetic ordering in crystalline solids, particularly

antiferromagnets, where traditional magnetometry is indirect and can be challenging. In an AF material, the magnetic moments of neighboring magnetic sites are typically aligned antiparallel (see Fig. 1.6), resulting in differing nuclear *vs*. magnetic structures and therefore differences in the diffraction patterns of neutrons *vs*. X-rays.

While neutron diffraction (ND) provides a direct route to characterizing the magnetic ordering of crystals, it is experimentally more challenging to implement compared to XRD. First, the intensity of neutron beams are generally lower than typical X-Ray beams, and neutrons also scatter less strongly, leading to challenges in achieving significant diffracted intensity and SNR, especially for low-mass samples like thin films. Second, continuous neutron sources require nuclear reactors, which are costly to build and maintain. As a result, ND facilities are concentrated around major nuclear reactor sites and National Laboratories, where relatively high-flux neutron beams can be achieved. In this work, ND experiments were carried out at Oak Ridge National Laboratory's (ORNL) High-Flux Isotope Reactor (HFIR). Figure 2.11(a) shows the layout of the fixed-incident-energy triple-axis (FIE-TAX) spectrometer instrument (which was recently renamed to "versatile, intense triple-axis spectrometer" or VERITAS) at the HB-1A beamline, using a wavelength of $\lambda = 2.37$ Å. ND was used to probe the magnetic order in $x = 1$ and $x = 0.5$ BM-LSCO thin films as a function of T. Due to the inherently low intensity in ND experiments, and the low volume of thin film samples, the ND sample films were grown on very large (15×15 mm^2 or 20×20 mm^2) single crystal substrates, and to very high t (200 nm for BM-LSCO). In the case of BM-SCO, where films of high t could not be grown (more details in Chapter 6), a stack of six nominally identical 50-nm-thick films on 20×20 mm^2 LSAT substrates were used instead. Fig. 2.11(b) and (c) show the specific scattering geometry of the ND experiments from the top-down (b) and side-view (c) profiles. The samples were fixed to Al plates by Al wires (Al has very low neutron scattering and absorption cross sections), as shown in Fig. 2.11(d). The Al mount was then fixed to the end of a sample stick and inserted into a He-cooled cryostat in the path of the neutron beam. Low-T ND experiments (3.5 - 300 K) used a low pressure of He exchange gas (~75 Torr). While high-T experiments (300 - 600 K) were performed in vacuum.

Asymmetric scans of the expected magnetic (201) film peak were taken to probe for G-type AF order in the above-mentioned BM film samples. First, alignment to the substrate (002) and (220) (along with corresponding tilts scans) were performed to align the sample in the beam and to generate the orientation matrix of the substrate. This procedure is depicted schematically in Figs. 2.11(b) and (c), with scattering vector $\boldsymbol{Q}$ and relevant substrate atomic planes indicated. Then, using the known relationship between the film and substrate (see Fig. 1.15(a)) and the known c lattice parameter of the film (determined from previous lab HRXRD (Section 2.2.1)), an analogous alignment (using the film (002) and (200) or (202)) was performed to establish an orientation matrix for the *film*. With this in hand, film peaks of arbitrary index within the *h0l* plane (and within the experimental angular limits), could then be probed. Final scans about the film (201) magnetic peak consisted of $\theta/2\theta$ coupled scans, and RCs (ω scans) at various T (3.5 - 450 K) using dwell times of 600 seconds (10 minutes) per point, to achieve sufficient diffracted intensity counting statistics (see Chapter 6 for more experimental details).

Chapter 3: Doping- and strain-dependent electrolyte-gate-induced perovskite to brownmillerite transformation in epitaxial $La_{1-x}Sr_xCoO_{3-\delta}$

This chapter is based on the publication "*Doping- and strain-dependent electrolyte-gate-induced perovskite to brownmillerite transformation in epitaxial $La_{1-x}Sr_xCoO_{3-\delta}$ films*" in ACS Applied Materials and Interfaces Vol. 13, pg. 51205-51217 (2021), by Vipul Chaturvedi, William M. Postiglione, Rohan D. Chakraborty, Biqiong Yu, Wojciech Tabiś, Sajna Hameed, Nikolaos Biniskos, Andrew Jacobson, Zhan Zhang, Hua Zhou, Martin Greven, Vivian E. Ferry, and Chris Leighton. Here, it has been adapted with permission from Ref. [242], copyright (2021) American Chemical Society.

This chapter addresses the first set of goals for this thesis, outlined in Section 1.4, namely, to investigate the generality of the P-BM transformation across the LSCO phase diagram, and to understand its dependencies on composition, x, and epitaxial strain. As discussed in Section 1.3.5, much recent attention has focused on the voltage-driven reversible transformation between ferromagnetic metallic P-SCO and V_O-ordered antiferromagnetic insulating BM-SCO. This is emerging as a paradigmatic example of the power of electrochemical gating (using, *e.g.*, ionic liquids/gels), demonstrating wide modulations of electronic, magnetic, optical, and thermal properties. SCO films are challenging with respect to stability, however, and there has been little exploration of alternate compositions. In this chapter, the first study of ion-gel-gating-induced P → BM transformations, across almost the entire LSCO phase diagram ($0 \leq x \leq 0.70$) is presented, under both tensile and compressive strain. Electronic transport, magnetometry, and *operando* synchrotron X-ray diffraction (SXRD) establish that voltage-induced P → BM transformations are possible at essentially all x, including $x \leq 0.50$, where both P and BM phases are highly stable. Fig. 3.1 highlights the stability of $x = 0.5$ P-LSCO films over long time periods, where a very small increase in resistivity is the only observable change after 9 months of storage. Under small compressive strain, the transformation threshold voltage decreases from approximately +2.7 V at $x = 0$ to near zero at $x = 0.70$. Both larger compressive strain and tensile strain induce further threshold voltage lowering, particularly at low x. The P → BM threshold voltage is thus tunable, *via* both composition and strain.

At x = 0.50, voltage-controlled ferromagnetism, transport, and optical transmittance are then demonstrated, achieving Curie temperature and resistivity modulations of ~220 K and at least 5 orders of magnitude, respectively, and enabling estimation of the voltage-dependent Co valence. The results are analyzed in the context of doping- and strain-dependent oxygen vacancy formation energies and diffusion coefficients, establishing that it is thermodynamic factors, not kinetics, that underpin the decrease in the threshold voltage with x, that is, with increasing formal Co valence. These findings substantially advance the practical and mechanistic understanding of this voltage-driven transformation, with fundamental and technological implications.

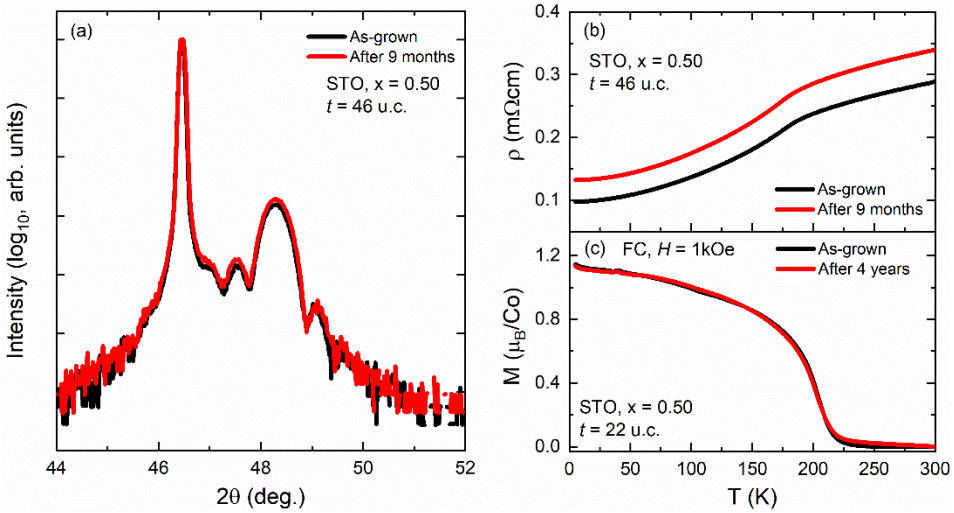

Figure 3.1: Long-term stability of $La_{0.5}Sr_{0.5}CoO_{3-\delta}$ films in the perovskite phase; shown are datasets for x = 0.50 films grown on STO substrates, stored at room temperature under N_2 flow. (a) $\theta/2\theta$ specular HRXRD for a 46-unit-cell-thick film recorded over a period of 9 months, revealing no discernible structural change. (b) Temperature (T) dependence of zero-field resistivity (ρ) for a 46-unit-cell-thick film measured over 9 months, revealing only a small increase in resistivity. (c) T dependence of in-plane magnetization (M) (field-cooled and measured in 1 kOe) for a 22-unit-cell-thick film, revealing near-identical behavior after a period of 4 years. Such data strongly reinforce the stability of the perovskite phase at x = 0.50 relative to x = 1.00, *i.e.*, $SrCoO_{3-\delta}$.

3.1 Methods

The growth and characterization of LSCO films was outlined in Chapter 2, and described extensively in prior work [48,107,108,169,176,179], therefore, it will be described here in brief. Perovskite LSCO films of $0 \leq x \leq 0.7$ were deposited using high-pressure-oxygen sputtering from bulk polycrystalline targets under previously optimized conditions [48,107,108,169,176,179]. Films were deposited on single crystal substrates: $SrLaAlO_4$ (SLAO), $LaAlO_3$ (LAO), and $(LaAlO_3)_{0.3}(SrTaAlO_6)_{0.7}$ (LSAT) (all substrates

used were (001)-oriented). Substrates were annealed at 900 °C in flowing O_2 prior to growth. Deposition conditions ranged from 600 - 700 °C, 60 - 70 W DC power, and ~1.5 Torr O_2. Unless otherwise indicated, all films in this work were ~28 unit cells (u.c.) thick (~11 nm), as determined by WAXRD and GIXR (see Section 2.2.3). Such films have been extensively characterized in other work using various XRD (and SXRD) techniques, AFM, cross-sectional STEM, *etc*. [48,52,105,107,108,169,176,179]. Briefly, such films have been demonstrated to be phase-pure, (001)-oriented perovskite, fully strained to the substrates, and have unit-cell-level roughness [48,52,105,107,108,169,176,179].

Ion gel EDLT devices were fabricated from the above as-deposited films using the procedures outlined in Section 2.5, in accordance with previously established methods [169,173,176,179,183]. Different device geometries were used for different experiments, as follows: 1 × 1 mm^2 devices (on 5 × 5 mm^2 substrates) were used for electronic transport, 2 × 1.8 mm^2 devices (on 5 × 5 mm^2 substrates) were used for magnetometry, and 4 × 3.5 mm^2 devices (on 10 × 10 mm^2 substrates) were used for *operando* SXRD and *ex situ* optical transmittance measurements. Four-terminal DC resistance measurements were performed in a Quantum Design PPMS with a closed-cycle He refrigerator. Keithley 2400 source-measure units were used to measure the channel resistance and to apply V_g during gating experiments. *In situ* resistance measurements were taken at 260 K in vacuum (< 10^{-5} Torr) as a function of time during different (stepped) V_g applications. Each V_g was applied for 30 minutes, followed by 30 minutes of V_g = 0 V. *T*-dependent resistance measurements were taken on warming (1 K min^{-1}) also as a function of (stepped) V_g. *Ex situ* measurements of *M vs*. *T* (from 5 - 300 K, in 100 Oe in-plane field) were taken in a Quantum Design MPMS. *Ex situ* optical transmittance measurements were performed using a Cary 7000 ultraviolet/visible/near-infrared spectrophotometer, where samples were mounted on an opaque holder with a 1-mm-diameter circular opening at the center. Transmittance spectra were collected at normal incidence using an unpolarized light source and were referenced to the transmittance of air. *Operando* SXRD measurements were performed at the 12-ID-D beamline at the APS at Argonne National Lab, using a six-circle Huber goniometer and a Pilatus II 100K area detector. The energy of incident X-rays was 20 keV (~0.62 Å), the beam spot size on the LSCO channel was ~300 μm, and

measurements were made at 150 K, in a liquid-N_2-flow cryocooler after V_g application at 280 K for 30 mins.

3.2 Doping dependence of the electrostatic *vs*. electrochemical response

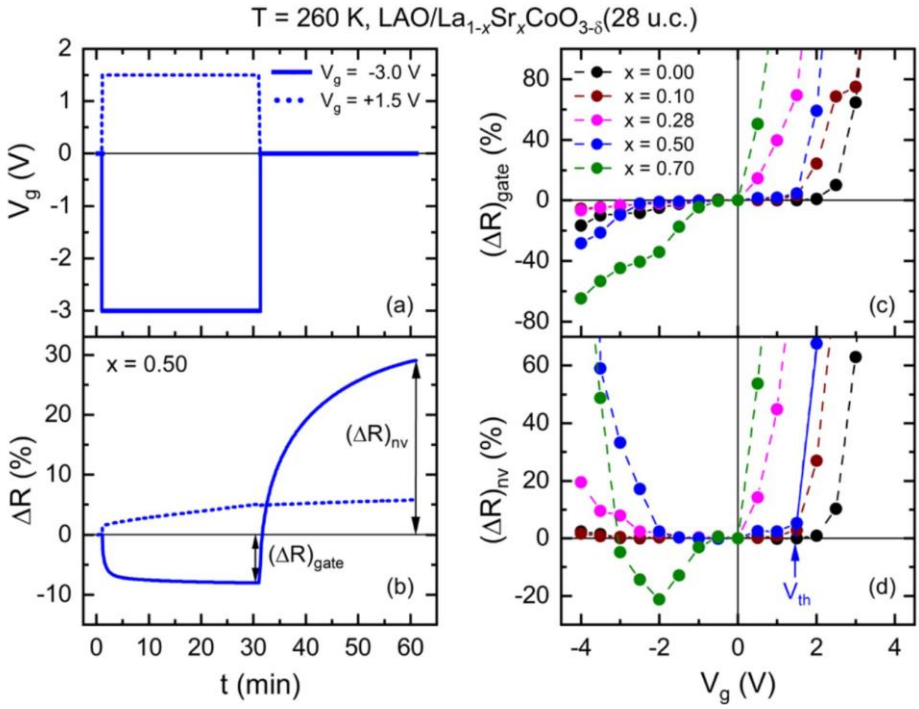

Figure 3.2: Time (t) evolution of (a) the gate voltage (V_g) and (b) the induced resistance change (ΔR) during voltage applications of +1.5 V (dashed lines) and −3.0 V (solid lines) to representative 28-unit-cell-thick x = 0.50 P LSCO films on LAO. V_g dependence of (c) the gate-induced resistance change [ΔR_{gate}, defined in panel (b)] and (d) the nonvolatile resistance change [ΔR_{nv}, also defined in panel (b)] for 28-unit-cell-thick P LSCO films (x = 0, 0.10, 0.28, 0.50, and 0.70) on LAO. All data were taken at 260 K in vacuum (<10^{-5} Torr). As discussed in the text, positive and negative V_g data were collected on two different devices. The threshold voltage (V_{th})is defined *via* linear extrapolation in (d), using x = 0.50 as an example.

Basic transport characterization of ion-gel-gated P LSCO films with x of 0, 0.10, 0.28, 0.50, and 0.70 is shown in Fig. 3.2. We initially focus on films on LAO, that is, small compressive strains (− 1.2 to − 0.6%), studying the x dependence. Fig. 3.2(a),(b) (for x = 0.50) first illustrates the measurement scheme [179,183], where various V_g values are applied for 30 min at 260 K in vacuum (< 10^{-5} Torr) (Fig. 3.2(a)), and then the time (τ) evolution of the gate-induced resistance change (ΔR) is tracked (Figure 3.2(b)). In the example shown in Fig. 3.2(b), V_g = − 3.0 V (solid lines) is seen to induce ΔR that saturates at around −8%, the slow response, being related to the side gate [173,176,179,183]. Applying such negative V_g to pristine P LSCO (x = 0.50) films with low δ results in a

predominantly electrostatic gate effect [169,176,179], that is, an increase in hole doping and mean Co valence ($\bar{V}_{Co}$). At some point, the induced elevated $\bar{V}_{Co}$ leaves the system unstable toward V_O formation, however, increasing δ. After removal of the negative V_g (t > 30 min in Fig. 3.2(a),(b)), substantial positive ΔR is then observed, that is, film resistance larger than at $\tau = 0$ [169,176,179]. In contrast, application of a positive V_g of +1.5 V to a pristine P LSCO ($x = 0.50$) film is seen (Fig. 3.2(a),(b)) to induce a positive ΔR (~6%) that is essentially entirely nonvolatile after V_g removal. This is due to predominantly electrochemical response at positive V_g through V_O formation (increased δ), as proven previously by *operando* SXRD [176], X-ray absorption spectroscopy (XAS) / X-ray magnetic circular dichroism (XMCD) [180], and PNR [176] and reinforced below by SXRD observations of a cell volume increase and eventual P → BM transformation. To track the full V_g dependence of the behavior in Fig. 3.2(b), two parameters are defined: $(\Delta R)_{gate}$, the gate-induced resistance change after 30 min, and $(\Delta R)_{nv}$, the resistance difference between $\tau = 0$ and the end of the cycle (60 min). In essence, $(\Delta R)_{gate}$ quantifies the gate effect, while $(\Delta R)_{nv}$ quantifies the nonvolatile resistance change. Fig. 3.2(c),(d) shows the V_g dependence of these quantities for x = 0, 0.10, 0.28, 0.50, and 0.70 LAO/LSCO films. Importantly, these were collected in a mode where one device was used for progressively larger negative V_g, followed by a second (nominally identical) device for progressively larger positive V_g. The situation on applying negative V_g from a pristine state is relatively straightforward for $x \leq 0.50$. Small, negative $(\Delta R)_{gate}$ occurs, consistent with the electrostatic hole accumulation just described [169,176,179]. Correspondingly, $(\Delta R)_{nv}$ is very small at all negative V_g for x = 0 and 0.10, increasing only modestly at x = 0.28. Again, such a positive $(\Delta R)_{nv}$ at the largest magnitudes of negative V_g arises from the induced increase in $\bar{V}_{Co}$, which leaves LSCO films unstable toward V_O formation after bias removal, thus inducing positive $(\Delta R)_{nv}$. As reported previously, by x = 0.50, this effect is prominent [169,176,179], large positive $(\Delta R)_{nv}$ occurring at $V_g \leq -2.0$ V. Such effects are then dramatically enhanced at $x = 0.70$, the negative $(\Delta R)_{gate}$ becoming larger in magnitude (up to −65% at −4.0 V), accompanied by nonmonotonic $(\Delta R)_{nv}(V_g)$. This is ascribed to an abrupt increase in initial (as deposited) δ in P LSCO films at $x > 0.50$, as discussed below.

The situation on applying positive V_g from a pristine state is relatively simpler. At low x, both $(\Delta R)_{gate}$ (Fig. 3.2(c)) and $(\Delta R)_{nv}$ (Fig. 3.2(d)) are first flat with increasing V_g before undergoing a rapid increase at fairly well-defined thresholds. This indicates a large (extending beyond the scale in Fig. 3.2) and essentially entirely nonvolatile resistance change (compare Fig. 3.2(c),(d)) at some critical voltage, which is confirmed below to be coincident with a P → BM transformation in SXRD. We thus define a threshold voltage, V_{th}, by extrapolation of straight-line fits at high V_g (*e.g.*, the solid line for $x = 0.50$) to $\Delta R = 0$. Fig. 3.2(d) illustrates this for $(\Delta R)_{nv}$, although a similar process for $(\Delta R)_{gate}$ results in similar V_{th}. The composition and strain dependence of this behavior will be discussed in detail below, the most significant observation for now being the striking reduction in V_{th} with x, which, in these low-compressive-strain LAO/LSCO films, falls from ~2.5 V at $x = 0$ to ~0 V at $x = 0.70$. V_{th} is thus *tunable*, the P → BM transformation at $x = 0.70$ becoming almost spontaneous.

3.3 The P → BM transformation from SXRD and its doping dependence

The remainder of this Chapter focuses on positive V_g, seeking detailed understanding of the composition and strain dependence of the V_g-induced P → BM transformation and its impact on transport and magnetism. Fig. 3.3 shows *operando* SXRD characterization of this transformation, starting with a schematic in Fig. 3.3(a). Fig. 3.3(b) then shows a representative [LAO/LSCO ($x = 0.50$, 28 u.c.)] V_g dependence of specular SXRD data, that is, intensity *vs.* L scans. Prior to ion gel application ("no gel" in Fig. 3.3(b)), such wide-range specular SXRD reveals high-intensity (002), (003), and (004) P peaks, accompanied by extensive Laue oscillations. After applying the ion gel, but before applying V_g ("0.0 V" in Fig. 3.3(b)), changes in the SXRD are already detectable. First, the background intensity increases, presumably due to diffuse scattering from the ion gel. More significantly, the P peaks decrease in intensity and downshift in L, indicating a slight increase in c-axis lattice parameter. Increasing V_g to +1.0, +2.0, +3.0, and +4.0 V then induces dramatic changes, the (002), (003), and (004) P peaks being strongly suppressed,

concomitant with the appearance of (006), (008), ..., (00<u>16</u>) BM peaks. Such data conclusively demonstrate a P → BM transition, which we now analyze in detail.

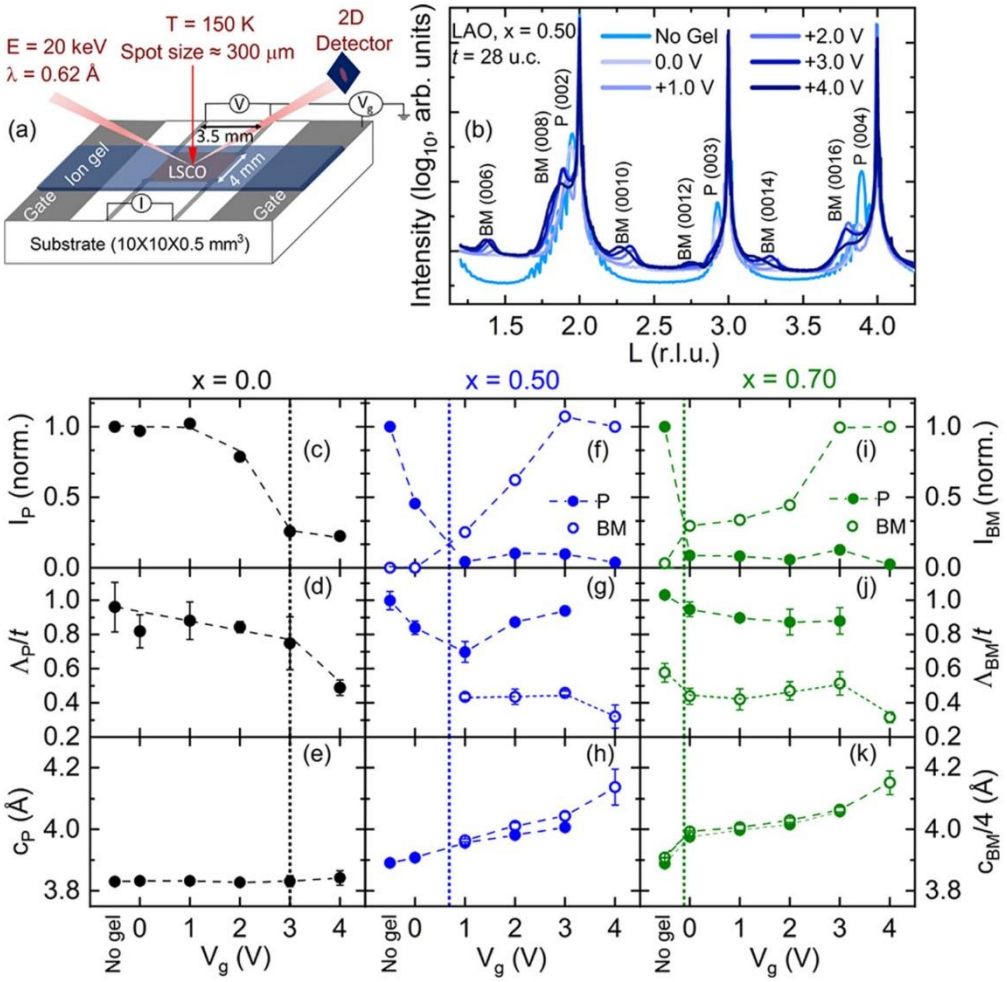

Figure 3.3: (a) Device schematic for *operando* SXRD on ion-gel-gated LSCO films. I, V, and V_g are the measurement current, measurement voltage, and gate voltage, respectively. (b) Representative wide-range specular *operando* SXRD scan of a 28-unit-cell-thick x = 0.50 LSCO film on LAO(001), ion-gel-gated at V_g = 0.0, +1.0, +2.0, +3.0, and +4.0 V. L is shown in substrate r.l.u. Perovskite (P) and BM reflections are labeled. (c)-(k) V_g dependence of the SXRD intensities of the P (002) and BM (006) peaks (I_P and I_{BM}, left and right axes, respectively, normalized to their maxima), average Scherrer lengths normalized to the as-deposited film thickness for the P and BM phases (Λ_P/t and Λ_{BM}/t, left and right axes, respectively), and c-axis lattice parameters for the P and BM phases (c_P and $c_{BM}/4$, left and right axes, respectively). Data are shown for representative ion-gel-gated LAO/LSCO films with x = 0 (c)-(e), 0.50 (f)-(h), and 0.70 (i)-(k). Solid and open points are used for P and BM, respectively, and the "−0.5 V" points correspond to "no gel". The SXRD threshold voltage for the P to BM transformation (V_{th}) is marked by the vertical dotted lines. As discussed in the text, this is defined as the crossing point of I_P and I_{BM}; in(c)-(e), where no BM is directly detected, the dotted line is placed where I_P falls below 0.25.

Shown in Fig. 3.3(c)-(k) are parameters extracted from SXRD of the type shown in Fig. 3.3(b), on films with x = 0 (left panels), 0.50 (middle panels), and 0.70 (right panels).

The plotted quantities are the peak intensities (normalized to their maxima) of the P (002) and BM (006) peaks (I_P and I_{BM}, top panels, left and right axes, respectively), the average Scherrer lengths (Λ) extracted from P and BM peaks (normalized to the film thickness, t), and the c-axis lattice parameters of the P and BM phases (c_P and $c_{BM}/4$, on the left and right axes, respectively). As already noted, we focus on $V_g > 0$ only, the points at "−0.5 V" signifying the "no gel" case. Starting with the middle panels, that is, (f)-(h), the $x = 0.50$ composition shown in Fig. 3.3(b),(f) indicates undetectable BM intensity in the "no gel" and "0 V" cases. I_P and Λ_P/t (Fig. 3.3(f),(g)) nevertheless decrease upon gel application (from the $\Lambda_P/t = 1.0$ expected in a pseudomorphic epitaxial film), while c_P displays a corresponding small increase (Fig. 3.3(h)). The situation then changes dramatically at +1.0 V, where I_P is strongly suppressed and I_{BM} turns on. Further increasing V_g leads to steady growth of I_{BM}, gradual increases in c_P and c_{BM}, and eventual flattening of I_{BM} at $V_g > +3.0$ V, where I_P becomes near-zero. Notably, Λ_{BM}/t is much smaller than Λ_P/t (this is clearly visible in the peak widths in Fig. 3.3(b)), and the Laue oscillations in the P phase are absent in the BM phase.

Based on Fig. 3.3(b),(f)-(h), we deduce a detailed picture of the V_g-induced P → BM transformation for $x = 0.50$. First, application of the ion gel apparently already results in slight reduction, as evidenced by the c_P increase between "−0.5" (no gel) and 0.0 V in Fig. 3.3(h). This is the chemical expansion effect due to V_O formation in P LSCO [176], the fact that this occurs at $V_g = 0$ being consistent with prior work [179]; in ionic liquid/gel gating, typically either the ionic liquid cation or anion has an affinity for the surface of the gated material, leading to a gate effect even at $V_g = 0$ [179,183]. As evidenced by the accompanying decrease in both I_P and Λ_P/t (Fig. 3.3(g),(h)), this reduction of the P phase apparently deteriorates crystalline coherence. There is no detectable BM at $V_g = 0$ after gel application, however, indicating only an increase in δ in the P phase.

At $V_g \geq +1.0$ V, the situation is very different. The first thing to note is the distinctly gradual evolution in lattice parameters with V_g (Fig. 3.3(h)), related to the continuous progression from the P (002) peak at $V_g = 0$ to the BM (008) peak at $V_g = +4.0$ V (Fig. 3.3(b)). This indicates a gradual, not discontinuous, increase in δ with V_g. Interestingly, the literature on voltage-triggered BM ↔ P transitions in related $SrCoO_{3-\delta}$ suggests no

consensus on this point, the nature of the transition being variable and often different for BM → P than P → BM [97,112,117,120,124,129–131]. By +1.0 V, I_P is dramatically suppressed (Fig. 3.3(f)) and I_{BM} becomes nonzero (consider Fig. 3.3(f) and the (006) BM peak in Fig. 3.3(b)), indicating that not only has δ increased, but ordering of V_O into the BM motif has occurred. At this point, both P and BM phases are detectable, which remains true up to +3.0 V (Fig. 3.3(f)). It is only at V_g > +3.0 V that I_{BM} saturates and I_P vanishes, indicating phase-pure BM. It is also only at +3.0 V that the ratio of BM (008) to (006) intensities becomes comparable to the literature for phase-pure BM [97,112,117,120,124,129–131]; below this V_g, the BM (008) to (006) ratio is far above expectations, indicating that the intensity in the BM (008) / P (002) region derives from downshifted P (002) intensity due to increasing δ. Together, Fig. 3.3(b),(f)-(h) thus reveals an evolution from phase-pure P at V_g < +1.0 V (with increasing δ but disordered V_O) to a regime of P-BM phase coexistence (both V_O-disordered and V_O-ordered regions) to phase-pure BM at V_g > +3.0 V (entirely V_O-ordered). While this is not commented on in the gated SCO literature, our observations, particularly the distinct phase coexistence regime, are consistent with a 1st-order transformation [243]. In our side-gate geometry (Fig. 3.3(a)), the P-BM phase boundary would then be expected to migrate laterally across the gated LSCO film [131] in the +1.0 V ≤ V_g ≤ +3.0 V window. To facilitate simple and approximate comparison to V_{th} from transport, we nevertheless simply define a single SXRD P → BM threshold voltage as the linearly interpolated point at which I_P and I_{BM} cross, for example, 0.7 V for x = 0.50 in Fig. 3.3(f), as marked by the vertical dotted line.

As final comments on the P → BM transformation in these LAO/LSCO (x = 0.50) films, we first note that the distinctly lower Λ_{BM}/t than Λ_P/t indicates lesser through-plane structural coherence, likely indicating multiple BM domains through the film thickness, potentially with additional microstrain contributions, that is, a distribution in local lattice parameters. Related to this, the BM reflections in Fig. 3.3(b) have no Laue fringes, indicating substantial disorder associated with these BM domains. Future work to understand how this structural disorder in the BM influences the microstructure after gating back to the P phase at negative V_g would clearly be worthwhile, with important potential implications for reversibility and endurance. Second, we note that our data at x = 0.50

exclusively evidence BM-like V_O-ordered phases at high V_g, with the quadrupled lattice parameter with respect to the P phase; we find no evidence, for example, of Grenier phases with alternative V_O modulations at this x. Third, in SCO, ordered H-intercalated phases have been detected in addition to P and BM, *via* a second transformation with further expansion of the lattice parameter. Our data on LSCO (*e.g.*, Fig. 3.3(b),(e),(h),(k)) provide no obvious indications of such phases, however. As discussed below, we also do not observe any of the magnetic or optical characteristics of these ordered H-intercalated phases (*i.e.*, weak F behavior and very wide gaps). These observations could indicate suppression of such protonation effects with La incorporation in SCO or simply disordered H incorporation. Future work with techniques such as secondary ion mass spectrometry and neutron reflectivity could shed light on this.

Turning to x other than 0.50, as shown in Fig. 3.3(i)-(k), the main difference in behavior for $x = 0.70$ is that, consistent with transport (Fig. 3.2(c),(d)), BM phase formation is essentially spontaneous at $V_g = 0$ after gel application (Fig. 3.3(i)). With further increase in V_g, the situation is then similar to $x = 0.50$: I_{BM} gradually increases and saturates, I_P eventually becomes undetectable (Fig. 3.3(i)), Λ_{BM}/t is substantially reduced relative to Λ_P/t (Fig. 3.3(j)), and c_P and c_{BM} gradually increase (Fig. 3.3(k)). Also consistent with Fig. 3.2(c),(d), the situation at $x = 0$ is very different. Fig. 3.3(c)-(e) in fact reveals only P peaks, with no detectable BM at any V_g. Nevertheless, a clear change occurs around +3.0 V, where I_P dramatically drops (Fig. 3.3(c)), Λ_P/t falls (Fig. 3.3(d)), and a small increase in c_P is detected (Fig. 3.3(e)). We hypothesize that while the long-range V_O order required for BM reflections is not yet present here, it is possible that short-range V_O order occurs, as is well known even in as-deposited LSCO films at higher x [52,53,105,107,108]. This phenomenon could also occur as a precursor to the onset of BM reflections at higher x, perhaps associated with the decrease in I_P prior to BM detection in Fig. 3.3(f), for example. Moreover, we find evidence of a broad hump in intensity to the left of the P (002), (003), and (004) peaks after gating to the highest voltages. This could potentially indicate some formation of a Grenier phase at $x = 0$ (*i.e.*, a different V_O order modulation period to BM with different δ), which would be worthy of further investigation in future work.

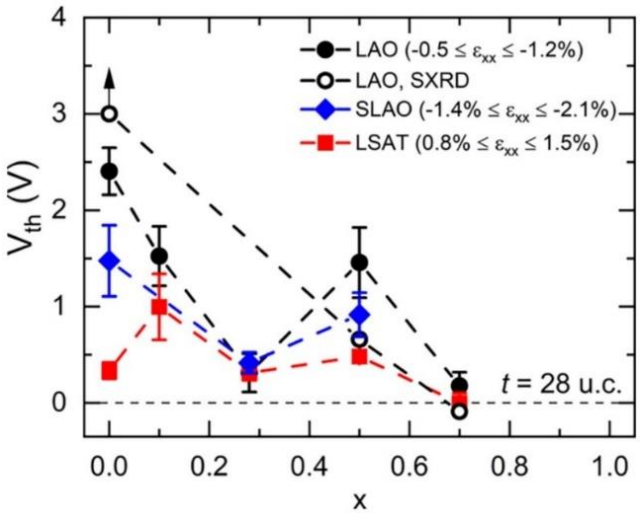

Figure 3.4: Threshold voltage for the perovskite (P) to BM transformation (V_{th}) *vs*. *x* for ion-gel-gated 28-unit-cell-thick LSCO films. V_{th} is shown from both transport (solid points, averaged from both Fig. 3.2(c),(d) and *operando* SXRD (open points). Data are shown for films on LAO, SLAO, and LSAT substrates, labeled with the "in-plane" ε_{xx} range (due to the varied *x*). Error bars on the points from transport correspond to the fitting errors on the extrapolations to determine V_{th}, as illustrated by the solid line in Fig. 3.2(d). Error bars on the points from SXRD (which are smaller than the points themselves) correspond to analogous fitting errors on the interpolations used to determine the crossover points for the P and BM intensities (see, *e.g.*, Fig. 3.4(f)).

The central issue of the *x*-dependence of the threshold voltage for the P → BM transformation is highlighted in Fig. 3.4, which plots V_{th} from both transport (*e.g.*, Fig. 3.2(c),(d)) and SXRD (*e.g.*, Fig. 3.3(c) –(k)). The black circles in Fig. 3.4 are for LAO/LSCO; the solid circles correspond to transport [an average from $(\Delta R)_{gate}(V_g)$(Fig. 3.2(c)) and $(\Delta R)_{nv}(V_g)$(Fig. 3.2(d))], and the open circles correspond to SXRD (dotted vertical lines in Fig. 3.3(c)-(k)). Consistent with inspection of Figs. 3.2(c),(d) and 3.3(c)-(k), an overall reduction in V_{th} with *x* is revealed in Fig. 3.4 for LAO/LSCO, transport and SXRD being reasonably consistent, given the error bars. V_{th} drops from at least 2.4 to 3.0 V at $x = 0$ (where the upward arrow indicates that long-range BM order was not detected in SXRD) to negligible at $x = 0.70$. Below, we discuss specific conclusions regarding the origin of the overall decrease in V_{th} with *x* and its apparent nonmonotonicity in Fig. 3.3; for now, we note only that V_{th} is clearly doping-tunable, a feature that may be attractive for applications such as neuromorphic computing [149,150,152,189,193,194,244].

3.4 Strain dependence of the P → BM transformation

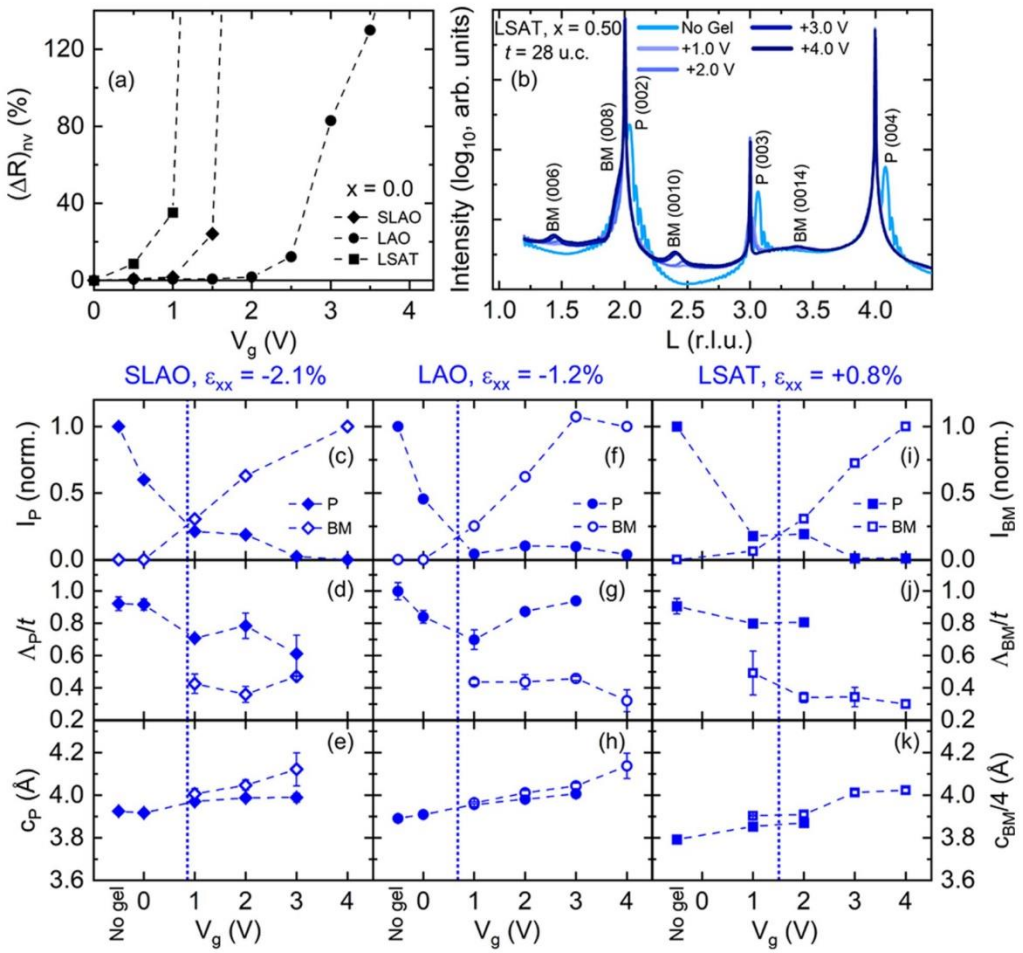

Figure 3.5: (a) Positive V_g dependence of ΔR_{nv} in ion-gel-gated 28-unit-cell-thick $LaCoO_{3-\delta}$ films (x = 0) on SLAO, LAO, and LSAT substrates. Conditions are the same as for Fig. 3.2(d). (b) Representative wide-range specular *operando* SXRD scans of a 28-unit-cell-thick x = 0.50 LSCO film on LSAT(001), ion-gel-gated at V_g = 0.0, +1.0, +2.0, +3.0, and +4.0 V. L is shown in substrate r.l.u. Perovskite (P) and brownmillerite (BM) reflections are labeled. (c)-(k) V_g dependence of the SXRD intensities of the P (002) and BM (006) peaks (I_P and I_{BM}, left and right axes, respectively, normalized to their maxima), average Scherrer lengths normalized to the as-deposited film thickness for the P and BM phases (Λ_P/t and Λ_{BM}/t, left and right axes, respectively), and c-axis lattice parameters for the P and BM phases (c_P and $c_{BM}/4$, left and right axes, respectively). Data are shown for the representative ion-gel-gated x = 0.50 LSCO films on SLAO (c)-(e), LAO (f)-(h), and LSAT (i)-(k). Solid and open points are used for P and BM, respectively, and the "−0.5 V" points correspond to "no gel". The SXRD threshold voltage for the P to BM transformation (V_{th}) is marked by the vertical dotted lines; as discussed in the text, this is defined as the crossing point of I_P and I_{BM}. For the three substrates, the associated in-plane strains, ε_{xx}, are shown.

Also shown in Fig. 3.4 are data for LSCO films on SLAO (blue diamonds) and LSAT (red squares), as opposed to the LAO substrates emphasized thus far. As noted in the figure, ε_{xx} on SLAO is −2.1 to −1.4% (*i.e.*, stronger compression than LAO), whereas

ε_{xx} on LSAT is +0.8 to +1.5% (*i.e.*, tensile strain), exposing another important conclusion. Specifically, both higher compressive strain (on SLAO) and tensile strain (on LSAT) result in lower V_{th}, particularly at low x, that is, where V_{th} in LAO/LSCO is large. The transport and SXRD data underpinning this are summarized in Fig. 3.5. Shown first in Fig. 3.5(a) are $(\Delta R)_{nv}$ *vs.* V_g data at $x = 0$, on SLAO ($\varepsilon_{xx} = -2.1\%$), LAO ($\varepsilon_{xx} = -1.2\%$), and LSAT ($\varepsilon_{xx} = +0.8\%$). The trend with heteroepitaxial strain is clear, V_{th} being maximum at +2.4 V under small compressive strain (LAO), falling to +1.5 V under higher compressive strain (SLAO), and decreasing to only +0.3 V under tensile strain (LSAT). Larger ε_{xx} magnitudes thus decrease V_{th} at low x, tensile strain having the strongest influence. Representative wide-range specular *operando* SXRD as a function of V_g is shown in Fig. 3.5(b), this time using LSAT/LSCO ($x = 0.50$) as an example. The (002) P peak (now to the right of the substrate peak) is strongly suppressed with increasing V_g, while 00L BM peaks emerge, again signaling a P → BM transformation. The systematics are analyzed in Fig. 3.5(c)-(k) for $x = 0.50$ films on SLAO (left panels), LAO (middle panels), and LSAT (right panels), where the plotted quantities are identical to Fig. 3.3. By now familiar behavior occurs in all three cases, particularly the decrease in I_P with V_g, the onset of I_{BM}, the smaller Λ_{BM}/t than Λ_P/t, and the gradual increase in c_P and c_{BM} with V_g. We thus again conclude an evolution from phase-pure epitaxial P to P-BM coexistence, to phase-pure BM. As in Fig. 3.3, the vertical dotted lines indicate the linearly interpolated point where I_P and I_{BM} cross. This is approximately strain-independent at $x = 0.50$ (Fig. 3.5(c)-(k)), although it can be seen from Fig. 3.4 that V_{th} drops significantly with strain as $x \rightarrow 0$, particularly under tension. Specific conclusions regarding the origin of this decrease in V_{th} with increasing strain magnitudes will be presented later; for now, we note only that V_{th} is clearly strain-tunable, in addition to being composition-tunable, adding further flexibility for applications. As a final comment on Fig. 3.5, note that on all substrates, the V_g-induced BM phase is (001)-oriented, meaning that the alternating planes of the V_O order are parallel to the substrate/film interface. This is consistent with the BM phase being under compressive strain with respect to all three substrates [52,53].

3.5 Control of magnetism, electronic transport, and optical properties

Switching from characterization of the V_g-induced P → BM transformation to understanding the extent to which it can control magnetic, transport, and optical properties, Fig. 3.6(a),(b) shows *ex situ T*-dependent measurements of magnetization (*M*, in a 100 Oe in-plane field) and resistivity (ρ) after gating to various V_g. These are shown for the representative case of LSAT/LSCO [x = 0.50, 35 u.c. (~13.5 nm)]. Such films are initially F and metallic, with in-plane magnetization, $T_C \approx 220$ K (Fig. 3.6(a)), positive $d\rho/dT$ at all T, and ~100 μΩ cm residual resistivity (Fig. 3.6(b)) agreeing with prior reports on moderately tensile-strained x = 0.50 P LSCO films of comparable t [107,108]. As expected based on Figs. 3.3 and 3.5, application of ion gels while maintaining $V_g = 0$ already has some impact, ρ increasing slightly in response to increased δ. Increasing V_g to +1.0 and then +1.2 V induces more significant changes, T_C dropping by ~14 K (Fig. 3.6(a)), M falling noticeably (Fig. 3.6(a)), and the apparent ρ increasing over 10-fold to a state with negative $d\rho/dT$ at all T (Fig. 3.6(b)). It should be noted here that while the nominal $\rho(T)$ is plotted in Fig. 3.6(b), absolute values and the exact form of $\rho(T)$ at intermediate V_g should be treated with caution due to the expectation of both depth-wise and lateral inhomogeneity. Depth-wise variations in δ and the extent of V_O order are of course expected in such gated devices, lateral inhomogeneity likely being accentuated here by P-BM phase coexistence, and the side-gate geometry (Fig. 3.3(a)). Above +1.2 V, more dramatic effects emerge, V_g of +1.4 V through +2.0 V completely suppressing the F magnetization and T_C. This occurs *via* a reduction in T_C to ~170 K, followed rapidly at higher V_g by vanishing of F magnetization. We believe that this is consistent with the bulk LSCO phase diagram, where the magnetic ordering temperature rapidly decreases on lowering the doping below x = 0.18, as long-range F order breaks into a magnetically phase-separated cluster glass [58,59,66]. This transition is driven here *via* decreasing effective doping, $x_{eff} = x - 2\delta(V_g)$, that is, by each induced V_O compensating two doped holes (in the simplest model [105,169]), along with the simultaneous ordering of V_O that drives the topotactic transformation to non-F BM. Commensurate with the observed changes in $M(T)$, ρ at V_g = +2.0 V increases to as much as ~0.1 Ω cm, that is, 100 times larger than the initial state. Beyond this, +3.5 V then results in ρ(300 K) ≈ 1 Ω cm, increasing rapidly to ~10 Ω cm at 250 K, below which DC transport measurements become prohibitively difficult.

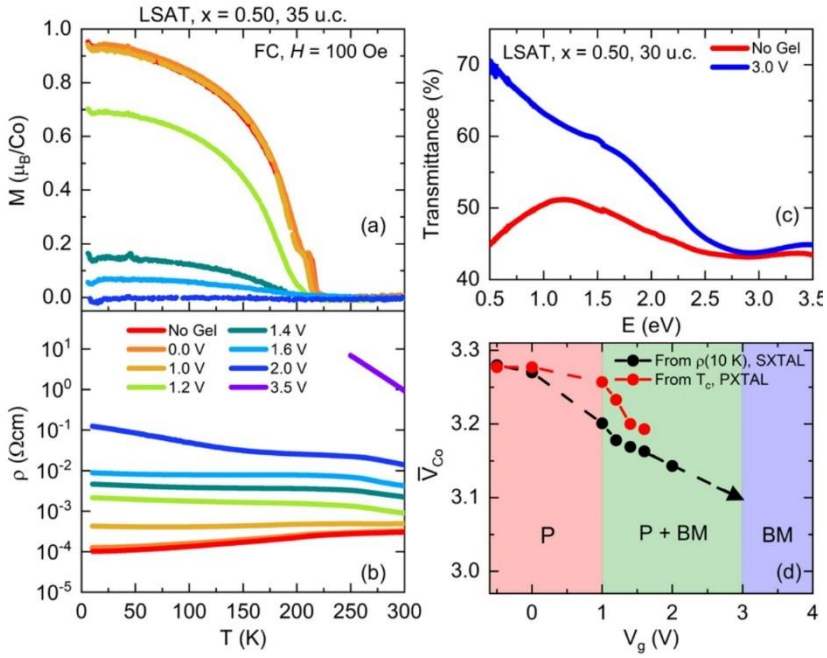

Figure 3.6: Temperature (T) dependence of (a) the in-plane magnetization (M) measured in 100 Oe after field cooling (FC) in 10 kOe and (b) the zero-field resistivity (ρ) of a 35-unit-cell-thick x = 0.50 LSCO film on LSAT ion-gel-gated to V_g = 0.0, +1.0, +1.2, +1.4, +1.6, +2.0, and +3.5 V. (c) Energy-dependent optical (UV/vis/NIR) transmittance spectra for 30-unitcell-thick x = 0.50 LSCO films on LSAT prior to ion gel application (red) and after V_g = +3.0 V (blue). (d) V_g dependence of the average Co valence ($\bar{V}_{Co}$) estimated by comparison to both bulk single-crystal 10 K resistivities [ρ(10 K)] and bulk polycrystalline Curie temperatures (T_C), as discussed in the text. The colored shading indicates the phase-pure P, phase coexistence, and phase-pure BM regions, as deduced from SXRD (Fig. 3.4(i)-(k)). As in Figs. 3.2 and 3.4, "V_g = −0.5 V" corresponds to the "no gel applied" case.

In totality, ρ in this illustrative LSAT/LSCO (x = 0.50, 35 u.c.) case can thus be tuned over at least 5 orders of magnitude (much more at low T) *via* the ion-gel-gating-induced P → BM transformation, the accompanying T_C modulation being ~220 K, that is, from ~220 to 0 K. Importantly, these findings map well to the corresponding V_g-dependent LSAT/LSCO (x = 0.50) SXRD data (Fig. 3.5(i)-(k)). Specifically, the clear P-BM phase coexistence between +1.0 and +3.0 V (Fig. 3.5(i)), the crossing of P and BM intensities at ~1.5 V (where M becomes rapidly suppressed in Fig. 3.6(a)), and the onset of phase-pure BM at ≥ +3.0 V [where ρ(T) becomes strongly insulating in Fig. 3.6(b)] all point to consistency between SXRD and transport/magnetometry. An interesting goal for future work will be to probe any magnetic order in the V_g-induced LSCO BM state, which, while clearly non-F, is not entirely clarified by the current measurements. An x-dependent study of this issue in LSCO would clearly be worthwhile, perhaps *via* neutron diffraction. Even

the heavily studied x = 1 (SCO) composition would benefit from such effort, as the suspected AF order in thin-film BM has not been rigorously verified. This issue will be returned to and addressed in Chapter 6.

As shown in Fig. 3.6(c), the V_g-driven P → BM transition in LSAT/LSCO [x = 0.50, 30 u.c. (~11.5 nm)] films also has a dramatic impact on optical (ultraviolet/visible/near-infrared) transmittance. The initial P state exhibits relatively weakly energy dependent transmittance, but with a noticeable decrease at energies less than ~1.2 eV, consistent with the free carrier absorption expected of a metal. After gating at V_g = +3.0 V, the latter effect is eradicated. The transmittance in fact increases substantially relative to ungated LSCO, specifically below photon energies of ~3 eV; by 0.5 eV, the two transmittances differ by as much as 70% *vs*. 45%. Such observations are in good qualitative agreement with optical studies of the P → BM transformation in SCO, which report similar features in optical transmittance spectra [97] and a prominent decrease in the absorption coefficient of the BM phase below a direct band gap of 2 - 3 eV [97,110,245]. The transmittance spectra in Fig. 3.6(c) thus provide yet further evidence, *via* optical spectroscopy, that our gate-induced BM LSCO has the anticipated electronic structure, specifically an insulating, gapped nature.

With regard to quantification, while not yet carried out to our knowledge in the literature on the V_g-driven BM ↔ P transformation in SCO, magnetic and transport data of the type in Fig. 3.6(a),(b) also enable estimates of the V_g-dependent δ, and thus $\bar{V}_{Co}$. To do this, we assume that the electronic and magnetic behavior of these relatively thick gated films is controlled by $x_{eff} \approx x - 2\delta(V_g)$, the well-documented x-dependent bulk properties establishing baseline behavior for relatively negligible δ. We use two well-established bulk relations for this purpose: the low-T (10 K) single-crystal ρ *vs*. x [169] and the polycrystalline T_C *vs*. x [59,179], resulting in the black and red points in Fig. 3.6(d). Explicitly, plotted here is the mean Co valence, $\bar{V}_{Co}(V_g) \approx 3 + x_{eff}(V_g)$, where $x_{eff}(V_g)$ is estimated by comparing ρ(10 K) and T_C at each V_g to the established bulk (relatively V_O-free) ρ(x) and $T_C(x)$. This procedure was previously validated even in ultrathin gated LSCO films [169,179]. The two methods are seen to be in reasonable agreement in Fig. 3.6(d) (at least to V_g = +1.6 V, where the F state is suppressed and T_C can no longer be used), the

significant finding being the approximately linear decrease in $\bar{V}_{Co}$ with V_g. Shaded on Fig. 3.6(d) are the approximate pure-P, P + BM, and pure-BM regimes from SXRD (Fig. 3.5(i)). While our $\bar{V}_{Co}$ estimates apply strictly only to the P phase, transport will be dominated by the P phase even in the P-BM coexistence region, justifying plotting such data beyond the phase-pure P region.

Notably, the "no gel" and $V_g = 0$ points in Fig. 3.6(d) are at $\bar{V}_{Co} \approx 3.28$, not the nominal 3.50 for an $x = 0.50$ LSCO film. This is unsurprising, particularly for films under tension on LSAT, indicating non-negligible δ, as deposited. To explore the x dependence of this, which could play a role in our finding of decreasing V_{th} with x (Fig. 3.4), the method of comparison to the low-T bulk single-crystal ρ(x) [169] was applied to pristine P films with x = 0, 0.10, 0.28, 0.50, and 0.70, resulting in the estimated δ(x) and $\bar{V}_{Co}(x)$ in Fig. 3.7(a),(b). Under both tensile and compressive strain (LSAT and LAO), the as grown δ is negligibly small at $x = 0$, as expected (this corresponds to relatively stable Co^{3+}), increasing only weakly to $x = 0.28$. Further increasing x then leads to not only rapidly increasing δ (reaching ~0.25 at $x = 0.70$) but also distinct strain dependence, δ becoming larger under tension than compression. The effect on $\bar{V}_{Co}(x) \approx 3 + x - 2\delta(x)$ (Fig. 3.7(b)) is dramatic, increases in Sr doping above $x = 0.50$ being outweighed by the increase in δ, leading to lower x_{eff} and $\bar{V}_{Co}$. This is similar to the behavior in bulk LSCO reported by Jonker and Van Santen [66] and reinforced in Refs. [58] and [59]. This is typically ascribed to decreasing ΔH_{Vo} as $x \rightarrow 1$, due to the instability of formal Co^{4+} valence in octahedral coordination, as in perovskites such as SCO. This is consistent with the aforementioned challenges with stability of $SrCoO_3$ films [97,117] and the fact that synthesis of bulk $SrCoO_3$ requires high O_2 pressure [78]. Clearly, this growing instability to V_O formation with increasing x and the increased initial δ at high x and under tensile strain are important as we consider the origin of the V_{th} trends uncovered in this work.

3.6 Interpretation of x and strain dependence of the P → BM transformation

The decreasing V_{th} for the P → BM transformation with increasing x and strain magnitude (particularly under tension) are central results of this work, which we now attempt to understand. Clearly, the V_g-driven P → BM transformation in LSCO requires

initial formation of V_O in the P LSCO near the LSCO/ion gel interface [176,193,194,246], subsequent proliferation of these V_O through the film thickness [176,193,194], and ordering of these V_O into the BM motif [53,193,194,247]. The initial δ in the P phase, ΔH_{Vo}, D_{Vo}, and the energetics/kinetics of the V_O disorder/order transition are thus all potentially important factors, which we now consider. As discussed in the prior section, the initial δ in the as-deposited P LSCO films clearly increases with x and strain (particularly tensile) (Fig. 3.7(a)), meaning that the V_g-driven P → BM transformation is being induced from a state with δ closer to the nominal 0.5 in BM. As already noted, we ascribe this x dependence to decreasing ΔH_{Vo} with x. As shown in Fig. 3.7(c), both experimental reports of ΔH_{Vo} [68] and density functional theory (DFT) calculations of the formation energy (E_{Vo}) [95,248–250] support substantial decreases with x in LSCO. Scatter between various studies exists, but the enthalpies/energies tend to decrease by a substantial ~2 eV from $LaCoO_{3-\delta}$ to $SrCoO_{3-\delta}$. DFT studies as a function of heteroepitaxial strain are similarly revealing, suggesting decreased E_{Vo} with increasing strain magnitude (both compressive and tensile) [251], at least at $x = 0.50$. We thus conclude that these established trends impact our observed $V_{th}(x, \varepsilon_{xx})$ in at least two ways: by leading to increased initial δ at higher x and $|\varepsilon_{xx}|$ in P films grown (and cooled) under fixed conditions and by enabling more facile V_g-induced formation of V_O at the LSCO/ion gel interface at higher x and $|\varepsilon_{xx}|$. As pointed out by Zhang *et al*. [193,194], these two points are connected, nonzero initial δ being capable of lowering the P → BM transformation barrier.

As gating proceeds, proliferation of V_O through the film is required, rendering D_{Vo} important. Experimental data on this in P LSCO (from electrochemical chronoamperometry [69,75,252,253]) are shown in Fig. 3.7(d). As noted previously [176] and as is likely at the root of the extensive recent literature focus on electrochemical gating of cobaltites [97,112,117,120,124,129–131,142,143,169,176,179], D_{Vo} in LSCO is exceptionally high [254], to the degree that even at 300 K, the V_O diffusion length, $l_d = (D_{Vo}\tau)^{1/2}$, on the 30 min time scales here, is substantial. As illustrated by the blue points and the dashed vertical line in Fig. 3.7(d), the data of Mefford *et al*. [69], for example, suggest several-hundred-nm V_O diffusion lengths under our gating conditions, significantly larger than the film thickness (28 u.c.), even at $x = 0$ ($LaCoO_3$). This indicates that at these

V_g application rates, the reduction of P LSCO is not diffusion-limited, meaning that thermodynamic factors, not kinetics, control the *x*- and strain-dependent V_{th}. We offer two additional thoughts on this. First, this situation could clearly change for higher frequency gating in top-gated devices, and second, it is not yet understood what role V_g plays in assisting V_O diffusion; both of these issues are ripe for further study.

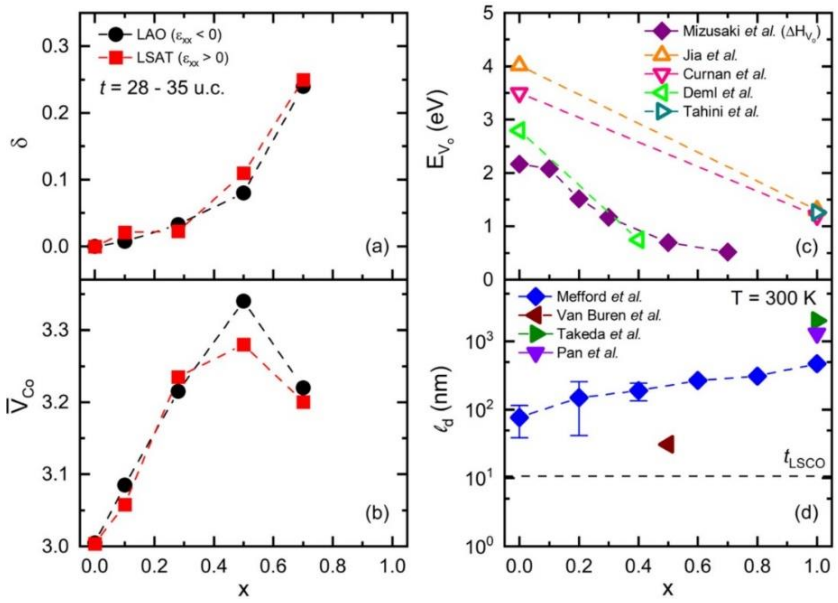

Figure 3.7: Sr doping (*x*) dependence of (a) oxygen deficiency (δ) estimated by comparison to bulk single-crystal 10 K resistivities [169] and (b) estimated average Co valence ($\bar{V}_{Co}$) of as-deposited $La_{1-x}Sr_xCoO_{3-\delta}$ films (28 - 35 u.c. thick) on LAO and LSAT substrates. Literature values of the *x*-dependent (c) oxygen vacancy formation energy (E_{Vo}) and (d) 300-K oxygen vacancy diffusion length (l_d) for $La_{1-x}Sr_xCoO_{3-\delta}$. In (c), the values of Mizusaki *et al*. [68] are experimentally measured enthalpies from thermogravimetry, while the values of Jia *et al*. [249], Curnan and Kitchin [248], Deml *et al*. [250], and Tahini *et al*. [95] are from DFT. In (d), the values of Mefford *et al*. [69], Pan *et al*. [252], Takeda *et al*. [75], and Van Buren *et al*. [253] are from electrochemical chronoamperometry. The horizontal dashed line marks the thickness (*t*) of $La_{1-x}Sr_xCoO_{3-\delta}$ (LSCO) films (28 u.c. ≈ 10 nm).

After initial V_O formation at the P LSCO/ion gel interface and subsequent depth-wise V_O diffusion, the final issue is the V_O disorder/order transition that constitutes the P → BM transformation. Important in this context is the recent work of Zhang *et al*. [193,194], focused on DFT- and model-based electronic structure understanding of the P → BM transformation specifically in LSCO. Key findings include reproduction of the P cell expansion with increasing δ, detailed understanding of the structure and electronic structure with δ (including the opening of a gap), confirmation of decreasing E_{Vo} with *x*, and, perhaps most significantly, calculations of V_{th} for the P → BM

transformation [193,194]. The latter predict not only decreasing V_{th} with x but also absolute values in the 0.5 - 1.2 V range, in reasonable agreement with our data (Fig. 3.4) [193,194]. Moreover, the dependence of V_{th} on the initial δ is also predicted to be nonmonotonic [193,194], providing a potential explanation for another noticeable feature of Fig. 3.4, namely, the apparent dip in V_{th} around $x = 0.28$. According to Fig. 3.7(a), the initial δ at this x is significant, reaching ~0.03. In terms of the overall decrease with x, approximate magnitude, and nonmonotonic behavior, we thus conclude at least qualitative agreement with literature trends in key thermodynamic and kinetic factors with doping and strain, approaching quantitative agreement with recent computational theory. Particularly, given the significant effect of strain on V_{th} even at $x = 0$ (see Fig. 3.4), where the initial δ is small and negligibly strain-dependent, it would be of high interest to extend such DFT calculations to different heteroepitaxial strain states.

3.7 Summary and conclusions

We have presented the first study of the voltage-induced topotactic perovskite to BM transformation across almost the entire phase diagram of ion-gel-gated $La_{1-x}Sr_xCoO_{3-\delta}$ ($0 \leq x \leq 0.70$), employing epitaxial films on three different substrates to understand the impact of strain. Electronic transport and *operando* SXRD confirm that the perovskite to BM transformation can be driven at essentially all x, including, critically, $x \leq 0.50$, where the perovskite phase is highly stable. The detailed systematics are consistent with a 1st-order transformation, proceeding from the phase-pure perovskite, through perovskite-BM coexistence, to phase-pure BM. Importantly, the threshold voltage for the transformation is tunable (between ~3 and ~0 V) *via* Sr doping and strain, of interest for device applications. The decreasing threshold voltage with doping and strain (particularly tensile) are interpreted in terms of trends in oxygen vacancy formation enthalpy (not diffusivity), highlighting the essential role of thermodynamics (over kinetics), driven by the instability of formal Co^{4+} in these compounds. Finally, the perovskite to BM transition was shown to enable voltage control of the resistivity and Curie temperature over windows of at least 10^5 and ~220 K, respectively. Such findings substantially advance the practical and mechanistic understanding of this voltage-driven transformation, which is emerging as paradigmatic in electrochemical gating, with fundamental and technological implications.

Chapter 4: Modulation of thermal and optical properties *via* the electrolyte-gate-induced perovskite-brownmillerite transformation in $La_{1-x}Sr_xCoO_{3-\delta}$ films

This chapter is based on the following publications:

(1) "*Wide-range continuous tuning of the thermal conductivity of $La_{0.5}Sr_{0.5}CoO_{3-\delta}$ films via room-temperature ion-gel gating*" in Nature Communications Vol. 14, pg. 2626 (2023), by Yingying Zhang, William M. Postiglione, Rui Xie, Chi Zhang, Hao Zhou, Vipul Chaturvedi, Kei Heltemes, Hua Zhou, Tianli Feng, Chris Leighton, and Xiaojia Wang, adapted with permission from Ref. [255], copyright (2023) Nature.

(2) "*Optical properties of electrochemically gated $La_{1-x}Sr_xCoO_{3-\delta}$ as a topotactic phase-change material"* in Advanced Optical Materials Vol. 11, pg. 2300098 (2023), by Rohan D. Chakraborty, William M. Postiglione, Supriya Ghosh, K. Andre Mkhoyan, Chris Leighton, and Vivian E. Ferry, adapted with permission from Ref. [256], copyright (2023) John Wiley & Sons, Inc.

The aim of this chapter is to outline the above works while highlighting their common themes, *i.e*., electrochemical gating of LSCO, but focusing on different materials properties: thermal conductivity and optical properties in the visible-to-mid-infrared range, respectively. The overarching theme is that electrochemistry-based electrolyte gating and the P-BM transformation can be used to not only control electronic and magnetic properties but also thermal and optical properties over extraordinary ranges, with much application potential. The above studies were primarily led by my collaborators at the University of Minnesota: Yingying Zhang from Prof. Xiaojia Wang's group in Mechanical Engineering, and Rohan Chakraborty from Prof. Vivian Ferry's group in Chemical Engineering and Materials Science.

4.1 Wide-range continuous tuning of thermal conductivity in $La_{0.5}Sr_{0.5}CoO_{3-\delta}$

4.1.1 Methods

45 - 58-nm-thick LSCO (x = 0.5) thin films were grown on LAO (001)-oriented substrates, and ion-gel-based EDLT devices were fabricated from them, using the procedures previously described in Sections 2.1.2 and 2.5. Ion gel gating was conducted in

a similar manner to Refs. [169,176,179] and Section 2.5, but with several distinctions. First, the gating was conducted entirely in vacuum (< 10^{-5} Torr) at room *T*. The gate voltages were not 'stepped', but rather swept at a rate of 0.5 mV s^{-1} to the desired setpoint, and then the experiment was stopped. This experimental procedure is outlined in Fig. 4.1, where panel (a) shows a schematic of the gating setup, and panel (b) shows representative data of the source-drain resistance (R_{SD}) as a function of V_g. By choosing a specific set of V_g 'stopping points' and then preparing the samples for *ex situ* structural, electronic, and thermal characterization, the properties of the gated film were probed *vs*. V_g in a semi-continuous manner. V_g was applied between the gate pads (see Fig. 4.1(a)) and two diagonal channel contact electrodes, while the source-drain resistance was measured between the other two contact electrodes. A constant source-drain voltage of 0.2 V was used to measure source-drain current and thus deduce R_{SD}. After gating, the ion gel was removed, and the sample was cleaned by sonication in acetone. Film structure and electronic transport properties were then probed by wide-angle HRXRD and ρ(*T*) measurements, respectively.

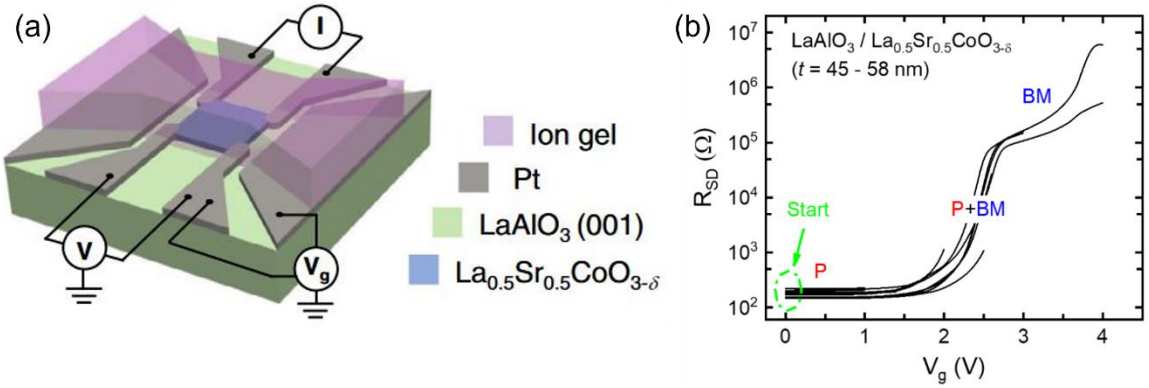

Figure 4.1: (a) Schematic of the $La_{0.5}Sr_{0.5}CoO_{3-\delta}$-film-based side-gated electrolyte-gate devices used in this study, with an overlying ion gel as the electrolyte. *I* and *V* are the current and voltage for measurement of four-wire channel resistance, while V_g is the gate voltage. (b) Source-drain two-terminal resistance (R_{SD}) *vs*. gate voltage (V_g) for eleven 1 × 1 mm^2 channel area ion-gel-gated LSCO films of 45 - 58 nm thickness on LAO(001) substrates. Gating was performed at 300 K under vacuum.

Thermal transport properties were measured *ex situ* using time-domain thermoreflectance (TDTR) (see Section 2.4.1). To do this, an ~70-nm-thick Pt transducer layer was first deposited over the top of the film (after gating). Pt was chosen over Al as a transducer material because Al was found to act as an 'oxygen getter', as in other similar

systems [257], effectively removing oxygen from the LSCO film, *i.e.*, creating V_O, even at room *T*. At the TDTR laser wavelength of 783 nm, the extinction coefficient is ~7.4 for Pt [258]; therefore, 70 nm is sufficient for the Pt transducer to be considered optically opaque. In TDTR, a mode-locked Ti:sapphire laser produces a train of optical pulses (~100 fs in duration) at a repetition rate of 80 MHz and a central wavelength of ~780 nm. The laser is divided into a pump beam and a probe beam, with two orthogonal polarizations by a polarizing beam splitter. The pump beam is modulated by an electro-optical modulator, which heats the sample. The probe beam is modulated by a mechanical chopper and detects the temperature response of the sample upon pump heating. An objective lens is used to focus the pump and probe beams onto the sample surface. A mechanical delay stage then varies the optical path of the pump beam, which produces a time delay of up to 4 ns between pump heating and probe sensing. The probe beam reflected from the sample is collected with a fast-response Si detector and then amplified by an RF lock-in amplifier for the data reduction. By varying the modulation frequency in the TDTR approach, the measurement sensitivity to the LSCO thermal conductivity and the thermal interfaces can be tailored. A schematic of the sample geometry and a representative dataset for typical TDTR results in this study are shown in Fig. 4.2.

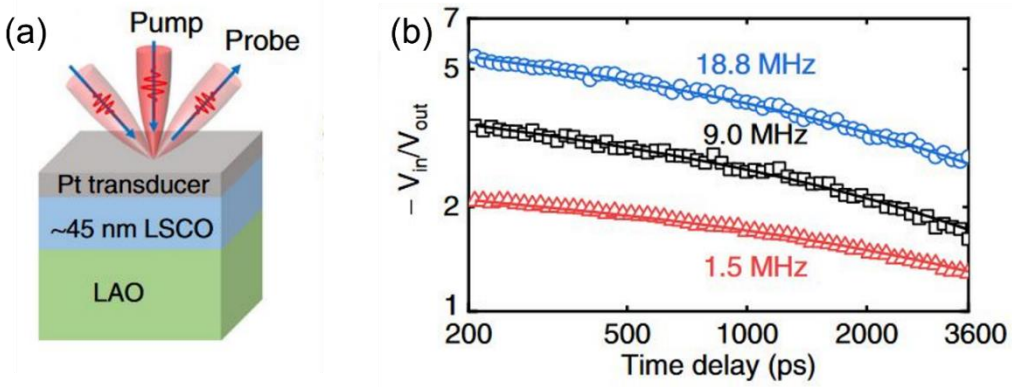

Figure 4.2: (a) Sample configuration for TDTR measurements. (b) Representative TDTR ratio signals of the ungated LSCO film measured at three modulation frequencies. The solid lines are the best fits to the through-plane thermal measurement data based on a heat diffusion model. The data reduction gives a through-plane thermal conductivity of 4.6 ± 2.0 W m^{-1} K^{-1} for this ungated LSCO film.

4.1.2 Structural characterization and electronic transport

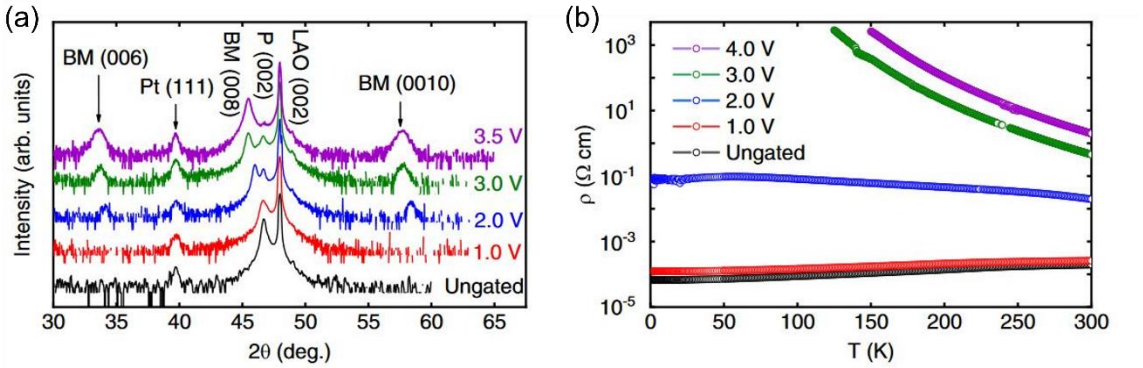

Figure 4.3: (a) Specular HRXRD scans from LSCO devices on LAO(001) substrates after gating to various V_g. The *y*-axis represents the diffracted intensity in arbitrary units, plotted on a logarithmic scale and offset for better visualization. (d) Temperature (T)-dependence of the resistivity (ρ) (from a four-wire measurement) for selected LSCO films after gating to various V_g.

Fig. 4.3(a) shows high-resolution wide-angle specular XRD scans of representative LSCO film devices after ion-gel gating to various V_g from 0 to 3.5 V. To facilitate TDTR measurements, each scan here is from a *different* ion-gel-gated sample. The ungated data (black) reveal the expected phase-pure epitaxial P-LSCO on the LAO(001) substrate (in addition to a Pt (111) peak from the device electrodes), consistent with previous reports on LSCO deposited *via* high-pressure-oxygen sputtering [169,176,179,180,242]. Moving to the gated-LSCO film XRD patterns in Fig. 4.3(a), we find a clear downshift of the P (002) peaks with increasing V_g, indicating expansion of the P-LSCO *c*-axis lattice constant due to V_O formation in the P phase [176,242]. At 2 V and beyond, a (001)-oriented BM structure is then detected *via* the emergence of additional peaks around 34 and 58°, due to the BM (006) and BM (00$\underline{10}$) reflections. This signifies the quadrupling of the unit cell in the V_O-ordered BM phase. Initially, these BM-LSCO peaks occur along with P (002) peaks, indicating a mixed phase region, as observed previously and interpreted in terms of phase coexistence across a first-order P → BM transformation [242]. At 3 V, however, the P (002) peak continues to downshift, indicating further lattice expansion, additional V_O formation, and near-complete transformation to BM (the P (002) reflection then becomes the BM (008)). Concomitantly, the BM (006) and (00$\underline{10}$) peaks intensify, while the P (002) peak diminishes. Interestingly, little difference is then observed between films gated to 3 and 3.5 V. We interpret this as resistance to further removal of oxygen beyond the BM-LSCO stoichiometry (*i.e.*, $\delta \approx 0.5$) at voltages above 3 V. Regarding the structural

perfection of the gated BM-LSCO, more detailed analysis (peak fitting) of the 3.5 V sample (purple) on a larger-channel-area device revealed additional disorder in the V_O sublattice compared to as-deposited BM films (*e.g.*, $SrCoO_{2.5}$) reported in literature [97,112,120,129,186,259]. Overall, we thus conclude from Fig. 4.3(a) that a reduced P phase exists up to ~1 V, beyond which P+BM phase coexistence persists to ~3 V, followed by near phase-pure BM. These findings are in good general agreement with prior LSCO gating studies [242]. As a final comment on these data, we note that, consistent with prior work on gated LSCO [176,242], we find no significant evidence of the hydrogenated phase seen in gating studies of $SrCoO_{3-\delta}$. The transformation in this work is thus simply between P and BM phases; it is therefore bi-state not tri-state switching.

Due to the very different electronic characteristics of the LSCO P and BM phases, major changes in electronic transport accompany the V_g-induced P → P + BM → BM transformation deduced above. Fig. 4.3(b) shows ρ *vs*. T data for an ungated LSCO film, as well as for films gated to 1 - 4 V. The ungated LSCO film is a metallic ferromagnet with a residual resistivity $\rho_0 \approx 70$ μΩ cm, a residual resistivity ratio of ~3, and $T_C \approx 220$ K. This is as expected for relatively thick films of $La_{1-x}Sr_xCoO_{3-\delta}$ with $x = 0.5$, where metallic conduction and long-range ferromagnetism are observed for $x > 0.17$ [58,59,108]. After gating to 1 V, the metallic conduction in the LSCO film is maintained, albeit with slightly higher ρ, reflecting the additional V_O density introduced into the P lattice. As electron donors, V_O compensate holes (the dominant charge carriers in LSCO), thus increasing ρ. The relatively small change in ρ for LSCO at 1 V compared to ungated LSCO is consistent with Fig. 4.3(a) in that the P phase is retained, but with a higher δ. After applying 2 V, however, the 300-K ρ increases nearly 100-fold, reflecting not only a substantial increase in V_O concentration (larger δ), but also entry into the P + BM phase coexistence region. The unusual form of ρ *vs*. T for the 2 V-gated sample (note the flattening at low T) is also consistent with this; lateral inhomogeneity would be expected in this situation and indeed we detected in-plane anisotropy in the orthogonal electrical resistances in four-wire van der Pauw measurements at low T. For the samples gated to 3 and 4 V, where XRD reveals near-phase-pure BM (Fig. 4.3(a)), the LSCO films then exhibit completely insulating behavior in Fig. 4.3(b), with ρ(300 K) of ~0.5 and ~2 Ω cm, respectively. This represents

a factor of ~10^4 between the 300 K ρ of ungated P-LSCO and BM-LSCO, comparable to literature values for electrolyte-gated $SrCoO_{3-\delta}$ and $La_{0.5}Sr_{0.5}CoO_{3-\delta}$ [97,242].

4.1.3 Tuning of thermal conductivity with gate voltage

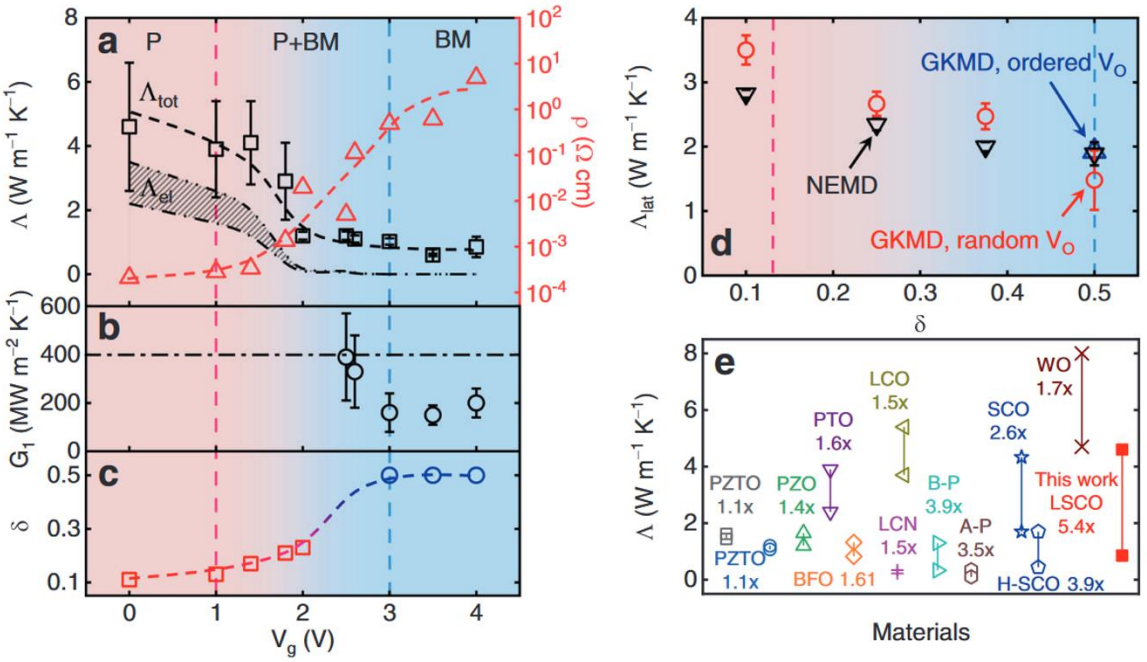

Figure 4.4: (a) The thermal conductivity (left axis) and electrical resistivity (right axis) of LSCO films, (b) the interfacial thermal conductance between Pt and LSCO, and (c) oxygen non-stoichiometry due to vacancies, as functions of V_g. In panel (a), Λ_{tot} represents the measured total thermal conductivity, Λ_{el} represents the electronic thermal conductivity estimated from the Wiedemann-Franz law. The black dash-dotted lines represent the upper and lower limits of Λ_{el} based on different Lorenz numbers. The dashed lines serve as guides to the eye. In panel (c), $\delta = 0.5$ (blue circles) is assumed for the complete transition to brownmillerite ($V_g \geq 3$ V). The red-blue graded dashed line serves as a guide to the eye. (d) Molecular dynamic (MD) simulation results, obtained from both Green-Kubo MD (GKMD) and nonequilibrium MD (NEMD), for the lattice thermal conductivity (Λ_{lat}) of LSCO with different δ. In all panels, the vertical pink and blue dashed lines represent, respectively, the starting and ending points of the P → P + BM → BM transformations. (e) Comparison of thermal conductivity tuning factor through bi-state tuning process in this work and previous experimental studies [117,260–272].

The thermal conductivities of LSCO thin films gated to various V_g (from 0 to 4 V) were measured with the TDTR approach, which is an ultrafast laser-based pump-probe technique [229,230]. All TDTR measurements were made *ex situ*, after gating and ion-gel removal / cleaning, taking advantage of the non-volatile nature of the electrolyte gating in this case [97,113,117,129,242]. Fig. 4.2(b) shows representative TDTR ratio data of the in-phase and out-of-phase thermoreflectance signals ($-V_{in}/V_{out}$) measured on the ungated LSCO film at 300 K. Three modulation frequencies (1.5, 9.0, and 18.8 MHz) were used to

enable tailoring of the measurement sensitivity. The solid lines in Fig. 4.2(b) are best fits to the TDTR data based on a heat diffusion model for a multi-layer structure [229,273]. At 300 K, the fitted through-plane thermal conductivity of the ungated LSCO sample is 4.6 ± 2.0 W m^{-1} K^{-1}. The interfacial thermal conductances of the Pt/LSCO (G_1) and LSCO/LAO (G_2) interfaces are determined as 400 and 800 MW m^{-2} K^{-1}, respectively. The 300 K electrical resistivity and thermal conductivity of LSCO thin films are summarized as functions of V_g in Fig. 4.4(a). As V_g increases from 0 to 4 V, the change in ρ reaches almost five orders of magnitude, a clear reflection of the metal-insulator transition shown in Fig. 4.3(b). Coincident with this, the central experimental result of this work is that the through-plane thermal conductivity of LSCO decreases from 4.6 ± 2.0 to 0.85 ± 0.32 W m^{-1} K^{-1} as V_g varies from 0 to 4 V, *i.e.*, a factor of more than 5 reduction *via* ion-gel gating. We consider this record-high tuning factor to be for the *through-plane* thermal conductivity, *i.e.*, Λ_z (See Section 2.4.1), acknowledging the possibility of thermal transport anisotropy in the BM-LSCO film. It is reasonable, however, to convert the in-plane electrical resistivity to a through-plane thermal conductivity for the purposes of comparison. We emphasize that the thermal conductivity can be continuously tuned over this range, in a non-volatile fashion, at room temperature. It should be noted that the thermal conductivity of our as-deposited P-LSCO films (with $x = 0.5$ and $\delta \approx 0.1$) is 4.6 ± 2.0 W m^{-1} K^{-1},which is less than half the equivalent values for several unsubstituted ABO_3 perovskites (*e.g.*, 11 W m^{-1} K^{-1} for $SrTiO_3$ [274], 13 W m^{-1} K^{-1} for $BaSnO_3$ [275], and 13 W m^{-1} K^{-1} for $LaAlO_3$ [276]). Also, prior experimental studies reported a bulk thermal conductivity of 6 W m^{-1} K^{-1} for single-crystal $La_{0.7}Sr_{0.3}CoO_3$ [276,277]. The significantly smaller thermal conductivities of $La_{0.7}Sr_{0.3}CoO_3$ and $La_{0.5}Sr_{0.5}CoO_3$ are partially attributed to enhanced phonon-defect scattering resulting from the mass mismatch and local strains induced by Sr substitution for La [275,275,277]. Below, we analyze the change of thermal conductivity versus V_g in detail, including discussing the contributions to the thermal conductivity from various critical factors.

It is important to note that the V_g-driven P → BM and metal-insulator transitions also impact thermal transport across the Pt / LSCO interfaces. Fig. 4.4(b) summarizes the results on G_1 extracted from TDTR, where a smaller G_1 is observed when LSCO is gated

to higher V_g. For BM-LSCO, with insulating behavior, heat can be transferred across the Pt / BM-LSCO interface *via* two channels: electron-phonon interactions in Pt, in series with the phonon–phonon interactions (between Pt and BM-LSCO). The average measured G_1 (170 MW m^{-2} K^{-1}) of our BM-LSCO is comparable to the values of interfacial thermal conductance between Pt and oxides reported in literature [278–281]. However, for $V_g < 3$ V, the P phase in the LSCO films provides an additional channel for interfacial heat transfer, *via* electron-electron interactions (between Pt and P-LSCO) across the interface [282,283], thus leading to larger G_1. This increase in G_1 reduces the measurement sensitivity to G_1. As a result, we used a nominal value for G_1 of 400 MW m^{-2} K^{-1} (black dashed line in Fig. 4.4(b)) for LSCO films at $V_g < 2$ V, when measurement sensitivity is insufficient to determine G_1 (*i.e.*, the choice of G_1 value does not change the fitting results of the LSCO thermal conductivity). Besides, G_2 of the LSCO/LAO epitaxial interface is measured to be 800 WM m^{-2} K^{-1} using the dual-frequency TDTR approach with enhanced measurement sensitivity to G_2 [284]. This value of G_2 is consistent with literature data for strongly bonded interfaces [285].

As already noted, the V_g-driven P → BM phase transformation in electrolyte-gated LSCO involves several factors, including a large change in δ, lowered crystal symmetry, V_O ordering, and an accompanying metal-insulator transition. The P → BM (cubic to orthorhombic) crystal structure change, induced by the V_g-driven increase in δ, impacts phonon transport, thus modifying thermal conductivity *via* the phonon contribution. To better quantify the impact of V_O on the thermal conductivity in Fig. 4.4(a), it is useful to correlate V_g with V_O concentration. To this end, we estimated δ using an established empirical approach based on electrical transport data [169,242,276]. The resulting values are plotted in Fig. 4.4(c). The expected increasing trend in δ is observed for V_g from 0 to 2 V. For films gated above 2 V, however, our approach is no longer applicable, and we simply assign the nominal $\delta = 0.5$ implied by our XRD observation of near-phase-pure BM-LSCO at 3, 3.5, and 4 V (blue circles in Fig. 4.4(c)).

To gain further insight into the thermal conductivity change in Fig. 4.4(a), we decompose it into electronic and lattice contributions, *i.e.*, $\Lambda_{tot} = \Lambda_{el} + \Lambda_{lat}$ (with Λ_{el} being the electronic thermal conductivity and Λ_{lat} the lattice thermal conductivity). Λ_{el} can be

estimated from the electrical conductivity ($\sigma = 1/\rho$) *via* the Wiedemann-Franz law (WFL), *i.e.*, $\Lambda_{el} = L\sigma T$, with L being the Lorenz number. Since the value of L varies non-trivially depending on the nature of the material system, we used the lower and upper limits on L commonly accepted in the literature (1.5 and 2.44×10^{-8} V^2 K^{-2}), to estimate Λ_{el} [286–289]. The results are plotted as the shaded 'envelope' between black dash-dotted lines in Fig. 4.4(a), exhibiting the expected generally decreasing trend with V_g due to the metal-insulator transition. For the as-deposited P-LSCO film with $\delta \approx 0.1$ (Fig. 4.4(c)), the lower and upper limits of Λ_{el} are estimated as 2.2 and 3.5 W m^{-1} K^{-1}, resulting in the upper and lower limits of $\Lambda_{lat} = \Lambda_{tot} - \Lambda_{el}$ of 2.4 and 1.1 W m^{-1} K^{-1}, respectively. The upper limit of Λ_{lat} decreases from 2.4 to 0.85 W m^{-1} K^{-1}, a 65% reduction, as V_g increases from 0 to 4 V, at which point the P → BM transformation is complete. Importantly, we thus find that electrons contribute comparably with phonons for P-LSCO, which is reasonable for "dirty", *i.e.*, higher resistivity, metals [290]. This is notably different from the P-$SrCoO_{3-\delta}$ reported by Lu *et al*. [117], where the electronic contribution to thermal conductivity was deduced to be negligible. We attribute this difference to the likely larger δ and disorder level in the P phase in ref. [117], where the P-$SrCoO_{3-\delta}$ was achieved from as-deposited BM films *via* gating, in contrast to our as-deposited high epitaxial-quality P-LSCO. Supporting this, Lu *et al*. reported ρ(300 K) $\approx 5 \times 10^{-2}$ Ω-cm in their P-$SrCoO_{3-\delta}$ [117], compared to ρ(300 K) $\approx 2 \times 10^{-4}$ Ω-cm in our as-deposited P-LSCO, *i.e.*, our P conductivity is ~250 times higher.

To further understand the trend of Λ_{lat} *vs.* V_g (and therefore also δ), we performed Green-Kubo molecular dynamics (GKMD) and nonequilibrium molecular dynamics (NEMD) simulations of thermal conductivity, with results shown in Fig. 4.4(d). The GKMD and NEMD results agree reasonably well. The MD simulations predict a ~62% Λ_{lat} reduction (from 3.9 to 1.5 W m^{-1} K^{-1}) as δ increases from 0.1 to 0.5, assuming random spatial distributions of V_O. Considering that the V_O in the BM phase of our LSCO films are ordered [242], we also calculated the thermal conductivity of orthorhombic BM-LSCO, with ordered V_O, using MD simulations; this yields a larger Λ_{lat} = 1.9 Wm^{-1} K^{-1} at $\delta = 0.5$ due to the decrease of phonon-defect scattering. There is thus a ~50% lattice thermal conductivity reduction from $\delta = 0.1$ in the disordered P phase to $\delta = 0.5$ in the ordered BM phase. Importantly, these 62% and 50% reductions in Λ_{lat} agree reasonably with the upper

limit of 65% obtained from our $\Lambda_{lat} = \Lambda_{tot} - \Lambda_{el}$ extraction. Note that the absolute values of Λ_{lat} from the experiment and MD simulations are not directly compared because the classical interatomic potential used in our MD simulations provides only qualitative insights. Based on the above discussion, we conclude that the decrease in thermal conductivity with increasing V_g originates from comparable reductions in both the electronic and lattice contributions. This plays an important role in our record-high (> 5-fold) tuning of thermal conductivity achieved here *via* bi-state gating. Fig. 4.4(e) summarizes the tuning factor of material thermal conductivities in our work, and in prior experimental studies, *via* a bi-state tuning process [117,260–272]. Evidently, the tuning factor of LSCO thermal conductivity in our work is the largest among experimental reports.

4.1.4 Reversibility of voltage-induced thermal conductivity changes

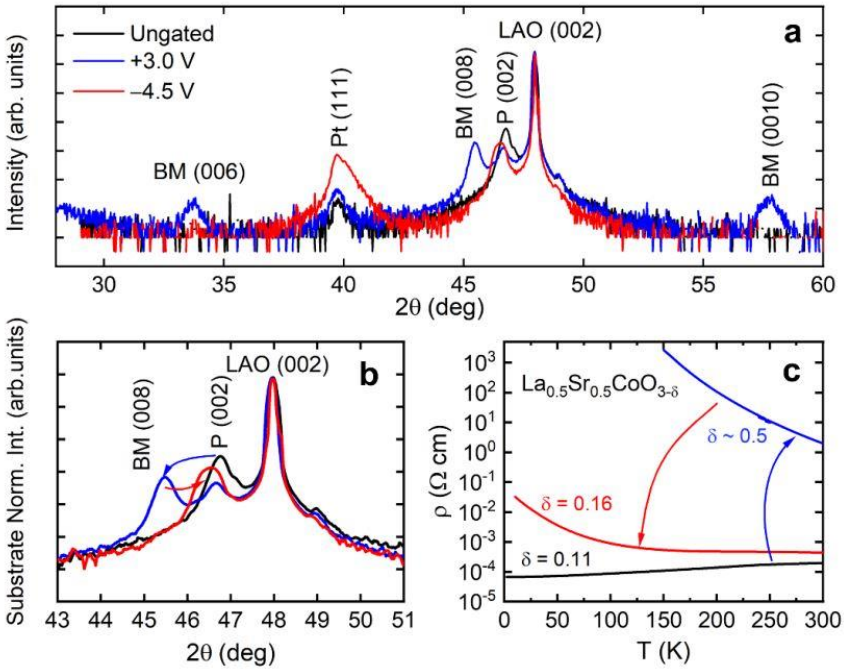

Figure 4.5: (a) Wide-angular-range HRXRD results from LSCO devices on LAO(001) substrates after gating to +3.0 V and after reverse gating to −4.5 V. The *y*-axis is on a logarithmic scale. (b) An enlarged version of the same scans as in (a), around the film and substrate perovskite (P) (002) peak / brownmillerite (BM) (008) peak, with the intensity axis (log scale) normalized to the substrate intensity. (c) Temperature (*T*)-dependent electrical resistivity (ρ) measurements of the as-deposited P-LSCO (black), after gating to +3.0 V (blue), and after reverse gating to −4.5 V (red). The color code is the same for all panels.

To explore the reversible nature of the V_g-induced P ↔ BM phase transformation in LSCO, we also reverted some gated BM-LSCO films back to the P phase by applying

reverse-polarity gate voltages of up to –4.5 V at 300 K. The 300 K thermal conductivity of one reverse-gated P-LSCO film (P → BM → P) was measured to be 3.5 ± 1.1 W m^{-1} K^{-1}, compared to 4.6 ± 2.0 W m^{-1} K^{-1} for the ungated P. This ~20% reduction in the Λ_{tot} of recovered P-LSCO compared to the as-deposited P-LSCO film arises from additional structural disorder induced during the cyclic gating. This can be seen from the HRXRD measurements shown in Fig. 4.5(a),(b) on the as-deposited P-LSCO film (black, labeled as "ungated"), after gating to +3.0 V (*i.e.*, transformed to BM, blue), and after reverse gating to −4.5 V (*i.e.*, recovered to P, red). The ideal situation after negative V_g would be a P (002) reflection exactly overlapping with the ungated peak. In reality, the reverse-gated P (002) peak has a remnant downshift in Fig. 4.5(a),(b) from the ungated P (002) (*i.e.*, a larger out-of-plane lattice parameter). However, the BM (006) and (00$\underline{1}$0) peaks are entirely extinguished, definitively establishing that long-range V_O order is annihilated, yet the lattice parameter of the recovered P phase remains expanded. This indicates that the V_O concentration is higher than it was originally for the ungated sample. This difference between as-deposited and reverse-gated P can be further analyzed through electronic transport measurements, as shown in Fig. 4.5(c). Specifically, the above approach to determine δ from transport yields 0.11 for the as-deposited P-LSCO film and 0.16 for the reverse-gated film (following P → BM → P). This additional disorder is unsurprising after topotactic transformation from P to BM back to P, and no doubt plays some role in the reduced thermal conductivity. Nevertheless, such data confirm the overall reversibility of the approach presented here. Further improvement of reversibility can likely be achieved through better device design and optimized gating conditions.

4.2 Optical properties of electrochemically gated $La_{1-x}Sr_xCo_{3-\delta}$

4.2.1 Methods

In the following study, the optical properties of as-deposited and ion-gel-gated LSCO films of varying Sr doping ($0 \leq x \leq 0.7$) were characterized and their properties analyzed and contrasted. Film growth, device fabrication, and ion-gel-gating experiments were conducted following the procedures outlined in prior work [242,255]. Here, all films were grown on (001)-oriented LSAT substrates due to the lack of twin-domain boundaries,

which are prevalent in, *e.g.*, LAO. As in Section 4.1.1, ion-gel gating experiments consisted of sweeping V_g at 0.5 mV s^{-1} from 0.0 V to a pre-determined terminal voltage (3.5 V in this case), removing the gel, and cleaning with acetone, to prepare the gated film for *ex situ* structural (XRD and TEM), electronic, and optical characterization. All gating was performed at 300 K in vacuum (< 10^{-5} Torr) on LSCO film EDLTs fabricated on 10 × 10 mm^2 substrates (both 1- and 2-side-polished), with channel area ~4 × 3.5 mm^2.

Scanning transmission electron microscopy (STEM) samples were prepared by using an FEI Helios Nanolab G4 dual focused-ion beam (FIB) microscope. The sample was coated with amorphous carbon prior to ion beam exposure in the FIB, to prevent damage to the film surface. The sample was first thinned using 30 keV Ga ion beams followed by a 2 keV ion beam shower to remove damaged surface layers. High angle annular dark field (HAADF)-STEM imaging was performed on an aberration-corrected FEI Titan G2 60–300 (S)TEM which is equipped with a monochromator and a CEOS-DCOR probe corrector. The microscope was operated at 200 keV, with a probe current of 100 pA and probe convergence angle of 18.2 mrad. The HAADF detector inner and outer collection angles used were 58.5 and 200 mrad, respectively.

Spectroscopic ellipsometry was performed on LSCO EDLTs grown on 1-side-polished substrates using a J.A. Woollam VASE ellipsometer in the wavelength range of 350 - 1100 nm. All ellipsometric measurements were performed at a 40° incident angle, which produces a spot width small enough (< 4 mm) to probe only the LSCO channel and not the surrounding electrodes. Separately, optical transmittance measurements were performed on LSCO EDLTs grown on 2-side-polished substrates. Transmittance data from 350 - 2500 nm were collected using a Cary 7000 UV–vis–NIR spectrophotometer, where samples were mounted on an opaque holder with an opening smaller than 4 × 3.5 mm^2 such that only the LSCO channel was illuminated. Transmittance data from 2500 - 5000 nm were collected using a Bruker Hyperion 2000 Fourier-transform infrared spectroscopy (FTIR) microscope with a liquid N_2-cooled MCT detector coupled to a Bruker Invenio-R FTIR spectrometer. All transmittance spectra were collected at normal incidence using unpolarized light and were normalized to the transmittance of air. For each composition of LSCO, the corresponding transmittance data were loaded into the J. A. Woollam

ellipsometry software, and both the ellipsometric and transmittance data for that composition were then fit *together* to Kramers-Kronig-consistent refractive index models of LSCO ranging from 350–5000 nm following a previously demonstrated technique [291]. To enable this fitting process for LSCO, the refractive index of each 2-side-polished LSAT substrate used for in study was separately modeled in a similar manner.

4.2.2 Structural, electronic, and optical properties of as-deposited films

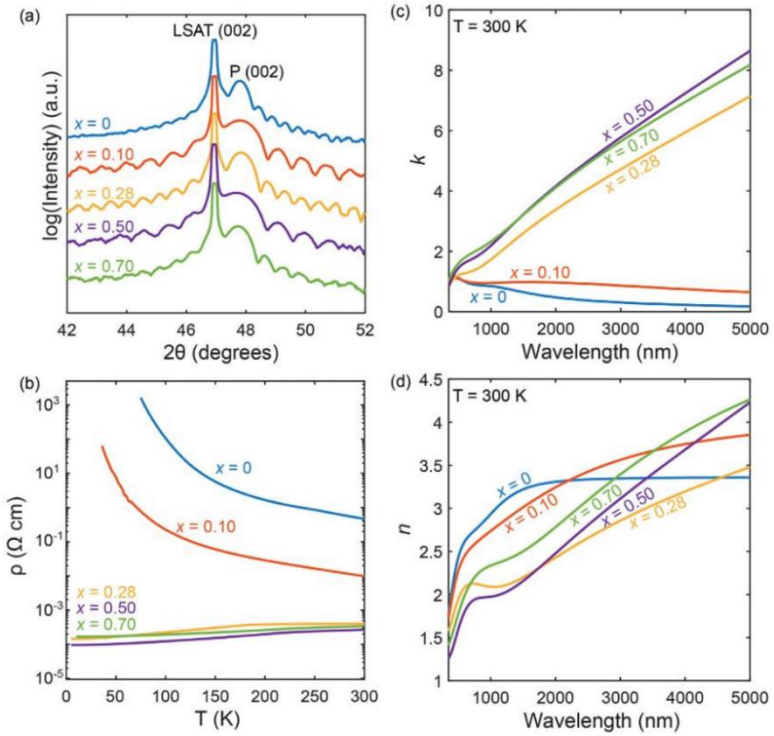

Figure 4.6: (a) Specular HRXRD scans of 12 - 22 nm-thick perovskite LSCO films at x = 0, 0.10, 0.28, 0.50, and 0.70 on LSAT(001) substrates, showing the P LSCO (002) reflections present at all x. Scans are offset for clarity. Differences in Laue fringe spacing between scans are due to sample-to-sample variations in thickness. (b) T-dependent resistivity (ρ) of the same LSCO films at x = 0, 0.10, 0.28, 0.50, and 0.70, again on LSAT(001) substrates. The ρ(T) data for x = 0 is reproduced from Chaturvedi *et al.* [48] (c) Imaginary, k, and (d) real, n, parts of the 300-K wavelength-dependent complex refractive index of as-deposited perovskite LSCO films at all x studied, obtained from fitting room-temperature spectroscopic ellipsometry and optical transmittance data to Kramers-Kronig dispersion models.

Fig. 4.6(a) shows specular HRXRD scans of heteroepitaxial, tensile-strained LSCO films with in-plane strain (ε_{xx}) of $0.8\% \leq \varepsilon_{xx} \leq 1.5\%$ grown on LSAT(001) substrates, at all five compositions (x = 0, 0.10, 0.28, 0.50, 0.70) studied here. The LSAT (002) reflections and well-defined P LSCO (002) reflections (with prominent Laue oscillations) are seen at

all x. These films have low surface / interface roughness and are phase-pure [48,52,105,108,242]. In Fig. 4.6(b), we highlight the corresponding temperature (T) dependent resistivity (ρ) of these LSCO films, which shows the percolation insulator-metal transition expected for P LSCO. At $x = 0$ and 0.10, P LSCO films display clearly insulating behavior, but the $x = 0.10$ films have room-temperature ρ nearly two orders of magnitude lower than at $x = 0$, due to hole doping. Consistent with the $x = 0.18$ percolation threshold [59,60], $x = 0.28$ LSCO has much lower resistivity, now with a positive $d\rho/dT$, indicating clearly metallic behavior (the slope changes near 175–250 K reflect the F Curie temperature). As x is further increased, $\rho(T)$ maintains a similar shape and decreases to $x = 0.50$, before increasing slightly at $x = 0.70$. This nonmonotonicity at high x has also been seen in bulk LSCO [59], and occurs due to redox instability as x exceeds ~0.50, resulting in oxygen vacancies that compensate the Sr doped holes [59,66,105,107,242].

The rest of Fig. 4.6 shows our room-temperature Kramers-Kronig-consistent complex refractive index models for as-deposited P LSCO films with $0 \leq x \leq 0.70$, where the wavelength-dependent imaginary refractive index (k) is shown in Fig. 4.6(c) and the real index (n) is shown in Fig. 4.6(d). We first focus on Fig. 4.6(c), where LCO ($x = 0$ LSCO) exhibits k that decreases with wavelength, showing two absorption features centered at ~400 and ~1000 nm. This imaginary index for LCO shows excellent agreement with previous experimental studies, specifically a stronger and narrower absorption peak at higher photon energy (~400 nm) due to the O^{2p}-Co^{3d} e_g transition, and a weaker but broader absorption peak at lower photon energy (~1000 nm) due to the Co^{3d} t_{2g}-e_g intraband transition [41,292–296]. Moving to $x = 0.10$ LSCO, we observe a similar spectrum overall, with a slight reduction in the magnitude of the peak near 400 nm, and significant increases in both the magnitude and width of the longer-wavelength absorption peak, attributed to metallic cluster formation due to Sr doping. The light absorption in $x = 0.28$ LSCO is then consistent with metallic cluster percolation (see Fig. 1.10(b)). The shorter-wavelength interband absorption feature is retained, but the longer-wavelength absorption increases with wavelength and is much stronger in magnitude, indicating free-carrier Drude light absorption from the Co^{3d} t_{2g}-e_g intraband transition [292,293]. Considering the $x = 0$, 0.10, and 0.28 compositions together, we also note the slight decrease in the shorter-wavelength

absorption feature, and the increase and broadening of the longer-wavelength feature, with *x*. We attribute this spectral weight transfer to a filling-controlled insulator-metal transition, previously described in terms of a Mott insulator-to-metal transition [292,293]. These findings are consistent with both our established theoretical picture (Fig. 1.10(b)) and the measured $\rho(T)$ at different *x* (Fig. 4.6(b)).

Moving to light absorption at higher *x*, Fig. 4.6(c) shows a notable increase in *k* from $x = 0.28$ to 0.50, in agreement with the decrease in resistivity in Fig. 4.6(b). The magnitude and overall shape of the refractive index are also similar to prior refractive index measurements of $x = 0.50$ LSCO films, some of which used similar Drude–Lorentz refractive index models [297]. Finally, $x = 0.70$ LSCO shows a slight decrease in *k* relative to $x = 0.50$ at longer infrared wavelengths, but higher *k* at shorter wavelengths. As discussed in Fig. 4.6(b), this decrease in longer-wavelength light absorption is due to the valence instability of Co at $x = 0.70$ and the subsequent formation of V_O that compensate doped holes [59,66,105,107,242]. Overall, the trends in the imaginary refractive index in Fig. 4.6(c) capture the relevant electronic transitions expected in LSCO across the studied Sr doping window.

In Fig. 4.6(d), we present the corresponding real refractive index (*n*) of P LSCO films, where the magnitude and shape of *n* are directly linked to that of *k* (Fig. 4.6(c)) *via* the Kramers-Kronig relations. For $x = 0$, we see that *n* increases significantly between ~350 and 1500 nm, with shoulders around 600 and 1100 nm, then increases more slowly between 1500 - 5000 nm, finally leveling off at $n \approx 3.35$. Based on the Kramers-Kronig relations, the two shoulders observed in the *n* of LCO are attributed to the two absorption features in *k* at similar wavelengths, while the decreasing dispersion at longer wavelengths is attributed to the general decrease in absorption at those wavelengths. LSCO at $x = 0.10$ also shows stronger dispersion in the visible than in the infrared, but greater overall dispersion than LCO, due to stronger absorption throughout the infrared. The $x = 0.28$, 0.50, and 0.70 LSCO then show higher dispersion in *n* compared to the insulating compositions ($x = 0$ and 0.10), due to strong free-carrier light absorption (*k*) in the infrared. When we compare LSCO at $x = 0.28$ and 0.50 specifically, we see that $x = 0.50$ LSCO has comparatively smaller *n* at wavelengths below 1800 nm, but larger *n* at longer wavelengths,

most likely due to the interband-to-intraband spectral weight transfer observed in *k*. This trend should also extend to $x = 0.70$, but is partly obscured by the redox instability of Co at high *x*.

4.2.3 Electrolyte-gating-induced electronic and structural changes

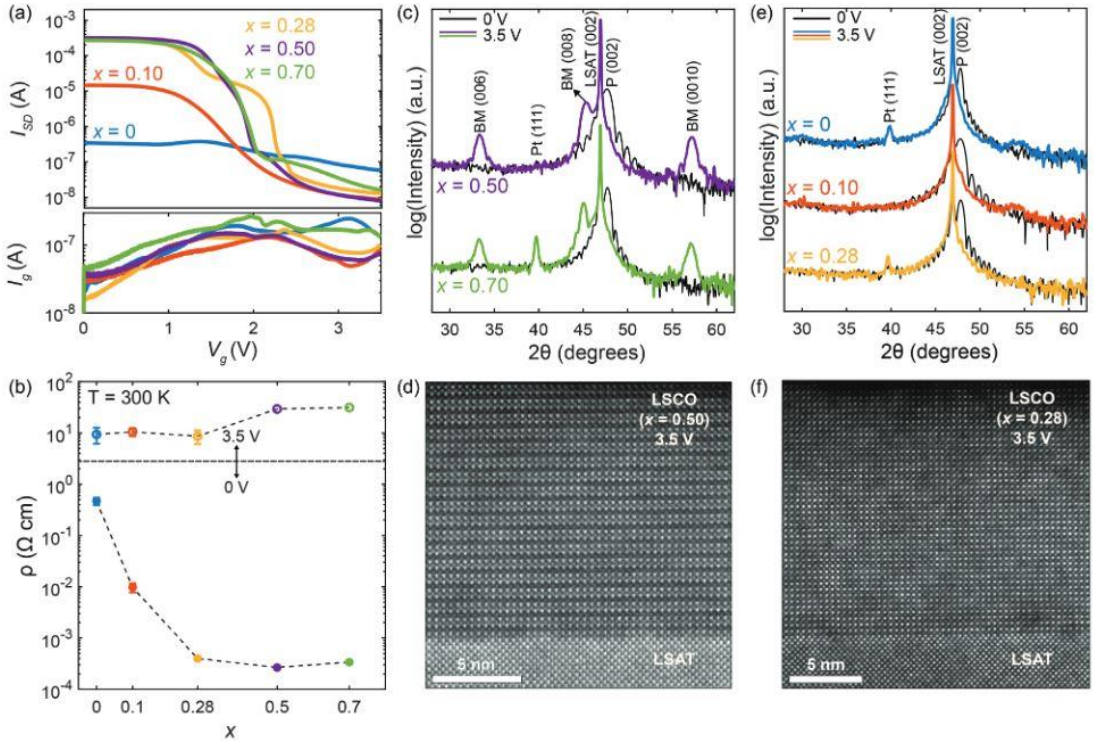

Figure 4.7: (a) Gate voltage (V_g) dependence of the 300-K source-drain current (I_{SD}) (top panel) and 300-K gate current (I_g) (bottom panel) in ion-gel-gated LSCO films at various *x*, as V_g is swept from 0 to 3.5 V at a rate of 0.5 mV s^{-1}. (b) Sr-doping (*x*) dependence of the 300-K four-terminal resistivity (ρ) of LSCO films at $x = 0$, 0.10, 0.28, 0.50, and 0.70 before ($V_g = 0$ V, closed symbols) and after ($V_g = 3.5$ V, open symbols) ion-gel gating. The dashed lines connect data points, and error bars are shown for cases where the error is larger than the data points themselves. For as-deposited LSCO films (0 V), the error bars represent the standard deviation between multiple samples. For gated LSCO films (3.5 V), the error bars represent the sum of systematic and random measurement uncertainty. (c) specular HRXRD scans of as-deposited ($V_g = 0$) and gated ($V_g = 3.5$ V) LSCO at $x = 0.50$ and 0.70. (d) Atomic-resolution HAADF-STEM image of gated ($V_g = 3.5$ V) LSCO at $x = 0.50$ at the film/substrate interface. (e) specular HRXRD scans of as-deposited ($V_g = 0$) and gated ($V_g = 3.5$ V) LSCO at $x = 0$, 0.10, and 0.28. (f) Atomic-resolution HAADF-STEM image of gated ($V_g = 3.5$ V) LSCO at $x = 0.28$ at the film/substrate interface.

Having characterized the complex refractive index of as-deposited P LSCO films, we now discuss the electrochemical gating of these films. Fig. 4.7(a) first shows the 300-K source-drain current (I_{SD}) and gate current (I_g) in electrolyte-gated films of LSCO at various *x* as V_g is swept (at 0.50 mV s^{-1}) from 0 to 3.5 V. In general, LSCO films at all *x*

exhibit lower I_{SD} (top panel) as gating proceeds to 3.5 V, indicating the expected increases in ρ due to V_O formation and proliferation. However, I_{SD} decreases by less than an order of magnitude with gating in LCO films, while decreasing by 3 orders of magnitude in $x = 0.10$ LSCO films, and almost 5 orders of magnitude for $x \geq 0.28$ films. Some of the $I_{SD}(V_g)$ curves in Fig. 4.7(a) also display clear features, such as abrupt slope changes at specific V_g values. In general, these slope changes coincide with local maxima in I_g at the same voltages, emphasizing that electrochemical activity is occurring at these points in the V_g sweep. More specifically, the features in I_{SD} and I_g mark the onset of V_O formation and the transformation to BM, as will be discussed in Chapter 5. We also draw attention to the overall low I_g magnitude (< 500 nA cm^{-2}) for all x during the sweep, confirming the insulating nature of our ion gel. Complementary to Fig. 4.7(a), Fig. 4.7(b) shows 300-K four-wire ρ measurements of LSCO films before ($V_g = 0$ V) and after ($V_g = 3.5$ V) gating. Consistent with Fig. 4.6(b), the resistivity in the as-deposited P phase decreases quickly from $x = 0$ to $x = 0.50$, before increasing slightly at $x = 0.70$. After gating, however, LSCO films with $x = 0$, 0.10, and 0.28 show nearly identical resistivity of ~10 Ω cm, while gated films with $x = 0.50$ and 0.70 show noticeably higher resistivities of 29–31 Ω cm. These findings broadly agree with the results in Fig. 4.7(a), where the overall drop in I_{SD} with V_g increases significantly from $x = 0$ to 0.10, becoming largest at $x = 0.50$.

In order to map the above transport results to the relevant phase evolution, Fig. 4.7(c)–(f) shows XRD and cross-sectional HAADF-STEM images of the film/substrate interface before and after gating. Focusing first on $x = 0.50$ and 0.70 films, Fig. 4.7(c) shows specular HRXRD scans before ($V_g = 0$, black) and after ($V_g = 3.5$ V, purple and green, respectively) gating. The peaks at ~33° and 57° after gating (the BM (006) and (00$\underline{10}$) peaks, respectively) clearly evidence a transformation to the BM structure. Simultaneously, the primary P (002) film peak reduces slightly in intensity and shifts to lower 2θ, transforming into the (008) peak of the BM (the unit cell is quadrupled out-of-plane). Similar gate-induced P → BM transformations were shown in Chapter 3 and Section 4.1 in LSCO and have been observed before in SCO (see Section 1.3.5). (Note that the Pt (111) peaks in Fig. 4.7(c) arise from the device electrodes). These gated $x = 0.50$ and 0.70 LSCO films are in fact phase-pure BM. The long-range V_O order characteristic of the

BM structure is also evident in atomic-resolution HAADF STEM images of gated $x = 0.50$ LSCO films, as shown in Fig. 4.7(d), where the alternating lines of horizontal light and dark contrast correspond to the oxygen-sufficient Co-O octahedral planes and oxygen-deficient Co-O tetrahedral planes of the BM structure (see Fig. 1.15). In clear contrast, the XRD scans in Fig. 4.7(e) reveal no obvious BM peaks in gated films with $x \leq 0.28$. The P (002) film peaks do downshift into the LSAT (002) peak, however, indicating substantial increases in the P out-of-plane lattice parameter, meaning that significant V_O creation has taken place. The electrochemically generated V_O in gated films with $x \leq 0.28$ are thus *disordered*, in the P phase, while those in gated films with $x \geq 0.50$ are ordered (in the BM phase). Interestingly, the overlap of the P (002) film and P (002) LSAT substrate peaks in Fig. 4.7(e) indicates that the films have assumed near-ideal cubic symmetry, as in-plane lattice parameter matching is known to be maintained in LSCO after electrolyte gating [97], and the out-of-plane lattice parameter now matches that of the substrate. It is thus possible that symmetry matching plays a role in stabilizing this structure and the associated oxygen stoichiometry ($\delta \approx 0.25$, from the methods described in Chapter 6). In agreement with Fig. 4.7(e), the HAADF-STEM images of gated $x = 0.28$ LSCO in Fig. 4.7(f) reveal no long-range V_O ordering (compare to Fig. 4.7(d)), instead showing isolated local regions with variable contrast, potentially indicating short-range V_O ordering. In Section 3.3, we speculated on such short-range V_O ordering or Grenier phase formation (, *i.e.*, $La_{1-x}Sr_xCoO_{2.67}$), and, interestingly, broad, low-intensity features do arise around 29° and 55° in Fig. 4.7(e), near where Grenier phase peaks would be expected [139]. While definitive proof of short-range V_O order in lower x films remains to be established, the clear conclusion from Fig. 4.7(c),(d) is a V_g-driven P → BM transformation in LSCO films with $x = 0.50$ and 0.70, explaining the large modulation in I_{SD} and ρ in these cases (Fig. 4.7(a),(b)). The distinctly lower ρ after gating for $x = 0$, 0.10 and 0.28 films (Fig. 4.7(b)) is then simply due to a gate-induced increase in V_O concentration, but incomplete vacancy ordering into the BM structure. In essence, there thus exists a critical x^* (*i.e.*, a critical level of redox instability) in order to gate LSCO to the fully ordered BM phase, at least under the gating conditions and substrate choice employed here.

4.2.4 Optical characterization of electrochemically gated $La_{1-x}Sr_xCo_{3-\delta}$

We now return to optical properties, beginning with the characterization of the refractive index of electrochemically gated LSCO at all x, as shown in Fig. 4.8(a),(b). We note immediately that, at all x, gated LSCO films show significant changes in both k and n relative to P LSCO (Fig. 4.6(c),(d)), with all gated LSCO films showing insulating behavior. Electrochemical gating of LSCO films thus produces insulator-insulator refractive index modulation for $x = 0$ and 0.10, and metal-insulator modulation for $x = 0.28$, 0.50, and 0.70, facilitated by the V_g-induced P → P changes for $x \leq 0.28$ and the P → BM transformation for $x \geq 0.50$, as seen in Fig. 4.7(c)-(f). These observations agree with the V_g-induced changes in I_{SD} and ρ(300 K) in Fig. 4.7(a),(b). Focusing on the detailed refractive index trends in gated LSCO, we first observe in Fig. 4.8(a) that the k of LCO and LSCO films with $x = 0.10$ and 0.28 reaches a maximum near 420 nm, then steadily decreases at longer wavelengths. The absorption is nearly identical in all three cases, which is unsurprising given the clear similarities in structure, but the absorption peak slightly decreases in magnitude and blueshifts with increasing x, and $x = 0.28$ LSCO also shows a slight broadening in absorption. Through similar Kramers-Kronig-related arguments as employed above, these light absorption trends in $x \leq 0.28$ gated LSCO films translate to the real index trends observed in Fig. 4.8(b), namely an n that is slightly blue-shifted and lower in magnitude between LCO and $x = 0.10$ LSCO, followed by an n of $x = 0.28$ that is slightly more dispersive and higher-index in the IR due to the broadened absorption peak.

Shifting to BM LSCO at $x \geq 0.50$, we now observe the presence of two absorption peaks in $x = 0.50$ and 0.70 gated LSCO. Specifically, we see a stronger, shorter-wavelength peak that occurs at similar wavelengths to the single absorption peak in $x \leq 0.28$ LSCO, as well as a second, broader absorption peak centered at ~750 - 900 nm. As x increases from 0.50 to 0.70, both absorption peaks slightly redshift and increase in magnitude, with much larger absorption changes in the shorter-wavelength peak. While n decreases slightly from $x = 0.50$ to 0.70 at visible wavelengths, the absorption trends in BM LSCO generally translate to increases in n between $x = 0.50$ to 1.00 compositions, as expected.

Finally, we note that the presence of one *vs*. two absorption features in $x \leq 0.28$ *vs*. $x \geq 0.50$ gated LSCO further aligns with the presence of disordered *vs*. ordered V_O in these compositions, as described in conjunction with Fig. 4.7. Firstly, the presence of two

absorption peaks in the visible and near-IR is a common optical signature for BM order, related to Co ions in both tetrahedral (tet) and octahedral (oct) coordination, as seen in our as-deposited SCO film (Fig. 4.8(a), bottom panel) and in prior experimental optical studies of BM-SCO films [97,245,298]. This further reinforces our observation from Fig. 4.7 of full BM order in $x = 0.50$ and $x = 0.70$ LSCO, but a lack thereof in $x \leq 0.28$ LSCO. Previous studies of BM SCO assert that the shorter-wavelength feature is due to an interband transition from the O^{2p} orbital to a mostly octahedral Co^{3d} orbital and that the longer-wavelength feature is due to an intraband transition between Co^{3d} orbitals [97,245,298]. Based on this picture, it is reasonable that the O^{2p} - $Co^{3d,oct}$ transition is present in gated LSCO at all x (as it was also observed in P LSCO based on our previous discussion), and does not involve the $Co^{3d,tet}$ orbital, which arises from BM ordering. Still, the slightly stronger and broader absorption of $x = 0.28$ relative to $x = 0$ and 0.10 suggests the formation of some $Co^{3d,tet}$ regions due to V_O (Fig. 4.7(f)), and therefore the possibility of Co^{3d} intraband transitions even at $x \leq 0.28$.

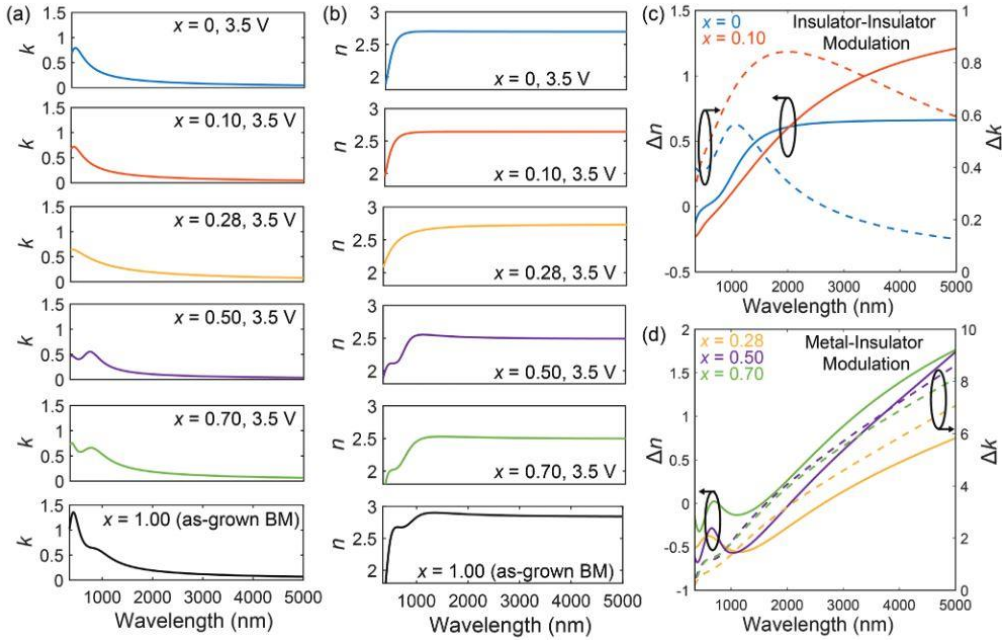

Figure 4.8: (a) Imaginary and (b) real parts of the wavelength-dependent complex refractive index of gated ($V_g = 3.5$ V) LSCO films ($0 \leq x \leq 0.70$), along with an as-deposited brownmillerite (BM) SCO film ($x = 1.00$) for comparison (black, bottom panels). (c) and (d) show the difference in real (Δn, solid lines) and imaginary (Δk, dashed lines) parts of the refractive index between as-deposited ($V_g = 0$ V) and gated ($V_g = 3.5$ V) LSCO for compositions that show insulator-insulator ($x = 0$ and 0.10) and metal-insulator ($x = 0.28$, 0.50, and 0.70) refractive index modulation, respectively. The black circles with arrows serve as guides to the eye.

4.2.5 Electrochemically gated $La_{1-x}Sr_xCo_{3-\delta}$ for active metasurfaces

Metasurfaces are artificially engineered surface structures. Through precise control of their meso- to nano-scale features, they can be designed to achieve electromagnetic light/matter interactions not possible in bulk materials or simple films, leading to exotic phenomena and a broad range of potential applications. Once fabricated, however, a metasurface's optical response is *static*, and is dictated by the specific materials / geometry. Combining the functionality of metasurfaces with the voltage-tunablity of electrolyte gating is therefore an exciting prospect. In this section, we place the refractive index modulation observed in electrochemically gated LSCO in the broader context of active metasurfaces. First, we return to the observation that electrochemically gated LSCO is capable of both insulator-insulator (x = 0, 0.10) and metal-insulator (x = 0.28, 0.50, 0.70) voltage-driven refractive index modulation, stemming from the combination of the x-dependent percolation insulator-metal transition in as-deposited P LSCO and the significant electrochemical reduction induced by electrolyte gating. To better quantify these voltage-induced refractive index changes at all x, Fig. 4.8(c),(d) shows the index modulation (Δn) and loss modulation (Δk) in LSCO, grouped by compositions that show insulator-insulator (c) and metal-insulator (d) contrast, respectively. In Fig. 4.8(c), we observe significant index modulation in low-x LSCO (~0.6 for LCO and up to ~1.3 for x = 0.10 LSCO in the infrared). The refractive indices themselves of LCO and x = 0.10 LSCO are attractive, with both compositions displaying high index ($n > 2.5$) with moderate to low loss ($k < 1.0$) throughout the infrared, both before and after gating. Based on these attributes, $x \leq 0.10$ LSCO can be compared with chalcogenide alloys such as $Ge_xSb_yTe_z$ (GST), which transform between an $n > 3.5$ amorphous phase and an $n > 6$ crystalline phase, with both phases showing moderate to low loss in the infrared [299–301]. While electrochemically gated LCO and x = 0.10 LSCO show both lower index and lower index modulation than GST, these compositions can still tune the optical response of metamaterials significantly, as seen in the case of electrochemical modulation of lower-index TiO_2 [302]. Analogously, in Fig. 4.8(d), we observe significant loss modulation (Δk) in LSCO at x = 0.28, 0.50, and 0.70, due to the opening of an electronic bandgap during gating, with the gated phases of these compositions again showing high index and low loss.

These metal-insulator transitions are reminiscent of similar changes in VO_2 and $SmNiO_3$, where the insulating phase of each material supports resonant effects in many metamaterial geometries, but the strong optical loss in the metallic phase removes the resonance [303–305]. In LSCO, however, we observe for the first time the ability to achieve both types of refractive index modulation using a single material system, along with the significant additional convenience of nonvolatile, low power, room-temperature phase changes.

4.3 Summary and conclusions

The extraordinary voltage control over materials properties afforded by the P-BM transformation in electrolyte gated LSCO films, has in this Chapter, now been firmly extended to the regime of phonon transport and light/matter interactions. In Section 4.1, this technique was demonstrated in $x = 0.5$ LSCO films to produce continuous, reversible, record-large bi-state tuning of thermal conductivity over an ~5-fold range. This result was found to be driven by the combination of proliferation of V_O defects, symmetry lowering on transformation to the BM, and the accompanying metal-insulator transition (eliminating thermal conduction through mobile charge carriers), thus drastically lowering the thermal conductivity in the BM phase *vs*. the P phase. Such wide-ranging active tailoring of thermal conductivity opens the possibility of voltage-tunable thermal materials for applications in thermal management and energy conversion. Next, in Section 4.2, characterization of the complex refractive index, *i.e.*, n and k, over a broad spectral range (visible to near-IR) and across nearly the entire LSCO phase diagram ($0 \leq x \leq 0.7$), revealed a wealth of wavelength- and x-dependent modulations with electrolyte gating. For example, in $x = 0.5$ LSCO gating to 3.5 V, *i.e.*, V_g-induced P → BM, leads to changes in n and k as large as 1.8 and 8.2, respectively. As expected at $x \geq 0.5$, LSCO films readily form the BM structure on gating, however, for $x \leq 0.28$ no long-range V_O ordering was observed. Nevertheless, the voltage-tunable optical properties for both high- and low-x LSCO present promising candidates as phase change materials for active metasurfaces, *via* low-power, non-volatile, room-temperature electrolyte gating. LSCO may thus serve as a library of tunable photonic materials for infrared active metasurfaces, potentially enabling diverse applications such as dynamic thermal imaging, camouflage, and optical memory devices.

Chapter 5: Hysteresis and reversibility across the voltage-driven perovskite-brownmillerite transformation in ultrathin $La_{1-x}Sr_xCoO_{3-\delta}$

Perovskite cobaltites have emerged as archetypes for electrochemical control of materials properties in electrolyte-gate devices. Voltage-driven redox cycling can be performed between fully oxygenated perovskite and oxygen-vacancy-ordered brownmillerite phases, enabling exceptional modulation of crystal structure, electronic transport, thermal transport, magnetism, and optical properties. The vast majority of studies, however, focus heavily on the perovskite and brownmillerite *endpoints*. In contrast, here we focus on hysteresis and reversibility across the entire perovskite ↔ brownmillerite topotactic transformation, combining gate-voltage hysteresis loops, minor hysteresis loops, quantitative *operando* synchrotron X-ray diffraction, and temperature-dependent (magneto)transport, on ion-gel-gated ultrathin (10-unit-cell) epitaxial $La_{0.5}Sr_{0.5}CoO_{3-\delta}$ films. Gate-voltage hysteresis loops combined with *operando* diffraction reveal a wealth of new mechanistic findings, including asymmetric redox kinetics due to differing oxygen diffusivities in the two phases, non-monotonic transformation rates due to the first-order nature of the transformation, and limits on reversibility due to first-cycle structural degradation. Minor loops additionally enable the first rational design of an optimal gate-voltage cycle. Combining this knowledge, we demonstrate state-of-the-art cycling of electronic and magnetic properties, encompassing $>10^5$ transport ON/OFF ratios at room temperature, and reversible metal-insulator-metal and ferromagnet-nonferromagnet-ferromagnet cycling, all at 10-unit-cell thickness with high room-temperature stability. This paves the way for future work establishing the ultimate cycling frequency and endurance of such devices.

5.1 Methods

10-unit-cell-thick P LSCO films were deposited from ceramic targets onto single-crystal LAO(001) substrates by high-pressure-oxygen sputtering. High-quality LSCO films grown by this method have been reported previously and have been extensively characterized [107,108,169,179,242,255,256]. In brief, prior to film deposition 5×5 mm^2 LAO substrates (MTI Corp.) were pre-annealed for 15 minutes in ~1 Torr of flowing O_2 at

900 °C. Previously optimized growth conditions were employed [107,108,169,179,242,255,256], involving 600 °C substrate temperature, 1.5 Torr O_2 pressure, and 55 - 65 W sputtering power, resulting in 15 - 20 Å/min growth rates (calibrated from XRD Laue fringes). Post deposition, films were cooled in 600 Torr of O_2 to minimize δ in the P phase; based on resistivity [169], an as-deposited $\delta \approx 0.14$ was estimated. Side-gate electrolyte transistors (Fig. 1(c)) were then fabricated from LAO/LSCO films using steel masks, Ar ion milling, sputtering of Pt film contact and gate electrodes, and ion-gel lamination, as previously [169,176,179,242,255,256]. Ion gels were first spin coated onto sacrificial glass wafers from a 1:4:8 (by weight) solution of polymer (P(VDF-HFP)) / ionic liquid (EMIM-TFSI) / solvent (acetone) [169,176,179,242,255,256], followed by drying in vacuum at 70 °C for 1 day. Gels were then applied to LSCO devices using "cut and stick" methods [147,157]. Devices with 1.0×1.0 mm^2 channels were used for all measurements except *operando* SXRD, which employed 4.0×3.5 mm^2 channels on 10×10 mm^2 substrates (Fig. 1(c)).

Unless otherwise noted, electrolyte gating was performed at 300 K in vacuum ($<10^{-5}$ Torr). Gate voltage (V_g) and gate current (I_g) were applied and measured with a Keithley 2400 source-measure unit, and V_g was swept at 1 mV s^{-1}. (Note, see Appendix A for a discussion of V_g sweep rate dependence and additional experimental considerations during ion-gel-gating experiments). Source-drain current (I_{SD}) and the four-terminal van der Pauw sheet resistance and film ρ were then measured with a Keithley 2400 source-measure unit and Keithley 2002 multimeter, using a source-drain voltage of ±0.1 V (± V for offset compensation). *Operando* *T*- and *H*-dependent transport measurements were made in a Quantum Design Physical Property Measurement System from 10 - 300 K in fields up to 90 kOe. After sweeping at 1 mV s^{-1} to a chosen V_g, devices were then cooled to 10 K (with V_g left floating) in zero field at 3 K min^{-1}, and $\rho(T)$ was measured on warming at 1 K min^{-1}. Then, after re-cooling in field (±90 kOe), Hall resistance measurements were made at ±50 Oe (remanence) to determine $\sigma_{xy}(T)$, with complementary $\sigma_{xy}(H)$ loops taken at 50 K. Warming (at 1 K min^{-1}) back to 300 K the gating experiment was resumed sweeping to the next V_g. In all cases Keithley based DC measurements were utilized, with careful choice of excitation currents to avoid self-heating and non-ohmicity.

Operando SXRD during ion-gel gating was done at beamline 12-ID-D of the APS at Argonne National Laboratory, using a five-circle Huber goniometer. 22 keV incident X-rays (~0.59 Å wavelength) with a lateral beam spot size ~200 μm were illuminated on the LSCO channel area, and scattered X-rays were collected by a Pilatus II 100 K 2D pixeled area detector. While *operando* V_g sweeps were performed at 300 K (under flowing N_2), diffraction data were taken at 150 K (using a liquid-N_2-flow cryocooler) to minimize beam damage; each scan took ~30 min. To further mitigate potential beam damage, each scan was acquired on a fresh film spot, shifted by ~500 μm from the prior spot. Background subtraction employed a Matlab routine specific to the beamline. The structural refinement employed was developed for this work by Guichuan Yu and described in detail elsewhere [306]. Briefly, this involves a one-dimensional substrate-interface-film model and a newly developed constrained-phase-retrieval algorithm. The model describes the one-dimensional projected (averaged) electron density along the in-plane directions as a function of depth, for the film and substrate. The electron density of each atomic layer and the corresponding positions are determined by minimizing the mean-square error between the model-predicted and observed intensities.

5.2 I_{SD} *vs.* V_g hysteresis loops with complementary *operando* SXRD

Figs. 5.1(a),(b) present schematics of the P and BM crystal structures of LSCO, and the principle of operation of ion-gel-gated LSCO thin-film electrochemical transistors. Fig. 5.1(c) provides additional detail on the experimental setup, showing the device geometry, electrical wiring for transport measurements, and configuration for *operando* SXRD, as described in the preceding section. These devices are based on high-quality, epitaxial, single-phase, smooth LAO/LSCO(10 unit cell) films that have been extensively characterized [107,108,169,179,242,255,256]; their electronic/magnetic properties are among the best reported [107,108,169,179] at this thickness and strain state (–1.2%, compression). Importantly, LSCO films are in the P phase as-deposited [242,255,256,307], in contrast to $SrCoO_{3-\delta}$ gating studies, which start from as-deposited BM [97,117,124–133,178] due to the difficulty of stabilizing P $SrCoO_{3-\delta}$ under typical growth

conditions [112,118]. We estimate an initial $\delta \approx 0.14$ for these P LSCO films, using established methods based on comparisons of resistivity to bulk single crystals [169].

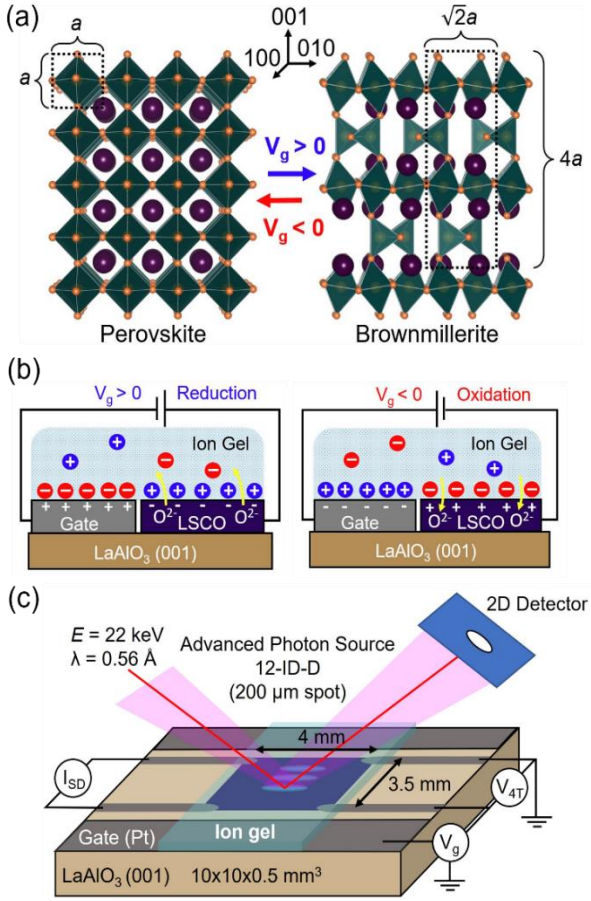

Figure 5.1: (a) Crystal structures of LSCO in perovskite (P, left) and brownmillerite (BM, right) phases. Purple spheres are La/Sr ions, gold spheres are O ions, and the CoO_6 octahedra and CoO_4 tetrahedra are shown in green. Note the quadrupling of the *c*-axis lattice parameter in the BM phase due to the V_O. (b) Schematic LSCO-based ion-gel-gate electrochemical transistor operating in both reduction ($V_g > 0$, left) and oxidation ($V_g < 0$, right) modes. (c) Schematic experimental device setup showing the $LaAlO_3$ substrate, LSCO channel, ion gel, Pt gate and film electrodes, incoming/outgoing synchrotron X-ray beam, source-drain current (I_{SD}), measured voltage for four-terminal measurements (V_{4T}), and gate voltage (V_g).

We begin the discussion of the primary results and analyses with Fig. 5.2(a), which shows a 300-K I_{SD}-V_g hysteresis loop for an ion-gel-gated 10-unit-cell LAO/LSCO film. This loop was recorded at a slow V_g sweep rate of 1 mV s^{-1} but was interrupted at the numbered points to record *operando* SXRD data. As discussed below, uninterrupted constant-sweep-rate loops provide substantial finer detail, but Fig. 5.2(a) nevertheless serves as a good starting point to discuss initial observations. The loop starts (Point 1) at

V_g = 0, in the as-deposited P phase, where I_{SD} at this source-drain voltage (0.1 V) is ~1 × 10^{-4} A. More extensive four-terminal transport data are discussed below, but we note for now that this corresponds to ρ ≈ 300 μΩ cm at 300 K, representative of high-quality 10-unit-cell LAO/LSCO films [107,108,169,179]. As V_g is increased, a reasonably well-defined threshold voltage of ~1 V is apparent [242], above which I_{SD} drops rapidly by orders of magnitude, before slowing at ~2 V (Point 2). I_{SD} then flattens by 3 V (Point 3), at which stage the V_g sweep direction was reversed. A more gradual increase of I_{SD} is observed at negative V_g (centered on ~-2 V), followed by saturation at –3 V (Point 5). Notably, returning V_g to zero (Point 6) results in substantially recovered I_{SD} but not to exactly the initial level (Point 1). Quantitatively, the ON/OFF I_{SD} ratio of this device on gating P → BM (at positive V_g) is ~9 × 10^3, whereas the ON/OFF I_{SD} ratio on gating BM → P (at negative V_g) is ~2 × 10^3, meaning that there is a factor of ~4 difference in I_{SD} between the initial (Point 1) and final (Point 6) states. As returned to below, this factor is only ~2 for ρ, meaning that a significant part of the I_{SD} decrease from Point 1 to Point 6 is contact-related (see Appendix B for further discussion of contact degradation).

SXRD data at Points 1 - 6 around the loop in Fig. 5.2(a) confirm that the above behavior results from P → BM → P cycling and clarifies the origin of the loop non-closure. Figs. 5.2(b)-(g) show specular (00*L*) SXRD scans centered on the LAO (002) reflection, *i.e.*, $\log_{10}$ intensity *vs*. *L* in substrate reciprocal lattice units (r.l.u.). At Point 1 (Fig. 5.2(b)), SXRD confirms high-quality smooth LAO(001)/LSCO. The primary reflection is just to the left of the LAO substrate (002), corresponding to an out-of-plane lattice parameter *a* = 3.89 Å, in good agreement with the 1.2% mismatch and LSCO Poisson ratio of ~1/3 [107,108]. Laue fringes are pronounced, consistent with high structural quality and low surface/interface roughness. By Point 2 at 1.9 V, however (Fig. 5.2(c)), the situation changes: The LSCO reflection near the substrate downshifts (indicating lattice expansion, consistent with V_O formation [176,242]), while clear BM (006) and (00$\underline{10}$) peaks emerge, indicating the quadrupling of the *c*-axis lattice parameter in the BM phase. The broad primary reflection in fact appears to have both P (002) and BM (008) components, consistent with prior observation of P/BM coexistence at intermediate voltages, implying a first-order transition [242]. By Point 3 (3.0 V, Fig. 5.2(d)), only BM (006), (008), (00$\underline{10}$),

and (00$\underline{12}$) peaks are apparent, indicating nominally phase-pure BM. Fig. 5.2(e) at Point 4 then shows that the BM is retained at -1.6 V, albeit with an upshift of the primary reflection, consistent with V_O annihilation. In contrast, at Points 5 and 6 in Figs. 5.2(f),(g) (–3.0 and 0.0 V, respectively), the primary features of BM are removed, leaving only the P (002) and associated Laue fringes. The SXRD data at Points 1 - 6 are thus qualitatively consistent with an interpretation of the hysteresis loop in Fig. 5.2(a) in terms of P → BM → P cycling, with P/BM phase coexistence at intermediate points. As an aside, we note that the BM in Figs. 5.2(c)-(e) is (00*L*)-oriented, *i.e.*, the alternating octahedral and tetrahedral Co-O layers (Fig. 1(a)) are in-plane. This is as in our prior work [242], independent of the strain state and V_g cycling; this is in contrast to some observations [132,308], for reasons that are not entirely clear.

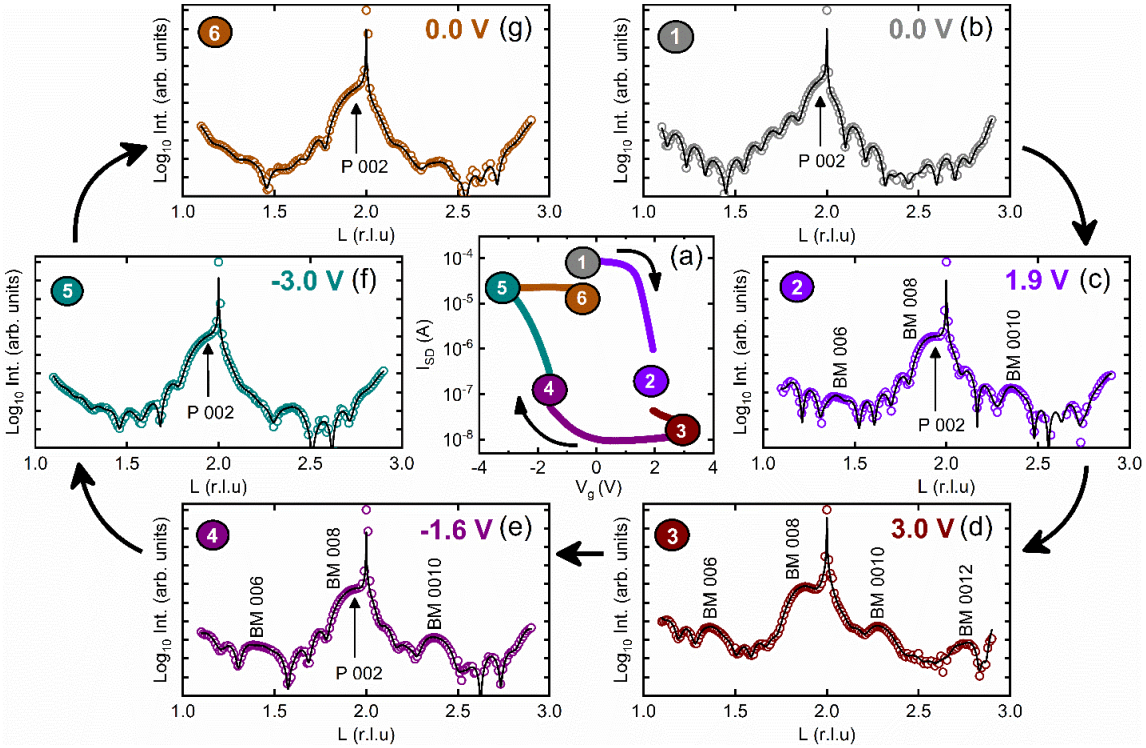

Figure 5.2*:* (a) Log_{10}-scale source-drain current (I_{SD}) *vs.* gate voltage (V_g) hysteresis loop from an ion-gel-gated 10-unit-cell-thick LSCO film. Gating was performed at 300 K, in N_2, at a sweep rate of 1 mV s^{-1}, and a source-drain voltage of 0.1 V. The colored and numbered circles represent points where the V_g sweep was paused, the device was cooled to 150 K, and synchrotron X-ray diffraction (SXRD) scans were collected; the device was then warmed to 300 K and the process repeated. (b)-(g) *Operando* specular (00*L*) SXRD scans around the $LaAlO_3$ substrate (002) reflection at the points 1 - 6 labeled in (a); these correspond to V_g = 0.0, 1.9, 3.0, –1.6, –3.0 and 0.0 V, respectively. Open circles are data points while the solid lines are refinements. Perovskite (P) and brownmillerite (BM) peaks are labeled. Reciprocal lattice units (r.l.u.) are based on the substrate. Black arrows illustrate the sweep direction.

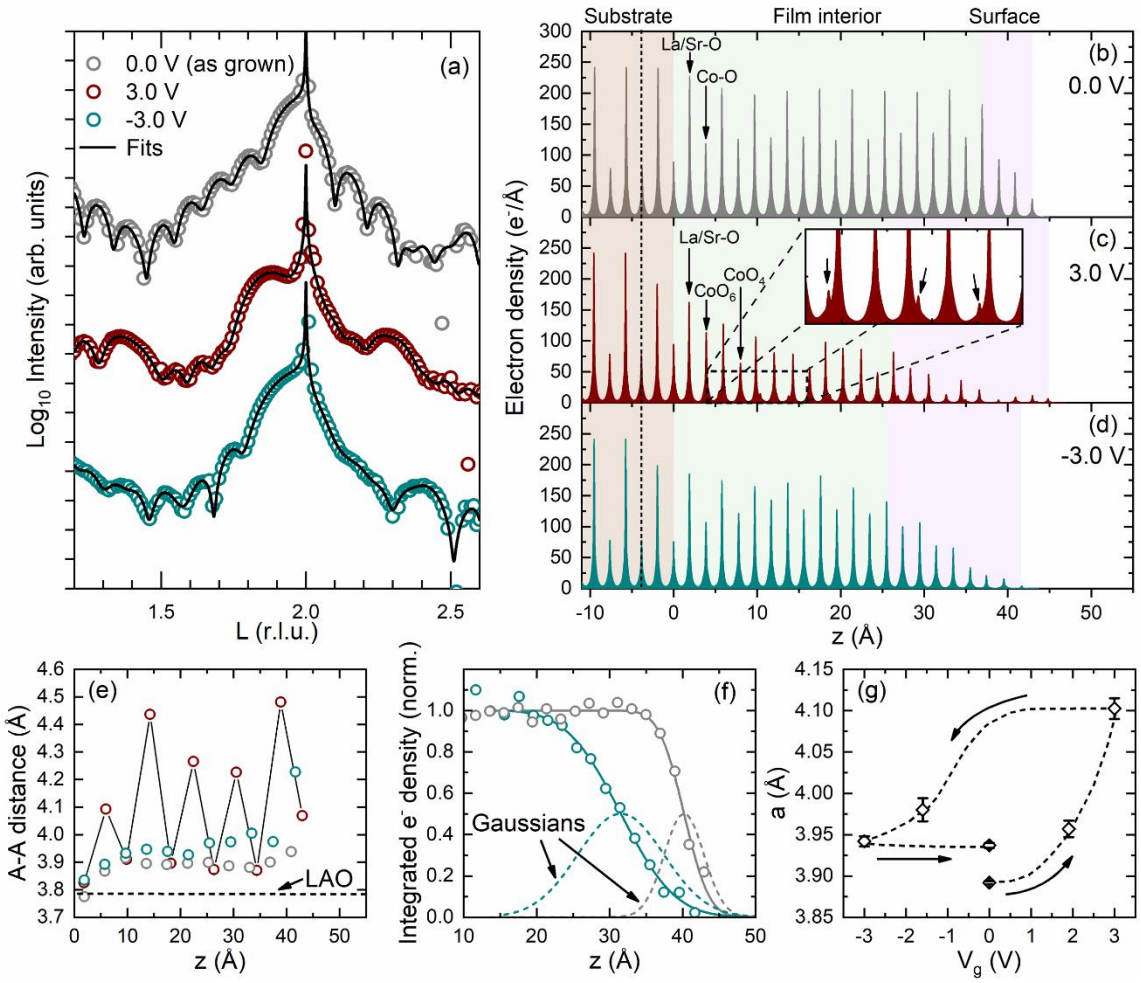

Figure 5.3: (a) *Operando* synchrotron X-ray diffraction (SXRD) data (open points) and refinements (black lines) at selected gate voltages (V_g): 0.0 V (as-deposited, grey), 3.0 V (maroon), and –3.0 V (green), as in Figs. 2(b),(d),(f). Reciprocal lattice units (r.l.u.) are based on the substrate. (b)-(d) Electron density *vs*. depth (*z*) profiles extracted from the refinements in (a), at 0.0 V (as-deposited, grey), 3.0 V (maroon), and –3.0 V (green). The substrate (light brown), LSCO film interior (light green), and LSCO film surface region (pink, from the first atomic plane above which significant drops in electron density occur) are labeled, and the vertical dashed line marks the start of the refined range. In the LSCO, the more intense peaks are the La/Sr-O layers, while the less intense peaks are Co-O layers. The inset in (c) highlights the features due to brownmillerite. (e) Depth dependence of the A-site-to-A-site vertical distance extracted from (b)-(d), using the same V_g color scheme. The dashed line corresponds to the substrate ($LaAlO_3$ (LAO)) value. (f) Electron density normalized to the film interior *vs*. depth (*z*) for the 0.0 V (as-deposited perovskite) and –3.0 V (gated back to perovskite) cases. The solid curves are Gaussian distributions of film thickness illustrating the different surface locations and roughness. (g) Extracted out-of-plane lattice parameter (*a*) *vs*. V_g. Black arrows illustrate the sweep direction, and the dashed line is a guide to the eye. The error bars represent the standard deviation of the mean value of the A-site-to-A-site distance in the film interior.

In terms of understanding the loop non-closure in Fig. 5.2(a), *i.e.*, the inequivalence of Points 1 and 6, it is noteworthy that the SXRD scans in Figs. 5.2(b) and (g) are different. The primary LSCO P (002) reflection in (g) is broader and less intense than in (b), and the Laue fringes are less pronounced and wider-spaced. This immediately suggests that the high epitaxial quality in the as-deposited P state is reduced after the first P → BM → P cycle. Although the P ↔ BM transformation is topotactic, this is perhaps unsurprising. Deeper insight is provided by quantitative analysis of SXRD data. This was achieved through a structural refinement based on a newly developed constrained phase-retrieval algorithm [306]. This procedure refines the one-dimensional, laterally averaged, layer-by-layer electron density profile as a function of depth through the film and substrate. Example refinements are shown in close-up in Fig. 5.3(a) for the $V_g = 0$ (as-deposited), 3.0 V, and –3.0 V cases, as in Figs. 5.2(b),(d),(f). The open points here are data, and the solid lines are refinements, which describe the data very well (as in Figs. 5.2(b)-(g)). Figs. 5.3(b)-(d) show the corresponding extracted depth (z) profiles of the electron density. At $V_g = 0$ (Fig. 5.3(b)), the determined structure is near-ideal, with a sharp LAO/LSCO interface, uniform electron density in the LSCO interior (with alternating La/Sr-O and Co-O layers), and a low-roughness top surface. The extracted root-mean-square (RMS) roughness is 2.7 ± 0.3 Å, resulting in a surface region (pink background in Figs. 5.3(b)-(d), shown as the first atomic plane above which a significant drop in electron density occurs) of ~2 unit cells.

At $V_g = 3.0$ V (Fig. 5.3(c)), as expected, the refined depth profile is much different. First, the electron densities of the atomic planes in the film interior are distinctly suppressed relative to Fig. 5.3(b), and a subtle two-peak structure develops on the La/Sr-O planes (inset to Fig. 5.3(c)). We ascribe the overall electron density decrease to diminished coherence of the BM phase relative to the as-deposited P film, likely due to formation of multiple BM domains during topotactic reduction. The two-peak structure in the inset is expected in BM, due to the non-coplanar O^{2-} ions (Fig. 5.1(a)). Associated with this, the inter-A-site distance oscillates *vs*. depth, due to the alternating octahedrally and tetrahedrally coordinated Co-O layers. This is shown in Fig. 5.3(e), where the depth profile of the A-A distance clearly oscillates in the $V_g = 3.0$ V (*i.e.*, BM) case, in contrast with the $V_g = 0$ and –3.0 V (*i.e.*, P) cases. In the latter cases there is only a weak increase in A-A distance towards the surface,

potentially reflecting a mild compositional gradient. The conclusion of nominally phase-pure BM at 3.0 V is thus supported by not only the BM peaks in Figs. 5.2(d) and 5.3(a), but also the details of the depth profile. Another observation from the V_g = 3.0 V data (Fig. 5.3(c)) is that the LSCO surface roughness is higher in the BM phase. The RMS surface roughness in fact increases to 6.7 ± 1.2 Å, generating a surface region (pink background) of ~4 pseudocubic unit cells. Finally, we note that some of the findings at 3.0 V depend on an assumption in the refinement, specifically whether the first LSCO layer (at the substrate interface) is octahedral or tetrahedral Co-O. Based on prior literature [309,310], we assume octahedral CoO_6.

Fig. 5.3(d) moves to V_g = –3.0 V, in the recovered P state, revealing several differences from the as-deposited P state (Fig. 5.3(b)). First, the electron density in the LSCO interior, particularly on La/Sr-O planes, does not fully recover after the BM → P transformation, very likely reflecting that oxidation from the multi-domain BM state results in a lower structural coherence P phase compared to as-deposited. Second, there are striking changes near the surface. The surface region (pink background in Fig. 5.3(d)) not only broadens relative to Fig. 5.3(b) but also shifts to lower *z*, indicating decreased thickness. This is illustrated in Fig. 5.3(f), where the integrated electron density of each atomic layer is plotted (normalized to the interior) *vs. z*, comparing the V_g = 0 and –3.0 V cases. P → BM → P cycling is seen to decrease the thickness from 40.2 to 31.5 Å, simultaneously increasing the RMS roughness from 2.7 ± 0.3 to 5.9 ± 0.4 Å. These points are further emphasized by the solid lines in Fig. 5.3(f), which show Gaussian distributions of thickness based on the shown density profiles at 0 and –3.0 V. The ~2 unit cell decrease in LSCO thickness may seem surprising, but is likely simply due to mild etching at large positive V_g; this is known in electrolyte gating [172,179,311], including of oxides [172,179], and LSCO [179]. This is thought to be due to electrochemical splitting of residual H_2O in ionic liquids/gels, generating H^+ ions that acid etch the film at large positive V_g, decreasing thickness and increasing roughness [179]. Such effects are more noticeable here in very thin films compared to the majority of studies at 10 - 50 nm.

As a final finding from *operando* SXRD, Fig. 5.3(g) shows the extracted out-of-plane lattice parameter, *a*, around the first P → BM → P cycle. As noted in connection

with Fig. 5.1(b), the V_g = 0 as-deposited a = 3.89 Å is as-expected based on the strain state on LAO [107,108,176,242,255]. As V_g is increased, V_O formation leads to a rapidly increasing above ~1 V, reaching 4.10 Å at 3.0 V in the BM phase, consistent with prior work [242]. (This is a pseudocubic lattice parameter here, *i.e.*, ¼ of the BM out-of-plane lattice parameter). Decreasing V_g then decreases a due to V_O annihilation, reaching $a \approx 3.94$ Å in the recovered P phase at –3.0 and 0 V. The slight (1.2%) difference in lattice parameters between the as-deposited and recovered P states is consistent with the above findings, highlighting that, in addition to lower structural quality than the as-deposited film, the δ of the cycled P film is also slightly larger. Based on the known $a(\delta)$ in the P phase of LAO/LSCO [169,176,242], we estimate a final δ of 0.19, compared to the initial 0.14.The loop non-closure in Fig. 5.2(a) thus results from a combination of factors in the cycled P film, including slightly larger δ, reduced structural coherence, and increased roughness.

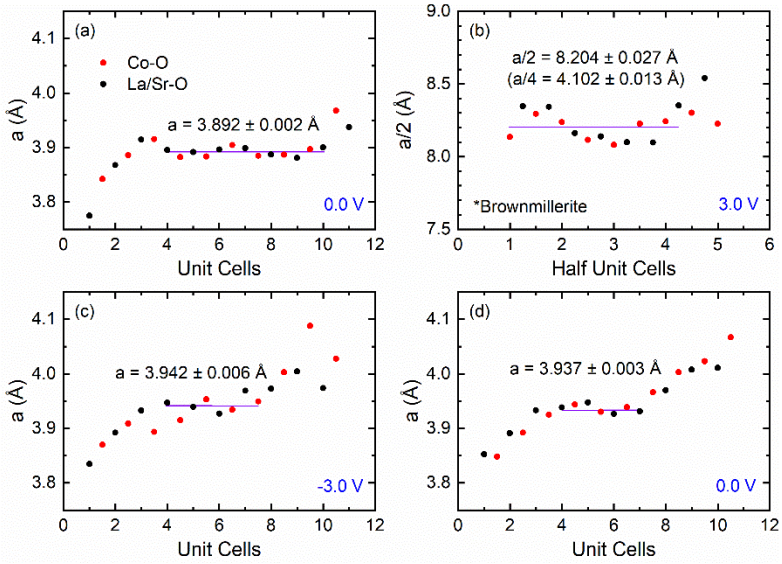

Figure 5.4: Shown are the depth (z) profiles (in unit cells) of the local out-of-plane lattice parameters (a) for a 10-unit-cell-thick LSCO film ion-gel-gated to 0 V (a), 3.0 V (b), –3.0 V (c), then back to 0 V (d). The data points are the distances between adjacent La/Sr-O (black circles) and Co-O (red circles) peaks, taken from refined electron density profiles such as those in Figs. 3(b)-(d). The solid purple horizontal lines represent the average value of a in the interior of the LSCO, as determined from the range of points spanned by the line (the resulting a values and standard deviations are shown).

To add more context to the discussion of the out-of-plane lattice parameter as a function of V_g, Fig. 5.4 shows the depth-dependent atomic spacing (between adjacent La/Sr-O and Co-O peaks, respectively, in the refined electron density profiles) at different V_g, from which a (in Fig. 5.3(g)) was extracted. The 0 V (as-deposited) data in Fig. 5.4(a)

indicate quite uniform *a* with depth. At 3.0 V Fig. 5.4(b), the structure is now BM, featuring a quadrupling of the perovskite cell (hence the different *x*- and *y*-axis labels). The average *a*/4 lattice parameter at 3.0 V is ~4.10 Å, again in good agreement with previous reports for BM LSCO on LAO [242]. Fig. 5.4(c) and (d) then show the recovered P phase after gating to –3.0 V and back to 0 V, respectively. In the recovered P, the LSCO lattice remains somewhat expanded compared to the as-deposited film, and the expansion at the surface is significantly increased, likely due to induced non-stoichiometry, *e.g.*, δ.

5.3 Detailed analysis of the continuous I_{SD} *vs.* V_g hysteresis loop

With the main features of the I_{SD} *vs.* V_g hysteresis loop in Fig. 5.2(a) understood in terms of structural insights from quantitative *operando* SXRD, we turn to additional insights revealed by *uninterrupted* constant-sweep-rate hysteresis loops. Fig. 5.5(a) shows a typical loop, recorded at 300 K, 1 mV s^{-1} sweep rate, and 0.1 V source-drain voltage. Similar to Fig. 5.2(a), I_{SD} starts at ~1×10^{-4} A in the as-deposited P phase; this corresponds to $\rho \approx 300$ μΩ cm at 300 K (and $\rho \approx 150$ μΩ cm at 10 K), representative of high-quality 10-unit-cell LAO/LSCO [107,108,169,179]. While the main features of Fig. 5.2(a) are retained in Fig. 5.5(a), such as the clear P → BM and BM → P transitions (at positive and negative V_g, respectively), and the loop non-closure, interesting new features emerge in constant-sweep-rate loops. First, the P → BM transformation at positive V_g completes more abruptly (between ~1.5 and ~2.5 V) than the BM → P transition at negative V_g (between ~0.5 and ~-2.5 V), leading to distinctly asymmetric loops. Second, there emerge obvious shelf features on the right and left sides of the loop, which are sharp on the right and broader on the left. Along with these unusual features, the peak ON/OFF I_{SD} ratio reaches almost 10^5, comparable to the best reported in electrochemically gated cobaltites [97,132,242,256,307]. Fig. 5.5(b) highlights and quantifies these observations by plotting the V_g dependence of a logarithmic derivative of I_{SD}, *i.e.*, $d\log_{10}(I_{SD})/|dV_g|$. This reveals two sharp, closely spaced, negative peaks at positive V_g, along with two broader, further-spaced positive peaks at negative V_g. The minima (maxima) in the logarithmic derivative between these peaks reflect the shelf features in Fig. 5.5(a), while the larger spacing between the peaks at negative V_g reflects the asymmetry in Fig. 5.5(a). The corresponding $I_g(V_g)$ loop in Fig. 5.5(c) reveals a broad positive-V_g peak centered on the

two sharp peaks in the logarithmic derivative in Fig. 5.5(b), along with two broader negative-V_g peaks aligned with the broader peaks in the logarithmic derivative in Fig. 5.5(b). The alignment of these features is highlighted by the vertical dotted lines in Fig. 5.5. In Fig. 5.5(c) the features are superimposed on the typical increases in the magnitude of I_g at the extremes of V_g (particularly negative V_g), which indicate the approach to the limits of the electrochemical stability window [147,149].

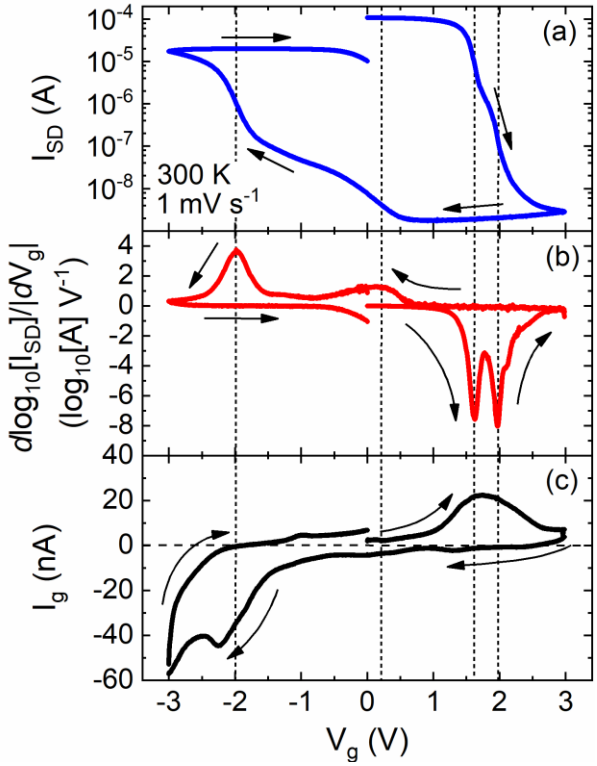

Figure 5.5: (a) Log_{10}-scale source-drain current (I_{SD}) *vs*. gate voltage (V_g) hysteresis loop from an ion-gel-gated 10-unit-cell-thick LSCO film. Gating was performed at 300 K, in vacuum ($< 1 \times 10^{-5}$ Torr), at a sweep rate of 1 mV s^{-1}, and a source-drain voltage of 0.1 V. (b) Corresponding logarithmic derivative of I_{SD} *vs*. V_g, *i.e.*, $d\log(I_{SD})/|dV_g|$. (c) Corresponding gate current (I_g) *vs*. V_g. Black arrows illustrate the sweep direction. Vertical dashed lines mark the features in the data described in detail in the text.

Based on current understanding of the voltage-driven P → BM → P topotactic phase transformation in gated cobaltite films, we provide simple interpretations of the phenomena in Fig. 5.5. First, we believe that the distinct V_g asymmetry in Figs. 5.5(a),(b) simply reflects the known differences in mass transport dynamics between P → BM and BM → P transformations [96]. Due to the one-dimensional V_O channels in the O-deficient planes of BM LSCO (Fig. 5.1(a)), the dimensionality for O diffusion is distinctly reduced compared to the three-dimensional situation in V_O-disordered P LSCO. Consequently, the

kinetics of the oxidative transformation from BM to P should be slower than the reductive transformation from P to BM, which we propose results in the V_g asymmetry in Figs. 5.5(a),(b). Both experimental and theoretical literature supports this interpretation. X-ray photon correlation spectroscopy on thermally transforming $SrCoO_{3-\delta}$, for example, evidences one-dimensional ionic migration processes from BM → P, in contrast to three-dimensional processes from P → BM [96]. Calculations of activation energies for migration of O defects also yield minimum values of only 0.5 - 0.6 eV in the P phase of $SrCoO_{3-\delta}$, compared to a more anisotropic 0.6 - 0.8 eV in the BM phase [94,95].

Second, with respect to the shelf features in Fig. 5.5(a) that generate the split peaks in Fig. 5.5(b), we believe the key factor is the first-order nature of the P ↔ BM transformation [96,113,242]. Specifically, we interpret these features not as twin peaks *per se*, but in terms of a region of anomalously low transformation rate in the middle of the transformation. We believe this occurs as the system enters the P/BM coexistence regime, where additional work must be done to propagate P/BM phase boundaries before a single-phase state can be reached. Using positive V_g as an example, reduction commences at 1.0 - 1.5 V in Fig. 5.5, with the formation of V_O in the P phase, reaching a maximum transformation rate shortly thereafter. At this point, BM regions appear, resulting in P/BM coexistence, slowing the transformation due to the work needed to propagate P/BM boundaries to expand the BM domains. As these boundaries are extinguished, and phase-pure BM is approached, the transformation rate again peaks, before the final stage of reduction and V_O ordering in phase-pure BM. These processes occur in reverse at negative V_g, but with smaller, broader, wider-spaced peaks in Fig. 5.5(b) due to the abovementioned asymmetry in D_{Vo} in P and BM phases. Similar features then arise in Fig. 5.5(c), particularly peaks in electrochemical gate current when the P ↔ BM transformation rates peak. Such details of the P ↔ BM transformation mechanism in electrolyte-gated cobaltite films have not been previously detected, highlighting the power of V_g hysteresis loops.

5.4 Minor hysteresis loop analysis: Design of an optimized V_g cycle

There exist a number of powerful methodologies to probe hysteretic phenomena in condensed matter systems, not yet applied to V_g hysteresis in these types of electrochemical

transistors. Perhaps the simplest is *minor* hysteresis loops, which are explored in detail for ion-gel-gated LAO/LSCO(10 unit cell) in Fig. 5.6. Shown in Fig. 5.6(a) is a series of 300-K minor $I_{SD}(V_g)$ loops recorded by sweeping from $V_g = 0$ to varied maximum positive V_g (labeled next to each curve), then back to a constant minimum V_g of –4.0 V. The first striking observation is that the curves trace essentially the same trajectory at positive V_g, exhibiting a sharp decrease beyond ~1 V (due to reduction of P LSCO), the now familiar shelf at intermediate V_g (across the P → BM transformation), then saturation at low I_{SD} beyond ~3 V (the ON/OFF ratio again reaches ~10^5 as phase-pure BM is reached). In stark contrast, the recoil trajectories when the V_g sweep is reversed depend strongly on the maximum positive V_g. When the maximum V_g is only 1.5 V, the recoil trajectory is initially roughly horizontal to ~-1.5 V, below which I_{SD} recovers to almost exactly its initial (V_g = 0) value. This is therefore a highly reversible cycle in terms of initial and final I_{SD}, but with an ON/OFF ratio of only 4×10^1, likely involving little BM formation/annihilation. As the maximum V_g is increased to 2.0 - 3.0 V, somewhat similar behavior prevails, an initially roughly horizontal recoil trajectory occurring prior to substantial recovery of I_{SD} at negative V_g. The I_{SD} ON/OFF ratio progressively increases (to 1×10^5 at a maximum V_g of 3.0 V), indicating a full P → BM transition, at the cost of relatively modest decreases in recovery in terms of initial and final I_{SD}. At maximum $V_g \geq 3.5$ V, however, while marginal additional gains in ON/OFF ratio are achieved, these come at the cost of dramatic decreases in recovery. By 3.5 V, for example, I_{SD} at –4.0 V reaches only 10^{-6} A, a factor of $>10^2$ below the initial I_{SD}. By 4.0 V maximum V_g, the recovery at negative V_g is negligible. As this progression occurs, the $I_g(V_g)$ curves (Fig. 5.6(b)) reveal broad peaks at positive V_g centered on the P → BM transformation (as in Fig. 5.5(c)), but with larger changes at negative V_g. Specifically, larger maximum V_g generally leads to a larger magnitude, steeper I_g at negative V_g, indicating large electrochemical currents.

Fig. 5.6(c) summarizes these results by plotting the ON/OFF ratio (left axis, black points) and the recovery ratio (right axis, blue points) *vs*. the maximum positive V_g applied. The ON/OFF ratio is defined as I_0/I_{min}, where I_0 is the initial ($V_g = 0$) I_{SD} and I_{min} is the minimum I_{SD} at positive V_g. The recovery ratio is defined as I_{max}/I_0, where I_{max} is the maximum recovered I_{SD} at negative V_g. Ideal behavior thus corresponds to the largest

possible ON/OFF ratio at a recovery ratio close to unity. What is found in Fig. 5.6(c) is instead a clear compromise. At higher maximum V_g the ON/OFF ratio can be driven above 10^5, even approaching 10^6, but at the cost of diminishing recovery, particularly above 3 V. The light blue shaded region at 2 - 3 V thus defines the optimal maximum V_g, realizing ON/OFF ratios near 10^5 with recovery ratios up to ~0.6 (60%).

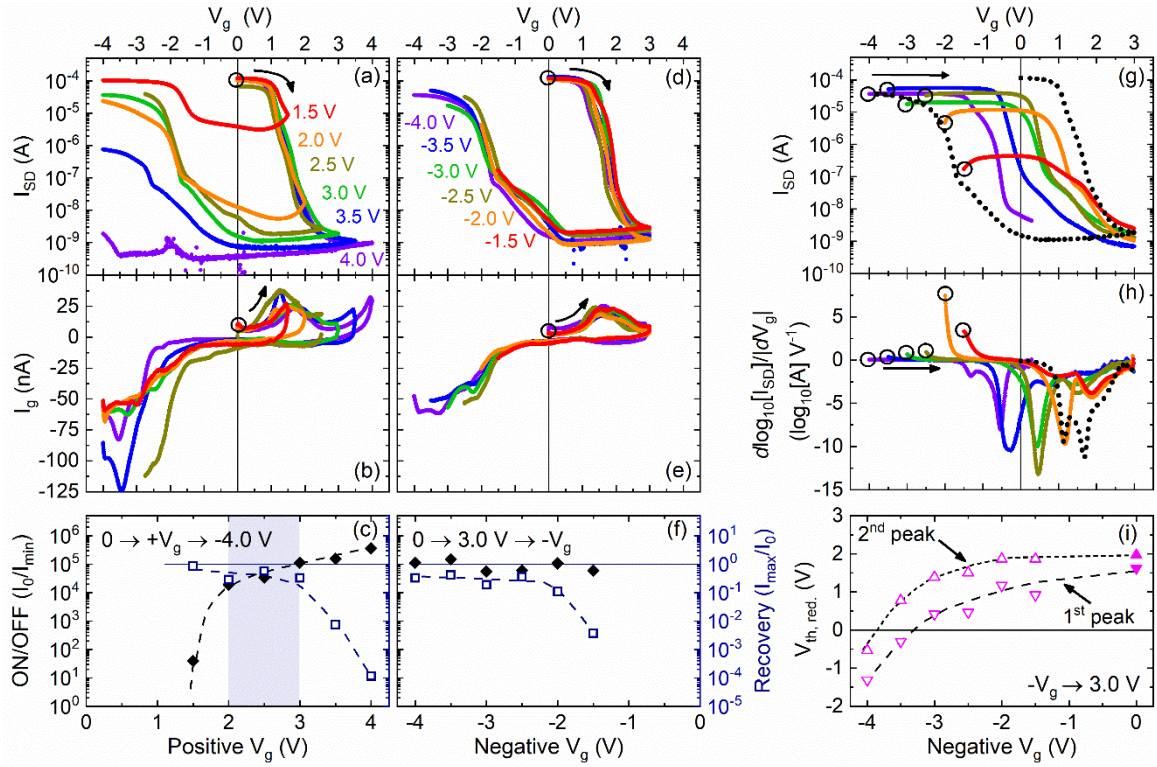

Figure 5.6: (a)-(c) Minor hysteresis loops with fixed minimum (negative) V_g (–4.0 V) but varied maximum (positive) V_g (1.5 to 4.0 V, in varied colors). Plotted are the V_g dependences of (a) the source-drain current (I_{SD}) on a $\log_{10}$ scale, (b) the gate current (I_g), and (c) the current ON/OFF ratio (black, left axis) and current recovery ratio (blue, right axis). (d)-(f) Minor hysteresis loops with fixed maximum (positive) V_g (3.0 V) but varied minimum (negative) V_g (–1.5 to –4.0 V, in varied colors). Plotted are the V_g dependences of (d) I_{SD} on a $\log_{10}$ scale, (e) I_g, and (f) the current ON/OFF ratio (black, left axis) and current recovery ratio (blue, right axis). The ON/OFF ratio is defined as I_0/I_{min}, where I_0 is the initial (V_g = 0) value of I_{SD} and I_{min} is the minimum value (at any V_g > 0) of I_{SD}. The recovery ratio is defined as I_{max}/I_0, where I_0 is the initial (V_g = 0) value of I_{SD} and I_{max} is the maximum value (at any V_g < 0) of I_{SD} after cycling from positive to negative V_g. (g),(h) Increasing V_g sweeps (varied colors) after sweeping from 0 V to 3.0 V, to varied negative voltages. Plotted are the V_g dependences of (g) I_{SD} on a $\log_{10}$ scale and (h) $d\log(I_{SD})/|dV_g|$. The dotted black line is a major hysteresis loop for reference. Shown in (i) are the dependences of the threshold voltages for reduction ($V_{th,red}$), defined by the peaks in (h), on the magnitude of the minimum (negative) V_g All data were taken at 300 K, in vacuum (< 1×10^{-5} Torr), at a sweep rate of 1 mV s^{-1}, and a source-drain voltage of 0.1 V. Black circles and arrows indicate the starting points of the highlighted loops and the sweep directions, respectively. In (c),(f) the blue horizontal lines mark ideal recovery, *i.e.*, a recovery ratio of 1.

Complementary to Fig. 5.6(a), Fig. 5.6(d) shows $I_{SD}(V_g)$ minor loops recorded with a constant maximum V_g of 3.0 V, but varied minimum (negative) V_g, from –1.5 to –4.0 V. The positive V_g curves are tightly consistent, as are the corresponding I_g behaviors in Fig. 5.6(e). The threshold, shelf, and saturation effects again arise in $I_{SD}(V_g)$, accompanied by broad peaks in $I_g(V_g)$, as explained above. Interestingly, the various traces also overlap at negative V_g. Decreasing minimum V_g thus leads to increased recovery while maintaining the 10^5 ON/OFF ratio set by the maximum V_g = 3.0 V. This is illustrated in Fig. 5.6(f), where the recovery ratio increases as the minimum (negative) V_g is decreased, then saturates at < –2.5 V. These data thus suggest that all minimum V_g values below –2.5 V result in optimal recovery to the P state. Further analysis, however, reveals another factor. Figs. 5.6(g),(h) illustrate what evolves in I_{SD} when devices are cycled from 0 to 3.0 V, to varied minimum (negative) V_g, then back to positive V_g to induce a *second* P → BM transformation. The open circles here label the minimum V_g for each loop. The data reveal a new phenomenon, where the threshold V_g at which I_{SD} begins to decrease on the *second* cycle progressively decreases with the minimum (negative) V_g applied during the first cycle. By the time the blue curve is reached, for example (minimum V_g = –3.5 V), the threshold V_g on the second cycle has shifted to *negative* voltage, indicating substantial reduction from P to BM even at V_g = 0. By a minimum applied V_g of –4.0 V (purple), the second-cycle P → BM transformation appears to be near-complete by V_g = 0. It must be emphasized that such behavior corresponds to a loss of non-volatile retention of the P (ON) and BM (OFF) states at V_g = 0, which would be undesirable for some applications. Fig. 5.6(h) shows that the second-cycle P → BM transformations are again marked by two peaks in the logarithmic derivative (as in Fig. 5.5(b)), the positions of which are plotted *vs.* minimum (negative) V_g on the first cycle in Fig. 5.6(i). The threshold voltages are approximately constant (and positive) down to –2 V. At lower minimum V_g, however, they decrease, switching sign below ~-3.5 V. To avoid this inversion in threshold voltage on the second cycle, the minimum (negative) V_g applied should thus be above ~-3.5 V. In totality, the analyses of minor loops in Fig. 5.6 thus quantitatively establish the optimal operating range of ion-gel-gated LSCO for the first time, at approximately –3.5 V < V_g < 3.0 V. This range ensures large enough maximum V_g to obtain high ON/OFF ratio at workable recovery

ratio, while the minimum V_g is large enough to avoid threshold voltage inversion on the second cycle.

At the highest level, the above analysis of minor $I_{SD}(V_g)$ loops simply establishes a general finding that is highly analogous to more extensively studied electrochemical devices such as Li-ion batteries [312]. Specifically, limits on voltages must be adhered to for maximal cyclability [313], in order to avoid over-oxidation and over-reduction of the electrodes, in this case specifically LSCO. Deeper understanding of the specifics of the origins of the over-oxidation and over-reduction phenomena in LSCO electrochemical transistors are more challenging and require separation of effects in the LSCO, the electrolyte, and their interface. With respect to the limit on the maximum (positive) V_g that can be applied (Figs. 5.6(a)-(c)), we believe that the LSCO itself is not the limiting factor. Multiple observations, including optical inspection of failed devices and lower recovery ratios in I_{SD} compared to ρ (discussed above with Figs. 5.2(a) and 5.5(a) and returned to with Fig. 5.7(a) below), in fact indicate that device factors, particularly contact degradation [314], are the central issue. Further work could thus realize substantial improvements through better device design. With respect to the limit on the minimum (negative) V_g that can be applied, conversely, we believe that the LSCO may be the limiting factor. As shown in Fig. 5.6(g), application of negative V_g below this limit does not prevent reduction to BM on the second cycle, indicating that the devices continue to function. Large negative V_g instead likely over-oxidizes $x = 0.5$ LSCO to the point that the mean Co valence reaches the limits of stability of a 10-unit-cell film at ambient conditions [179,242], making V_O formation spontaneous as the V_g sweep direction is reversed, as in the blue and purple curves in Fig. 5.6(g). This is the same phenomenon detected in earlier work through cruder voltage-step measurements [179,242]. Another possible cause, however, could be electrochemical degradation of anions in the ion gel ($TFSI^-$ in this case), which may breakdown at lower V_g magnitudes than the cations (EMI^+) [315,316]. This would result in a shift of the charge neutral point to lower (*i.e.*, negative) V_g; further study is needed to decouple these possible effects.

5.5 Reversibility of electronic and magnetic properties

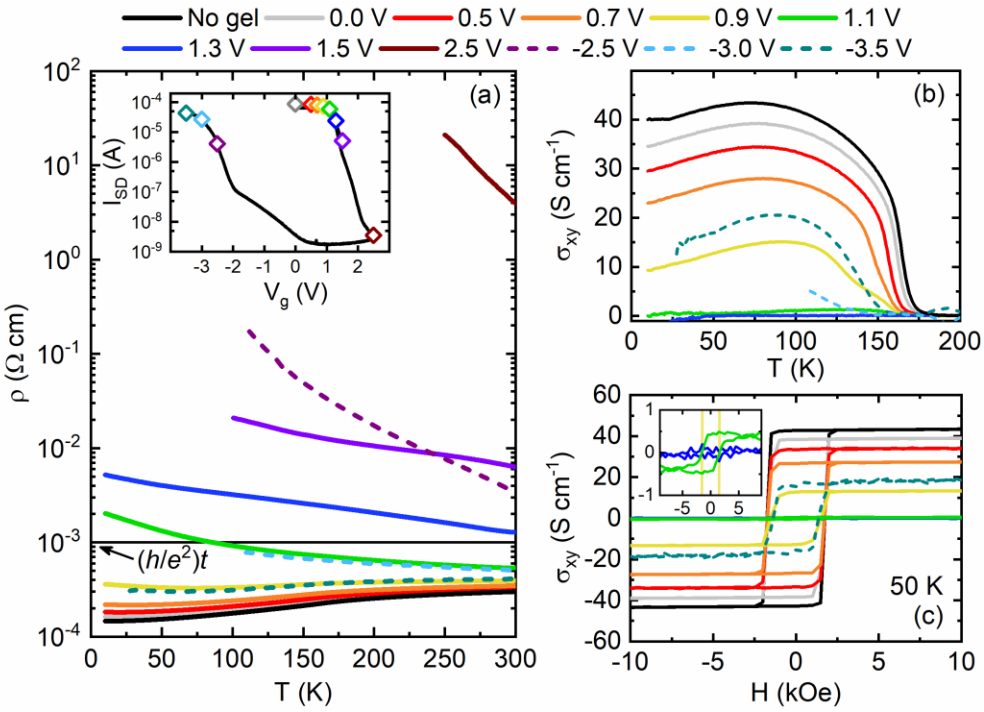

Figure 5.7: (a) Temperature (T) dependence of the resistivity (ρ) of a 10-unit-cell-thick LSCO film at various gate voltages (V_g) around the 300-K hysteresis loop shown in the inset. The hysteresis loop plots the source-drain current (I_{SD}) *vs.* V_g (solid black line), with the various V_g values in the main panel highlighted by points, which are color coded with the main panel (and defined at the top of the figure). In the main panel, solid lines are for increasingly positive V_g (P → BM), dashed lines are for increasingly negative V_g (BM → P). The horizontal black line marks the quantum resistance multiplied by the film thickness, *i.e.*, ht/e^2, where h is Planck's constant, e is the elementary charge, and t is film thickness. (b) Corresponding T-dependence of the transverse (Hall) conductivity (σ_{xy}) at the same V_g as in (a). (c) Corresponding 50-K magnetic field (H) dependence of σ_{xy} at the same V_g as in (a),(b). The inset to (c) is a zoomed-in view of the solid green and blue data, at 1.1 and 1.3 V, showing the vanishing of the anomalous Hall effect in the BM phase. For accuracy, in all parts of this figure, data after gating to the BM phase were treated using the reduced thickness determined from Fig. 5.3.

With the optimal parameters for V_g cycling established, Fig. 5.7 moves to probing magnetotransport and magnetic properties of ion-gel-gated LAO/LSCO(10 unit cell) films around the P → BM → P cycle. The inset to Fig. 5.7(a) first shows a typical 300-K $I_{SD}(V_g)$ loop, from 0 V → 2.5 V → –3.5 V, *i.e.*, within the determined optimal range. The colored points on the loop indicate voltages at which the loop was paused and the device cooled, to perform ρ(T) and Hall effect measurements, before rewarming and continuing the V_g sweep. As shown in the main panel of Fig. 5.7(a), the initial (V_g = 0) state of these LAO/LSCO(10 unit cell) films corresponds to state-of-the-art metallic ρ(T) (black line)

with a residual resistivity ratio of 2.0 [169,179]. The low-ρ (< 10^{-3} Ω cm) portion of Fig. 5.7(a) is replotted in Fig. 5.8(a) (along with $d\rho/dT$ in Fig. 5.8(b),(c)) for selected V_g, to more easily discern the subtle features. These include the inflection point at ~165 K in ρ(T) (shown as a peak in $d\rho/dT$ in Fig. 5.8(b)) for V_g = 0, marking T_C [108,169,179], which is comparable to the best reports at this thickness [107,108,169,179]. As V_g is increased to 0.9 V (yellow, in Fig. 5.7 and 5.8), weakly metallic behavior persists, but with increased residual resistivity, consistent with increased δ in the P phase. In addition, the peak in $d\rho/dT$ (Fig. 5.8(b)) is markedly reduced, and even appears to split at V_g = 0.9 V, implicating two distinct T_C values. This situation changes at 1.1 V (green line) where ρ(T) becomes insulating and $\rho(T \rightarrow 0)$ exceeds the quantum resistance multiplied by thickness, $(h/e^2)t$ (black horizontal line in Fig. 5.7(a)). This indicates a metal-insulator transition, very close to the point at which the sharp decrease in I_{SD} occurs in the inset of Fig. 5.7(a), and to the point at which the first BM forms (from Figs. 5.2 - 5.6). Interestingly, from the plot of $d\rho/dT$ *vs.* T in Fig. 5.8(c), despite predominantly insulating behavior ($d\rho/dT$ < 0 at all T), there remains an inflection point near ~150 K for V_g = 1.1 V, indicating some portion of the film is still F. This provides yet further evidence for the mixed-phase state of the film at this V_g.

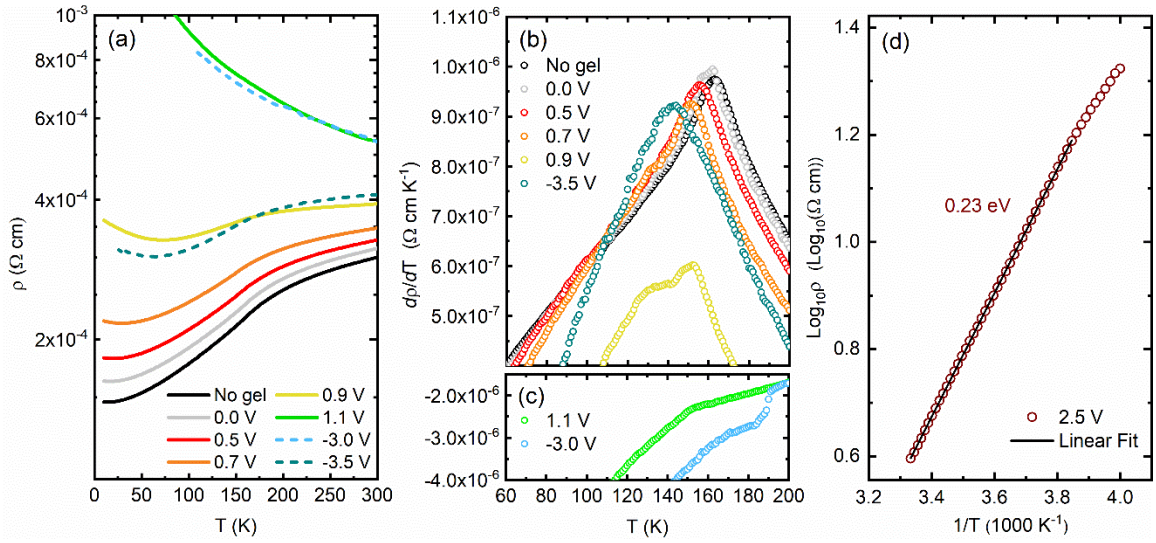

Figure 5.8: (a) Temperature (T) dependence of resistivity (ρ) in the low-resistivity region (replotted from Fig. 5.7(a)), (b) the corresponding $d\rho/dT$ at selected V_g, and (c) the equivalent $d\rho/dT$ at 1.1 and –3.0 V. All data are on the same 10-unit-cell-thick LSCO device shown in Fig. 5.7, gated to various V_g (see inset of Fig. 5.7(a)). (d) ρ on a $\log_{10}$ scale *vs.* inverse temperature ($1/T$) for the same film ion-gel-gated to 2.5 V to generate nominally phase-pure insulating brownmillerite.

At larger V_g, progressively more insulating behavior evolves, eventually reaching the brown (2.5 V) line in Fig. 5.7(a), where the 300-K ρ is 1.3×10^4 higher than the initial state, and ρ rapidly increases on cooling; this corresponds to nominally phase-pure BM. The insulating behavior of the film in the at $V_g = 2.5$, in the BM state, is expounded in Fig. 5.8(c), where a plot of $\log_{10}\rho$ *vs.* $1/T$ evidences Arrhenius behavior, with an activation energy of ~0.23 eV. At intermediate V_g (specifically $V_g = 1.3$ and 1.5, blue and purple in Fig. 5.7(a)) the forms of $\rho(T)$ are somewhat unusual due to P-BM coexistence and thus inhomogeneous transport [242,255]. The dashed lines in Fig. 5.7(a) then show the evolution in $\rho(T)$ on gating back to the P state, *i.e.* sweeping back to negative V_g. Close-to-metallic transport first emerges at –3.0 V (light blue dashed line), followed at –3.5 V (dark green dashed line) by metallic behavior. The latter is unambiguous, from finite $\rho(T \rightarrow 0)$, $\rho < (h/e^2)t$, and the substantial regime of positive $d\rho/dT$. Our optimal V_g cycle thus enables non-volatile metal → insulator → metal cycling around the P → BM → P transformation. Consistent with one of the main messages from above, however, the recovery of the metallic P state is imperfect (Figs. 5.2 - 5.6). The $V_g = –3.5$ V curve in Fig. 5.7(a) is in fact similar to the $V_g = 0.9$ V curve, the 300-K ρ being 1.8-times larger than the initial state. This is due to the combined effects of diminished structural perfection in the recovered P state (Figs. 5.2(g), 5.3(a), 5.3(d)), slightly higher δ (Figs. 5.3(g), 5.4(d)), and higher surface roughness (Figs. 5.2(g), 5.3(a), 5.3(d), 5.3(f)). Again, the recovery is better in terms of ρ than I_{SD}, indicating contact degradation.

Notably, the $V_g = –3.5$ V curve in Fig. 5.7(a) and Fig. 5.8(a) displays an inflection point at ~145 K (peak in $d\rho/dT$ in Fig. 5.8(b)), strongly suggesting a well-defined T_C [108,169,179], which would indicate full F → non-F → F cycling. This was probed further through anomalous Hall effect measurements, which offer distinct advantages over (signal-limited) magnetometry measurements in such thin films [169,179]. Fig. 5.7(b) therefore shows the T dependence of the remanent transverse (Hall) conductivity, $\sigma_{xy} = [(\rho_{xy}(T, 50\text{ Oe}) – \rho_{xy}(T, –50\text{ Oe})]/2[\rho_{xx}(T, 0)]^2$. The $V_g = 0$ behavior is characteristic of LSCO [169,179,223], exhibiting a sharp turn on in σ_{xy} at $T_C \approx 168$ K (in reasonable agreement with our estimate from $\rho(T)$ and expectations at this thickness [107,169,179]),

and a broad maximum at intermediate T. This is characteristic of the anomalous Hall effect in x = 0.5 LSCO [223]. As V_g is increased, σ_{xy} progressively decreases in amplitude down to 0.9 V (yellow solid line). By 1.1 V (green solid line), coincident with the metal-insulator transition in Fig. 5.7(a), σ_{xy} practically vanishes, evidencing only a weak magnetic transition at ~150 K. This is consistent with prior work on LSCO bulk crystals [60] and epitaxial films [105,107], which lose metallicity near $T_C \approx 150$ K, effective dopings beneath this inducing glassy, phase-separated magnetism [59]. As V_g is reversed in Fig. 5.7(b), critically, a F-like $\sigma_{xy}(T)$ re-emerges, the –3.5 V case (green dashed line, $T_C \approx 152$ K) coinciding closely with the 0.9 V case (yellow solid line), as for $\rho(T)$ in Fig. 5.7(a). Our optimal V_g cycle thus enables non-volatile F → non-F → F cycling in addition to metal → insulator → metal cycling. We emphasize that while the non-F BM phase of bulk $SrCoO_{2.5}$ is known to be AF with a high T_N of 540 K [93], AF order in electrochemically reduced $SrCoO_{2.5}$ films has not been directly verified. In x = 0.5 LSCO, the existence or otherwise of AF order is not established in bulk, let alone gated films. Further work to address this issue is therefore clearly needed, and we thus refer to BM-LSCO films here simply as "non-F".

Finally, Fig. 5.7(c) provides additional insight into V_g cycling of magnetic properties by plotting 50-K σ_{xy} *vs.* applied perpendicular magnetic field (H) hysteresis loops at various V_g. The behavior is remarkably simple, the square, wide, hysteresis loops simply dropping in amplitude as V_g increases from 0 to 0.9 V. (LSCO films under compressive stress are known to have substantial perpendicular magnetic anisotropy [107]). At V_g = 1.1 V, coincident with the metal-insulator transition in Fig. 5.7(a), and consistent with $\sigma_{xy}(T)$ in Fig. 5.7(b), F behavior in $\sigma_{xy}(H)$ almost vanishes. As emphasized in the close-up in the inset to Fig. 5.7(c), the anomalous Hall effect truly disappears by 1.3 V. Consistent with Figs. 5.7(a),(b), reversing V_g to –3.5 V then recovers the F state (green dashed line), albeit with diminished maximum σ_{xy} relative to the as-deposited P state.

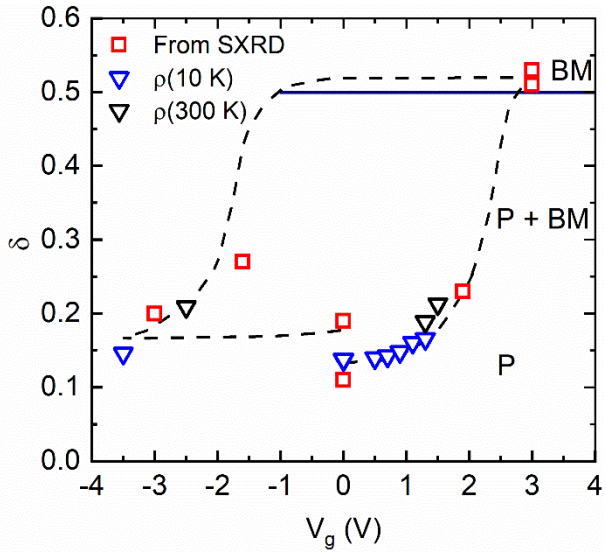

Figure 5.9: Oxygen deficiency (δ) *vs*. gate voltage (V_g), forming a δ *vs.* V_g hysteresis loop, for a 10-unit-cell-thick ion-gel-gated LSCO film. Three methods were used to estimate δ, depending on the situation. For films studied with *operando* SXRD, the known P (δ ≈ 0.1, a ≈ 3.89 Å [176,242,255,276]) and BM (δ = 0.5, $a/4$ ≈ 4.10 Å [242]) endpoints from thicker LSCO films on LAO (> 28 u.c.) enable linear interpolation to estimate δ from the lattice parameter (a). This method (red squares) has been used in similar P ↔ BM transforming ferrite films [314]. For P-phase films where low-T electronic transport data are also available, the resistivity at 10 K (ρ(10 K)) was used to estimate δ (blue triangles), using a commonly applied method involving comparison to single-crystal (nominally δ = 0) P LSCO data at various doping levels [169,242,255,276]. Finally, for films where the low-T resistivity was not measurable, ρ(300 K) was used (black triangles) [255].

As discussed in Section 5.2, the value of δ, the oxygen nonstoichiometry, can be estimated using both electronic transport measurements [169,242,276] and XRD [314]. In this work, both were used to quantify δ around the V_g-hyeseresis loop, *i.e.*, P → BM → P, as shown in Fig. 5.9. From low-T transport (blue triangles) the ungated film (V_g = 0 V) corresponds to δ ≈ 0.14, as mentioined above. This value grows as V_g is increased, reaching ~0.17 at V_g = 1.3 V. Beyond this point the film is insulating (x_{eff} ≈ 0.16), and thus ρ could not be measured to low-T, so we adjusted our method to instead use the 300 K resistivity (black triangles). This is less accurate, but still can be informative [255]. Note that the method to estimate δ from resistivity is limited to 0 < δ < 0.25, because it relies on the relation, $x_{eff} = x - 2\delta$, where x_{eff} cannot be < 0. Another method to estimate δ is based on interpolation of the film a, from XRD (SXRD in this case), between known P and BM endpoints (red quares, see Fig. 5.9 caption). This method is highly dependent on the accuracy of the endpoints used, but can be used to find δ across the entire δ range (0.1 - 0.5). In Fig. 5.9, the three methods can be seen to be in reasonable agreement, within ~0.05

throughout. The largest discrepancy between the points appears for the region of the loop $V_g \approx -3$ V $\rightarrow$ 0 V, where the red squares are from a separate sample (blue and black are from the sample shown Fig. 5.7) and is thus subject to sample-to-sample variability. Overall, the shape of the δ *vs*. V_g hystersis loop in Fig. 5.9 is in close agreement with the I_{SD} and *a vs*. V_g loops above, outlining the P $\rightarrow$ BM $\rightarrow$ P transformation.

5.6 Summary and conclusions

In summary, we have presented the first full study of hysteresis and reversibility across the voltage-induced P $\leftrightarrow$ BM topotactic phase transformation in electrochemically gated perovskite cobaltite thin films. Gate-voltage hysteresis loops around the entire P $\rightarrow$ BM $\rightarrow$ P cycle reveal a wealth of new mechanistic understanding, particularly in tandem with quantitative *operando* synchrotron X-ray diffraction. Examples include asymmetric hysteresis due to differing oxygen diffusion characteristics in the P and BM phases, non-monotonic transformation rates due to the first-order nature of the transformations, and limits on first-cycle recovery due to diminished structural coherence, oxygen content, and surface perfection. Extensive minor hysteresis loop studies were then shown to provide yet deeper insight, enabling the first rational and quantitative design of an optimal gate voltage cycle in such devices. This cycle was then used to realize state-of-the-art voltage control of transport and magnetic properties, encompassing $>10^5$ room-temperature ON/OFF ratios, high recovery, and metal $\rightarrow$ insulator $\rightarrow$ metal and ferromagnet $\rightarrow$ non-ferromagnet $\rightarrow$ ferromagnet cycling, all with high room-temperature stability and non-volatility. This was achieved in ultrathin (10-unit-cell) ion-gel-gated $La_{0.5}Sr_{0.5}CoO_{3-\delta}$ thin films, setting the stage for future assessment of the ultimate limits on switching speed and durability of such redox-based electrochemical transistors.

Chapter 6: Probing the nature of the magnetic order in brownmillerite $SrCoO_{2.5}$ and $La_{0.5}Sr_{0.5}CoO_{2.5}$ films *via* neutron diffraction

The P-BM topotactic transformation has received much recent attention, especially in electrolyte-gated SCO films, where a small voltage can be used to switch between the two phases at room temperature. In bulk, P-SCO is a F metal ($T_C \approx 305$ K), whereas the BM is an AF insulator ($T_N \approx 540$ K), thus presenting the exciting prospect of switching between F and AF states, with both ordering temperatures near or above room temperature. However, despite myriad demonstrations of P-BM switching and accompanying structural / metal-insulator / F - non-F transitions, the presumed AF order of the BM has yet to be experimentally verified in SCO films. This is primarily due to the inherent challenges of probing AF order, especially in thin film samples. Here, using neutron diffraction (ND), we show unambiguously, for the first time, that BM-SCO thin films under small compressive strain on LSAT (001) substrates exhibit G-type AF ordering, in analogy to the bulk compound. However, the ordering temperature, T_N, is significantly lower, ~330 K in films *vs.* ~540 K in bulk. In addition, the magnetic order in BM $x = 0.5$ LSCO films was also probed for the first time, finding that, in contrast to $x = 1$ BM-SCO, there is no evidence for G-type AF ordering. We instead observe an unexpected weak F signal, with $T_C \approx 100$ - 120 K and $M_s \approx 0.1$ μB/Co, from magnetometry and confirmed by ND. Additionally, a new magnetic phase diagram was generated as a function of the oxygen stoichiometry δ for films of the important composition $x = 0.5$ LSCO, revealing further mechanistic details of the P → BM transformation and accompanying magnetic properties.

6.1 Methods

100 - 200 nm thick $x = 0.5$ P-LSCO and 50 nm thick $x = 1$ BM-SCO films were grown on (001)-oriented LSAT substrates using high-pressure-oxygen sputtering. High quality $x = 0.5$ P-LSCO films were deposited using previously optimized conditions [107,108,242,255,256], while $x = 1$ BM-SCO films required slightly different growth conditions (see Section 2.1.2). The primary difference was the post-deposition cooling atmosphere. For $x = 0.5$ P-LSCO, films were cooled in 600 Torr O_2 from the growth temperature, while for $x = 1$ BM-SCO as-deposited films were cooled in the O_2 pressure

used during growth, *i.e.*, ~1.5 Torr. In addition, BM-SCO films tended to phase separate at high thicknesses (>~50 nm), imposing a practical limit to $x = 1$ BM-SCO film thickness in this study of 50 nm. More details on the sputter deposition of BM-SCO films are included in Appendix C. In contrast to $x = 1$, $x = 0.5$ BM-LSCO films were prepared by post-deposition vacuum annealing of P films, at T (experimental) > 500 °C and $P < 1 \times 10^{-7}$ Torr. Note that vacuum annealing was preferred to ion-gel-gating, in this study, due to the high film thickness, large area, and high structural quality necessary ND experiments involving thin films.

Temperature-dependent ND experiments with $\lambda = 2.37$ Å were performed at the VERITAS (HB-1A) beamline of the High-Flux Isotope Reactor (HFIR) at Oak Ridge National Laboratory. For $x = 1$ BM-SCO, diffraction experiments were performed on a stack of six nominally identical 50-nm-thick films, all on LSAT(001) 20 × 20 mm^2 substrates, whereas a single 200-nm-thick film was used for $x = 0.5$ BM-LSCO (also on 20 × 20 mm^2 LSAT(001)). The samples were wired to thin Al plates, with the film (*h*0*l*) scattering plane horizontal, and then loaded into a closed cycle refrigerator that could achieve temperatures between 3.5 and 750 K. A collimation configuration of 40’-40’-40’-80’ yielded an energy resolution (FWHM) of ~1 meV at the elastic line. The combination of the double-bounce monochromator system and the placement of the pyrolytic graphite crystal analyzer for energy discrimination before the single He-3 detector provided an excellent signal-to-noise ratio (SNR). Higher-order wavelength contamination of the incident beam was minimized with the use of two PG filters. Magnetometry was performed using a Quantum Design PPMS VSM and MPMS-3 SQUID-VSM from 10 - 300 K in applied magnetic fields of up to ±70 kOe.

6.2 Structure of as-deposited $SrCoO_{2.5}$ films and the vacuum-annealing-induced perovskite-to-brownmillerite transformation in $La_{0.5}Sr_{0.5}CoO_{3-\delta}$ films

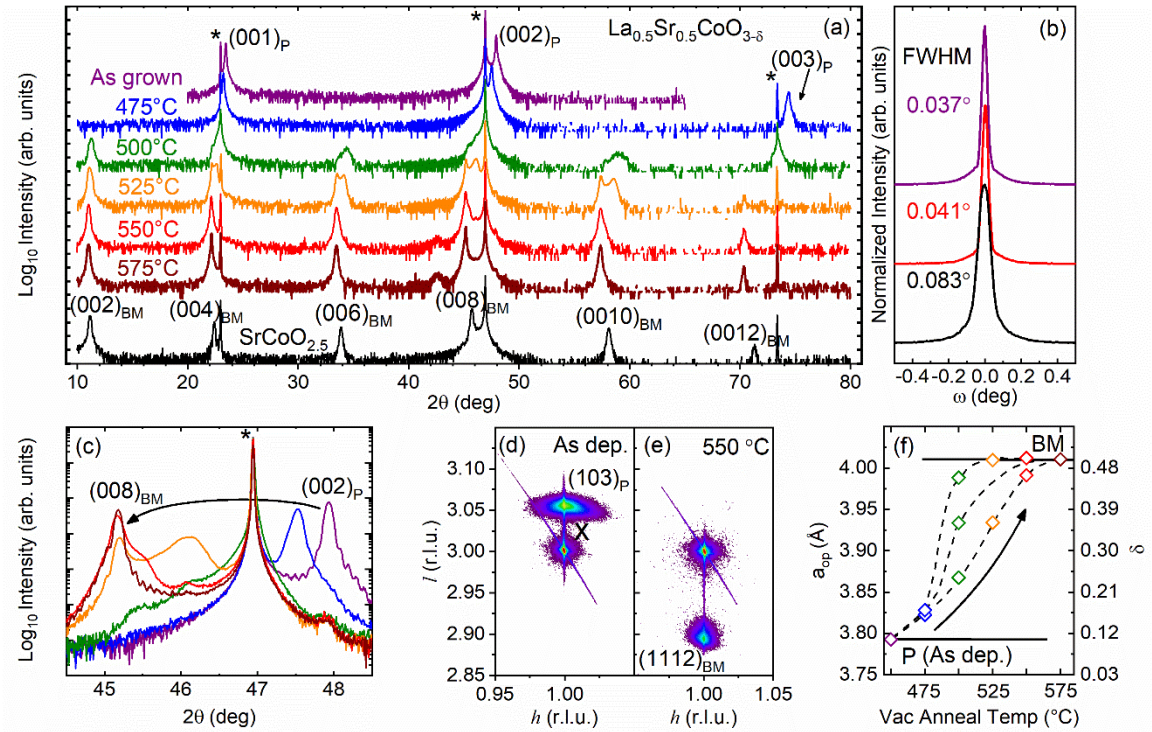

Figure 6.1: (a) Wide-angle specular HRXRD scans of a 100-nm-thick x = 0.5 LSCO film on LSAT(001) in the as-deposited perovskite (P) phase (purple) and after being subject to vacuum annealing at various temperatures (other colors, see legend). An as-deposited 50-nm-thick x = 1 brownmillerite (BM)-SCO film (black) is shown for reference, with the BM peak indexes marked. The curves are offset for clarity, and the substrate peaks are marked with an *. (b) P (002) / BM (008) rocking curves for selected films in (a), using the same color scheme. (c) The same data as in (a) but zoomed into the region near the film and substrate P (002) / BM (008) reflection. (d),(e) RSMs about the substrate (103) for an x = 0.5 P-LSCO film as-deposited (d), and after 550 °C anneal (e). The bulk position for x = 0.5 P-LSCO is marked in by a black "×". (f) Out-of-plane lattice parameter (a_{op}) *vs.* vacuum anneal temperature, where the point at 450 °C corresponds to the as-deposited film state. Multiple points at the same anneal temperatures represent a_{op} from multi-peak fits to the film peak in (c). The approximate δ value is also shown along the y-axis (see text). Color coding consistent with (a),(b),(c) and black dashed lines are for visualization purposes.

We begin with a brief discussion of our as-deposited x = 1 BM-SCO films. Fig. 6.1(a),(b) shows specular wide-angle HRXRD (a) and (008) RC (b) scans for a representative 50-nm-thick as-deposited LSAT(001)/$SrCoO_{2.5}$ film (black lines). The film can be indexed to the BM structure (quadrupling of the P a out-of-plane) and is seen to be phase pure. An important indicator of structural quality in BM films, particularly pertaining to the anion sublattice, is the intensity ratio of, *e.g.*, the (008) and (006) peak [242,256],

which was found to be ~21 for the film in Fig. 6.1(a), further indicating phase pure BM. The out-of-plane lattice parameter, a_{op}, was determined to be 3.964 Å, consistent with prior reports of fully-strained BM-SCO films on LSAT(001) substrates [114]. In addition, GIXR (not shown) and the presence of Laue fringes about the most intense peaks in Fig. 6.1(a) indicate the film has low surface and interface roughness. Scherrer-length-to-thickness ratio and RC FWHM (Fig. 6.1(b)) were found to be 0.87 and 0.083°, respectively. Together, these observations demonstrate high-quality BM-SCO films, the first, that we are aware of, to be deposited by sputtering.

To demonstrate the thermally induced P → BM transformation in x = 0.5 LSCO films, Fig. 6.1(a) also shows the wide-range specular HRXRD for a 100-nm-thick P-LSCO film, as-deposited and after a series of vacuum annealing treatments (colored curves). For clarity, a "zoomed-in" version, with the intensity y-axis scale, is shown in Fig. 6.1(c), focusing on the region around the film / substrate P (002) / BM (008) peaks. The as-deposited P-LSCO is initially phase pure with Scherrer length (Λ) ~840 Å, yielding $\Lambda/t \approx$ 0.88, indicating good coherence out-of-plane and little microstrain. After vacuum annealing at 475 °C, the film peaks downshift to lower 2θ, indicating an expansion of the lattice out-of-plane consistent with V_O formation [176]. This expansion is accompanied by a slight decrease in peak intensity and slight broadening. However, the film structure remains fully P, indicating no long-range V_O ordering. Upon increasing the anneal T to 500 °C (green curve), additional diffraction peaks appear at half-integer positions of the P index, indicating the formation of the V_O-ordered BM, that results from quadrupling of the unit cell out of plane (Fig. 1.15(a)). However, these initial BM peaks have very low intensity, indicating a small BM phase fraction at this stage. Notably, the film peaks after 500 °C anneal mostly coincide with the substrate peaks, but with significantly broadened "shoulders" toward lower 2θ. Increasing the anneal T again to 525 °C (orange curve) further increases this apparent inhomogeneity, as the film peaks split into two distinct peaks. This splitting is due to a laterally inhomogeneous distribution of oxygen stoichiometry. During the annealing sequences, it was observed, from changes in optical transparency, that the outer edges of the film were reduced more rapidly than the innermost region. The most likely explanation is that the sample experienced some level of

temperature inhomogeneity during our vacuum annealing treatments. Nonetheless, as the vacuum anneal temperature was further increased to 550 and to 575 °C the observed lateral inhomogeneity vanished, the film peaks narrowing and intensifying at the expected 2θ positions for x = 0.5 BM-LSCO on LSAT [242,256]. The disappearance of lateral inhomogeneity above ~550 °C thus provides evidence for the added stability of the film in the BM phase. In fact, little change is observed between the peak positions in the 550 and 575 °C scans; with only slight changes to the peak shape being notable, including the disappearance of the higher 2θ shoulder and the reappearance of prominent Laue fringes.

The structural quality of the annealed BM-LSCO film after 575 °C is nearly identical to the as-deposited P. In fact, the Λ/t ratio is slightly higher for the annealed BM-LSCO (~0.91), indicating lower microstrain, as would be expected due to the lower in-plane strain for the x = 0.5 BM-LSCO ($\varepsilon_{xx} \approx -0.3\%$, see Appendix D for bulk BM-LSCO lattice parameters) *vs*. P-LSCO ($\varepsilon_{xx} \approx 0.8\%$). The comparable structural quality between as-deposited P and vacuum-annealed BM is further shown by the film RCs in Fig. 6.1(b), where the P (002) / BM (008) film FWHM are essentially the same (both at ~0.04°). For reference, the final 575 °C-annealed structure of the x = 0.5 BM-LSCO film is contrasted with the as-deposited 50-nm-thick x = 1 BM-SCO film (black curves in Fig. 6.1(a),(b)), where both show phase-pure (001)-oriented BM structure. We should note, however, that a minor additional peak does appear after ~550 °C anneal at ~42.5°. This corresponds to the position of the (200) peak of CoO, which has been previously reported to occur in sputtered LSCO films grown at high T [317]. The RC FWHM of the x = 0.5 BM-LSCO is roughly half that of x = 1 BM-SCO film, indicating a lower mosaicity and thus higher crystalline quality in the latter.

Asymmetric RSMs about the film and substrate (103) (and BM-equivalent ($11\underline{2}$)) peaks are shown in Fig. 6.1(d),(e). The as-deposited P-LSCO appears fully strained to the substrate, *i.e*. pseudomorphic, evidenced by the primary peak intensity along the same h as the substrate. The epitaxial strain of x = 0.5 LSCO on LSAT ($\varepsilon_{xx} \approx 0.8\%$), combined with the large film thickness (~100 nm), leads to some scattered intensity from the film away from the pseudomorphic (h = 1) line. This perhaps indicates the onset of some relaxation effects, but the film is nevertheless considered predominantly strained. From Fig. 6.1(e),

after 550 °C vacuum anneal, the film transforms to the BM structure but remains fully strained to the substrate. The film's crystalline quality and relationship with the substrate thus remains essentially unchanged despite the large expansion of the lattice out-of-plane (~6%) during the P → BM transformation.

Finally, Fig. 6.1(f) shows the film a_{op} (as estimated from (multi)peak fitting to the P (002) / BM (008) of Fig. 6.1(c)) as a function of vacuum anneal temperature. Plotting the data this way aids in the visualization of the transformation, highlighting the large lattice expansion, as well as the onset and subsequent collapse of lateral inhomogeneity as the final BM structure is approached. Importantly, a_{op} can also be used to approximate the oxygen stoichiometry, δ, of the sample. By linearly interpolating between the two end states, *i.e.*, P (a_{op} = 3.79 Å, δ = 0.1 [242]) and BM (a_{op} = 4.01 Å, δ = 0.5 [242,256]), for a given a_{op} we can then estimate the film δ (shown on the right axis in Fig. 6.1(f)). The quantification of oxygen non-stoichiometry of perovskite films is notoriously challenging. An accurate measure of δ is perhaps only verifiable by *Z*-contrast STEM, with complementary electron-energy-loss spectroscopy [105]. However, simpler, more approximate techniques, have also proven to be powerful tools to guide the understanding of structure/chemistry/property relationships in perovskites, particularly in cobaltites [105,114,169,242,255]. The method of linear interpolation from $a_{op}(\delta)$ described above, has been employed for $SrFeO_{3-\delta}$ [314], $SrCoO_{2.5}$ [114], and in LSCO films, where in the latter it has been checked against other more rigorous electronic-transport-based methods [169,255]. This technique thus allows an extremely convenient, yet reasonably accurate, probe of δ across the entire δ range, from P to BM, requiring only lab XRD. Later in this chapter, we demonstrate the practical value of this method by combining the results shown in Fig. 6.1 with complementary *ex situ* magnetometry, to develop a magnetic phase diagram as a function of δ for x = 0.5 LSCO films.

6.3 Neutron diffraction of brownmillerite $SrCoO_{2.5}$ and $La_{0.5}Sr_{0.5}CoO_{2.5}$ films

6.3.1 Probing the (201) magnetic-only peak: G-type antiferromagnetism in $SrCoO_{2.5}$

Neutron diffraction (ND) is uniquely suited to probing magnetic order in AF materials, where traditional volume-averaged probes of magnetism are indirect and

oftentimes ambiguous. This is especially true in thin films, where inherently low sample mass and potential contamination from the substrate can make definitive magnetometry measurements difficult or impossible. Therefore, in this work we employed ND to investigate the magnetic ordering in $x = 1$ and $x = 0.5$ BM-LSCO films, using the VERITAS instrument at the HB-1A beamline at ORNL (see Section 6.1 for details).

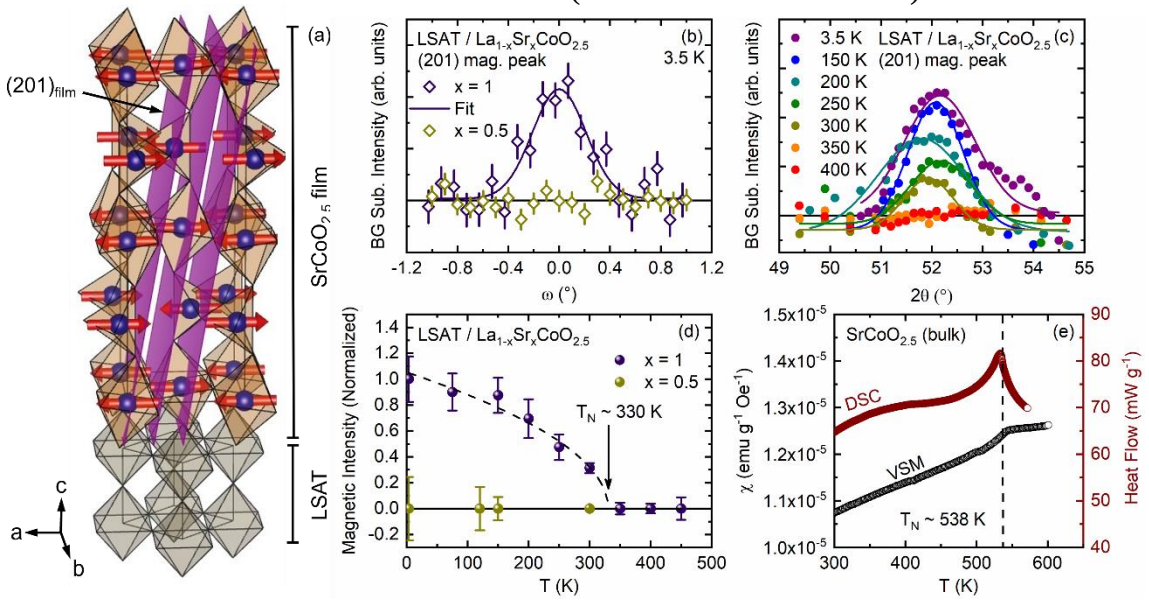

Figure 6.2: (a) A schematic diagram illustrating the crystal structure of a brownmillerite (BM) $SrCoO_{2.5}$ film (based on a bulk reference pattern [318]), its relationship to the substrate (LSAT), the magnetic ordering structure [93], and the (201) planes probed in this work. For clarity only the Co atoms and their geometric relationship to O, *i.e.*, octahedra or tetrahedra, are shown. (b) neutron diffraction RCs at 3.5 K at the expected position of the magnetic (201) peak for $x = 1$ and $x = 0.5$ BM-LSCO film samples. Error bars in (b) represent the square root of the total detected counts. (c) $\theta/2\theta$ coupled scans of the same peak as in (b) for the $x = 1$ BM-SCO sample only at selected temperatures. The data in (b),(c) are shown after appropriate background subtraction (see Appendix E). Solid lines representing gaussian fits to the data. (d) Integrated intensity from the (201) peak fits *vs*. temperature (T) (normalized to the lowest T data point). The dashed line is a fit: $\{T < T_N\}\ I = A(T - T_N)^{\beta}$, $\{T > T_N\}\ I = 0$, where I is the intensity, A is a scaling factor, T_N, is the Néel temperature, and β is the critical exponent (held fixed at $\beta = 0.5$ for mean-field approximation). Error bars in (d) below 350 K correspond to standard errors from the gaussian fits, while above 350 K they represent the absolute value of the total integrated intensity after background subtraction (for the $x = 0.5$ BM-LSCO sample, all error bars represent the absolute value of total integrated intensity after background subtraction). The methods used for background subtraction were consistent between $x = 1$ and $x = 0.5$ samples. (d) Bulk $SrCoO_{2.5}$ vibrating sample magnetometry (VSM) (black, left axis), in χ *vs*. T, and differential scanning calorimetry (DSC) (dark red, right axis) for the same T range, showing the coincident features marking the AF transition, T_N (black dashed vertical line).

Fig. 6.2(a) shows a schematic diagram of the LSAT(001)/$SrCoO_{2.5}$ (50 nm) film / substrate crystal structure probed in these experiments, where the tetragonal BM-SCO film

is related to the underlying cubic LSAT perovskite structure by a 45° in-plane rotation: *i.e.*, $a_{LSAT} \times a_{LSAT} \times a_{LSAT} = a_{BM}/\sqrt{2} \times a_{BM}/\sqrt{2} \times c_{BM}/4$ (here, $c_{BM}/4$ is equivalent to the a_{op} shown in Fig. 6.1(f)). The magnetic structure of BM-SCO has been well-characterized in the bulk by neutron powder diffraction, exhibiting G-type AF order [93,100–103], as shown schematically in Fig. 6.1(a). This AF ordering gives rise to a magnetic structure featuring magnetic-only reflections, that are forbidden in the nuclear structure. From the structure factor, the (102) and (012) magnetic peaks are the most intense and have thus far provided the primary evidence of G-type AF in SCO in prior NPD studies [93,100]. Unfortunately, however, in our case, these peaks were entirely masked due to their coincidence by the (½,½,½) family of peaks from the substrate (previously thought to be forbidden). We detected such (½,½,½) peaks in all of the substrates probed in this study: LSAT(001), $NdGaO_3$(110), and $SrTiO_3$(001). Such 'forbidden' substrate peaks have been seen previously in ND studies in the perovskite oxide substrate $DyScO_3$ [319], but in general are of unknown origin. Having access to only the *h*0*l* plane in our scattering experiments, we thus chose to probe the (201) BM film peak. This peak is also predicted to be magnetic-only (with a structure factor roughly 10-times lower than the (102)) but is not near any other reflections from the substrate or sample holder (polycrystalline Al). The (201) film peak ND results at base *T* (*T* = 3.5 K) are shown in Fig. 6.2(b), where the *x* = 1 BM-SCO film sample shows a clear peak in the RC. Note that the observation of this peak was near the limit of detection in this experiment (see Appendix E), requiring 10-minute-per-point dwell times to provide sufficient statistics to unambiguously prove the presence of a peak. Nevertheless, the detection of this peak alone directly confirms that the *x* = 1 BM-SCO films exhibit G-type AF order, in analogy to the bulk material. As far as we are aware, this is the first demonstration of this in *x* = 1 BM-SCO films.

In stark contrast to *x* = 1 the *x* = 0.5 BM-LSCO film shows no intensity near the (201) position, as seen in Fig. 6.2(b), indicating that at *x* = 0.5, BM-LSCO films *do not* have G-type AF ordering. It is important to note here that the *x* = 0.5 BM-LSCO sample (one 200-nm-thick film on LSAT) yielded more intense (by roughly a factor of 2) nuclear scattering peaks *vs.* the *x* = 1 BM-SCO sample (a stack of six 50-nm-thick films on LSAT), meaning that, if there were a (201) peak in the former, we most likely would have been

able to detect it. We thus interpret the aforementioned lack of diffracted intensity at the (201) position for the x = 0.5 BM-LSCO sample (at 3.5 K) as strong evidence disproving G-type AF order at this composition. Literature studies on the magnetic order in BM LSCO are notably lacking, where only the x = 1 (SCO) has been well characterized. Based on the similarities between x = 1 and x = 0.5 in the P state (both metallic F, with T_C > 260 K), and the observation that both form the BM structure at δ = 0.5, one might expect the x = 0.5 BM would also exhibit strong AF interactions. In bulk at x = 0.67 BM-LSCO, one report has claimed evidence of such antiferromagnetism (from a large negative Weiss constant deduced from fitting high-T magnetometry data), but the nature of the ordering was not investigated [72]. Further work is therefore needed to definitively characterize the magnetic order in BM-LSCO, perhaps starting from bulk NPD and then continuing to epitaxial films.

After observing the (201) magnetic peak at 3.5 K in the x = 1 BM-SCO film sample, we then tracked this peak as a function of T, taking additional scans at every 50 K. The results are shown in Fig. 6.2(c) and (d). Fig. 6.2(c) shows the (201) peak from $\theta/2\theta$ coupled scans (after careful background intensity subtraction, see Appendix E), where the peak intensity clearly diminishes at higher temperatures, eventually vanishing above 350 K. By fitting the peaks to Gaussians (solid lines in Fig. 6.2(c)), and plotting the fit-determined area *vs*. T, the plot in Fig. 6.2(d) was generated. This plot shows the clear order-parameter shape expected for a magnetic peak, resulting in effectively zero intensity above the ordering temperature, T_N. (Note that the (201) peak scans for our x = 0.5 BM-LSCO film sample showed no intensity for any of the T probed.) By fitting an order parameter function to the data in Fig. 6.2(d), we estimated T_N to be ~330 ± 10 K.

To compare with the above findings, we also characterized *bulk* x = 1 BM-SCO using a combination of vibrating sample magnetometry (VSM) and differential scanning calorimetry (DSC). The results are shown in Fig. 6.2(e). Both VSM and DSC of bulk BM-SCO powders show clear evidence for a transition near $T \approx$ 540 K, in close agreement with prior studies indicating $T_N \approx$ 540 - 570 K [93,100–102]. Interestingly, the BM-SCO films discussed above exhibit a significantly reduced T_N compared to bulk. The strain state of the films on LSAT (ε_{xx} = –1.0 %, compression) and/or their tetragonal (a = b ≠ c) symmetry

vs. the orthorhombic symmetry in bulk (likely producing different tilt patterns and thus bond angles) may play central roles in the reduced T_N. It should be noted here also that some structural degradation of the BM-SCO film sample at high T was observed in these experiments (see Appendix C for more details). Regardless, further study is needed to explain the reduced T_N in these LSAT/$SrCoO_{2.5}$ films. Theoretical calculations, such as DFT, in combination with strain-dependent experimental analyses (i.e., study of BM-SCO on different substrates), may prove valuable in this regard. For now, it is enough to note that T_N, while substantially lower than the bulk value, is still above 300 K, maintaining promise for the prospects of room-temperature F → AF → F switching in devices based on the P-BM transformations in SCO.

6.3.2 Probing the (002) peak: weak ferromagnetism in $La_{0.5}Sr_{0.5}CoO_{2.5}$

While the (201) magnetic was not detected in the x = 0.5 BM-LSCO film sample, similar films did exhibit weak F signals from magnetometry measurements. Fig. 6.3(a) shows field-cooled *M vs. T* curves for x = 1 and x = 0.5 BM-LSCO for both film (200-nm-thick on LSAT solid lines) and bulk samples (dotted lines). Clearly, at x = 0.5, both the films and bulk show a F response with $T_C \approx 120$ K with similar M at low T's, while the x = 1 SCO samples do not show any F signal, as expected. Fig. 6.3(b) then shows corresponding $M(H)$ loops taken at 15 K for the film samples shown in Fig. 6.3(a), highlighting the extremely hard F character of the x = 0.5 LSCO sample ($H_c \approx 50$ kOe) and, again, the lack of F hysteresis at x = 1. Notably, the saturation magnetization (M_s) of the x = 0.5 film sample in Fig. 6.3(b) is very low, ~0.1 μ_B/Co. Such low saturation magnetization can be described as "weak" ferromagnetism (weak F). Magnetic materials exhibiting weak F are often insulating AF materials whose moments do not wholly cancel, *i.e.*, they have 'canted' AF structure, leading to a F net moment, and long-range F properties, despite local AF ordering.

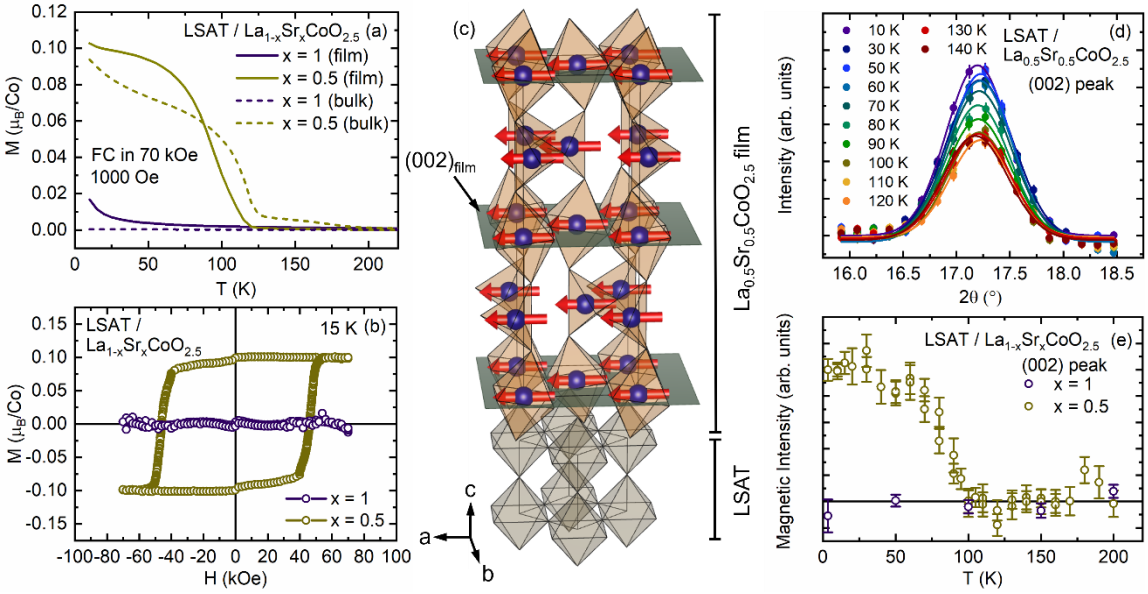

Figure 6.3: (a) Field cooled (70 kOe) magnetization (*M*) *vs*. temperature (*T*) measured (in 1000 Oe) for $x = 1$ and $x = 0.5$ BM-LSCO bulk (dashed lines) and film samples [LSAT/$SrCoO_{2.5}$ (50 nm) and LSAT/$La_{0.5}Sr_{0.5}CoO_{2.5}$ (200 nm)] (solid lines). (b) *M vs*. applied field (*H*) for the film samples in (a) taken at 15 K. Note, the field was applied in the plane of the film. The data are shown after subtraction of non-ferromagnetic components. (c) Schematic diagram illustrating the proposed crystal and magnetic structure of brownmillerite (BM) $La_{0.5}Sr_{0.5}CoO_{2.5}$ films on LSAT, and the (002) planes probed by ND. For clarity only the Co atoms and their geometric relationship to O, *i.e*., octahedra or tetrahedra, are shown. (d) neutron diffraction $\theta/2\theta$ coupled scans about the $x = 0.5$ BM-LSCO film (002) peak for selected *T* scans from 10 - 140 K (see legend). Error bars represent $\pm\sqrt{\text{counts}}$. (e) Normalized magnetic intensity of the (002) film peak *vs*. *T* for $x = 1$ and $x = 0.5$ BM-LSCO samples. The data were generated by the following procedure: (1) gaussian fitting of the (002) diffraction peaks (solid lines in (b)), (2) plotting the fit-determined peak area *vs*. *T*, and (3) subtracting a linear fit. For $x = 0.5$ the linear fitting range ignored data below 100 K, while for $x = 1$ the entire *T* range was used).

To directly probe if this small F signal detected in magnetometry was inherent to the film, we again performed ND, this time focusing on the low-*Q* nuclear (002) film peak. Fig. 6.3(c) shows a schematic of the $x = 0.5$ BM-LSCO film (002) planes, in analogous fashion to Fig. 6.2(a), where the moments on the Co sites represent the anticipated net-moment ordering implied from magnetometry (Fig. 6.3(a),(b)). Since the (002) is a nuclear film peak, any magnetic scattering would be additional to the nuclear scattered intensity. However, nuclear scattering varies less with temperature than magnetic scattering (especially around the ordering *T*), therefore, tracking the peak intensity *vs*. *T* (to look for order-parameter-like trends) can be used to detect magnetic scattering. Fig. 6.3(d) shows the diffracted intensity $\theta/2\theta$ scans for the (002) peak at selected temperatures below ~150 K. Above ~100 K the scans are nearly indistinguishable, exhibiting nearly the same peak

shape and intensity. Below ~100 K, however, the peak begins to increase in intensity rapidly with decreasing *T*, eventually saturating at the lowest *T*, implicating an order parameter shape and thus magnetic scattering. The solid lines in Fig. 6.3(d) represent Gaussian fits to the data. Such fits were then used to quantify the integrated intensity and these values were plotted as a function of *T*, as shown in Fig. 6.3(e). The data in Fig. 6.3(e) clearly indicate an order-parameter shape with a well-defined T_C around ~100 K, in reasonable agreement with the weak F detected from $M(T)$ (comparing Fig. 6.3(a) and (d)), thus proving that weak F is an inherent property of the film. As a final note on ND in this study, we also tracked various other film peaks *vs*. *T* in both the $x = 1$ and $x = 0.5$ samples, including the (202), (008), and (105), but found no signs of magnetic intensity outside of the (201) and (002) described above.

Although we lack additional evidence to put forth any specific explanation for the observed weak F in $x = 0.5$ BM-LSCO, a brief discussion of the possible origins is warranted. For context, our expectation of AF order in $x = 0.5$ BM-LSCO was mostly based on analogy to $x = 1$, and limited bulk and theoretical work at other x [72,193]. As mentioned above, a previous bulk report at $x = 0.67$ (as well as our own bulk work at $x = 0.75$ (see Appendix D)) provides some indirect evidence of canted AF order in BM-LSCO [72]. In addition, one theoretical report also predicted A-type AF order to be the most energetically favorable magnetic ground state for $x = 0.375$ BM-LSCO [193]. In general, weak ferromagnetism due to underlying canted-AF order is best known in the perovskite orthoferrites, $REFeO_3$, where RE = rare earth. Such non-colinear spin structures arise from competition between Dzyaloshinskii-Moriya interactions and magnetocrystalline anisotropy [320]. It is worth noting that $x = 0.5$ P-LSCO features exceptionally high magnetocrystalline anisotropy, even compared to $x = 1$ P-SCO [107,116] (which does not show weak F). However, so far in *films*, we have found no evidence that $x = 0.5$ BM-LSCO exhibits AF order. Of course, canted AF is not the only explanation for weak F behavior. In fact, a recent report on $x = 0$ $LaCoO_{2.5}$ films (non-BM structure) proposed a method where weak F may be due to an imbalance of the spin states at different cobalt sites, resulting in a small net F moment [140]. Finally, signs of weak F have also been reported in several other insulating cobaltite films, such as $LaCoO_{2.5}$ [140], $HSrCoO_{2.5}$ [97,178] and

x = 0.33 BM-LSCO [141], but there is no clear consensus on its origins. Further research is therefore clearly needed to elucidate the origin of the weak F moment in BM-LSCO.

6.4 δ-dependence of the magnetic properties of $La_{0.5}Sr_{0.5}CoO_{3-\delta}$ thin films

A significant motivation for this work was the overall lack of literature studies characterizing the magnetic order in oxygen-deficient LSCO, and specifically BM, despite its growing interest stemming from voltage-based control of P-BM transformations in thin films [97,117,124,127,129,131,132]. Indeed, only a few specific stoichiometries, most notably x = 1 (at δ = 0.5, *i.e.*, BM), are well-studied in the literature. We know of only 2 reports in bulk (one at x = 1 [104], and one at x = 0.67 [72]), one in films [114], and one theoretical study [298], where the magnetic properties were investigated systematically as a function of δ. In films, tracking magnetic properties as a function of *voltage* is instead more frequent [124,127,242], but this is potentially problematic given the lower degree of control over δ. Here, using the vacuum annealing treatments detailed in Section 6.1, and the structural characterization discussed in Section 6.2, we generate a new phase diagram for films of the important x = 0.5 LSCO composition as a function of the oxygen stoichiometry, 3 – δ.

The procedure consisted of repeated *ex situ* magnetometry measurement of a single ~100-nm-thick x = 0.5 LSCO film on LSAT(001) substrate after sequentially higher-T thermal reductions in vacuum (structural characterization shown in Fig. 6.1). Fig. 6.4(a) and (b) show the $M(T)$ and $M(H)$ results, respectively for the above film, labeled with the δ-values determined from specular HRXRD (Fig. 6.1(f)), as described in Section 6.2. The as-deposited film (δ = 0.12, purple curve) shows robust F, as expected for x = 0.5 P-LSCO at this thickness, which has been thoroughly characterized elsewhere [105,107]. Specifically, $T_C \approx 230$ K, $M_s \approx 1.5$ μB/Co, and H_c (10 K) ≈ 10 kOe. As the vacuum anneal T increases, increasing δ, the strength of this F signal falls off rapidly. At δ = 0.15, T_C has decreased to ~170 K, and by δ = 0.25 there is no sign of F signal in either $M(T)$ or $M(H)$ at 10 K. However, as δ is further increased to > ~0.4, a F signal reemerges, but with much lower T_C and M_s, like the results shown in Fig. 6.3(a) for BM-LSCO, *i.e.*, δ = 0.5. This is the same weak F order demonstrated by ND in Fig. 6.3(d) and (e).

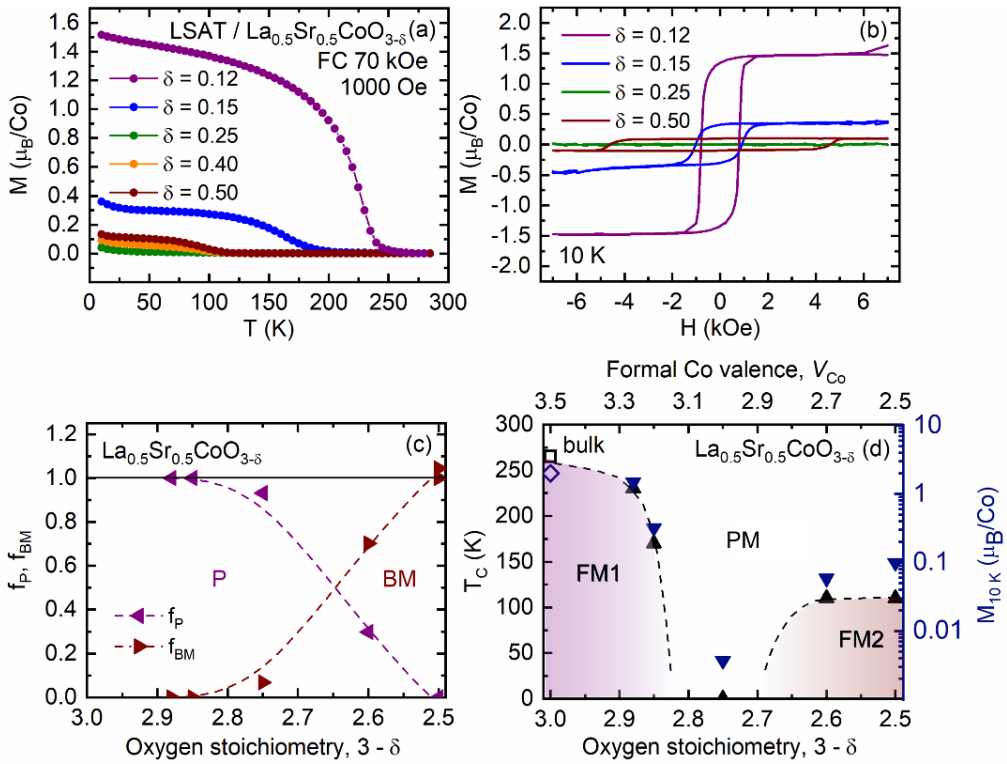

Figure 6.4: (a) Field-cooled (70 kOe) magnetization (*M*) *vs*. temperature (*T*) for a 100-nm-thick LSAT/$La_{0.5}Sr_{0.5}CoO_{3-\delta}$ film after vacuum annealing at various temperatures (*T*) to achieve different oxygen non-stoichiometry (δ) (see legend). All measurements were taken in 1000 Oe applied field. (b) *M vs*. applied field (*H*) hysteresis loops taken at 10 K (in the case of δ = 0.5 (dark red), *M*(*H*) was taken at 15 K). (c) Film perovskite (P) and brownmillerite (BM) phase fractions, f_P and f_{BM}, respectively, plotted *vs*. oxygen stoichiometry (3 – δ). The dashed colored lines indicate cubic spline fits to the data. (d) Magnetic phase diagram of LSAT/ $La_{0.5}Sr_{0.5}CoO_{3-\delta}$ films as a function of 3 – δ. Black upward triangles denote T_C, while downward blue triangles denote *M* at 10 K (M_{10K}) (right axis). The open black square and open blue diamond correspond to nominally δ = 0 bulk properties [59]. The top axis represents the formal cobalt valence, *i.e*., $V_{Co} = 3 + x - 2\delta$ (where x = 0.5). PM (white region) = paramagnet, FM1 (purple shaded region) = ferromagnet 1, and FM2 (brown shaded region) = ferromagnet 2. The dashed lines through the points serve as guides to the eye to approximate the phase boundaries.

Further analysis of the specular HRXRD in Fig. 6.1(a) also allowed us to construct the structural phase diagram shown in Fig. 6.4(c), where the phase fractions of P and BM phases, f_P and f_{BM}, respectively, are plotted as a function of oxygen stoichiometry, 3 – δ. f_P and f_{BM} were deduced from the integrated intensities of the film peaks and the known relationships between the (006) and (008) peak intensities in the phase-pure BM, as done previously [242,255,256]. From inspection of Fig. 6.4(c), the BM first appears near the oxygen stoichiometry 2.75 (δ = 0.25), or 'half-way' between the pure P and BM phases. Note that the lateral inhomogeneity in these samples, mentioned in Section 6.2, may

produce some uncertainty in this, as the value of δ was calculated from the average a_{op} (weighted by the intensity) of a notably (laterally) inhomogeneous film. Nevertheless, the value δ = 0.25 as the onset of BM formation makes intuitive sense, and is not without precedent, as similar topotactic-structural transitions in bulk and films at x = 1 SCO, have also been shown to occur near high-symmetry values, *e.g.*, 2.875, 2.825, 2.75, *etc.* [77,90,114]. Interestingly, however, no other members of the homologous series of oxygen-deficient structures, *i.e.*, $La_{0.5}Sr_{0.5}CoO_{3(n-1)/n}$, n = 3, 4, *etc.*, were observed in these experiments. This indicates a favoring of direct P ($n = \infty$) to BM (n = 2) transformation, as seen in other film studies [309], rather than forming any long-range intermediate-n structures. At δ ≥ 0.25, a phase-coexistence regime consisting of P + BM then emerges, persisting all the way until the terminal 2.5 stoichiometry, when the fully phase-pure BM (δ = 0.5) is reached (Fig. 6.3(c) and Fig. 6.1(a),(c),(f)). From cubic-spline fits to the data points in Fig. 6.3(c), the 50:50 point of the transformation (*i.e.*, where the fit line cross each other) lies close to the 2.65 stoichiometry (δ = 0.35). This phase coexistence has been demonstrated before in both x = 1 and x = 0.5 LSCO films [96,113,242], stemming from the 1st-order nature of the transformation [96]. In bulk BM-LSCO, similar phase coexistence has also been noted, but involves more complex intermediate n phases [72,77,90–92,104].

Finally, combining the above results, we generated the magnetic phase diagram shown in Fig. 6.4(d)), where the black points represent F T_C (left axis), and the blue points represent M(10 K) (as a substitute for M_s (right axis)). Also included in Fig. 6.4(d), are the bulk values, *i.e.*, nominally δ = 0 (open points), for reference. The colored regions correspond to the different magnetic states in the system: purple as ferromagnet "1" (FM1), brown as ferromagnet "2" (FM2), and white as paramagnet (PM). Shown along the top-axis of the diagram is the formal Co valence state (V_{Co}), deduced from simple charge balance of the chemical formula (assuming La, Sr, and O remain 3+, 2+, and 2-, respectively). To analyze the details of this phase diagram we start from the left side, near the fully perovskite stoichiometry (δ ≈ 0), where the as-deposited films (δ ≈ 0.12) are in close agreement with prior work [242]. The precipitous drop in T_C as δ increases reflects the x-dependent trends in bulk LSCO, where lower x results in lower hole-doping and

eventually, in the loss of long-range F order below $x \approx 0.18$ [58–60]. If we consider each V_O as contributing 2 electrons (compensating 2 holes), we can define an 'effective' x, *i.e.*, $x_{eff} = x - 2\delta$. This is conceptually analogous to the V_{Co} shown on the top axis, where $V_{Co} = 3 + x_{eff}$. In Fig. 6.4(d) the loss of long-range F appears to occur between $0.15 < \delta < 0.20$, which corresponds to $0.20 < x_{eff} < 0.10$, in rough agreement with expected trends from bulk LSCO. At the oxygen stoichiometry of 2.75, there is no long-range F order and the films are then presumably PM at all temperatures. Interestingly, from Fig. 6.4(c), this PM ground state occurs in a still predominantly perovskite-structured film, with a very high density of *disordered* (or possibly short-range ordered) V_O. Previous work on voltage-reduced films of $x = 0.28$ LSCO revealed such a structure via STEM at similar a_{op}, and thus presumably similar δ (see Fig. 4.7(f)). At higher δ (> 0.25) the fraction of the BM phase grows (Fig. 6.4(c)), and a F signal reemerges in the form of weak F. The last two data points on the right of the phase diagram in Fig. 6.4(d), corresponding to $\delta = 0.4$ and $\delta = 0.5$, show only a minor difference in the observed magnetic properties (see Fig. 6.4(a)). T_C is nearly identical for the two cases, but M(10 K) is slightly higher for $\delta = 0.5$ (~0.1 μ_B/Co), likely simply due to the higher f_{BM}. As mentioned above, the fundamental origins of the magnetic ground state of FM2 are unknown. Further study is thus still needed to fully map the evolution of magnetic properties through the P-BM transformation in $x = 0.5$ LSCO films.

6.5 Summary and conclusions

To summarize, in this work we used neutron diffraction to probe the magnetic structure of BM films of $x = 1$ and $x = 0.5$ LSCO on (001)-oriented LSAT substrates. By detecting the (201) magnetic-only peak, we presented the first direct evidence for G-type AF ordering in $SrCoO_{2.5}$ thin films, confirming the bulk-like magnetic ground state. However, the Néel temperature of the films was found to be significantly lower than in bulk: ~330 K *vs*. ~540 K, respectively. For $x = 0.5$ BM-LSCO films, on the other hand, G-type AF order was not observed. Instead, magnetometry measurements indicated weak F, and this was confirmed by ND, through observation of magnetic scattering at the nuclear (002) peak position. The origins of this weak F order ($T_C \approx 120$ K, $M_s \approx 0.1$ μ_B/Co), which exhibits giant low-temperature coercivity (H_c(15 K) ≈ 50 kOe), is currently not known as no AF peaks were observed. Interestingly, similar weak F was also observed in *bulk*

samples of $x = 0.5$ BM-LSCO, providing motivation for further neutron studies to elucidate the underlying magnetic structure. Finally, using film out-of-plane lattice parameter to estimate δ, we generated a magnetic phase diagram for $x = 0.5$ LSCO films as a function of oxygen stoichiometry. This work not only demonstrates the effectiveness of this convenient approach to quantifying δ, but also reveals key mechanistic details of the P-BM transformation in films and maps the δ dependence of the magnetic properties for this technologically relevant cobaltite.

Chapter 7: Summary and outlook

In total, the work presented in this thesis significantly advances the understanding of the voltage-induced P-BM transformation in cobaltite thin films. We demonstrated the viability of electrochemical ion-gel-gating to control the P-BM topotactic transformation across the LSCO phase diagram, including in the $x = 0.5$ composition, where both phases are robustly air stable, presenting an attractive alternative to SCO-based devices. In doing this, we were able to realize reversible control over various materials properties, spanning extraordinary ranges of electronic transport, magnetism, thermal, and optical properties. By carefully studying the voltage hysteresis loops, we also revealed key mechanistic details about the P-BM transformation, including its first-order nature and inherent asymmetry. While exploring the limits of reversibility in ultrathin (10 unit cell) films, we identified 1^{st}-cycle structural degradation, including surface roughening, as a primary driver of loop non-closure and incomplete recovery. Using minor hysteresis loop analysis, we further performed the first rational design of an optimized V_g cycle for ion-gel-gated LSCO devices. Finally, we provided the first direct evidence of AF order in BM-SCO thin films, while uncovering an unexpected weak F signal in $x = 0.5$ BM-LSCO, warranting future study. Such contributions set the stage for further development toward functional devices based on electrochemically induced P-BM transformations in cobaltite films.

Moving forward, the biggest questions are undoubtedly related to cycling endurance and speed of ion-gel-gated LSCO P ↔ BM transformations, *i.e.*, how fast can switching be made to occur? and over how many cycles? Some investigations toward this end have already been initiated (see Appendix A), but these issues are far from trivial and would likely require many detailed studies to address comprehensively. Regarding speed, the work in this thesis was entirely performed using side-gated devices, in which ions in the gel had to move macroscopic distances to form EDLs and subsequently induce electrochemistry. (In our work switching the fastest switching speeds were of the order of minutes). An obvious adaptation to the device geometry to boost speed would be to move to a "top gate" design (the more traditional setup for a FET), to reduce the time for EDL formation, thus allowing the electrochemistry needed for switching to start sooner. From purely *electrostatic* EDLT experiments this strategy has already led to device operating

speeds in excess of 1 MHz [187]. However, in electrochemical EDLTs ion speed in the gel is only half the battle, as time is also needed for electrochemical redox reactions to occur, and for diffusion of ionic species into / out of the channel material. To speed up these processes, several strategies could be employed and studied, such as higher temperatures (perhaps using alternative IL / gel materials) or back-contact device geometries. The latter is an interesting concept that has yet to see widespread adoption in the field, but has produced some promising results [314].

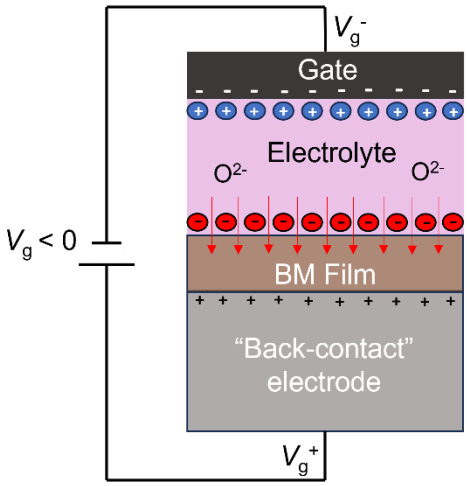

Figure 7.1: Schematic representation of a "back-contacted" electrochemical EDLT device (operated at negative voltage, *i.e.*, $V_g < 0$). The simplest implementation of this idea involves a film grown on an electrically conductive substrate, where the substrate itself then serves as the counter-electrode to the gate. In this setup, the migrating ions (in this case O^{2-}) are driven into the film by both initial concentration gradient (diffusion) *and* a potential gradient of the applied V_g.

In a back contacted EDLT device, the potential applied between the gate and channel (V_g) is dropped through the thickness of the channel. In other words, the contact electrode (*i.e.*, the counter electrode to the gate) is a uniform layer *underneath* the film channel, rather than on top of the film, as shown schematically in Fig. 7.1. This leads to chemical-potential-assisted diffusion rather than purely concentration-gradient-driven diffusion. Such a strategy has the potential to significantly increase the speed and completeness of a transformation, especially for highly resistive channel materials, *e.g.*, insulators such as BM. However, it does have some notable limitations. For instance, the back contact material must be suitable to the design of the device (*i.e.*, one needs to be able to grow high-quality films on top of it), it must be itself resistant to electrochemistry, and, importantly, it necessarily precludes electronic-transport-based device function (as the

back contact acts as an electrical shunt). Nevertheless, this strategy has been implemented in ion-gel-gate devices based on $SrFeO_{2.5}$ films grown on conductive Nb:STO substrates (where the Nb:STO substrate *is* the back contact) [314]. Lefler *et al*. used this setup to electrochemically gate highly resistive as-deposited films of BM-$SrFeO_{2.5}$ to produce fully oxygenated P-$SrFeO_3$, whereas a traditional top-contact design was found to be prohibitively slow and ineffective under comparable conditions [314].

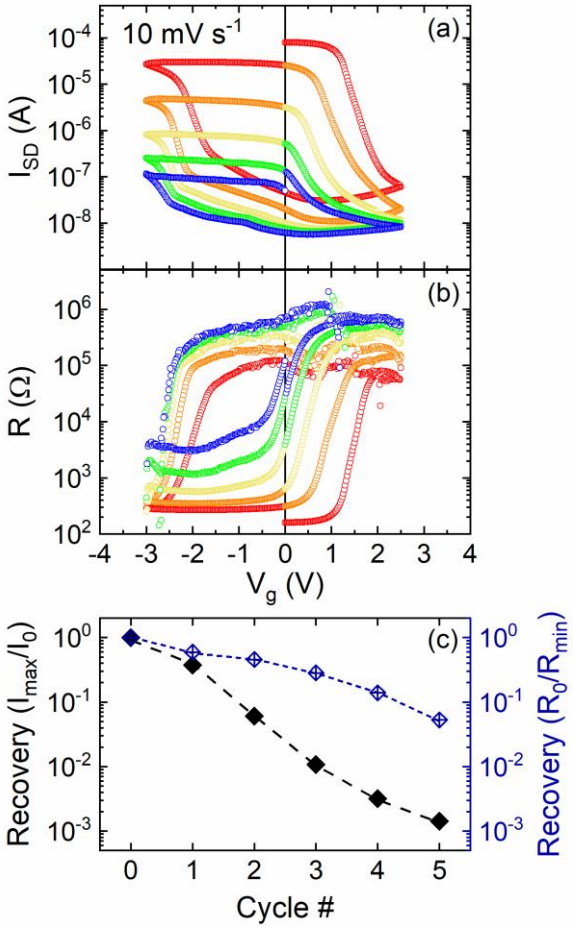

Figure 7.2: (a) Source-drain current (I_{SD}) *vs*. gate voltage (V_g) hysteresis loops for an ion-gel-gated 10 u.c. x = 0.5 LSCO film on LAO substrate. (b) four-terminal resistance (R) *vs*. V_g for the same film as in (a). The different colored loops represent sequentially increasing loop cycle number, *i.e*., red = loop 1, orange = loop 2, yellow = loop 3, green = loop 4, and blue = loop 5. (c) Recovery ratio for hysteresis loops shown in (a) and (b), where the black points (left axis) correspond to the two-terminal I_{SD} (panel (a)) recovery ratio: I_{max}/I_0, and the blue points (right axis) correspond to the four-terminal R (panel b) recovery ratio: R_0/R_{min}. Ion-gel gating was performed at 300 K, in vacuum (< 10^{-5} Torr), using a sweep rate of 10 mV s^{-1} (Notably, 10-times faster than in Chapter 5).

Exploring the limits of endurance, and ultimately pushing them, may be relatively more complex compared to the issue of speed. In our ion-gel-gated cobaltite films, the primary limitation in terms of endurance was found to be degradation of the source-drain

electrical contacts to the film, causing measurement of film electronic properties over multiple cycles to be unreliable or impossible. This observation is shown explicitly in Fig. 7.2. In panel (a) and (c), I_{SD} *vs.* V_g and four-terminal resistance, R, *vs.* V_g hysteresis loops are shown, respectively, over multiple cycles for an optimized V_g range (as determined from Section 5.4). Then, in panel (c) the recovery in terms of I_{SD} (*i.e.*, I_{max}/I_0) is compared to the recovery in terms of R (R_0/R_{min}). Clearly, the recovery of the device drops at higher cycle number in both cases, but the two-terminal (and thus contact-resistance-dependent) I_{SD} recovery drops off *much* faster than that of the four-terminal resistance, which is independent of the contact resistance. We therefore believe that the cycling endurance of our devices may be, in reality, much higher, but we simply cannot measure it beyond a certain point due to the contact degradation issue (which is of unknown origin). Resolving this issue of contact degradation, perhaps through improved device design, *e.g.*, protecting electrode contacts with an isolation layer, is a priority going forward.

Longer term, the issue of cycling endurance in such devices, will no doubt require further understanding of the mechanisms of electrochemistry involved in film oxidation and reduction. As described in Chapter 5, and elsewhere in the literature on electrolyte gated oxides, deleterious electrochemical effects in EDLTs are commonly reported. Moreover, even the processes which directly impart the functionality of such redox-based transistors, *i.e.*, oxygen species adsorption → oxidation → diffusion, are not fully understood in these systems. This is problematic, as promoting the necessary electrochemistry, while mitigating unwanted effects, *e.g.*, etching, ionic liquid breakdown, atmospheric contaminants, *etc.*, will be critical to the longevity of such devices. Fortunately, there are several promising strategies that should be explored to protect film surfaces and promote endurance in electrochemical transistors. One of these, which has so far been little explored, is to systematically investigate the effects of the chemistry of the ionic liquids and gels themselves. Many literature studies, at least in cobaltite EDLT systems, focus on a single IL: EMIM-TFSI. While this IL has proven successful over a few cycles in electrochemically gated SCO [97,124], there exist many ILs that remain unexplored in this context, some of which feature larger electrochemical stability windows [158,160,315,316]. Long-term endurance of such devices will likely require a

more systematic approach to optimizing the complex electrolyte / oxide interactions and environmental dependencies.

Beyond optimizing the electrolyte itself, inserting a protective layer between the film channel and the electrolyte may also prove beneficial to selectively promoting the wanted electrochemistry while mitigating adverse effects. Two possible routes to explore this are: (1) using a 2D material, such as hexagonal boron nitride (hBN), and (2) using an organic self-assembling layer (known as self-assembling monolayers, or SAM's). The former has already been successfully implemented in *electrostatic* IL EDLT's, proving to be effective in limiting the mobility-reducing coulombic scattering effects of the IL ions [321], but has yet to be explored in the context of *electrochemical* EDLTs.

Device speed and endurance are, for good reason, the most relevant areas to explore toward the development of application-ready devices, but there are other important material science considerations which also warrant further study. To conclude this chapter, I outline just a few relevant examples below:

(1) First, further exploration of the substitution / alloying effects of Fe for Co may be fruitful in raising the F T_C, to more application-friendly temperatures. For example, it has already been shown that 50:50 Co/Fe substitution in SCO, *i.e.*, $SrCo_{0.5}Fe_{0.5}O_{3-\delta}$, can be used to boost the F T_C significantly above room T [124], and such films were used to demonstrate room-T control of F in IL gated devices [124]. This idea has yet to be extended to the LSCO family, although some of our work does suggest a boost to T_C is possible with moderate Fe substitution. Fig. 7.3 summarizes our preliminary work investigating the impact of Fe substitution for Co on the F T_C in bulk LSCO powders, where an increase in T_C of ~20 K can be seen, in the best case. Due to the increased air-stability of the La-Sr compounds over their pure-Sr counterparts, even modest gains in T_C would likely make the study of electrolyte-gated $La_{1-x}Sr_xCo_{1-y}Fe_yO_{3-\delta}$ (LSCFO) films worthwhile.

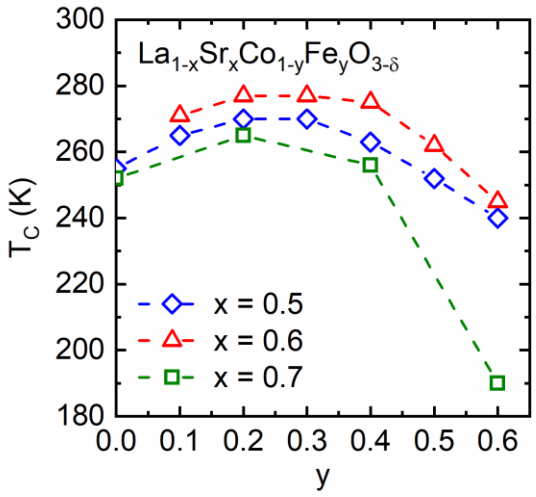

Figure 7.3: Ferromagnetic Curie temperature (T_C) *vs.* Fe-doping in the bulk mixed Co-Fe LSCO system, *i.e.*, $La_{1-x}Sr_xCo_{1-y}Fe_yO_{3-\delta}$. All samples were sintered at 1200 °C in 760 Torr O_2 for 24 hours. Like $SrCo_{1-y}Fe_yO_{3-\delta}$, Fe substitution can increase the T_C in these ferromagnetic cobaltites. Here, a boost in T_C of ~20 K is seen for $y \approx 0.2$ - 0.3. Note that the value of δ is not accurately known for these samples.

(2) Second, drawing on the discussion and open questions from Chapter 6, there is a clear need to further investigate the properties of the "OFF" state, *i.e.*, the non-F state in BM films. Our work in Chapter 6 confirmed the long-presumed G-type AF-order in BM-SCO thin films, but opened many questions as well, such as the origins of the significantly reduced T_N in films *vs.* the bulk, the nature of the underlying magnetic interactions in $x = 0.5$ BM (*e.g.*, canted-AF?), and the difference, if any, between the properties of thermally-induced BM *vs.* electrolyte-gating-induced BM. Additionally, in Chapter 6, we explored thin films of only two of potentially many important BM cobaltite / ferrite compositions, *e.g.*, $SrCo_{1-y}Fe_yO_{2.5}$, $La_{1-x}Sr_xCoO_{2.5}$, $La_{1-x}Sr_xCo_{1-y}Fe_yO_{2.5}$, *etc.*, many of which lack systematic property investigation in the existing literature (for both bulk and films). Therefore, basic studies based on bulk fabrication and characterization, including, for instance, thermogravimetric analysis, *T*-dependent XRD, neutron powder diffraction, and magnetometry, would no doubt provide a great benefit to future research around this critically important class of magnetic materials.

References

[1] R. Ramesh and S. Manipatruni, *Electric Field Control of Magnetism*, Proc. R. Soc. A. **477**, 20200942 (2021).

[2] T. Na, S. H. Kang, and S.-O. Jung, *STT-MRAM Sensing: A Review*, IEEE Trans. Circuits Syst. II **68**, 12-18 (2021).

[3] G. George, S. Rao Ede, and Z. Luo, *Fundamentals of Perovskite Oxides: Synthesis, Structure, Properties and Applications* (CRC Press, New York, 2021).

[4] P. Yadav, S. Yadav, S. Atri, and R. Tomar, *A Brief Review on Key Role of Perovskite Oxides as Catalyst*, ChemistrySelect **6**, 12947-12959 (2021).

[5] D. Li, D. Zhang, K.-S. Lim, Y. Hu, Y. Rong, A. Mei, N.-G. Park, and H. Han, *A Review on Scaling Up Perovskite Solar Cells*, Adv. Funct. Mater. **31**, 2008621 (2021).

[6] M. Z. Ahmad, S. H. Ahmad, R. S. Chen, A. F. Ismail, R. Hazan, and N. A. Baharuddin, *Review on Recent Advancement in Cathode Material for Lower and Intermediate Temperature Solid Oxide Fuel Cells Application*, Int. J. of Hydrog. Energy **47**, 1103-1120 (2022).

[7] E. Dagotto, *Correlated Electrons in High-Temperature Superconductors*, Rev. Mod. Phys. **66**, 763-840 (1994).

[8] H. Y. Hwang, Y. Iwasa, M. Kawasaki, B. Keimer, N. Nagaosa, and Y. Tokura, *Emergent Phenomena at Oxide Interfaces*, Nat. Mater. **11**, 103-113 (2012).

[9] G. H. Haertling, *Ferroelectric Ceramics: History and Technology*, J. Am. Ceram. Soc. **82**, 797-818 (1999).

[10] A. S. Bhalla, R. Guo, and R. Roy, *The Perovskite Structure—a Review of Its Role in Ceramic Science and Technology*, Mat. Res. Innovat. **4**, 3-26 (2000).

[11] T. Nuns, S. Duzellier, J. Bertrand, G. Hubert, V. Pouget, F. Darracq, J.-P. David, and S. Soonckindt, *Evaluation of Recent Technologies of Non-Volatile RAM*, in *2007 9th European Conference on Radiation and Its Effects on Components and Systems* (IEEE, Deauville, 2007).

[12] U. Muller, *Inorganic Structural Chemistry*, 2nd ed. (John Wiley & Sons, Sussex, England, 2006).

[13] J. B. Goodenough, *Electronic and Ionic Transport Properties and Other Physical Aspects of Perovskites*, Rep. Prog. Phys. **67**, 1915-1993 (2004).

[14] G. H. Kwei, A. C. Lawson, S. J. L. Billinge, and S.-W. Cheong, *Structures of the Ferroelectric Phases of Barium Titanate*, J. Phys. Chem. **97**, 2368-2377 (1993).

[15] D. Pelc, M. Vučković, M. S. Grbić, M. Požek, G. Yu, T. Sasagawa, M. Greven, and N. Barišić, *Emergence of Superconductivity in the Cuprates via a Universal Percolation Process*, Nat. Commun. **9**, 4327 (2018).

[16] A. P. Mackenzie and Y. Maeno, *The Superconductivity of Sr_2RuO_4 and the Physics of Spin-Triplet Pairing*, Rev. Mod. Phys. **75**, 657-712 (2003).

[17] A. Kovalevsky, V. Kharton, E. Naumovich, F. Marques, and J. Frade, *Ionic Transport in Perovskite-Related Mixed Conductors: Ferrite-, Cobaltite-, Nickelate-, and Gallate-Based Systems*, in *Mixed Ionic Electronic Conducting Perovskites for Advanced Energy Systems* (Springer Dordrecht, 2004), pp. 109-122.

[18] P. M. Grant, R. B. Beyers, E. M. Engler, G. Lim, S. S. P. Parkin, M. L. Ramirez, V. Y. Lee, A. Nazzal, J. E. Vazquez, and R. J. Savoy, *Superconductivity above 90 K in the Compound $YBa_2Cu_3O_x$: Structural, Transport, and Magnetic Properties*, Phys. Rev. B **35**, 7242-7244 (1987).

[19] J. M. D. Coey, M. Viret, and S. von Molnár, *Mixed-Valence Manganites*, Adv. Phys. **48**, 167-293 (1999).

[20] E. Dagotto, T. Hotta, and A. Moreo, *Colossal Magnetoresistant Materials: The Key Role of Phase Separation*, Phys. Rep. **344**, 1-153 (2001).

[21] R. E. Cohen, *Origin of Ferroelectricity in Perovskite Oxides*, Nature **358**, 136-138 (1992).

[22] J. Wang, J. B. Neaton, H. Zheng, V. Nagarajan, S. B. Ogale, B. Liu, D. Viehland, V. Vaithyanathan, D. G. Schlom, U. V. Waghmare, N. A. Spaldin, K. M. Rabe, M. Wuttig, and R. Ramesh, *Epitaxial $BiFeO_3$ Multiferroic Thin Film Heterostructures*, Science **299**, 1719-1722 (2003).

[23] T. Kimura, S. Kawamoto, I. Yamada, M. Azuma, M. Takano, and Y. Tokura, *Magnetocapacitance Effect in Multiferroic $BiMnO_3$*, Phys. Rev. B **67**, 180401 (2003).

[24] S. Jin, T. H. Tiefel, M. McCormack, R. A. Fastnacht, R. Ramesh, and L. H. Chen, *Thousandfold Change in Resistivity in Magnetoresistive La-Ca-Mn-O Films*, Science **264**, 413-415 (1994).

[25] H. J. Kim, U. Kim, H. M. Kim, T. H. Kim, H.S. Mun, B.-G. Jeon, K. T. Hong, W.-J. Lee, C. Ju, K. H. Kim, and K. Char, *High Mobility in a Stable Transparent Perovskite Oxide*, Appl. Phys. Express **5**, 061102 (2012).

[26] D. G. Schlom, L.-Q. Chen, X. Pan, A. Schmehl, and M. A. Zurbuchen, *A Thin Film Approach to Engineering Functionality into Oxides*, J. Am. Ceram. Soc. **91**, 2429-2454 (2008).

[27] A. Biswas, K.-S. Kim, and Y. H. Jeong, *Metal-Insulator Transitions and Non-Fermi Liquid Behaviors in 5d Perovskite Iridates*, in *Perovskite Materials - Synthesis, Characterization, Properties, and Applications* (IntechOpen, 2016), pp. 221-259.

[28] R. Schmidt, J. Wu, C. Leighton, and I. Terry, *Dielectric Response to the Low-Temperature Magnetic Defect Structure and Spin State Transition in Polycrystalline $LaCoO_3$*, Phys. Rev. B **79**, 125105 (2009).

[29] A. Szewczyk, M. Gutowska, and B. Dabrowski, *Specific Heat and Phase Diagram of Heavily Doped $La_{1-x}Sr_xMnO_3$ ($0.45 \leqslant x \leqslant 1.0$)*, Phys. Rev. B **72**, 224429 (2005).

[30] A. Bhattacharya and S. J. May, *Magnetic Oxide Heterostructures*, Annu. Rev. Mater. Res. **44**, 65-90 (2014).

[31] D. Khomskii, *Electronic Structure, Exchange and Magnetism in Oxides*, in *Spin Electronics* (Springer Berlin, Heidelberg, 2001), pp. 89-116.

[32] S. V. Streltsov and D. I. Khomskii, *Orbital Physics in Transition Metal Compounds: New Trends*, Phys.-Uspekhi **60**, 1121-1146 (2017).

[33] D. Fuchs, C. Pinta, T. Schwarz, P. Schweiss, P. Nagel, S. Schuppler, R. Schneider, M. Merz, G. Roth, and H. v. Löhneysen, *Ferromagnetic Order in Epitaxially Strained $LaCoO_3$ Thin Films*, Phys. Rev. B **75**, 144402 (2007).

[34] A. Biswas and Y. H. Jeong, *Strain Effect in Epitaxial Oxide Heterostructures*, in *Epitaxy* (InTech, Rijeka, Croatia, 2018), pp. 3-44.

[35] R. Ramesh, *Complex Functional Oxide Heterostructures*, CURRENT SCIENCE **105**, 1107-1114 (2013).

[36] P. Zubko, S. Gariglio, M. Gabay, P. Ghosez, and J.-M. Triscone, *Interface Physics in Complex Oxide Heterostructures*, Annu. Rev. Condens. Matter Phys. **2**, 141-165 (2011).

[37] J. M. Rondinelli, S. J. May, and J. W. Freeland, *Control of Octahedral Connectivity in Perovskite Oxide Heterostructures: An Emerging Route to Multifunctional Materials Discovery*, MRS Bull. **37**, 261-270 (2012).

[38] A. Ohtomo and H. Y. Hwang, *A High-Mobility Electron Gas at the $LaAlO_3/SrTiO_3$ Heterointerface*, Nature **427**, 423-426 (2004).

[39] F. M. Granozio, G. Koster, and G. Rijnders, *Functional Oxide Interfaces*, MRS Bull. **38**, 1017-1023 (2013).

[40] P. M. Raccah and J. B. Goodenough, *First-Order Localized-Electron ⇆ Collective-Electron Transition in $LaCoO_3$*, Phys. Rev. **155**, 932-943 (1967).

[41] S. Yamaguchi, Y. Okimoto, H. Taniguchi, and Y. Tokura, *Spin-State Transition and High-Spin Polarons in $LaCoO_3$*, Phys. Rev. B **53**, R2926-R2929 (1996).

[42] M. A. Korotin, S. Yu. Ezhov, I. V. Solovyev, V. I. Anisimov, D. I. Khomskii, and G. A. Sawatzky, *Intermediate-Spin State and Properties of $LaCoO_3$*, Phys. Rev. B **54**, 5309-5316 (1996).

[43] M. Imada, A. Fujimori, and Y. Tokura, *Metal-Insulator Transitions*, Rev. Mod. Phys. **70**, 1039-1263 (1998).

[44] S. R. English, J. Wu, and C. Leighton, *Thermally Excited Spin-Disorder Contribution to the Resistivity of $LaCoO_3$*, Phys. Rev. B **65**, 220407 (2002).

[45] R. F. Klie, J. C. Zheng, Y. Zhu, M. Varela, J. Wu, and C. Leighton, *Direct Measurement of the Low-Temperature Spin-State Transition in $LaCoO_3$*, Phys. Rev. Lett. **99**, 047203 (2007).

[46] A. Mineshige, M. Inaba, T. Yao, Z. Ogumi, K. Kikuchi, and M. Kawase, *Crystal Structure and Metal–Insulator Transition of $La_{1-x}Sr_xCoO_3$*, J. Solid State Chem. **121**, 423-429 (1996).

[47] V. V. Mehta, N. Biškup, C. Jenkins, E. Arenholz, M. Varela, and Y. Suzuki, *Long-Range Ferromagnetic Order in $LaCoO_{3-\delta}$ Epitaxial Films Due to the Interplay of Epitaxial Strain and Oxygen Vacancy Ordering*, Phys. Rev. B **91**, 144418 (2015).

[48] V. Chaturvedi, J. Walter, A. Paul, A. Grutter, B. Kirby, J. S. Jeong, H. Zhou, Z. Zhang, B. Yu, M. Greven, K. A. Mkhoyan, T. Birol, and C. Leighton, *Strain-Induced Majority Carrier Inversion in Ferromagnetic Epitaxial $LaCoO_{3-\delta}$ Thin Films*, Phys. Rev. Materials **4**, 034403 (2020).

[49] D. Fuchs, E. Arac, C. Pinta, S. Schuppler, R. Schneider, and H. v. Löhneysen, *Tuning the Magnetic Properties of $LaCoO_3$ Thin Films by Epitaxial Strain*, Phys. Rev. B **77**, 014434 (2008).

[50] D. Li, H. Wang, K. Li, B. Zhu, K. Jiang, D. Backes, L. S. I. Veiga, J. Shi, P. Roy, M. Xiao, A. Chen, Q. Jia, T.-L. Lee, S. S. Dhesi, D. O. Scanlon, J. L. MacManus-Driscoll, P. A. van Aken, K. H. L. Zhang, and W. Li, *Emergent and Robust Ferromagnetic-Insulating State in Highly Strained Ferroelastic $LaCoO_3$ Thin Films*, Nat. Commun. **14**, 3638 (2023).

[51] N. Biškup, J. Salafranca, V. Mehta, M. P. Oxley, Y. Suzuki, S. J. Pennycook, S. T. Pantelides, and M. Varela, *Insulating Ferromagnetic $LaCoO_{3-\delta}$ Films: A Phase Induced by Ordering of Oxygen Vacancies*, Phys. Rev. Lett. **112**, 087202 (2014).

[52] J. Gazquez, S. Bose, M. Sharma, M. A. Torija, S. J. Pennycook, C. Leighton, and M. Varela, *Lattice Mismatch Accommodation via Oxygen Vacancy Ordering in Epitaxial $La_{0.5}Sr_{0.5}CoO_{3-\delta}$ Thin Films*, APL Mater. **1**, 012105 (2013).

[53] D. O. Klenov, W. Donner, B. Foran, and S. Stemmer, *Impact of Stress on Oxygen Vacancy Ordering in Epitaxial $(La_{0.5}Sr_{0.5})CoO_{3-\delta}$ Thin Films*, Appl. Phys. Lett. **82**, 3427-3429 (2003).

[54] S. Stemmer, A. J. Jacobson, X. Chen, and A. Ignatiev, *Oxygen Vacancy Ordering in Epitaxial $La_{0.5}Sr_{0.5}CoO_{3-\delta}$ Thin Films on (001) $LaAlO_3$*, J. of Appl. Phys. **90**, 3319-3324 (2001).

[55] A. Podlesnyak, M. Russina, A. Furrer, A. Alfonsov, E. Vavilova, V. Kataev, B. Büchner, Th. Strässle, E. Pomjakushina, K. Conder, and D. I. Khomskii, *Spin-State Polarons in Lightly-Hole-Doped $LaCoO_3$*, Phys. Rev. Lett. **101**, 247603 (2008).

[56] A. Alfonsov, E. Vavilova, V. Kataev, B. Büchner, A. Podlesnyak, M. Russina, A. Furrer, Th. Strässle, E. Pomjakushina, K. Conder, and D. I. Khomskii, *Origin of a Spin-State Polaron in Lightly Hole Doped $LaCoO_3$*, J. Phys.: Conf. Ser. **150**, 042003 (2009).

[57] A. Podlesnyak, G. Ehlers, M. Frontzek, A. S. Sefat, A. Furrer, Th. Strässle, E. Pomjakushina, K. Conder, F. Demmel, and D. I. Khomskii, *Effect of Carrier Doping on the Formation and Collapse of Magnetic Polarons in Lightly Hole-Doped $La_{1-x}Sr_xCoO_3$*, Phys. Rev. B **83**, 134430 (2011).

[58] M. A. Señarís-Rodríguez and J. B. Goodenough, *Magnetic and Transport Properties of the System $La_{1-x}Sr_xCoO_{3-\delta}$ $(0 < x \leq 0.5)$*, J. Solid State Chem. **118**, 323-336 (1995).

[59] J. Wu and C. Leighton, *Glassy Ferromagnetism and Magnetic Phase Separation in $La_{1-x}Sr_xCoO_3$*, Phys. Rev. B **67**, 174408 (2003).

[60] H. M. Aarbogh, J. Wu, L. Wang, H. Zheng, J. F. Mitchell, and C. Leighton, *Magnetic and Electronic Properties of $La_{1-x}Sr_xCoO_3$ Single Crystals across the Percolation Metal-Insulator Transition*, Phys. Rev. B **74**, 134408 (2006).

[61] C. He, S. El-Khatib, J. Wu, J. W. Lynn, H. Zheng, J. F. Mitchell, and C. Leighton, *Doping Fluctuation-Driven Magneto-Electronic Phase Separation in $La_{1-x}Sr_xCoO_3$ Single Crystals*, Europhys. Lett. **87**, 27006 (2009).

[62] R. X. Smith, M. J. R. Hoch, P. L. Kuhns, W. G. Moulton, A. P. Reyes, G. S. Boebinger, J. Mitchell, and C. Leighton, *Spin Polarons in $La_{1-x}Sr_xCoO_3$ Single Crystals*, Phys. Rev. B **78**, 092201 (2008).

[63] P. P. Orth, D. Phelan, J. Zhao, H. Zheng, J. F. Mitchell, C. Leighton, and R. M. Fernandes, *Essential Role of Magnetic Frustration in the Phase Diagrams of Doped Cobaltites*, Phys. Rev. Mater. **6**, L071402 (2022).

[64] R. H. E. van Doorn and A. J. Burggraaf, *Structural Aspects of the Ionic Conductivity of $La_{1-x}Sr_xCoO_{3-\delta}$*, Solid State Ion. **128**, 65-78 (2000).

[65] J. Mastin, M.-A. Einarsrud, and T. Grande, *Structural and Thermal Properties of $La_{1-x}Sr_xCo_{3-\delta}$*, Chem. Mater. **18**, 6047-6053 (2006).

[66] G. H. Jonker and J. H. Van Santen, *Magnetic Compounds with Perovskite Structure III. Ferromagnetic Compounds of Cobalt*, Physica **19**, 120-130 (1953).

[67] A. Grimaud, O. Diaz-Morales, B. Han, W. T. Hong, Y.-L. Lee, L. Giordano, K. A. Stoerzinger, M. T. M. Koper, and Y. Shao-Horn, *Activating Lattice Oxygen Redox Reactions in Metal Oxides to Catalyse Oxygen Evolution*, Nat. Chem. **9**, 457-465 (2017).

[68] J. Mizusaki, Y. Mima, S. Yamauchi, and K. Fueki, *Nonstoichiometry of the Perovskite-Type Oxides $La_{1-x}Sr_xCoO_{3-\delta}$*, J. Solid State Chem. **80**, 102-111 (1989).

[69] J. T. Mefford, X. Rong, A. M. Abakumov, W. G. Hardin, S. Dai, A. M. Kolpak, K. P. Johnston, and K. J. Stevenson, *Water Electrolysis on $La_{1-x}Sr_xCoO_{3-\delta}$ Perovskite Electrocatalysts*, Nat. Commun. **7**, 11053 (2016).

[70] V. Vibhu, S. Yildiz, I. C. Vinke, R.-A. Eichel, J.-M. Bassat, and L. G. J. de Haart, *High Performance LSC Infiltrated LSCF Oxygen Electrode for High Temperature Steam Electrolysis Application*, J. Electrochem. Soc. **166**, F102-F108 (2019).

[71] S. P. Jiang, *Development of Lanthanum Strontium Cobalt Ferrite Perovskite Electrodes of Solid Oxide Fuel Cells – A Review*, Int. J. Hydrog. Energy **44**, 7448-7493 (2019).

[72] S. Kolesnik, B. Dabrowski, J. Mais, M. Majjiga, O. Chmaissem, A. Baszczuk, and J. D. Jorgensen, *Tuning of Magnetic and Electronic States by Control of Oxygen Content in Lanthanum Strontium Cobaltites*, Phys. Rev. B **73**, 214440 (2006).

[73] S. Ramesh, S. S. Manohara, M. S. Hedge, *Synthesis and Structure of Oxygen-Deficient La_2NiCoO_5 and $LaSrCo_2O_5$ Phases*, J. Mater. Chem. **5**, 1053-1057 (1995).

[74] H. Watanabe, *Magnetic Properties of Perovskites Containing Strontium I. Strontium-Rich Ferrites and Cobaltites*, J. Phys. Soc. of Jpn. **12**, 515-522 (1957).

[75] Y. Takeda, R. Kanno, T. Takada, O. Yamamoto, M. Takano, and Y. Bando, *Phase Relation and Oxygen-non-stoichiometry of Perovskite-Like Compound $SrCoO_x$ ($2.29 < x < 2.80$)*, Z. Anorg. Allg. Chem. **540/541**, 259-270 (1986).

[76] P. Bezdicka, A. Wattiaux, J. C. Grenier, M. Pouchard, and P. Hagenmuller, *Preparation and Characterization of Fully Stoichiometric $SrCoO_3$ by Electrochemical Oxidation*, Z. Anorg. Allg. Chem. **619**, 7-12 (1993).

[77] A. Nemudry, P. Rudolf, and R. Schöllhorn, *Topotactic Electrochemical Redox Reactions of the Defect Perovskite $SrCoO_{2.5+x}$*, Chem. Mater. **8**, 2232-2238 (1996).

[78] Y. Long, Y. Kaneko, S. Ishiwata, Y. Taguchi, and Y. Tokura, *Synthesis of Cubic $SrCoO_3$ Single Crystal and Its Anisotropic Magnetic and Transport Properties*, J. Phys.: Condens. Matter **23**, 245601 (2011).

[79] D. Zhang, H. Ishizuka, N. Lu, Y. Wang, N. Nagaosa, P. Yu, and Q.-K. Xue, *Anomalous Hall Effect and Spin Fluctuations in Ionic Liquid Gated $SrCoO_3$ Thin Films*, Phys. Rev. B **97**, 184433 (2018).

[80] A. V. Ushakov, S. V. Streltsov, and D. I. Khomskii, *Crystal Field Splitting in Correlated Systems with Negative Charge-Transfer Gap*, J. Phys.: Condens. Matter **23**, 445601 (2011).

[81] B. Raveau and Md. M. Seikh, *Cobalt Oxides From Crystal Chemistry to Phsyics* (Wiley-VCH Verlag & Co. KGaA, Weinheim, Germany, 2012).

[82] R. H. Potze, G. A. Sawatzky, and M. Abbate, *Possibility for an Intermediate-Spin Ground State in the Charge-Transfer Material $SrCoO_3$*, Phys. Rev. B **51**, 11501-11506 (1995).

[83] M. Abbate, G. Zampieri, J. Okamoto, A. Fujimori, S. Kawasaki, and M. Takano, *X-Ray Absorption of the Negative Charge-Transfer Material $SrFe_{1-x}Co_xO_3$*, Phys. Rev. B **65**, 165120 (2002).

[84] J. Kuneš, V. Křápek, N. Parragh, G. Sangiovanni, A. Toschi, and A. V. Kozhevnikov, *Spin State of Negative Charge-Transfer Material $SrCoO_3$*, Phys. Rev. Lett. **109**, 117206 (2012).

[85] M. C. Bennett, G. Hu, G. Wang, O. Heinonen, P. R. C. Kent, J. T. Krogel, and P. Ganesh, *Origin of Metal-Insulator Transitions in Correlated Perovskite Metals*, Phys. Rev. Res. *4*, L022005 (2022).

[86] D. Khomskii, *Unusual Valence, Negative Charge-Transfer Gaps and Self-Doping in Transition-Metal Compounds*, Lith. J. Phys. **37**, 1-12 (2001).

[87] R. B. Wexler, G. S. Gautam, E. B. Stechel, and E. A. Carter, *Factors Governing Oxygen Vacancy Formation in Oxide Perovskites*, J. Am. Chem. Soc. **143**, 13212-13227 (2021).

[88] A. Nemudry, E. L. Goldberg, M. Aguirre, and M. Á. Alario-Franco, *Electrochemical Topotactic Oxidation of Nonstoichiometric Perovskites at Ambient Temperature*, Solid State Sci. **4**, 677-690 (2002).

[89] R. A. De Souza, *Oxygen Diffusion in $SrTiO_3$ and Related Perovskite Oxides*, Adv. Funct. Mater. **25**, 6326-6342 (2015).

[90] R. Le Toquin, W. Paulus, A. Cousson, C. Prestipino, and C. Lamberti, *Time-Resolved in Situ Studies of Oxygen Intercalation into $SrCoO_{2.5}$, Performed by Neutron Diffraction and X-Ray Absorption Spectroscopy*, J. Am. Chem. Soc. **128**, 13161-13174 (2006).

[91] L. Karvonen, H. Yamauchi, and M. Karppinen, *Homologous Series of $SrCoO_{(3n-1)/n}$ Perovskites Obtained Through Br_2 Oxygenation of $SrCoO_{2.5}$*, Chem. Mater. **20**, 7143-7147 (2008).

[92] L. Karvonen, S. Yoon, P. Hug, H. Yamauchi, A. Weidenkaff, and M. Karppinen, *The n = 3 Member of the $SrCoO_{(3n-1)/n}$ Series of Layered Oxygen-Defect Perovskites*, MRS Bull. **46**, 1340-1345 (2011).

[93] A. Muñoz, C. de la Calle, J. A. Alonso, P. M. Botta, V. Pardo, D. Baldomir, and J. Rivas, *Crystallographic and Magnetic Structure of $SrCoO_{2.5}$ Brownmillerite: Neutron Study Coupled with Band-Structure Calculations*, Phys. Rev. B **78**, 054404 (2008).

[94] C. Mitra, T. Meyer, H. N. Lee, and F. A. Reboredo, *Oxygen Diffusion Pathways in Brownmillerite $SrCoO_{2.5}$: Influence of Structure and Chemical Potential*, J. Chem. Phys. **141**, 084710 (2014).

[95] H. A. Tahini, X. Tan, U. Schwingenschlögl, and S. C. Smith, *Formation and Migration of Oxygen Vacancies in $SrCoO_3$ and Their Effect on Oxygen Evolution Reactions*, ACS Catal. **6**, 5565-5570 (2016).

[96] Q. Zhang, G. Hu, V. Starchenko, G. Wan, E. M. Dufresne, Y. Dong, H. Liu, H. Zhou, H. Jeen, K. Saritas, J. T. Krogel, F. A. Reboredo, H. N. Lee, A. R. Sandy, I. C. Almazan, P. Ganesh, and D. D. Fong, *Phase Transition Dynamics in a Complex Oxide Heterostructure*, Phys. Rev. Lett. **129**, 235701 (2022).

[97] N. Lu, P. Zhang, Q. Zhang, R. Qiao, Q. He, H.-B. Li, Y. Wang, J. Guo, D. Zhang, Z. Duan, Z. Li, M. Wang, S. Yang, M. Yan, E. Arenholz, S. Zhou, W. Yang, L. Gu, C.-W. Nan, J. Wu, Y. Tokura, P. Yu, *Electric-Field Control of Tri-State Phase Transformation with a Selective Dual-Ion Switch*, Nature **546**, 124-128 (2017).

[98] F. Hong, B. Yue, Z. Liu, B. Chen, and H.-K. Mao, *Pressure-Driven Semiconductor-Semiconductor Transition and Its Structural Origin in Oxygen Vacancy Ordered $SrCoO_{2.5}$*, Phys. Rev. B **95**, 024115 (2017).

[99] S.-C. Tsang, J. Zhang, K. Tse, and J. Zhu, *Towards Understanding the Special Stability of $SrCoO_{2.5}$ and $HSrCoO_{2.5}$*, Phys. Rev. Mater. **3**, 024603 (2019).

[100] T. Takeda, Y. Yamaguchi, and H. Watanabe, *Magnetic Structure of $SrCoO_{2.5}$*, J. Phys. Soc. of Jpn. **33**, 970-972 (1972).

[101] J. C. Grenier, S. Ghodbane, and G. Demazeau, *Le Cobaltite de Strontium $Sr_2Co_2O_5$: Caracterisation et Proprietes Magnetiques*, MRS Bull. **14**, 831-839 (1979).

[102] J. Rodriguez, J. M. Gonzalez-Calbet, J. C. Grenier, J. Pannetier, and M. Anne, *Phase Transitions in $Sr_2Co_2O_5$: A Neutron Thermodiffractometry Study*, Solid State Commun. **62**, 231-234 (1987).

[103] C. de la Calle, A. Aguadero, J. A. Alonso, and M. T. Fernández-Díaz, *Correlation Between Reconstructive Phase Transitions and Transport Properties from $SrCoO_{2.5}$ Brownmillerite: A Neutron Diffraction Study*, Solid State Sci. **10**, 1924-1935 (2008).

[104] C. K. Xie, Y. F. Nie, B. O. Wells, J. I. Budnick, W. A. Hines, and B. Dabrowski, *Magnetic Phase Separation in $SrCoO_x$ ($2.5 \leq x \leq 3$)*, Appl. Phys. Lett. **99**, 052503 (2011).

[105] M. A. Torija, M. Sharma, J. Gazquez, M. Varela, C. He, J. Schmitt, J. A. Borchers, M. Laver, S. El-Khatib, and C. Leighton, *Chemically Driven Nanoscopic Magnetic Phase Separation at the $SrTiO_3(001)/La_{1-x}Sr_xCoO_3$ Interface*, Adv. Mater. **23**, 2711-2715 (2011).

[106] J. Walter, Ion Gel Gating of Perovskite Cobaltite Thin Films: Understanding Mechanisms and Control of Magnetism, Ph.D. Thesis, University of Minnesota, 2018.

[107] J. Walter, S. Bose, M. Cabero, G. Yu, M. Greven, M. Varela, and C. Leighton, *Perpendicular Magnetic Anisotropy via Strain-Engineered Oxygen Vacancy Ordering in Epitaxial $La_{1-x}Sr_xCoO_{3-\delta}$*, Phys. Rev. Mater. **2**, 111404 (2018).

[108] J. Walter, S. Bose, M. Cabero, M. Varela, and C. Leighton, *Giant Anisotropic Magnetoresistance in Oxygen-Vacancy-Ordered Epitaxial $La_{0.5}Sr_{0.5}CoO_{3-\delta}$ Films*, Phys. Rev. Mater. **4**, 091401 (2020).

[109] S. Bose, Complexity at Cobaltite Interfaces: The Interplay between Strain, Stoichiometry, Magnetism and Transport, Ph.D. Thesis, University of Minnesota, 2014.

[110] W. S. Choi, H. Jeen, J. H. Lee, S. S. A. Seo, V. R. Cooper, K. M. Rabe, and H. N. Lee, *Reversal of the Lattice Structure in $SrCoO_x$ Epitaxial Thin Films Studied by Real-Time Optical Spectroscopy and First-Principles Calculations*, Phys. Rev. Lett. **111**, 097401 (2013).

[111] F. J. Rueckert, Y. F. Nie, C. Abughayada, S. A. Sabok-Sayr, H. E. Mohottala, J. I. Budnick, W. A. Hines, B. Dabrowski, and B. O. Wells, *Suppression of Magnetic Phase Separation in Epitaxial $SrCoO_x$ Films*, Appl. Phys. Lett. **102**, 152402 (2013).

[112] H. Jeen, W. S. Choi, M. D. Biegalski, C. M. Folkman, I.-C. Tung, D. D. Fong, J. W. Freeland, D. Shin, H. Ohta, M. F. Chisholm, H. N. Lee, *Reversible Redox Reactions in an Epitaxially Stabilized $SrCoO_x$ Oxygen Sponge*, Nat. Mater. **12**, 1057-1063 (2013).

[113] H. Jeen, W. S. Choi, J. W. Freeland, H. Ohta, C. U. Jung, and H. N. Lee, *Topotactic Phase Transformation of the Brownmillerite $SrCoO_{2.5}$ to the Perovskite $SrCoO_{3-\delta}$*, Adv. Mater. **25**, 3651-3656 (2013).

[114] H. Jeen and H. N. Lee, *Structural Evolution of Epitaxial $SrCoO_x$ Films Near Topotactic Phase Transition*, AIP Adv. **5**, 127123 (2015).

[115] S. Hu, Z. Yue, J. S. Lim, S. J. Callori, J. Bertinshaw, A. Ikeda-Ohno, T. Ohkochi, C.-H. Yang, X. Wang, C. Ulrich, J. Seidel, *Growth and Properties of Fully Strained $SrCoO_x$ ($x \approx 2.8$) Thin Films on $DyScO_3$*, Adv. Mater. Interfaces **2**, 1500012 (2015).

[116] S. Hu, C. Cazorla, F. Xiang, H. Ma, J. Wang, J. Wang, X. Wang, C. Ulrich, L. Chen, and J. Seidel, *Strain Control of Giant Magnetic Anisotropy in Metallic Perovskite $SrCoO_{3-\delta}$ Thin Films*, ACS Appl. Mater. Interfaces **10**, 22348-22355 (2018).

[117] Q. Lu, S. Huberman, H. Zhang, Q. Song, J. Wang, G. Vardar, A. Hunt, I. Waluyo, G. Chen, and B. Yildiz, *Bi-Directional Tuning of Thermal Transport in $SrCoO_x$ with Electrochemically Induced Phase Transitions*, Nat. Mater. **19**, 655-662 (2020).

[118] Y. Wang, Q. He, W. Ming, M.-H. Du, N. Lu, C. Cafolla, J. Fujioka, Q. Zhang, D. Zhang, S. Shen, Y. Lyu, A. T. N'Diaye, E. Arenholz, L. Gu, C. Nan, Y. Tokura, S. Okamoto, P. Yu, *Robust Ferromagnetism in Highly Strained $SrCoO_3$ Thin Films*, Phys. Rev. X **10**, 021030 (2020).

[119] S. Chowdhury, R. J. Choudhary, and D. M. Phase, *Time Evolution of the Structural, Electronic, and Magnetic Phases in Relaxed $SrCoO_3$ Thin Films*, ACS Appl. Electron. Mater. **3**, 5095-5101 (2021).

[120] S. Hu, Y. Wang, C. Cazorla, and J. Seidel, *Strain-Enhanced Oxygen Dynamics and Redox Reversibility in Topotactic $SrCoO_{3-\delta}$ ($0 < \delta \leq 0.5$)*, Chem. Mater. **29**, 708-717 (2017).

[121] J. Song, Y. Chen, H. Zhang, F. Han, J. Zhang, X. Chen, H. Huang, J. Zhang, H. Zhang, X. Yan, T. Khan, S. Qi, Z. Yang, F. Hu, B. Shen, and J. Sun, *Strong Anisotropy and Its Electric Tuning for Brownmillerite $SrCoO_{2.5}$ Films with Different Crystal Orientations*, Phys. Rev. Mater. **3**, 045801 (2019).

[122] H. Han, H. Deniz, and S. S. P. Parkin, *Strain-Driven Formation of Epitaxial Nanostructures in Brownmillerite Strontium Cobaltite Thin Films*, Proc. Natl. Acad. Sci. U.S.A. **120**, e2221651120 (2023).

[123] H. Wang, J. Song, W. Wang, Y. Chen, X. Shen, Y. Yao, J. Li, J. Sun, and R. Yu, *$SrCoO_{3-\delta}$ Microstructures in Perovskite-Brownmillerite Heterostructure*, J. Cryst. Growth **572**, 126278 (2021).

[124] S. Ning, Q. Zhang, C. Occhialini, R. Comin, X. Zhong, and C. A. Ross, *Voltage Control of Magnetism above Room Temperature in Epitaxial $SrCo_{1-x}Fe_xO_{3-\delta}$*, ACS Nano **14**, 8949-8957 (2020).

[125] H.-Y. Huang, C. Ge, Q.-H. Zhang, C.-X. Liu, J.-Y. Du, J.-K. Li, C. Wang, L. Gu, G.-Z. Yang, and K.-J. Jin, *Electrolyte-Gated Synaptic Transistor with Oxygen Ions*, Adv. Funct. Mater. **29**, 1902702 (2019).

[126] T. Miao, B. Cui, C. Huang, D. Wang, L. Liu, W. Liu, Y. Li, R. Chu, X. Ren, L. Liu, B. Cheng, G. Zhou, H. Qin, G. Xing, and J. Hu, *Gate-Tunable Anisotropic Oxygen Ion Migration in $SrCoO_x$: Toward Emerging Oxide-Based Artificial Synapses*, Adv. Intell. Syst. **5**, 2200287 (2023).

[127] S. Hu, W. Han, S. Hu, J. Seidel, J. Wang, R. Wu, J. Wang, J. Zhao, Z. Xu, M. Ye, and L. Chen, *Voltage-Controlled Oxygen Non-Stoichiometry in $SrCoO_{3-\delta}$ Thin Films*, Chem. Mater. **31**, 6117-6123 (2019).

[128] D. Wang, L. Meng, L. Wei, P. Shi, Y. Chen, S. Yan, Y. Tian, G. Liu, and L. Mei, *Reversible Phase Switching Between Antiferromagnetic $SrCoO_{2.5}$ and Ferromagnetic $SrCoO_{3-\delta}$ by a Flexible Solid-State Electrolyte Gate*, J. Magn. Magn. Mater. **496**, 165926 (2020).

[129] Q. Lu and B. Yildiz, *Voltage-Controlled Topotactic Phase Transition in Thin-Film $SrCoO_x$ Monitored by In Situ X-Ray Diffraction*, Nano Lett. **16**, 1186-1193 (2016).

[130] Q. Lu, Y. Chen, H. Bluhm, and B. Yildiz, *Electronic Structure Evolution of $SrCoO_x$ During Electrochemically Driven Phase Transition Probed by In Situ X-Ray Spectroscopy*, J. Phys. Chem. C **120**, 24148-24157 (2016).

[131] B. Cui, P. Werner, T. Ma, X. Zhong, Z. Wang, J. M. Taylor, Y. Zhuang, and S. S. P. Parkin, *Direct Imaging of Structural Changes Induced by Ionic Liquid Gating Leading to Engineered Three-Dimensional Meso-Structures*, Nat. Commun. **9**, 3055 (2018).

[132] H. Han, A. Sharma, H. L. Meyerheim, J. Yoon, H. Deniz, K.-R. Jeon, A. K. Sharma, K. Mohseni, C. Guillemard, M. Valvidares, P. Gargiani, and S. S. P. Parkin, *Control of Oxygen Vacancy Ordering in Brownmillerite Thin Films via Ionic Liquid Gating*, ACS Nano **16**, 6206-6214 (2022).

[133] Y. Zhuang, B. Cui, H. Yang, F. Gao, and S. S. P. Parkin, *Ionic Liquid Gate-Induced Modifications of Step Edges at $SrCoO_{2.5}$ Surfaces*, ACS Nano **14**, 8562-8569 (2020).

[134] J. Song, Y. Chen, X. Chen, H. Wang, T. Khan, F. Han, J. Zhang, H. Huang, J. Zhang, H. Zhang, H. Zhang, X. Yan, S. Qi, F. Hu, B. Shen, R. Yu, and J. Sun, *Tuning the Magnetic Anisotropy of $La_{2/3}Sr_{1/3}MnO_3$ by Controlling the Structure of $SrCoO_x$ in the Corresponding Bilayers Using Ionic-Liquid Gating*, Phys. Rev. Appl. **12**, 054016 (2019).

[135] T. Katayama, A. Chikamatsu, H. Kamisaka, Y. Yokoyama, Y. Hirata, H. Wadati, T. Fukumura, and T. Hasegawa, *Topotactic Synthesis of Strontium Cobalt Oxyhydride Thin Film with Perovskite Structure*, AIP Adv. **5**, 107147 (2015).

[136] J. Zhao, Y. Luo, J.-O. Wang, H. Qian, C. Liu, X. He, Q. Zhang, H. Huang, B. Zhang, S. Li, E. Guo, C. Ge, T. Yang, X. Li, M. He, L. Gu, K.-J. Jin, K. Ibrahim, and H. Guo, *Electronic Structure Evolutions Driven by Oxygen Vacancy in $SrCoO_{3-x}$ Films*, Sci. China Mater. **62**, 1162-1168 (2019).

[137] P. Schöffmann, S. Pütter, J. Schubert, W. Zander, J. Barthel, P. Zakalek, M. Waschk, R. Heller, and T. Brückel, *Tuning the Co/Sr Stoichiometry of $SrCoO_{2.5}$ Thin Films by RHEED Assisted MBE Growth*, Mater. Res. Express **7**, 116404 (2020).

[138] T. K. Andersen, S. Cook, G. Wan, H. Hong, L. D. Marks, and D. D. Fong, *Layer-by-Layer Epitaxial Growth of Defect-Engineered Strontium Cobaltites*, ACS Appl. Mater. Interfaces **10**, 5949-5958 (2018).

[139] H. Huang, J. Zhang, H. Zhang, F. Han, X. Chen, J. Song, J. Zhang, S. Qi, Y. Chen, J. Cai, F. Hu, B. Shen, and J. Sun, *Topotactic Transition Between Perovskite and Brownmillerite Phases for Epitaxial $LaCoO_{3-\delta}$ Films and Effects Thus Resulted*, J. Phys. D: Appl. Phys. **53**, 155003 (2020).

[140] Q. Zhang, A. Gao, F. Meng, Q. Jin, S. Lin, X. Wang, D. Xiao, C. Wang, K.-J. Jin, D. Su, E.-J. Guo, and L. Gu, *Near-Room Temperature Ferromagnetic Insulating State in Highly Distorted $LaCoO_{2.5}$ with CoO_5 Square Pyramids*, Nat. Commun. **12**, 1853 (2021).

[141] I.-T. Chiu, M.-H. Lee, S. Cheng. S. Zhang, L. Heki, Z. Zhang, Y. Mohtashami, P. N. Lapa, M. Feng, P. Shafer, A. T. N'Diaye, A. Mehta, J. A. Schuller, G. Galli, S. Ramanathan, Y. Zhu, I. K. Schuller, and Y. Takamurs, *Cation and Anion Topotactic Transformations in Cobaltite Thin Films Leading to Ruddlesden-Popper Phases*, Phys. Rev. Mater. **5**, 064416 (2021).

[142] D. A. Gilbert, A. J. Grutter, P. D. Murray, R. V. Chopdekar, A. M. Kane, A. L. Ionin, M. S. Lee, S. R. Spurgeon, B. J. Kirby, B. B Maranville, A. T. N'Diaye, A. Mehta, E. Arenholz, K. Liu, Y. Takamura, and J. A. Borchers, *Ionic Tuning of Cobaltites at the Nanoscale*, Phys. Rev. Mater. **2**, 104402 (2018).

[143] G. Rippy, L. Trinh, A. M. Kane, A. L. Ionin, M. S. Lee, R. V. Chopdekar, J. M. Christiansen-Salameh, D. A. Gilbert, A. J. Grutter, P. D. Murray, M. V. Holt, Z. Cai, K. Liu, Y. Takamura, and R. Kukreja, *X-Ray Nanodiffraction Studies of Ionically Controlled Nanoscale Phase Separation in Cobaltites*, Phys. Rev. Mater. **3**, 082001 (2019).

[144] C. H. Ahn, J.-M. Triscone, and J. Mannhart, *Electric Field Effect in Correlated Oxide Systems*, Nature **424**, 1015-1018 (2003).

[145] C. H. Ahn, A. Bhattacharya, M. D. Ventra, J. N. Eckstein, C. D. Frisbie, M. E. Gershenson, A. M. Goldman, I. H. Inoue, J. Mannhart, A. J. Millis, A. F. Morpurgo, D. Natelson, and J.-M. Triscone, *Electrostatic Modification of Novel Materials*, Rev. Mod. Phys. **78**, 1185-1212 (2006).

[146] N. Agarwal, *N-Channel Enhancement MOSFET Working and V-I Characteristics*, March 2023, https://www.electronicsforu.com/technology-trends/learn-electronics/n-channel-enhancement-mosfet-working-vi-graph.

[147] S. H. Kim, K. Hong, W. Xie, K. H. Lee, S. Zhang, T. P. Lodge, and C. D. Frisbie, *Electrolyte-Gated Transistors for Organic and Printed Electronics*, Adv. Mater. **25**, 1822-1846 (2013).

[148] S. Z. Bisri, S. Shimizu, M. Nakano, and Y. Iwasa, *Endeavor of Iontronics: From Fundamentals to Applications of Ion-Controlled Electronics*, Adv. Mater. **29**, 1607054 (2017).

[149] C. Leighton, *Electrolyte-Based Ionic Control of Functional Oxides*, Nature Mater **18**, 13-18 (2019).

[150] C. Navarro-Senent, A. Quintana, E. Menéndez, E. Pellicer, and J. Sort, *Electrolyte-Gated Magnetoelectric Actuation: Phenomenology, Materials, Mechanisms, and Prospective Applications*, APL Mater. **7**, 030701 (2019).

[151] A. Sood, A. D. Poletayev, D. A. Cogswell, P. M. Csernica, J. T. Mefford, D. Fraggedakis, M. F. Toney, A. M. Lindenberg, M. Z. Bazant, and W. C. Chueh, *Electrochemical Ion Insertion from the Atomic to the Device Scale*, Nat. Rev. Mater. **6**, 847-867 (2021).

[152] M. Nichterwitz, S. Honnali, M. Kutuzau, S. Guo, J. Zehner, K. Nielsch, and K. Leistner, *Advances in Magneto-Ionic Materials and Perspectives for Their Application*, APL Mater. **9**, 030903 (2021).

[153] C. Leighton, T. Birol, and J. Walter, *What Controls Electrostatic vs Electrochemical Response in Electrolyte-Gated Materials? A Perspective on Critical Materials Factors*, APL Mater. **10**, 040901 (2022).

[154] Y. Guan, H. Han, F. Li, G. Li, and S. S. P. Parkin, *Ionic Gating for Tuning Electronic and Magnetic Properties*, Annu. Rev. Mater. Res. **53**, 25-51 (2023).

[155] T. Fujimoto and K. Awaga, *Electric-Double-Layer Field-Effect Transistors with Ionic Liquids*, Phys. Chem. Chem. Phys. **15**, 8983-9006 (2013).

[156] H. Du, X. Lin, Z. Xu, and D. Chu, *Electric Double-Layer Transistors: A Review of Recent Progress*, J. Mater. Sci. **50**, 5641-5673 (2015).

[157] K. H. Lee, M. S. Kang, S. Zhang, Y. Gu, T. P. Lodge, and C. D. Frisbie, *"Cut and Stick" Rubbery Ion Gels as High Capacitance Gate Dielectrics*, Adv. Mater. **24**, 4457-4462 (2012).

[158] M. Galiński, A. Lewandowski, and I. Stępniak, *Ionic Liquids as Electrolytes*, Electrochim. Acta **51**, 5567-5580 (2006).

[159] M. Armand, F. Endres, D. R. MacFarlane, H. Ohno, and B. Scrosati, *Ionic-Liquid Materials for the Electrochemical Challenges of the Future*, Nat. Mater. **8**, 621-629 (2009).

[160] H. Matsumoto, *Electrochemical Windows of Room-Temperature Ionic Liquids*, in *Electrochemical Aspects of Ionic Liquids* (John Wiley & Sons, New Jersey, 2005), pp. 35–54.

[161] T. P. Lodge, *A Unique Platform for Materials Design*, Science **321**, 50-51 (2008).

[162] J. H. Cho, J. Lee, Y. Xia, B. Kim, Y. He, M. J. Renn, T. P. Lodge, and C. Daniel Frisbie, *Printable Ion-Gel Gate Dielectrics for Low-Voltage Polymer Thin-Film Transistors on Plastic*, Nat. Mater. **7**, 900-906 (2008).

[163] Md. A. B. H. Susan, T. Kaneko, A. Noda, and M. Watanabe, *Ion Gels Prepared by in Situ Radical Polymerization of Vinyl Monomers in an Ionic Liquid and Their Characterization as Polymer Electrolytes*, J. Am. Chem. Soc. **127**, 4976-4983 (2005).

[164] M. Salsamendi, L. Rubatat, and D. Mecerreyes, *Polymeric Ion Gels: Preparation Methods, Characterization, and Applications*, in *Electrochemistry in Ionic Liquids* (Springer International Publishing, Switzerland, 2015), pp. 283–315.

[165] K. Ueno, S. Nakamura, H. Shimotani, A. Ohtomo, N. Kimura, T. Nojima, H. Aoki, Y. Iwasa, and M. Kawasaki, *Electric-Field-Induced Superconductivity in an Insulator*, Nat. Mater. **7**, 855-858 (2008).

[166] K. Ueno, S. Nakamura, H. Shimotani, H. T. Yuan, N. Kimura, T. Nojima, H. Aoki, Y. Iwasa, and M. Kawasaki, *Discovery of Superconductivity in $KTaO_3$ by Electrostatic Carrier Doping*, Nat. Nanotechnol. **6**, 408-412 (2011).

[167] A. T. Bollinger, G. Dubuis, J. Yoon, D. Pavuna, J. Misewich, and I. Božović, *Superconductor–Insulator Transition in $La_{2-x}Sr_xCuO_4$ at the Pair Quantum Resistance*, Nature **472**, 458-472 (2011).

[168] M. Nakano, K. Shibuya, D. Okuyama, T. Hatano, S. Ono, M. Kawasaki, Y. Iwasa, and Y. Tokura, *Collective Bulk Carrier Delocalization Driven by Electrostatic Surface Charge Accumulation*, Nature **487**, 459-462 (2012).

[169] J. Walter, T. Charlton, H. Ambaye, M. R. Fitzsimmons, P. P. Orth, R. M. Fernandes, and C. Leighton, *Giant Electrostatic Modification of Magnetism via Electrolyte-Gate-Induced Cluster Percolation in $La_{1-x}Sr_xCoO_{3-\delta}$*, Phys. Rev. Mater. **2**, 111406 (2018).

[170] H. Shimotani, H. Asanuma, A. Tsukazaki, A. Ohtomo, M. Kawasaki, and Y. Iwasa, *Insulator-to-Metal Transition in ZnO by Electric Double Layer Gating*, Appl. Phys. Lett. **91**, 082106 (2007).

[171] H. Yuan, H. Shimotani, A. Tsukazaki, A. Ohtomo, M. Kawasaki, and Y. Iwasa, *High-Density Carrier Accumulation in ZnO Field-Effect Transistors Gated by Electric Double Layers of Ionic Liquids*, Adv. Funct. Mater. **19**, 1046-1053 (2009).

[172] H. Wang, W. M. Postiglione, V. Chaturvedi, E. L. Runnerstrom, A. Cleri, J. Nordlander, J.-P. Maria, and C. Leighton, *Electrolyte-Gate-Driven Carrier Density Modulation and Metal–Insulator Transition in Semiconducting Epitaxial CdO Films*, APL Mater. **10**, 121106 (2022).

[173] H. Wang, A. Prakash, K. Reich, K. Ganguly, B. Jalan, and C. Leighton, *Scattering Mechanisms and Mobility Enhancement in Epitaxial $BaSnO_3$ Thin Films Probed via Electrolyte Gating*, APL Mater. **8**, 071113 (2020).

[174] J. Jeong, N. Aetukuri, T. Graf, T. D. Schladt, M. G. Samant, and S. S. P. Parkin, *Suppression of Metal-Insulator Transition in VO_2 by Electric Field-Induced Oxygen Vacancy Formation*, Science **339**, 1402-1405 (2013).

[175] H. Ji, J. Wei, and D. Natelson, *Modulation of the Electrical Properties of VO_2 Nanobeams Using an Ionic Liquid as a Gating Medium*, Nano Lett. **12**, 2988-2992 (2012).

[176] J. Walter, G. Yu, B. Yu, A. Grutter, B. Kirby, J. Borchers, Z. Zhang, H. Zhou, T. Birol, M. Greven, and C. Leighton, *Ion-Gel-Gating-Induced Oxygen Vacancy*

Formation in Epitaxial $La_{0.5}Sr_{0.5}CoO_{3-\delta}$ Films from in Operando *X-ray and Neutron Scattering*, Phys. Rev. Mater. **1**, 071403 (2017).

[177] M. Wang, S. Shen, J. Ni, N. Lu, Z. Li, H.-B. Li, S. Yang, T. Chen, J. Guo, Y. Wang, H. Xiang, and P. Yu, *Electric-Field-Controlled Phase Transformation in WO_3 Thin Films through Hydrogen Evolution*, Adv. Mater. **29**, 1703628 (2017).

[178] Q. Yang, J. Lee, H. Jeen, H. J. Cho, and H. Ohta, *Solid-State Electrochemical Protonation of $SrCoO_{2.5}$ into $H_xSrCoO_{2.5}$ (x = 1, 1.5, and 2)*, ACS Appl. Electron. Mater. **3**, 3296-3300 (2021).

[179] J. Walter, H. Wang, B. Luo, C. D. Frisbie, and C. Leighton, *Electrostatic versus Electrochemical Doping and Control of Ferromagnetism in Ion-Gel-Gated Ultrathin $La_{0.5}Sr_{0.5}CoO_{3-\delta}$*, ACS Nano **10**, 7799-7810 (2016).

[180] B. Yu, G. Yu, J. Walter, V. Chaturvedi, J. Gotchnik, S. Hameed, J. W. Freeland, C. Leighton, and M. Greven, *Soft X-Ray Absorption Spectroscopy and Magnetic Circular Dichroism as Operando Probes of Complex Oxide Electrolyte Gate Transistors*, Appl. Phys. Lett. **116**, 201905 (2020).

[181] P. P. Orth, R. M. Fernandes, J. Walter, C. Leighton, and B. I. Shklovskii, *Percolation via Combined Electrostatic and Chemical Doping in Complex Oxide Films*, Phys. Rev. Lett. **118**, 106801 (2017).

[182] W.-J. Lee, H. J. Kim, E. Sohn, H. M. Kim, T. H. Kim, K. Char, J. H. Kim, and K. H. Kim, *Oxygen Diffusion Process in a $Ba_{0.96}La_{0.04}SnO_3$ Thin Film on $SrTiO_3$(001) Substrate as Investigated by Time-Dependent Hall Effect Measurements*, Phys. Status Solidi A **212**, 1487-1493 (2015).

[183] H. Wang, J. Walter, K. Ganguly, B. Yu, G. Yu, Z. Zhang, H. Zhou, H. Fu, M. Greven, and C. Leighton, *Wide-Voltage-Window Reversible Control of Electronic Transport in Electrolyte-Gated Epitaxial $BaSnO_3$*, Phys. Rev. Mater. **3**, 075001 (2019).

[184] E. B. Watson, D. J. Cherniak, and E. A. Frank, *Retention of Biosignatures and Mass-Independent Fractionations in Pyrite: Self-Diffusion of Sulfur*, Geochim. Cosmochim. Acta **73**, 4792-4802 (2009).

[185] C. Clark and S. Friedemann, *Atomic Diffusion in the Surface State of Mott Insulator NiS_2*, J. Magn. Magn. Mater. **400**, 56-61 (2016).

[186] B. Cui, C. Song, F. Li, X. Y. Zhong, Z. C. Wang, P. Werner, Y. D. Gu, H. Q. Wu, M. S. Saleem, S. S. P. Parkin, and F. Pan, *Electric-Field Control of Oxygen Vacancies and Magnetic Phase Transition in a Cobaltite/Manganite Bilayer*, Phys. Rev. Appl. **8**, 044007 (2017).

[187] F. Z. Bidoky and C. D. Frisbie, *Sub-3 V, MHz-Class Electrolyte-Gated Transistors and Inverters*, ACS Appl. Mater. Interfaces **14**, 21295-21300 (2022).

[188] J. de Rojas, A. Quintana, G. Rius, C. Stefani, N. Domingo, J. L. Costa-Krämer, E. Menéndez, and J. Sort, *Voltage Control of Magnetism with Magneto-Ionic*

Approaches: Beyond Voltage-Driven Oxygen Ion Migration, Appl. Phys. Lett. **120**, 070501 (2022).

[189] A. Molinari, H. Hahn, and R. Kruk, *Voltage-Control of Magnetism in All-Solid-State and Solid/Liquid Magnetoelectric Composites*, Adv. Mater. **31**, 1806662 (2019).

[190] H. Ling, D. A. Koutsouras, S. Kazemzadeh, Y. van de Burgt, F. Yan, and P. Gkoupidenis, *Electrolyte-Gated Transistors for Synaptic Electronics, Neuromorphic Computing, and Adaptable Biointerfacing*, Appl. Phys. Rev. **7**, 011307 (2020).

[191] J.-S. Ro, H.-M. An, and H.-L. Park, *Electrolyte-Gated Synaptic Transistors for Brain-Inspired Computing*, Jpn. J. Appl. Phys. **62**, SE0801 (2023).

[192] C. D. Schuman, S. R. Kulkarni, M. Parsa, J. P. Mitchell, P. Date, and B. Kay, *Opportunities for Neuromorphic Computing Algorithms and Applications*, Nat. Comput. Sci. **2**, 10-19 (2022).

[193] S. Zhang and G. Galli, *Understanding the Metal-to-Insulator Transition in $La_{1-x}Sr_xCoO_{3-\delta}$ and Its Applications for Neuromorphic Computing*, Npj Comput. Mater. **6**, 170 (2020).

[194] S. Zhang, H. Vo, and G. Galli, *Predicting the Onset of Metal-Insulator Transitions in Transition Metal Oxides—A First Step in Designing Neuromorphic Devices*, Chem. Mater. **33**, 3187-3195 (2021).

[195] A. Hoffmann, S. Ramanathan, J. Grollier, A. D. Kent, M. J. Rozenberg, I. K. Schuller, O. G. Shpyrko, R. C. Dynes, Y. Fainman, A. Frano, E. E. Fullerton, G. Galli, V. Lomakin, S. P. Ong, A. K. Petford-Long, J. A. Schuller, M. D. Stiles, Y. Takamura, Y. Zhu, *Quantum Materials for Energy-Efficient Neuromorphic Computing: Opportunities and Challenges*, APL Mater. **10**, 070904 (2022).

[196] M. Ohring, *Materials Science of Thin Films* (Academic Press, London, UK, 2002).

[197] M. Brahlek, A. S. Gupta, J. Lapano, J. Roth, H.-T. Zhang, L. Zhang, R. Haislmaier, and R. Engel-Herbert, *Frontiers in the Growth of Complex Oxide Thin Films: Past, Present, and Future of Hybrid MBE*, Adv. Funct. Mater. **28**, 1702772 (2018).

[198] A. Prakash and B. Jalan, *Molecular Beam Epitaxy for Oxide Electronics*, in *Molecular Beam Epitaxy: Materials and Applications for Electronics and Optoelectronics* (John Wiley & Sons, 2019), pp. 423–452.

[199] W. Kautek, *Deposition Methods of High-T_c Superconductors*, Vacuum **43**, 403-411 (1992).

[200] H. Chou, P. I. Lin, C. C. Hsu, T. C. Chow, M. T. Hong, Y. C. Chen, J. R. Liu, and T. P. Tsai, *Polishing Effect of the Plasma on the Growth of $YBa_2Cu_3O_{7-\delta}$ Films by Radio Frequency Sputtering*, J. Vac. Sci. Technol. A **20**, 441-446 (2002).

[201] D. J. Kester and R. Messier, *Macro-Effects of Resputtering Due to Negative Ion Bombardment of Growing Thin Films*, J. Mater. Res. **8**, 1928-1937 (1993).

[202] U. Poppe, J. Schubert, R. R. Arons, W. Evers, C. H. Freiburg, W. Reichert, K. Schmidt, W. Sybertz, and K. Urban, *Direct Production of Crystalline*

Superconducting Thin Films of $YBa_2Cu_3O_7$ by High-Pressure Oxygen Sputtering, Solid State Commun. **66**, 661-665 (1988).

[203] M. I. Faley, *Epitaxial Oxide Heterostructures for Ultimate High-T_c Quantum Interferometers*, in *Applications of High-T_c Superconductivity* (InTech, Rijeka, Croatia, 2011), pp. 147–176.

[204] U. Poppe, N. Klein, U. Dähne, H. Soltner, C. L. Jia, B. Kabius, K. Urban, *Low-Resistivity Epitaxial $YBa_2Cu_3O_7$ Thin Films with Improved Microstructure and Reduced Microwave Losses*, J. Appl. Phys. **71**, 5572-5578 (1992).

[205] C. L. Jia, M. I. Faley, U. Poppe, and K. Urban, *Effect of Chemical and Ion-Beam Etching on the Atomic Structure of Interfaces in $YBa_2Cu_3O_7/PrBa_2Cu_3O_7$ Josephson Junctions*, Appl. Phys. Lett. **67**, 3635-3637 (1995).

[206] M. Varela, W. Grogger, D. Arias, Z. Sefrioui, C. León, C. Ballesteros, K. M. Krishnan, and J. Santamaría, *Direct Evidence for Block-by-Block Growth in High-Temperature Superconductor Ultrathin Films*, Phys. Rev. Lett. **86**, 5156-5159 (2001).

[207] Z. Sefrioui, D. Arias, V. Peña, J. E. Villegas, M. Varela, P. Prieto, C. León, J. L. Martinez, and J. Santamaría, *Ferromagnetic/Superconducting Proximity Effect in $La_{0.7}Ca_{0.3}MnO_3/YBa_2Cu_3O_{7-\delta}$ Superlattices*, Phys. Rev. B **67**, 214511 (2003).

[208] J. Garcia-Barriocanal, F. Y. Bruno, A. Rivera-Calzada, Z. Sefrioui, N. M. Nemes, M. Garcia-Hernández, J. Rubio-Zuazo, G. R. Castro, M. Varela, S. J. Pennycook, C. Leon, and Jacobo Santamaría, *"Charge Leakage" at $LaMnO_3/SrTiO_3$ Interfaces*, Adv. Mater. **22**, 627-632 (2010).

[209] F. Y. Bruno, J. Garcia-Barriocanal, M. Varela, N. M. Nemes, P. Thakur, J. C. Cezar, N. B. Brookes, A. Rivera-Calzada, M. Garcia-Hernández, C. Leon, S. Okamoto, S. J. Pennycook, and J. Santamaría, *Electronic and Magnetic Reconstructions in $La_{0.7}Sr_{0.3}MnO_3/SrTiO_3$ Heterostructures: A Case of Enhanced Interlayer Coupling Controlled by the Interface*, Phys. Rev. Lett. **106**, 147205 (2011).

[210] V. Chaturvedi, S. Ghosh, D. Gautreau, W. M. Postiglione, J. E. Dewey, P. Quarterman, P. P. Balakrishnan, B. J. Kirby, H. Zhou, H. Cheng, A. Huon, T. Charlton, M. R. Fitzsimmons, C. Korostynski, A. Jacobson, L. Figari, J. Garcia-Barriocanal, T. Birol, K. A. Mkhoyan, and C. Leighton, *Room-Temperature Valence Transition in a Strain-Tuned Perovskite Oxide*, Nat. Commun. **13**, 7774 (2022).

[211] P. Ambwani, P. Xu, G. Haugstad, J. S. Jeong, R. Deng, K. A. Mkhoyan, B. Jalan, and C. Leighton, *Defects, Stoichiometry, and Electronic Transport in $SrTiO_{3-\delta}$ Epilayers: A High Pressure Oxygen Sputter Deposition Study*, J. Appl. Phys. **120**, 055704 (2016).

[212] K. Ganguly, A. Prakash, B. Jalan, and C. Leighton, *Mobility-Electron Density Relation Probed via Controlled Oxygen Vacancy Doping in Epitaxial $BaSnO_3$*, APL Materials **5**, 056102 (2017).

[213] W. M. Postiglione, K. Ganguly, H. Yun, J. S. Jeong, A. Jacobson, L. Borgeson, B. Jalan, K. A. Mkhoyan, and C. Leighton, *Structure-Property Relationships and*

Mobility Optimization in Sputtered La-Doped $BaSnO_3$ Films: Toward 100 cm^2 V^{-1} s^{-1} Mobility, Phys. Rev. Mater. **5**, 044604 (2021).

[214] S. Bernal, F. J. Botana, R. García, and J. M. Rodríguez-Izquierdo, *Thermal Evolution of a Sample of La_2O_3 Exposed to the Atmosphere*, Thermochim. Acta **66**, 139-145 (1983).

[215] W. T. A. Harrison, S. L. Hegwood, and A. J. Jacobson, *A Powder Neutron Diffraction Determination of the Structure of $Sr_6Co_5O_{15}$, Formerly Described as the Low-Temperature Hexagonal Form of $SrCoO_{3-x}$*, J. Chem. Soc. Chem. Commun. **19**, 1953-1954 (1995).

[216] W.-W. Zhang, M. Chen, E. Povoden-Karadeniz, and P. V. Hendriksen, *Thermodynamic Modeling of the Sr–Co–Fe–O System*, Solid State Ion. **292**, 88-97 (2016).

[217] A. M. Narayanan, R. Parasuraman, and A. M. Umarji, *Stabilization of Brownmillerite-Type $SrCoO_{2.5}$ by a Cost-Effective Quenching Method for Oxygen-Scavenging Applications*, Ind. Eng. Chem. Res. **57**, 14749-14757 (2018).

[218] T. Gulden, Epitaxial Growth of Thin Film Strontium Cobaltite: A Feasibility Study, Master's Thesis, University of Minnesota, 2012.

[219] U. Pietsch, V. Holý, and T. Baumbach, *High-Resolution X-Ray Scattering*, 1st ed. (Springer-Verlag, Heidelberg, 1999).

[220] P. F. Fewster, *Reciprocal Space Mapping*, Crit. Rev. Solid State Mater. Sci. **22**, 69-110 (1997).

[221] L. J. van der Pauw, *A Method of Measuring Specific Resistivity and Hall Effects of Discs of Arbitrary Shape*, Philips Res. Repts. **13**, 1-9 (1958).

[222] R. C. O'Handley, *Modern Magnetic Materials Principles and Applications* (John Wiley & Sons, New York, 2000).

[223] T. Miyasato, N. Abe, T. Fujii, A. Asamitsu, S. Onoda, Y. Onose, N. Nagaosa, and Y. Tokura, *Crossover Behavior of the Anomalous Hall Effect and Anomalous Nernst Effect in Itinerant Ferromagnets*, Phys. Rev. Lett. **99**, 086602 (2007).

[224] R. Averitt, *Magnetic Properties of a Paper Clip (EM-QD-300-01, Rev. A0)* Quantum Design, Inc.

[225] Quantum Design, Inc., *Vibrating Sample Magnetometer (VSM) Option User's Manual*, Part Number 1096-100, B0 (2011).

[226] M. A. Garcia, E. F. Pinel, J. de la Venta, A. Quesada, V. Bouzas, J. F. Fernández, J. J. Romero, M. S. M. González, and J. L. Costa-Krämer, *Sources of Experimental Errors in the Observation of Nanoscale Magnetism*, J. of Appl. Phys. **105**, 013925 (2009).

[227] V. Chaturvedi, Strain- and Electrolyte-Gating Based Control of Magnetism in Cobaltite Thin Films, Ph.D. Thesis, University of Minnesota, 2021.

[228] J. E. Dewey, Strain-Tuned Pr-Based Cobaltite Thin Films: Electronic Ground State Control and Strain Relaxation Effects, Ph.D. Thesis, University of Minnesota, 2023.

[229] J. Zhu, X. Wu, D. M. Lattery, W. Zheng, and X. Wang, *The Ultrafast Laser Pump-Probe Technique for Thermal Characterization of Materials with Micro/Nanostructures*, Nanoscale Microscale Thermophys. Eng. **21**, 177-198 (2017).

[230] D. M. Lattery, J. Zhu, D. Huang, and W. Xiaojia, *Ultrafast Thermal and Magnetic Characterization of Materials Enabled by the Time-Resolved Magneto-Optical Kerr Effect*, in *Nanoscale Energy Transport: Emerging Phenomena, Methods and Applications* (IOP Publishing, 2020).

[231] T. Favaloro, J.-H. Bahk, and A. Shakouri, *Characterization of the Temperature Dependence of the Thermoreflectance Coefficient for Conductive Thin Films*, Rev. Sci. Instrum. **86**, 024903 (2015).

[232] P. Jiang, X. Qian, and R. Yang, *Tutorial: Time-Domain Thermoreflectance (TDTR) for Thermal Property Characterization of Bulk and Thin Film Materials*, J. Appl. Phys. **124**, 161103 (2018).

[233] J. Liu, J. Zhu, M. Tian, X. Gu, A. Schmidt, and R. Yang, *Simultaneous Measurement of Thermal Conductivity and Heat Capacity of Bulk and Thin Film Materials Using Frequency-Dependent Transient Thermoreflectance Method*, Rev. Sci. Instrum. **84**, 034902 (2013).

[234] A. Karttunen and E. Kultalahti, *Time-Domain Thermoreflectance*, 2022, https://wiki.aalto.fi/display/SSC/Time-domain+thermoreflectance.

[235] Y. Zhang, Understanding and Tailoring Thermal Transport in Materials and Across Interfaces, Ph.D. Thesis, University of Minnesota, 2022.

[236] H. Fujiwara, *Spectroscopic Ellipsometry Principles and Applications* (John Wiley & Sons, 2007).

[237] A. T. Wong, J. H. Noh, P. R. Pudasaini, B. Wolf, N. Balke, A. Herklotz, Y. Sharma, A. V. Haglund, S. Dai, D. Mandrus, P. D. Rack, and T. Z. Ward, *Impact of Gate Geometry on Ionic Liquid Gated Ionotronic Systems*, APL Mater. **5**, 042501 (2017).

[238] P. R. Willmott, *X-Ray Sources at Large-Scale Facilities*, in *Magnetism and Accelarator-Based Light Sources*, Vol. 262 (Springer, Mittelwihr, France, 2018).

[239] A. A. Aczel, *FIE-TAX (HB-1A) Fixed Incident Energy Triple Axis Spectrometer*, https://conference.sns.gov/event/242/attachments/600/4557/2020_SpectroscopySuiteReview_HB1A_AAA.pdf.

[240] S. H. Simon, *The Oxford Solid State Basics* (Oxford University Press, Oxford, United Kingdom, 2013).

[241] Z. L. Wang, Y. Liu, and Z. Zhang, *X-Ray and Neutron Scattering*, in *Handbook of Nanophase and Nanostructured Materials*, Volume II: Characterization (Springer, Boston, MA, 2003), pp. 344-371.

[242] V. Chaturvedi, W. M. Postiglione, R. D. Chakraborty, B. Yu, W. Tabiś, S. Hameed, N. Biniskos, A. Jacobson, Z. Zhang, H. Zhou, M. Greven, V. E. Ferry, and C. Leighton, *Doping- and Strain-Dependent Electrolyte-Gate-Induced Perovskite to Brownmillerite Transformation in Epitaxial $La_{1-x}Sr_xCoO_{3-\delta}$ Films*, ACS Appl. Mater. Interfaces **13**, 51205-51217 (2021).

[243] L. Cao, O. Petracic, P. Zakalek, A. Weber, U. Rücker, J. Schubert, A. Koutsioubas, S. Mattauch, and T. Brückel, *Reversible Control of Physical Properties via an Oxygen-Vacancy-Driven Topotactic Transition in Epitaxial $La_{0.7}Sr_{0.3}MnO_{3-\delta}$ Thin Films*, Adv. Mater. **31**, 1806183 (2019).

[244] J. del Valle, J. G. Ramírez, M. J. Rozenberg, and I. K. Schuller, *Challenges in Materials and Devices for Resistive-Switching-Based Neuromorphic Computing*, J. Appl. Phys. **124**, 211101 (2018).

[245] J. Zhao, H. Guo, X. He, Q. Zhang, L. Gu, X. Li, K.-J. Jin, T. Yang, C. Ge, Y. Luo, M. He, Y. Long, J.-o. Wang, H. Qian, C. Wang, H. Lu, G. Yang, and K. Ibrahim, *Manipulating the Structural and Electronic Properties of Epitaxial $SrCoO_{2.5}$ Thin Films by Tuning the Epitaxial Strain*, ACS Appl. Mater. Interfaces **10**, 10211-10219 (2018).

[246] M. Youssef, K. J. Van Vliet, and B. Yildiz, *Polarizing Oxygen Vacancies in Insulating Metal Oxides Under a High Electric Field*, Phys. Rev. Lett. **119**, 126002 (2017).

[247] Y. Ito, R. F. Klie, N. D. Browning, and T. J. Mazanec, *Atomic Resolution Analysis of the Defect Chemistry and Microdomain Structure of Brownmillerite-Type Strontium Cobaltite*, J. Am. Ceram. Soc. **85**, 969-976 (2004).

[248] M. T. Curnan and J. R. Kitchin, *Effects of Concentration, Crystal Structure, Magnetism, and Electronic Structure Method on First-Principles Oxygen Vacancy Formation Energy Trends in Perovskites*, J. Phys. Chem. C **118**, 28776-28790 (2014).

[249] T. Jia, Z. Zeng, X. Zhang, P. Ohodnicki, B. Chorpening, G. Hackett, J. Lekse, and Y. Duan, *The Influence of Oxygen Vacancy on the Electronic and Optical Properties of $ABO_{3-\delta}$ (A = La, Sr, B = Fe, Co) Perovskites*, Phys. Chem. Chem. Phys. **21**, 20454-20462 (2019).

[250] A. M. Deml, V. Stevanović, C. L. Muhich, C. B. Musgrave, and R. O'Hayre, *Oxide Enthalpy of Formation and Band Gap Energy as Accurate Descriptors of Oxygen Vacancy Formation Energetics*, Energy Environ. Sci. **7**, 1996-2004 (2014).

[251] W. Donner, C. Chen, M. Liu, A. J. Jacobson, Y.-L. Lee, M. Gadre, and D. Morgan, *Epitaxial Strain-Enhanced Chemical Ordering in $La_{0.5}Sr_{0.5}CoO_{3-\delta}$ Films on $SrTiO_3$*, Chem. Mater. **23**, 984-988 (2011).

[252] Y. Pan, X. Xu, Y. Zhong, L. Ge, Y. Chen, J.-P. M. Veder, D. Guan, R. O'Hayre, M. Li, G. Wang, H. Wang, W. Zhou, and Z. Shao, *Direct Evidence of Boosted Oxygen Evolution Over Perovskite by Enhanced Lattice Oxygen Participation*, Nat. Commun. **11**, 2002 (2020).

[253] F. R. Van Buren, G. H. J. Broers, A. J. Bouman, and C. Boesveld, *The Electrochemical Determination of Oxygen Ion Diffusion Coefficients in $La_{0.50}Sr_{0.50}CoO_{3-y}$*, J. Electroanal. Chem. **88**, 353-361 (1978).

[254] R. A. De Souza and J. A. Kilner, *Oxygen Transport in $La_{1-x}Sr_xMn_{1-y}Co_yO_{3\pm\delta}$ Perovskites Part I. Oxygen Tracer Diffusion*, Solid State Ion. **106**, 175-187 (1998).

[255] Y. Zhang, W. M. Postiglione, R. Xie, C. Zhang, H. Zhou, V. Chaturvedi, K. Heltemes, H. Zhou, T. Feng, C. Leighton, and X. Wang, *Wide-Range Continuous Tuning of the Thermal Conductivity of $La_{0.5}Sr_{0.5}CoO_{3-\delta}$ Films via Room-Temperature Ion-Gel Gating*, Nat. Commun. **14**, 2626 (2023).

[256] R. D. Chakraborty, W. M. Postiglione, S. Ghosh, K. A. Mkhoyan, C. Leighton, and V. E. Ferry, *Optical Properties of Electrochemically Gated $La_{1-x}Sr_xCoO_{3-\delta}$ as a Topotactic Phase-Change Material*, Adv. Opt. Mater. **11**, 2300098 (2023).

[257] N. Homonnay, K. J. O'Shea, C. Eisenschmidt, M. Wahler, D. A. MacLaren, and G. Schmidt, *Interface Reactions in LSMO–Metal Hybrid Structures*, ACS Appl. Mater. Interfaces **7**, 22196-22202 (2015).

[258] W. S. M. Werner, K. Glantschnig, and C. Ambrosch-Draxl, *Optical Constants and Inelastic Electron-Scattering Data for 17 Elemental Metals*, J. Phys. Chem. Ref. Data **38**, 1013-1092 (2009).

[259] T. Katase, Y. Suzuki, and H. Ohta, *Reversibly Switchable Electromagnetic Device with Leakage-Free Electrolyte*, Adv. Electron. Mater. **2**, 1600044 (2016).

[260] J. Cho, M. D. Losego, H. G. Zhang, H. Kim, J. Zuo, I. Petrov, D. G. Cahill, and P. V. Braun, *Electrochemically Tunable Thermal Conductivity of Lithium Cobalt Oxide*, Nat. Commun. **5**, 4035 (2014).

[261] B. M. Foley, M. Wallace, J. T. Gaskins, E. A. Paisley, R. L. Johnson-Wilke, J.-W. Kim, P. J. Ryan, S. Trolier-McKinstry, P. E. Hopkins, and J. F. Ihlefeld, *Voltage-Controlled Bistable Thermal Conductivity in Suspended Ferroelectric Thin-Film Membranes*, ACS Appl. Mater. Interfaces **10**, 25493-25501 (2018).

[262] J. F. Ihlefeld, B. M. Foley, D. A. Scrymgeour, J. R. Michael, B. B. McKenzie, D. L. Medlin, M. Wallace, and S. Trolier-McKinstry, *Room-Temperature Voltage Tunable Phonon Thermal Conductivity via Reconfigurable Interfaces in Ferroelectric Thin Films*, Nano Lett. **15**, 1791-1795 (2015).

[263] K. Aryana, J. A. Tomko, R. Guo, E. R. Hoglund, T. Mimura, S. Makarem, A. Salanova, Md S. B. Hoque, T. W. Pfeifer, D. H. Olson, J. L. Braun, J. Nag, J. C. Read, J. M. Howe, E. J. Opila, L. W. Martin, J. F. Ihlefeld, and P. F. Hopkins, *Observation of Solid-State Bidirectional Thermal Conductivity Switching in Antiferroelectric Lead Zirconate ($PbZrO_3$)*, Nat. Commun. **13**, 1573 (2022).

[264] E. Langenberg, D. Saha, M. E. Holtz, J.-J. Wang, D. Bugallo, E. Ferreiro-Vila, H. Paik, I. Hanke, S. Ganschow, D. A. Muller, L.-Q. Chen, G. Catalan, N. Domingo, J. Malen, D. G. Schlom, and F. Rivadulla, *Ferroelectric Domain Walls in $PbTiO_3$ Are Effective Regulators of Heat Flow at Room Temperature*, Nano Lett. **19**, 7901-7907 (2019).

[265] S. Ning, S. C. Huberman, C. Zhang, Z. Zhang, G. Chen, and C. A. Ross, *Dependence of the Thermal Conductivity of $BiFeO_3$ Thin Films on Polarization and Structure*, Phys. Rev. Appl. **8**, 054049 (2017).

[266] J. A. Tomko, A. Pena-Francesch, H. Jung, M. Tyagi, B. D. Allen, M. C. Demirel, and P. E. Hopkins, *Tunable Thermal Transport and Reversible Thermal Conductivity Switching in Topologically Networked Bio-Inspired Materials*, Nat. Nanotechnol. **13**, 959-964 (2018).

[267] J. Shin, J. Sung, M. Kang, X. Xie, B. Lee, K. M. Lee, T. J. White, C. Leal, N. R. Sottos, P. V. Braun, and D. G. Cahill, *Light-Triggered Thermal Conductivity Switching in Azobenzene Polymers*, Proc. Natl. Acad. Sci. U.S.A. **116**, 5973-5978 (2019).

[268] J. Shin, M. Kang, T. Tsai, C. Leal, P. V. Braun, and D. G. Cahill, *Thermally Functional Liquid Crystal Networks by Magnetic Field Driven Molecular Orientation*, ACS Macro Lett. **5**, 955-960 (2016).

[269] S. Ning, S. C. Huberman, Z. Ding, H.-H. Nahm, Y.-H. Kim, H.-S. Kim, G. Chen, and C. A. Ross, *Anomalous Defect Dependence of Thermal Conductivity in Epitaxial WO_3 Thin Films*, Adv. Mater. **31**, 1903738 (2019).

[270] Q. Yang, H. J. Cho, Z. Bian, M. Yoshimura, J. Lee, H. Jeen, J. Lin, J. Wei, B. Feng, Y. Ikuhara, H. Ohta, *Solid-State Electrochemical Thermal Transistors*, Adv. Funct. Mater. **33**, 2214939 (2023).

[271] A. Negi, H. P. Kim, Z. Hua, A. Timofeeva, X. Zhang, Y. Zhu, K. Peters, D. Kumah, X. Jiang, and J. Liu, *Ferroelectric Domain Wall Engineering Enables Thermal Modulation in PMN–PT Single Crystals*, Adv. Mater. **35**, 2211286 (2023).

[272] B. L. Wooten, R. Iguchi, P. Tang, J. S. Kang, K. Uchida, G. E. W. Bauer, and J. P. Heremans, *Electric Field–Dependent Phonon Spectrum and Heat Conduction in Ferroelectrics*, Sci. Adv. **9**, eadd7194 (2023).

[273] D. G. Cahill, *Analysis of Heat Flow in Layered Structures for Time-Domain Thermoreflectance*, Rev. Sci. Instrum. **75**, 5119-5122 (2004).

[274] D.-W. Oh, J. Ravichandran, C.-W. Liang, W. Siemons, B. Jalan, C. M. Brooks, M. Huijben, D. G. Schlom, S. Stemmer, L. W. Martin, A. Majumdar, R. Ramesh, and D. G. Cahill, *Thermal Conductivity as a Metric for the Crystalline Quality of $SrTiO_3$ Epitaxial Layers*, Appl. Phys. Lett. **98**, 221904 (2011).

[275] L. Chen, Y. Zhang, X. Wang, B. Jalan, S. Chen, and Y. Hou, *Roles of Point Defects in Thermal Transport in Perovskite Barium Stannate*, J. Phys. Chem. C **122**, 11482-11490 (2018).

[276] X. Wu, J. Walter, T. Feng, J. Zhu, H. Zheng, J. F. Mitchell, N. Biškup, M. Varela, X. Ruan, C. Leighton, and X. Wang, *Glass-Like Through-Plane Thermal Conductivity Induced by Oxygen Vacancies in Nanoscale Epitaxial $La_{0.5}Sr_{0.5}CoO_{3-\delta}$*, Adv. Funct. Mater. **27**, 1704233 (2017).

[277] K. Berggold, M. Kriener, C. Zobel, A. Reichl, M. Reuther, R. Müller, A. Freimuth, and T. Lorenz, *Thermal Conductivity, Thermopower, and Figure of Merit of $La_{1-x}Sr_xCoO_3$*, Phys. Rev. B **72**, 155116 (2005).

[278] J. Kimling, A. Philippi-Kobs, J. Jacobsohn, H. P. Oepen, and D. G. Cahill, *Thermal Conductance of Interfaces with Amorphous SiO_2 Measured by Time-Resolved Magneto-Optic Kerr-Effect Thermometry*, Phys. Rev. B **95**, 184305 (2017).

[279] J. Liu, G.-M. Choi, and D. G. Cahill, *Measurement of the Anisotropic Thermal Conductivity of Molybdenum Disulfide by the Time-Resolved Magneto-Optic Kerr Effect*, J. Appl. Phys. **116**, 233107 (2014).

[280] H.-C. Chien, D.-J. Yao, and C.-T. Hsu, *Measurement and Evaluation of the Interfacial Thermal Resistance Between a Metal and a Dielectric*, Appl. Phys. Lett. **93**, 231910 (2008).

[281] P. E. Hopkins, P. M. Norris, and R. J. Stevens, *Influence of Inelastic Scattering at Metal-Dielectric Interfaces*, J. Heat Transfer **130**, 022401 (2008).

[282] M. Li, Y. Wang, J. Zhou, J. Ren, and B. Li, *Thermal Boundary Conductance Across Metal-Nonmetal Interfaces: Effects of Electron-Phonon Coupling Both in Metal and at Interface*, Eur. Phys. J. B **88**, 149 (2015).

[283] B. Shi, X. Tang, T. Lu, T. Nakayama, Y. Li, and J. Zhou, *Interfacial Thermal Conductance at Metal–Nonmetal Interface via Electron–Phonon Coupling*, Mod. Phys. Lett. B **32**, 1830004 (2018).

[284] P. Jiang, B. Huang, and Y. K. Koh, *Accurate Measurements of Cross-Plane Thermal Conductivity of Thin Films by Dual-Frequency Time-Domain Thermoreflectance (TDTR)*, Rev. Sci. Instrum. **87**, 075101 (2016).

[285] R. B. Wilson, B. A. Apgar, W.-P. Hsieh, L. W. Martin, and D. G. Cahill, *Thermal Conductance of Strongly Bonded Metal-Oxide Interfaces*, Phys. Rev. B **91**, 115414 (2015).

[286] M. Thesberg, H. Kosina, and N. Neophytou, *On the Lorenz Number of Multiband Materials*, Phys. Rev. B **95**, 125206 (2017).

[287] X. Wang, V. Askarpour, J. Maassen, and M. Lundstrom, *On the Calculation of Lorenz Numbers for Complex Thermoelectric Materials*, J. Appl. Phys. **123**, 055104 (2018).

[288] A. J. Zhou, T. J. Zhu, and X. B. Zhao, *Thermoelectric Properties of Perovskite Oxides $La_{1-x}Sr_xCoO_3$ Prepared by Polymerlized Complex Method*, J. Mater. Sci. **43**, 1520-1524 (2008).

[289] H.-S. Kim, Z. M. Gibbs, Y. Tang, H. Wang, and G. J. Snyder, *Characterization of Lorenz Number with Seebeck Coefficient Measurement*, APL Mater. **3**, 041506 (2015).

[290] P. G. Klemens and R. K. Williams, *Thermal Conductivity of Metals and Alloys*, Int. Met. Rev. **31**, 197-215 (1986).

[291] S. Niu, G. Joe, H. Zhao, Y. Zhou, T. Orvis, H. Huyan, J. Salman, K. Mahalingam, B. Urwin, J. Wu, Y. Liu, T. E. Tiwald, S. B. Cronin, B. M. Howe, M. Mecklenburg, R. Haiges, D. J. Singh, H. Wang, M. A. Kats, and J. Ravichandran, *Giant Optical Anisotropy in a Quasi-One-Dimensional Crystal*, Nat. Photon. **12**, 392-396 (2018).

[292] S. Yamaguchi, Y. Okimoto, K. Ishibashi, and Y. Tokura, *Magneto-Optical Kerr Effects in Perovskite-Type Transition-Metal Oxides: $La_{1-x}Sr_xMnO_3$ and $La_{1-x}Sr_xCoO_3$*, Phys. Rev. B **58**, 6862-6870 (1998).

[293] Y. Tokura, Y. Okimoto, S. Yamaguchi, H. Taniguchi, T. Kimura, and H. Takagi, *Thermally Induced Insulator-Metal Transition in $LaCoO_3$: A View Based on the Mott Transition*, Phys. Rev. B **58**, R1699-R1702 (1998).

[294] Q. Chen, X. Wang, M. Zhang, Z. Xu, J. Gong, A. Rahman, L. Fan, R. Dai, Z. Wang, and Z. Zhang, *Temperature Dependent Optical Properties of $LaCoO_3/SrTiO_3$ Thin Film Studied by Spectroscopic Ellipsometry*, AIP Adv. **10**, 035117 (2020).

[295] D. W. Jeong, W. S. Choi, S. Okamoto, J.-Y. Kim, K. W. Kim, S. J. Moon, D.-Y. Cho, H. N. Lee, and T. W. Noh, *Dimensionality Control of d-Orbital Occupation in Oxide Superlattices*, Sci. Rep. **4**, 6124 (2014).

[296] T. Arima, Y. Tokura, and J. B. Torrance, *Variation of Optical Gaps in Perovskite-Type 3d Transition-Metal Oxides*, Phys. Rev. B **48**, 17006-17009 (1993).

[297] W. W. Li, Z. G. Hu, Y. W. Li, M. Zhu, Z. Q. Zhu, and J. H. Chu, *Growth, Microstructure, and Infrared-Ultraviolet Optical Conductivity of $La_{0.5}Sr_{0.5}CoO_3$ Nanocrystalline Films on Silicon Substrates by Pulsed Laser Deposition*, ACS Appl. Mater. Interfaces **2**, 896-902 (2010).

[298] J. H. Lee, W. S. Choi, H. Jeen, H.-J. Lee, J. H. Seo, J. Nam, M. S. Yeom, and H. N. Lee, *Strongly Coupled Magnetic and Electronic Transitions in Multivalent Strontium Cobaltites*, Sci. Rep. **7**, 16066 (2017).

[299] A. Nemati, G. Yuan, J. Deng, A. Huang, W. Wang, Y. T. Toh, J. Teng, and Q. Wang, *Controllable Polarization-Insensitive and Large-Angle Beam Switching with Phase-Change Metasurfaces*, Adv. Opt. Mater. **10**, 2101847 (2022).

[300] A. Leitis, A. Heßler, S. Wahl, M. Wuttig, T. Taubner, A. Tittl, and H. Altug, *All-Dielectric Programmable Huygens' Metasurfaces*, Adv. Funct. Mater. **30**, 1910259 (2020).

[301] M. Wuttig, H. Bhaskaran, and T. Taubner, *Phase-Change Materials for Non-Volatile Photonic Applications*, Nat. Photonics **11**, 465-476 (2017).

[302] J. Eaves-Rathert, E. Kovalik, C. F. Ugwu, B. R. Rogers, C. L. Pint, and J. G. Valentine, *Dynamic Color Tuning with Electrochemically Actuated TiO_2 Metasurfaces*, Nano Lett. **22**, 1626-1632 (2022).

[303] L. Liu, L. Kang, T. S. Mayer, and D. H. Werner, *Hybrid Metamaterials for Electrically Triggered Multifunctional Control*, Nat. Commun. **7**, 13236 (2016).

[304] Z. Zhu, P. G. Evans, R. F. Haglund Jr., and J. G. Valentine, *Dynamically Reconfigurable Metadevice Employing Nanostructured Phase-Change Materials*, Nano Lett. **17**, 4881-4885 (2017).

[305] Z. Li, Y. Zhou, H. Qi, Q. Pan, Z. Zhang, N. N. Shi, M. Lu, A. Stein, C. Y. Li, S. Ramanathan, and N. Yu, *Correlated Perovskites as a New Platform for Super-Broadband-Tunable Photonics*, Adv. Mater. **28**, 9117-9125 (2016).

[306] G. Yu, *New Phase Retrieval Algorithm to Resolve Thin-Film's Atomic Structure from Surface X-Ray Diffraction Data*, University of Minnesota Technology Commercialization, Technology No. 2024-089 (2023).

[307] Z. Yin, J. Wang, J. Wang, J. Li, H. Zhou, C. Zhang, H. Zhang, J. Zhang, F. Shen, J. Hao, Z. Yu, Y. Gao, Y. Wang, Y. Chen, J.-R. Sun, X. Bai, J.-T. Wang, F. Hu, T.-Y. Zhao, and B. Shen, *Compressive-Strain-Facilitated Fast Oxygen Migration with Reversible Topotactic Transformation in $La_{0.5}Sr_{0.5}CoO_x$ via All-Solid-State Electrolyte Gating*, ACS Nano **16**, 14632-14643 (2022).

[308] M. S. Saleem, C. Song, Y. Gu, R. Chen, M. U. Fayaz, Y. Hao, and F. Pan, *Orientation Control of Oxygen Vacancy Channels in Brownmillerite $SrFeO_{2.5}$*, Phys. Rev. Mater. **4**, 014403 (2020).

[309] S. Inkinen, L. Yao, and S. van Dijken, *Reversible Thermal Strain Control of Oxygen Vacancy Ordering in an Epitaxial $La_{0.5}Sr_{0.5}CoO_{3-\delta}$ Film*, Phys. Rev. Mater. **4**, 046002 (2020).

[310] X. Rui and R. F. Klie, *Atomic-Resolution In-Situ Cooling Study of Oxygen Vacancy Ordering in $La_{0.5}Sr_{0.5}CoO_{3-\delta}$ Thin Films*, Appl. Phys. Lett. **114**, 233101 (2019).

[311] J. Shiogai, Y. Ito, T. Mitsuhashi, T. Nojima, and A. Tsukazaki, *Electric-Field-Induced Superconductivity in Electrochemically Etched Ultrathin FeSe Films on $SrTiO_3$ and MgO*, Nat. Phys. **12**, 42-46 (2016).

[312] J. B. Goodenough and K.-S. Park, *The Li-Ion Rechargeable Battery: A Perspective*, J. Am. Chem. Soc. **135**, 1167-1176 (2013).

[313] S. S. Choi and H. S. Lim, *Factors That Affect Cycle-Life and Possible Degradation Mechanisms of a Li-Ion Cell Based on $LiCoO_2$*, J. Power Sources **111**, 130-136 (2002).

[314] B. M. Lefler, W. M. Postiglione, C. Leighton, and S. J. May, *Voltage Control of Patterned Metal/Insulator Properties in Oxide/Oxyfluoride Lateral Perovskite Heterostructures via Ion Gel Gating*, Adv. Funct. Mater. **32**, 2208434 (2022).

[315] P. Bonhote, A.-P. Dias, N. Papageorgiou, K. Kalyanasundaram, and M. Grätzel, *Hydrophobic, Highly Conductive Ambient-Temperature Molten Salts*, Inorg. Chem. **35**, 1168-1178 (1996).

[316] K. C. Lethesh, A. Bahaa, M. Abdullah, M. O. Bamgbopa, and R. A. Susantyoko, *Temperature-Dependent Electrochemical Stability Window of Bis(Trifluoromethanesulfonyl)Imide and Bis(Fluorosulfonyl)Imide Anion Based Ionic Liquids*, Front. Chem. **10**, 859304 (2022).

[317] M. Sharma, J. Gazquez, M. Varela, J. Schmitt, and C. Leighton, *Growth Temperature Control of the Epitaxy, Magnetism, and Transport in $SrTiO_3(001)/La_{0.5}Sr_{0.5}CoO_3$ Thin Films*, J. Vac. Sci. Technol. A **29**, 051511 (2011).

[318] T. Takeda and H. Watanabe, *Magnetic Properties of the System $SrCo_{1-x}Fe_xO_{3-y}$*, J. Phys. Soc. Jpn. **33**, 973-978 (1972).

[319] S. J. Callori, S. Hu, J. Bertinshaw, Z. J. Yue, S. Danilkin, X. L. Wang, V. Nagarajan, F. Klose, J. Seidel, and C. Ulrich, *Strain-Induced Magnetic Phase Transition in $SrCoO_{3-\delta}$ Thin Films*, Phys. Rev. B **91**, 140405 (2015).

[320] J.-S. Zhou, L. G. Marshall, Z.-Y. Li, X. Li, and J.-M. He, *Weak Ferromagnetism in Perovskite Oxides*, Phys. Rev. B **102**, 104420 (2020).

[321] P. Gallagher, M. Lee, T. A. Petach, S. W. Stanwyck, J. R. Williams, K. Watanabe, T. Taniguchi, and D. Goldhaber-Gordon, *A High-Mobility Electronic System at an Electrolyte-Gated Oxide Surface*, Nat. Commun. **6**, 6437 (2015).

[322] C. M. Folkman, S. H. Chang, H. Jeen, E. Perret, P. M. Baldo, C. Thompson, J. A. Eastman, H. N. Lee, and D. D. Fong, *In Operando Studies of CO Oxidation on Epitaxial $SrCoO_{2.5+\delta}$ Thin Films*, APL Mater. **7**, 081126 (2019).

[323] J. Ovenstone, J. S. White, and S. T. Misture, *Phase Transitions and Phase Decomposition of $La_{1-x}SrxCoO_{3-\delta}$ in Low Oxygen Partial Pressures*, J. Power Sources **181**, 56-61 (2008).

Appendix A: Other experimental variables in ion-gel-gated $La_{1-x}Sr_xCoO_{3-\delta}$

While the research presented in Chapter 5 focused on a specific set of experimental conditions in terms of ion gel gating, other parameters were also explored. Some of these are briefly summarized below.

I. Sweep rate dependence, $x = 0.5$

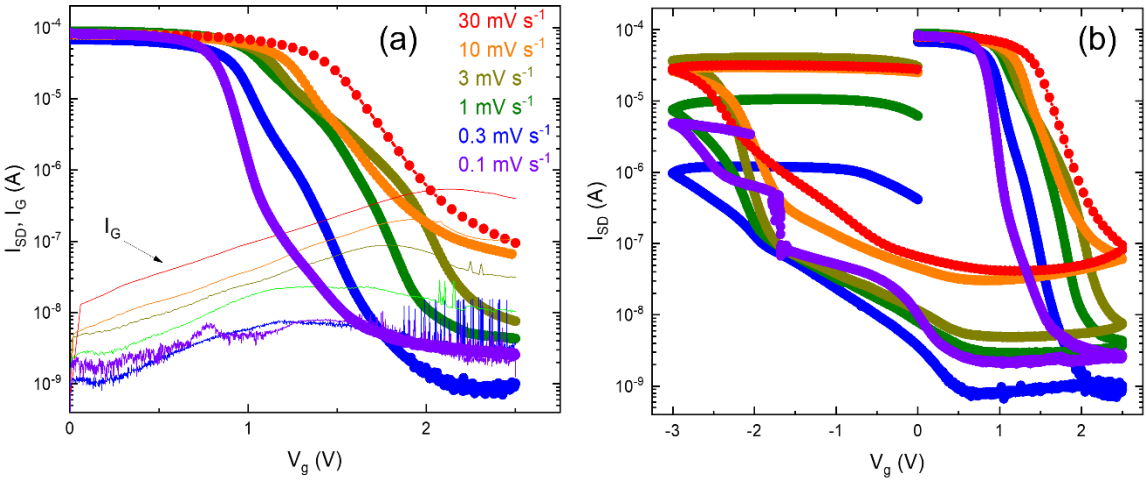

Figure A1: (a) Source-drain current (I_{SD}) and gate current (I_G) *vs.* gate voltage (V_g) for six nominally identical 10 u.c. $x = 0.5$ LSCO-film ion-gel-gate devices, gated from 0 to 2.5 V at various V_g sweep rates (see legend). IG is shown as thin lines while I_{SD} are represented as points connected by lines (for slow sweep rates the space between the points is too small to see). (b) Full I_{SD} *vs.* V_g hysteresis loops for the same LSCO film devices as in (a), but shown over the full V_g range, *i.e.*, 0 V → 2.5 V → –3 V → 0 V.

All the experimental data presented in Chapter 5 were collected using a constant V_g sweep rate of 1 mV s^{-1}. However, some rate-dependent ion-gel-gating experiments were also performed. Fig. A1 summarizes the sweep rate dependence of ion-gel-gated $x = 0.5$ LSCO 10-unit-cell-thick films on LAO substrates, under the same gating conditions described in Section 2.5 and 5.1. In panel (a) the focus is on the positive-V_g side of the loop only, where the slower rates clearly lead to a lower-V_g approach to the "OFF" current (~5 × 10^{-9} A). Only at rates ≤ 1 mV s^{-1} was the OFF current reached by the time the max voltage of the sweep (2.5 V) was reached. The gate current, I_G, is also shown in panel (a), and shows significant dependence on the V_g sweep rate. (I_G is a combination of electrostatic charging current of the electrolyte and the electrochemical current from the film, *e.g.*,

reduction). For faster sweep rates, there is less time for the ions in the gel to move, thus higher I_G is needed to achieve similar charging. Plots of the accumulated charge, *i.e.*, the integration of I_G with respect to time (not shown in Fig. A1), *vs.* V_g indicate that charging curves were nearly identical for rates ≤ 1 mV s^{-1}, whereas less accumulated charge was evident for faster rates. In Fig. A1(b) the full V_g-hysteresis loop is shown for each rate, where another trend emerges. Slower rates appear to adversely impact the reversibility, *i.e.*, "recovery," of the device at $V_g < 0$, possibly due to longer exposure times at high positive V_g, where etching effects are known to occur [179]. From these observations, 1 mV s^{-1} sweep rate appears to be near-optimal.

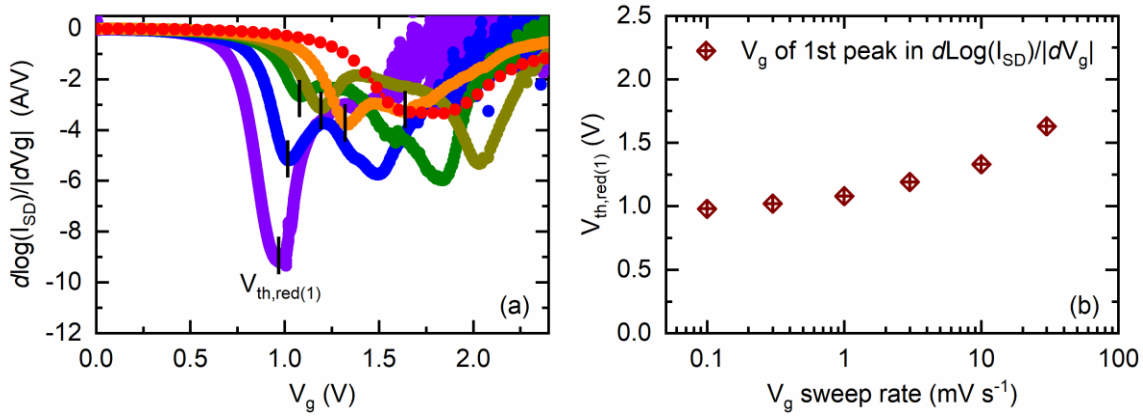

Figure A2: (a) Logarithmic derivative of I_{SD} with respect to V_g, $d(I_{SD})/|dV_g|$, plotted as a function of V_g for the same samples shown in Fig. A1. (b) Threshold voltage for reduction from the first appearing peak in the logarithmic derivative, $V_{th,red(1)}$, plotted as a function of sweep rate (on a $\log_{10}$ scale). The vertical black lines in (a) mark the $V_{th,red(1)}$ plotted in (b).

From inspection of Fig. A1, it appears that the threshold voltage for reduction drops as the sweep rate is reduced. While this is true, by plotting the logarithmic derivative of I_{SD} with respect to V_g, as shown in Fig. A2, we see that the threshold voltage shows an apparent *saturating* behavior at ~1 V (consistent with our prior work [242]) for rates slower than ~1 mV s^{-1}. A similar analysis was done in Chapter 5 (see Fig. 5.4 and Fig. 5.5). Taking the effects observed in Fig. A1 and Fig. A2 together, 1 mV s^{-1} was chosen as our probing sweep rate for the work shown in Chapter 5. The increase in V_{th} at faster rates and the incomplete transformation (not reaching the typical OFF current), are signs that either the ions in the gel do not have enough time to fully form the EDL or that the oxygen diffusion process in the film has not had enough time to complete. Unfortunately, these two effects cannot be decoupled by this experiment alone. Determining which is the limiting factor, *i.e.*, the

electrolyte or the film diffusion processes, is an active area of research. One possible way to decouple these effects is by adapting the EDLT device to a "top gate" geometry. This should, in principle, reduce the transit time for ions to form the EDL, by reducing the distance ions need to migrate (from ~0.5 mm to ~10 μm), and causing the diffusion process to be more likely rate limiting.

II. Thickness dependence, $x = 0.5$

The performance of electrochemical EDLTs is strongly dependent on the thickness of the channel material. The insertion / removal of ions from the channel is governed by diffusion, and thus controlled by the diffusivity of the relevant ionic species. The simple representation of a diffusion length (L) is helpful here, *i.e.*, $L = \sqrt{D\tau}$, where D is the diffusivity, and τ is diffusion time. If we consider L as an approximation of the film thickness, then the time needed for diffusion is proportional to the thickness *squared*. This is the primary reason why one needs very thin films to maximize switching speed.

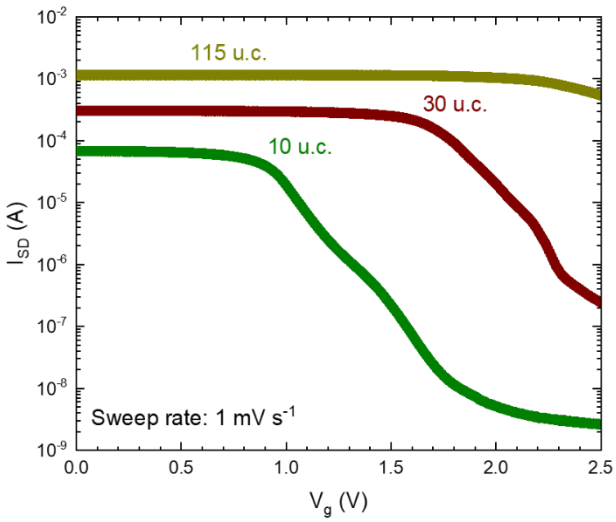

Figure A3: (a) Source-drain current (I_{SD}) *vs.* gate voltage (V_g) for three $x = 0.5$ LSCO ion-gel-gate devices of varying film thickness, gated from 0 to 2.5 V. Ion-gel gating was performed at 300 K, in vacuum (< 10^{-5} Torr), using a sweep rate of 1 mV s^{-1}

Fig. A3 shows the I_{SD} *vs.* V_g curves at $V_g > 0$ for three $x = 0.5$ LSCO films of different thicknesses, from 10 - 115 unit cells thick. Note that the resistance of the devices decrease at higher thickness, so that the I_{SD} is initially higher for the thicker films. Clearly, from Fig. A3, the 30 and 115 u.c. films do not reach the fully-BM "OFF" state. Moreover, the threshold voltage also appears delayed in the thicker films, likely due to a shunting

effect of underlying parts of the film which do not lose oxygen as quickly as the top layers. This is exactly the situation expected when the device speed is limited by V_O diffusion time. Varying film thickness is thus another way to potentially deconvolve effects of ion gel charging *vs.* film diffusion. This experiment further highlights the need for ultrathin films and slow V_g sweep rates to understand the near-equilibrium V_g characteristics of such devices.

III. Impact of atmosphere

The atmospheric conditions under which an electrolyte gating experiment is performed can have an impact on the response of the device. For example, the availability of atmospheric O_2 (*i.e.*, the partial pressure of O_2) has previously been shown to impact the performance and V_g-dependence of electrolyte gated oxides VO_2 [174] and LSCO [179]. Furthermore, it is currently understood that in electrolyte gated SCO / LSCO, oxidation of the films, even under vacuum, is facilitated by hydrolysis of H_2O, which is always present in ILs and gels even after aggressive drying procedures.

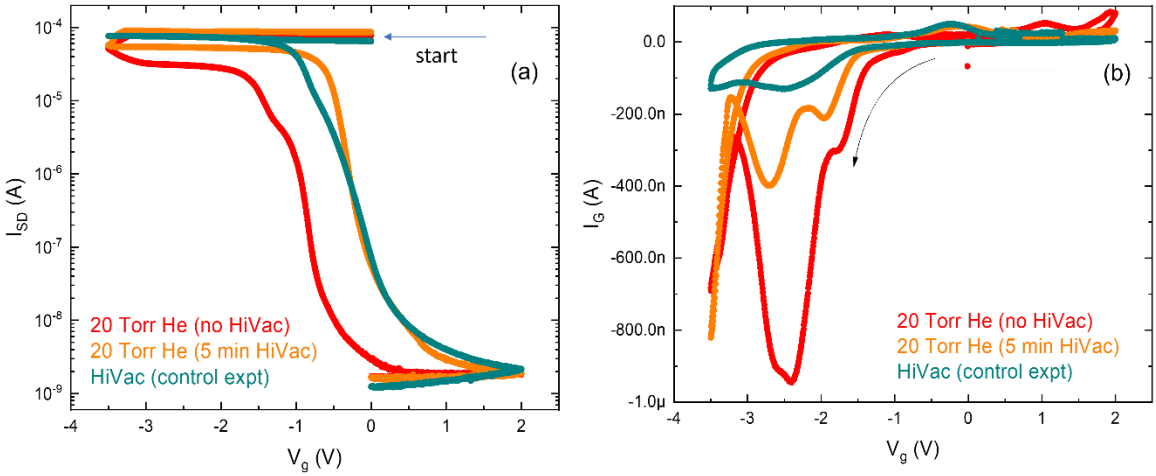

Figure A4: (a) Source-drain current (I_{SD}) and gate current (I_G) *vs.* gate voltage (V_g) for three nominally identical 10 u.c. x = 0.5 LSCO-film ion-gel-gate devices, gated from 0 → –3.5 V → 2 V, in different atmospheric conditions. (b) Gate current (I_G) *vs.* V_g for the same film devices as in (a). The red curves were generated by ion-gel-gating in ~20 Torr pure He gas (after purging), the orange after exposure of the ion gel EDLT to high-vacuum ($P < 10^{-5}$ Torr) for 5 minutes (then backfilled with ~20 Torr He), and the dark teal under our standard high-vacuum ($P < 10^{-5}$ Torr) conditions (*i.e.*, a control experiment sample).

In the context of the research presented in this work, one might assume re-oxidation of reduced films would be easier (*i.e.*, take place at lower voltage) when performed in open air or pure-O_2 environments. While we have some preliminary evidence that this is indeed

the case (and we already know reduction can be suppressed under O_2 [179]), additional unknown electrochemical effects were also observed, which significantly degraded device performance. Fig. A4 shows the results of one such experiment which highlights the need for our gating to be performed in dry environments. In this experiment, three nominally identical 10 u.c. x = 0.5 LSCO films were ion-gel gated after exposure to different atmospheric conditions. The gating was initially performed at negative V_g, in contrast to other the other experiments in this thesis, where no film-related electrochemistry is expected from prior work [179]. The dark teal curve in Fig. A4(a) shows a film gated under our typical vacuum conditions ($P < 10^{-5}$ Torr, throughout the experiment) and performing entirely electrostatically, until the sweep returns toward 0 V, at which point expected electrochemistry is seen (similar to that observed in Ref. [179], Chapter 3, and Chapter 5). The orange curve in Fig. A4(a) represents a film gated under very similar conditions to the dark teal, but instead of performing the gating under $P < 10^{-5}$ Torr the experiment was conducted in ~20 Torr of pure He after initially pumping to $P < 10^{-5}$ Torr for 5 minutes. The orange curve is overall very similar to the dark teal, but the I_{SD} begins to decline at very high negative V_g (< ~-3.3 V). This immediately indicates some electrochemical degradation of the film where we expect none. The effect is small, however, and the rest of the trace more-or-less follows the dark teal control experiment. Moving to the red curve, this experiment was performed in ~20 Torr of pure He without any high vacuum exposure. The red curve clearly shows much more significant degradation of the film at high negative V_g and leads to the subsequent reduction upon return to 0 V faster, *i.e.*, at lower V_g, than the other curves. In Fig. A4(b), the gate current, I_G, is plotted for the above experiments, where it is immediately obvious that the I_G for the orange and red curves is significantly higher than for the dark teal. The large electrochemical peaks observed in I_G *vs.* V_g plots are of unknown origin. All we can say definitively is that this electrochemistry is facilitated, at least in part, by unintentional contaminant species, and that these contaminants can be largely removed by performing the experiment in high vacuum. We strongly suspect a primary role of H_2O, OH^-, and H^+, but more work is needed to confirm this. The results of this experiment highlight the need for careful atmospheric consideration, and further research into electrochemical interactions caused by gel handling procedures and environmental exposure.

Appendix B: Contact degradation in ion-gel-gated $La_{0.5}Sr_{0.5}CoO_{3-\delta}$

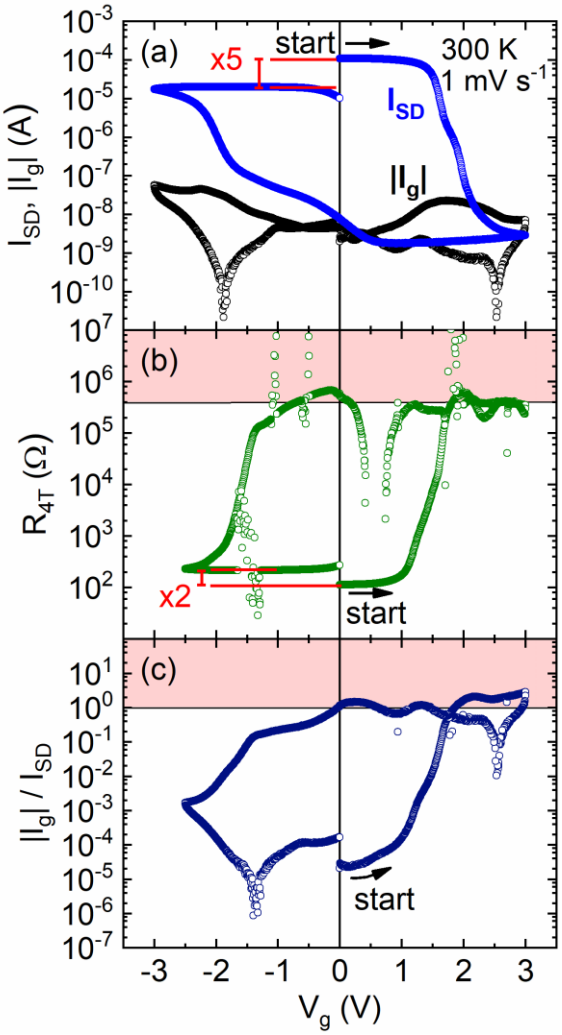

Figure B1: Gate voltage (V_g) hysteresis loops (at 300 K, 1 mV s^{-1}, and 0.1 V source-drain voltage) of: (a) the source-drain current (I_{SD}, blue) and gate current magnitude ($|I_g|$, black), (b) the four-terminal sheet resistance (R_{4T}), and (c) the $|I_g|/I_{SD}$ ratio, all on $\log_{10}$ scales. All data are from 10-unit-cell-thick ion-gel-gated LSCO films.

As mentioned in Chapter 5, signs of electrical contact degradation were observed during ion-gel-gating of LSCO films, *i.e.*, increasing two-terminal resistance not due to increasing resistivity of the film. This observation is summarized in Fig. B1, which shows the results of a representative ion-gel-gating experiment on a 10 unit-cell-thick x = 0.5 LSCO film, where V_g was swept at 1 mV s^{-1} from 0 V → 3.0 V → –3.0 V → 0 V. The typical measurements of the experiment are plotted all as a function of V_g: source-drain current (I_{SD}) and gate current magnitude ($|I_g|$) in panel (a), four-terminal resistance (R_{4T}) in panel (b), and the ratio $|I_g|/I_{SD}$ in panel (c). In Fig. B1(a) and (b) the red lines and text

highlight the extent of recovery of the device after the first cycle. The recovery is within a factor of 2 for R_{4T} (consistently over many devices), compared to within a factor of 5 for I_{SD} (typically between 2 and 5 over many devices). As discussed in Chapter 5, the worse recovery in I_{SD} compared to R_{4T} indicates contact resistance degradation with V_g cycling. Also noteworthy is that the measurement of R_{4T} (panel (b)) becomes unreliable in certain V_g ranges, particularly when $|I_g|/I_{SD}$ (panel (c)) approaches unity at high R_{4T} (pink regions), signaling non-uniform electric field distributions, *i.e.*, contamination of the I_{SD} measurement by I_g.

Appendix C: Additional details on the high-pressure-oxygen sputter deposition of brownmillerite $SrCoO_{2.5}$ films

In this work, BM-structured SCO films were grown using high-pressure-oxygen sputtering. Previous attempts to grow SCO films by this method were done using RF sputtering [218], but here we used DC. Although great effort was put forth in optimizing the DC-sputtering conditions, the greatest contributing factor to the growth of high-quality BM-SCO films was using a freshly sintered sputtering target. For each target, after extended sputtering time, film quality began to deteriorate, eventually leading to phase separation and non-BM films, despite using the same deposition conditions. The origins of this degradation were not pinned down but may originate from the fact that the target material itself was bi-phase (a mix of hexagonal $SrCo_xO_y$, $x \approx 0.8$, $y \approx 2.4$ (~95 wt%) and Co_3O_4 (~5 wt%)). One likely possibility is that the preferential sputtering of one of the target phases over the other alters the stoichiometry of the target surface over time. In any case, target longevity could be temporarily extended by three methods: (1) increasing the deposition temperature, (2) increasing the DC-sputter power, or (3) sanding the surface of the target. However, such 're-optimization' efforts were labor-intensive and costly, whereas starting from a fresh sputtering target was far more efficient and robust. The near-optimal sputtering conditions for a 'new' target are those displayed in Table 2.1.

Alternate film phases beside that of the desired BM were commonly observed in thin films when grown under non-optimal conditions. These phases included the tetragonal $SrCoO_x$ (where $2.75 < x < 2.825$), the cubic Co_3O_4, and the hexagonal $Sr_6Co_5O_{15}$. Examples of these phases are shown from HRXRD in Fig. C1(a) and (b). In panel (a), a mostly tetragonal $SrCoO_x$ film is seen, grown under the following conditions: T = 725 °C, P_{O_2} = 1.625 mbar, DC power = 26 W, and z =108 mm. Occurrence of this phase indicated higher-than-desired oxygen stoichiometry, and it could often be mitigated by increasing T, increasing deposition rate (through lower separation z, or higher DC power), and occasionally reducing P_{O_2}. Fig. C1(b) shows what happens to films when they are grown beyond a certain thickness. As discussed in the next section initially phase-pure BM films phase separate into $Sr_6Co_5O_{15}$ and Co_3O_4 at high film thickness.

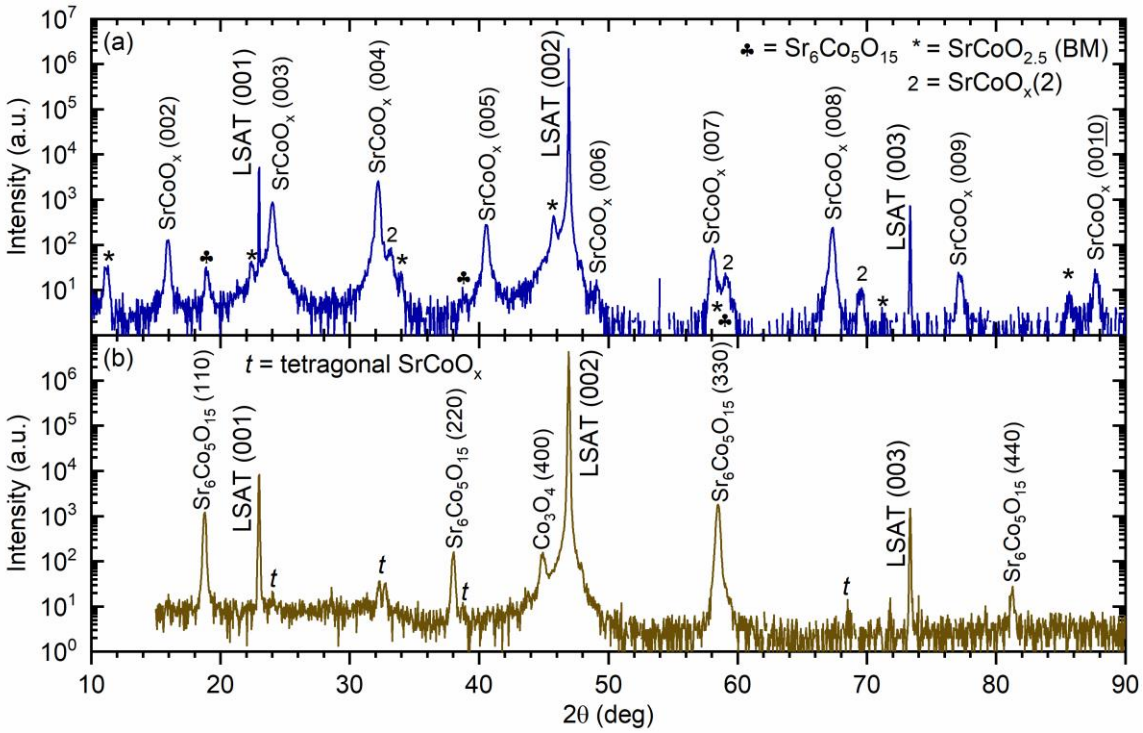

Figure C1: Wide-angle specular HRXRD scans of two example films of $SrCoO_x$ on LSAT(001) substrates grown by high-pressure-oxygen DC sputtering. In (a), a mostly tetragonal $SrCoO_x$ phase is observed in the film (with peaks indexed). Peaks marked "2" are due to another tetragonal phase, likely with higher oxygen content, peaks marked with a "*" are BM, and peaks marked with a "club" are from $Sr_6Co_5O_{15}$. In (b) the film consists almost entirely of $Sr_6Co_5O_{15}$ and Co_3O_4, *i.e.*, the bulk equilibrium composition, but remains largely epitaxial. The small peaks marked with "*t*" in panel (b) correspond to tetragonal $SrCoO_x$.

I. Phase separation at high thickness

As alluded to above, an interesting phase-separation phenomenon was observed in BM-SCO films when grown beyond a certain thickness. Fig. C2 shows a series of HRXRD scans for SCO films grown to increasingly higher thickness. At low thickness, the growth parameters were optimized such that the films exhibit a phase-pure BM structure. Such films feature out-of-plane lattice parameter close to that expected for fully-strained BM-SCO on LSAT(001), low surface roughness from GIXR (not shown), and good out-of-plane coherence (from Scherrer-length-to-thickness ratio ~0.9). However, above ~50 nm, the film structure abruptly transforms to a phase-impure structure, with the intensity of the tetragonal phase peaks increasing and those of the BM decreasing with thickness. Above ~80 nm the film further transforms into the phase-separated bulk-like mixture of $Sr_6Co_5O_{15}$ and Co_3O_4 (the 180 nm film in Fig. C2 is the same as that in Fig. C1(b)). Because this

composition closely resembles the bulk (at thermodynamic equilibrium in air [215–217]), we interpret this transition with thickness to likely be triggered by strain relaxation. As a final note on this observed phase separation, the sputtering technique employed here may not be the optimal method to grow such oxygen-deficient structures. For the same reason high-pressure-oxygen sputtering is advantageous for growing highly oxygenated perovskites, it may not be ideal for growing the necessarily oxygen-deficient BM, where indeed most of the literature reports of BM-SCO films are grown by PLD under much lower P_{O_2}. We speculate that the high P_{O_2} in our sputtering system makes this phase-separation more facile, from a thermodynamic perspective, and that lower P_{O_2}, perhaps using a mix of O_2 and Ar, may allow the growth of thicker films.

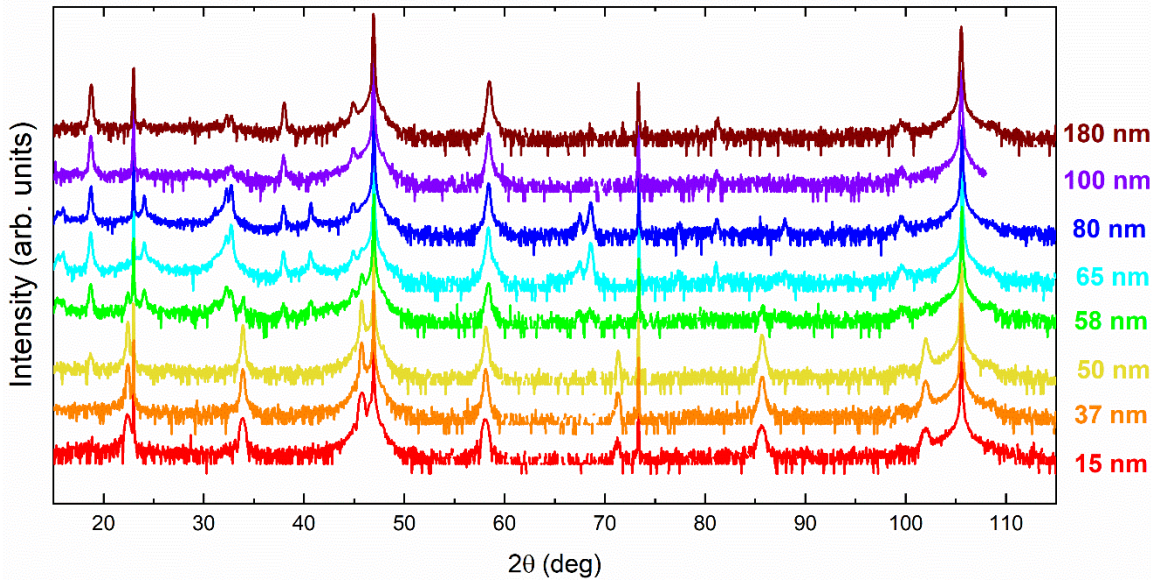

Figure C2: Wide-angle specular HRXRD scans of $SrCoO_x$ films grown on LSAT(001) substrates at varying thickness (see color-coded legend to the right of the plot). All the films were grown by high-pressure-oxygen sputtering using the deposition conditions shown at the top of the plot: Substrate temperature of 700 °C, oxygen pressure of 1.75 mbar, separation coordinate (*z*, see Section 2.1.2) of 108 mm, and 100 mA of DC current. The films at low thickness are phase-pure BM but evolve into a mixed phase at ~58 - 80 nm, and finally form the bulk equilibrium mixture of $Sr_6Co_5O_{15}$ and Co_3O_4 at high thickness (≥ 100 nm).

II. Structural degradation at high temperature

By now, hopefully the reader has an appreciation for the sensitivity of high valence cobaltites to oxygen. Not only in their ability to take-up or lose oxygen from the lattice to the environment, and *vice versa*, but also in the relative mobility of oxygen (and V_O) in the lattice, readily changing the structure and properties both when desired and not. High

temperature measurements (and film growth) of such materials are thus exceptionally difficult. As alluded to in Chapter 6, we observed that BM-SCO films structurally degrade at high temperatures in vacuum, presumably due to the loss of oxygen. Fig. C3 shows the results of one such experiment where HRXRD of a phase-pure BM-SCO film was performed at various temperatures in vacuum ($P \approx 0.1$ Torr), from 300 K to 700 K, and back to 300 K. Panel (a) shows the wide-angle HRXRD around the film BM (008) and substrate (002) reflections, showing the downshift in peak positions corresponding to a elongation (due to thermal expansion) of the out-of-plane lattice parameter, *c*. Panel (b) then shows *c* (as determined from the film peak position in (a)) *vs.* *T*, from 300 K to 700 K (warming, black data points), and from 700 K to 300 K (cooling, blue points). The film BM (008) peak shows two approximately linear trends *vs.* *T*: one below ~540 K and one above. This abrupt change in slope likely indicates some other phenomenon is further serving to expand the lattice (possibly V_O formation), in addition to thermal expansion. Upon cooling back to 300 K, the film peak is then split into two (Purple dashed curve in Fig. C3(a), blue points at 300 K in Fig. E3(b)), both with similar widths. (Wider 2θ range scans confirm the film structure from both peaks still corresponds to a BM-like phase). This indicates a lateral inhomogeneity, likely caused by varying oxygen content in the film. After the thermal treatment, the higher lattice parameter portion (lower 2θ peak) likely has $\delta > 0.5$, *i.e.*, oxygen stoichiometry < 2.5, leading to an expansion of the film *c*.

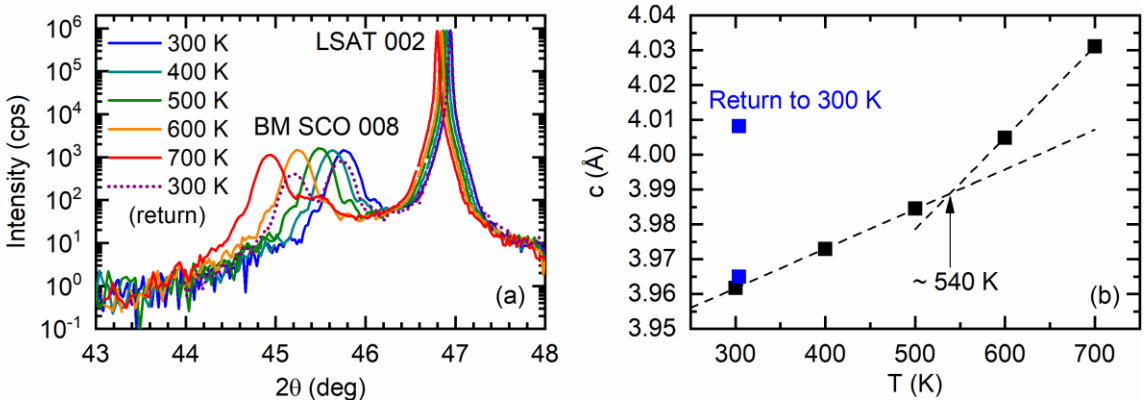

Figure C3: (a) Wide-angle specular high-resolution XRD scans of a BM-$SrCoO_{2.5}$ film on LSAT(001) substrate, around the film (008) and substrate (002) reflections, taken at various temperatures (see legend). (b) The BM-$SrCoO_{2.5}$ film out-of-plane lattice parameter (*c*), determined from the BM (008) peak position in (a), *vs.* temperature (*T*). Overlaid with the data in (b) are linear fits to the low- and high-*T* data points showing an intersection around 540 K. Black data were taken on warming, while the blue data were taken after cooling back to 300 K and represent the two-peak BM structure shown in (a) (purple dashed curve).

Although not observed in the above experiment, decomposition (or phase separation) into the bulk equilibrium phases $Sr_6Co_5O_{15}$ and Co_3O_4, is also known to occur in BM-SCO films at high *T* [322]. Note that such decomposition (and decomposition rate) will be highly dependent on the precise experimental conditions (*T*, O_2 partial pressure, *etc*.). This is an important consideration, as structural degradation was also observed in our BM-SCO film samples during ND experiments at high *T*, as discussed in Chapter 6 (*T*'s > ~400 K, $P \approx 10$ mTorr). Although the exact nature of said degradation was not investigated, it resulted in noticeable reduction of the diffracted intensity from the nuclear BM film peaks. This loss in peak intensity was accounted for in Fig. 6.2(d) by introducing a corrective scaling factor to the integrated magnetic intensity, to account for the loss of intensity observed in the nuclear (002) peak. This factor was equal to the ratio of initial (002) peak intensity divided by its final 'degraded' intensity (at the same *T*) and was ~1.5. This correction was only made for two of the (201) peak scans in Fig. 6.2(d), which were taken after the film was exposed to a long (~8 hour) dwell at 400 K (namely 3.5 K (one of two scans at that *T* (see Fig. 6.2 caption) and 75 K).

Appendix D: Properties of brownmillerite $La_{1-x}Sr_xCoO_{2.5}$ powders

Bulk polycrystalline versions of several brownmillerite LSCO compositions were prepared as a part of the work described in Chapter 6. This was done primarily to provide a comparative reference to help explain the observations made in the BM films.

I. Powder XRD

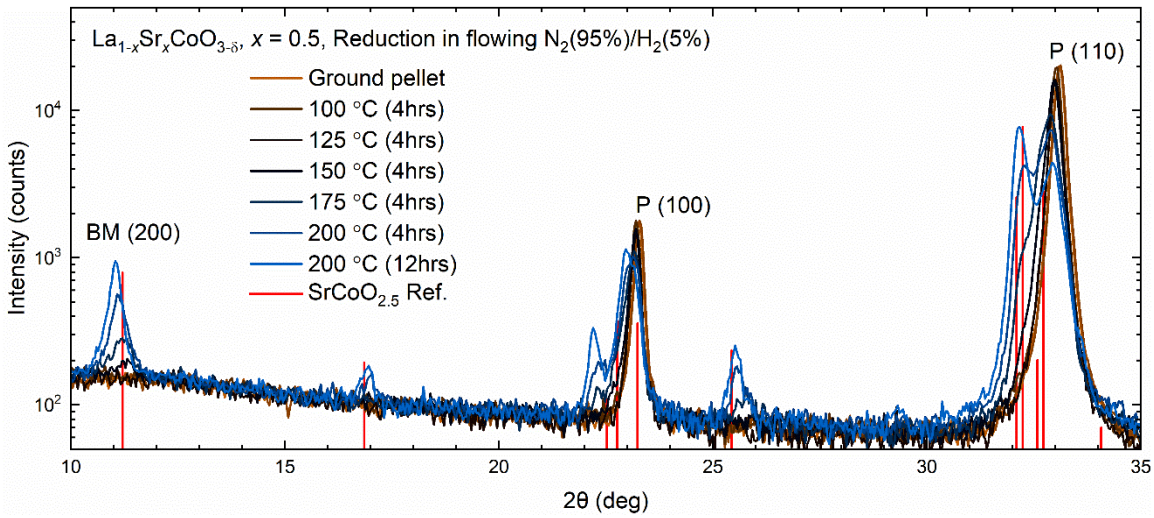

Figure D1: Powder XRD scans of a $x = 0.5$ LSCO powder sample (ground from a sintered pellet) taken after thermal reduction at varying temperatures and times (see legend). The red vertical lines mark the expected positions for brownmillerite (BM) $SrCoO_{2.5}$ from Ref. [103]. The starting P peaks are indexed, while only the (002) peak is indexed for the BM.

$La_{1-x}Sr_xCoO_{2.5}$ bulk polycrystalline powders were prepared from nominally fully stoichiometric, *i.e.*, $La_{1-x}Sr_xCoO_3$, sintered pellets by powdering and subsequent reduction in forming gas (95% N_2 / 5% H_2) at intermediate temperatures (100 - 350 °C). We found that a BM-like structure (very close to the reference powder XRD pattern of $SrCoO_{2.5}$) was readily achievable for compositions of $x = 0.5$ and $x = 0.75$, by reduction at ~200 °C. However, in $x = 0$ and $x = 0.25$ samples, no BM-like structure was observed at any temperature, reminiscent of the lack of BM structure in the V_g-reduced low-x LSCO films described in Chapters 3 and 4 [242,256]. This indicates that either the BM does not form in these compounds or that more precise reduction conditions are required. Note that, in these reduction experiments, no quantitative measure of the oxygen stoichiometry was performed (by *e.g.*, thermogravimetric analysis and / or chemical methods). Instead, the nominal $\delta \approx 0.5$ stoichiometry was assumed simply by comparison of the powder XRD

pattern to that of the known reference pattern for bulk $SrCoO_{2.5}$, and by observation that further reduction did not change the peak positions, indicating a stable structure. Fig. D1, shows a series of powder XRD scans for a single sample of $x = 0.5$ LSCO powder, reduced at increasing temperature (and time) in 95% N_2 / 5% H_2 forming gas. The scans show a phase-pure cubic P initially, but after $T > 150$ °C, the P peaks begins to drop in intensity, downshift to lower 2θ, and several new diffraction peaks begin to appear. The most important of which is the (200) peak which is characteristic of the BM CoO_4 / CoO_6 layered structure. Eventually, after the 12-hour reduction at 200 °C, a fully BM-like structure was formed. Preliminary Rietveld refinement (only allowing the lattice parameters to change), resulted in lattice parameters: $a = 5.43$, $b = 5.54$ Å, $c = 15.99$ Å, in close agreement with two prior reports at $x = 0.67$ [72] and $x = 0.7$ [323], but at odds with another ($x = 0.5$) [73]. It should be noted that our Rietveld refinement fitting to *only* BM $SrCoO_{2.5}$ reference pattern was not successful. Instead, an additional cubic $LaCoO_3$ phase was added to the fitting to allow it to converge. The fitting process thus indicates our powder is likely a mixed phase of orthorhombic BM and a some higher-symmetry (and likely higher oxygen content) phase. Such a phase was found in Ref. [72], labelled as tetragonal "224", which appeared in their samples from $\delta \approx 0.25$ to $\delta \approx 0.4$. It is likely then, that our reduced powder is comprised of a similar mix (further evidence to support this is given in the following section). Further structural characterization could confirm this. At $x = 0.75$, the P proved easier to reduce, as expected, needing only one 12 hour 200 °C sequence. The resulting powder also yielded a much better fit to the reference $SrCoO_{2.5}$ pattern after refinement (needing no additional cubic phase to converge), as shown in Fig. D2.

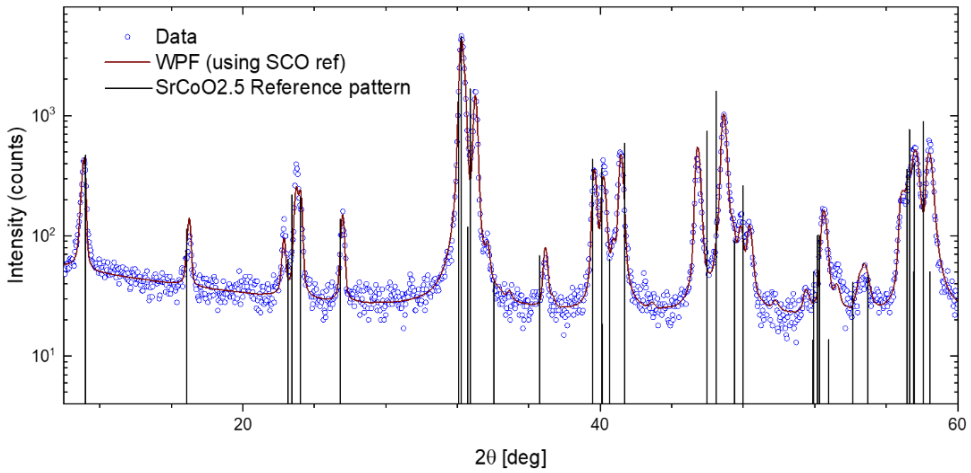

Figure D2: Powder XRD scan of a $x = 0.75$ LSCO powder sample (ground from a sintered pellet) taken after thermal reduction in 95% N_2 / 5% H_2 forming gas at 200 °C for 12 hours (blue circles). Also shown are the expected peak positions of the reference pattern for $SrCoO_{2.5}$ brownmillerite (black vertical lines), and the whole pattern fit (WPF) generated *via* Rietveld refinement to the reference pattern using the powder XRD software package JADE (red trace).

II. Magnetometry and differential scanning calorimetry

The above section outlines the preparation and structural characterization of bulk BM LSCO at $x = 0.5$ and $x = 0.75$. After proving such samples could be fabricated, this section now highlights the preliminary results of the study of their magnetic properties, through magnetometry and differential scanning calorimetry (DSC). Fig. D3(a) shows the field-cooled M *vs*. T of 3 different BM-LSCO compositions, $x = 0.5$, $x = 0.75$, and $x = 1$. At low T, $x = 1$ shows essentially no magnetization ($< 5 \times 10^{-4}$ μ_B/Co), while $x = 0.5$ and $x = 0.75$ show a weak F signal, of similar magnitude to that observed in $x = 0.5$ BM-LSCO thin films as discussed in Chapter 6. The F signals with T_C's $\geq$ ~200 K in $x = 0.5$ and $x = 0.75$ samples, considering their extremely small moments, likely originate from impurity phases still present, such as the "224" tetragonal phase as seen in Ref. [72]. The inset of Fig. D3 shows the same wide-T-range $M(T)$ for a 100 mg $x = 1$ BM-SCO sample, as in the main figure, but on a linear scale to better resolve its subtle features. These include the low-T F signals with varying T_C (similar to those seen in literature [93,104]), likely due to magnetic impurity phases, and the 'kink' at around 540 K, indicating T_N for the expected AF order transition [93,100–102]. Fig. D3(b) then shows characteristic M *vs*. H loops for $x = 0.5$ and $x = 1$ (at 50 K and 10 K, respectively), highlighting the weak F in $x = 0.5$ BM-

LSCO (M_s = 0.1 μ_B/Co) and the lack of any detectable F hysteresis in the x = 1 sample (10 mg).

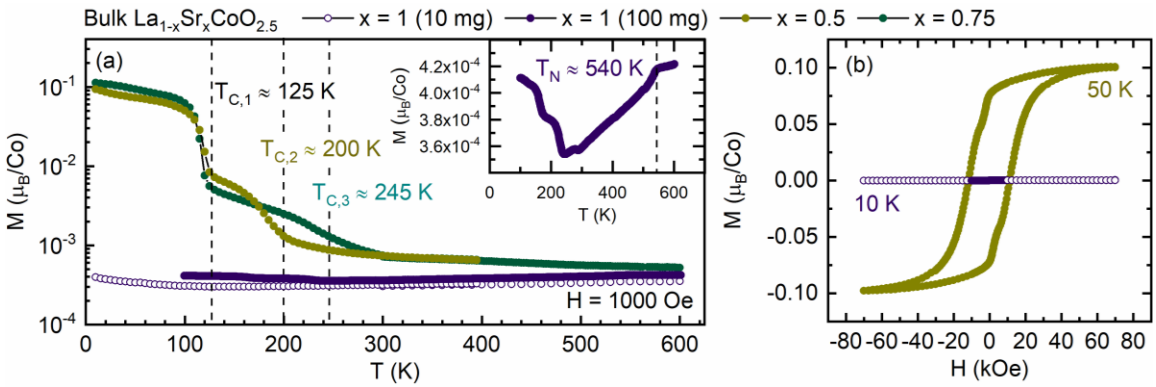

Figure D3: (a) Field-cooled (70 kOe) magnetization (M) *vs*. temperature (T) for bulk samples of x = 0.5, x = 0.75, and x = 1 brownmillerite (BM) $La_{1-x}Sr_xCoO_{2.5}$. The BM structure was confirmed by powder XRD for each sample prior to measurement. All measurements were taken in a 1000 Oe field. The y-axis, M, is shown on a $\log_{10}$ scale to better visualize the low-signal, high T_C, F features in x = 0.5 and x = 0.75 samples, and to highlight the ultra-low magnetization of the x = 1 sample. Various F T_C's are marked by vertical dashed lines, where $T_{C,1}$ is the primary phase of the sample due to weak F, while $T_{C,2}$ and $T_{C,3}$ are likely due to impurity phases (*e.g.*, incomplete reduction of $La_{1-x}Sr_xCoO_{3-\delta}$ to BM). Note that two x = 1 samples are shown in (a): one from a ~10 mg sample and one from a ~100 mg sample. The higher mass x = 1 sample data is re-plotted in the inset with a linear y-axis scale, where various small F signals are visible below ~300 K (again, likely due to impurities), and the T_N is visible (marked by a vertical dashed line). (b) Selected M *vs*. applied magnetic field (H) hysteresis loops for x = 0.5 and x = 1 BM-$La_{1-x}Sr_xCoO_{2.5}$ samples taken at 50 K and 10 K, respectively.

Due to the low signal of some AF transitions, it is often useful to probe magnetic ordering temperatures by other means, such as by heat capacity. DSC is one such method, where a sample pan and control pan are subjected to T sweeps, while the energy required to maintain the same temperature in each, is recorded. DSC has previously been used as further confirmation of the T_N in bulk x = 1 BM-SCO [93]. Fig. D4(b),(d),(f) show DSC of the same bulk samples as in Fig. D3, with the M *vs*. T reproduced in top panels (D4(a),(c),(e)) for reference. Note that Fig. D4(a) and (b) are also reproduced from Fig. 6.2(e), again showing the $T_N \approx$ 540 K, expected for bulk x = 1 BM-SCO [93,100–102]. For x = 0.75 BM-LSCO (Fig. D4(c),(d)), DSC clearly evidences a peak at ~350 K, while there is a small, but significant, feature near the same T from magnetometry. (Note, both high-T and low-T scans using different instruments are shown with overlap in the T range 300 - 400 K, differences are likely due to uncertainty from sample mass). These features, in combination, thus provide some evidence for an AF transition, as might be expected by

analogy to $x = 1$. Interestingly, however, $x = 0.75$ also shows clear weak F (Fig. D3), similar to that seen in $x = 0.5$ BM-LSCO, possibly indicating a *canted*-AF structure below the weak F T_C (~125 K). Lastly, at $x = 0.5$ (Fig. D4(e),(f)), DSC indicates a relatively weak broad peak at ~235 K, but there is no evidence for a corresponding feature in $M(T)$, perhaps being masked by the contaminating F signal from impurity phases. Combining the results from the above sections, Fig. D5 then shows a preliminary magnetic phase diagram for bulk BM-LSCO, where paramagnetic (PM), antiferromagnetic (AF) and weak ferromagnetic (Weak FM) phases are shown, along with their ordering temperatures, T_C (from magnetometry) and T_N (average between magnetometry and DSC). Neutron powder diffraction would be an essential tool to confirm or disprove the trends implicated in Fig. D3 - D5, as well as to identify the types of potential AF order. Such characterization represents a crucial step before extending such research to thin films and eventually P-BM-based electrolyte-gate devices.

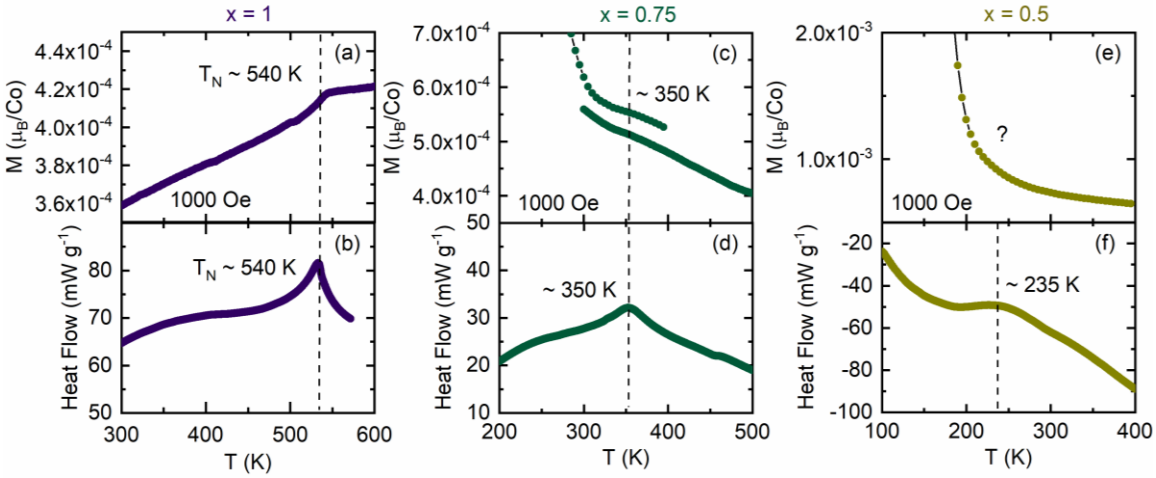

Figure D4: (a), (c), and (e) show magnetization (M) *vs.* temperature (T) reproduced from Fig. D3 for bulk samples of $x = 1$ (purple), $x = 0.75$ (dark teal), and $x = 0.5$ (gold) brownmillerite (BM) $La_{1-x}Sr_xCoO_{2.5}$, over specific T-ranges in correspondence with the differential scanning calorimetry (DSC) measurements below. (b), (d), and (f) show DSC for different masses from the same sample batches as measured in (a), (c), and (e). For $x = 1$, the sample pan was hermetically sealed in air. The sample environment during DSC measurement was flowing He. Note all measurements were taken on warming. For M *vs.* T, 1 K min^{-1} was used, while for DSC T-sweep of 10 K min^{-1} was used. Also note the negative heat flow of the y-axis DSC scan in (f), indicating more energy was required to heat the (empty) control pan *vs.* the sample pan. This may have been due to a combination of low sample-to-pan mass ratio (~0.1) and improper choice of the control pan but requires further investigation.

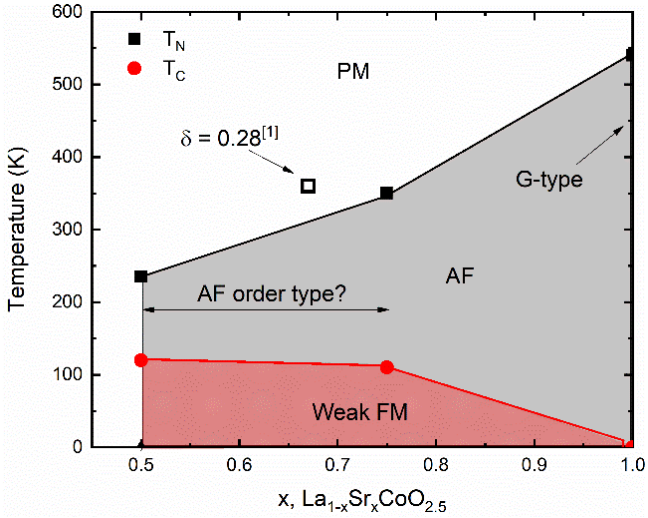

Figure D5: Preliminary magnetic phase diagram for bulk brownmillerite $La_{1-x}Sr_xCoO_{2.5}$. "PM" = paramagnetic (white region), AF = antiferromagnetic (grey region), and "Weak F" = weak ferromagnetism (red region). Note the "Weak F" region may have underlying AF interactions due to spin canting as previously suggested [72], but this has yet to be confirmed. The black points are taken from both magnetometry and differential scanning calorimetry (averaged, when available), while the red points are from magnetometry only. The AF ordering type at $x = 1$ ($SrCoO_{2.5}$) is known to be G-type [93,100,102], while the ordering type at other BM-LSCO compositions are not yet known. The open square data point for the T_N of a bulk $\delta = 0.28$ (non-BM) sample, taken from another report [72], is shown for reference.

Appendix E: Details of background subtraction for neutron diffraction data

As discussed in Chapter 6, the (201) magnetic-only peak was probed *via* ND to look for signs of G-type antiferromagnetic order in thin film samples of $x = 1$ and $x = 0.5$ BM-LSCO. Due to the inherently low signal of this experiment, very long counting times (10 minutes per point) were needed to resolve the peak with sufficient counting statistics (Poisson distribution, standard error = $\sqrt{\text{counts}}$). In addition to low SNR, a non-trivial background intensity was also observed, that required careful systematic treatment. The background subtraction procedures used to generate Fig. 6.2(b), (c), and (d) are outlined in the following sections.

I. Background subtraction for (201) peak rocking curves

Fig. E1(a) shows the raw detected intensity (in counts) *vs*. s1 (the sample rocking angle, which has an arbitrary offset to ω), *i.e*., a rocking curve (RC), about the (201) peak position at 3.5 K for an $x = 1$ BM-LSCO film sample probed by ND, as described in Chapter 6. The purple circled data points in panel (a) were used to fit a linear background, that was subsequently subtracted, point-by-point, from the data, yielding the data in panel (b). Fig. E1(c) shows an equivalent RC collected at 400 K (above T_N), where the entire scan is effectively a flat background signal. In this case, the background was determined as the mean of all the points, and subsequently subtracted point-by-point. The results of the above treatments are presented in Fig. E(d), which shows the final background subtracted intensity for the (201) peak at both 3.5 K (blue) and 400 K (red). The SNR in this experiment was determined by: counts-per-second (cps) of signal / cps of background. For Fig. E1(a),(b), this corresponds to roughly: 0.833 cps (the maximum count rate at the peak) / 9.7 cps (the background count rate) ≈ 0.1, a remarkably small number, underpinning the need for exceptionally long counting times in this experiment (10 minutes per point).

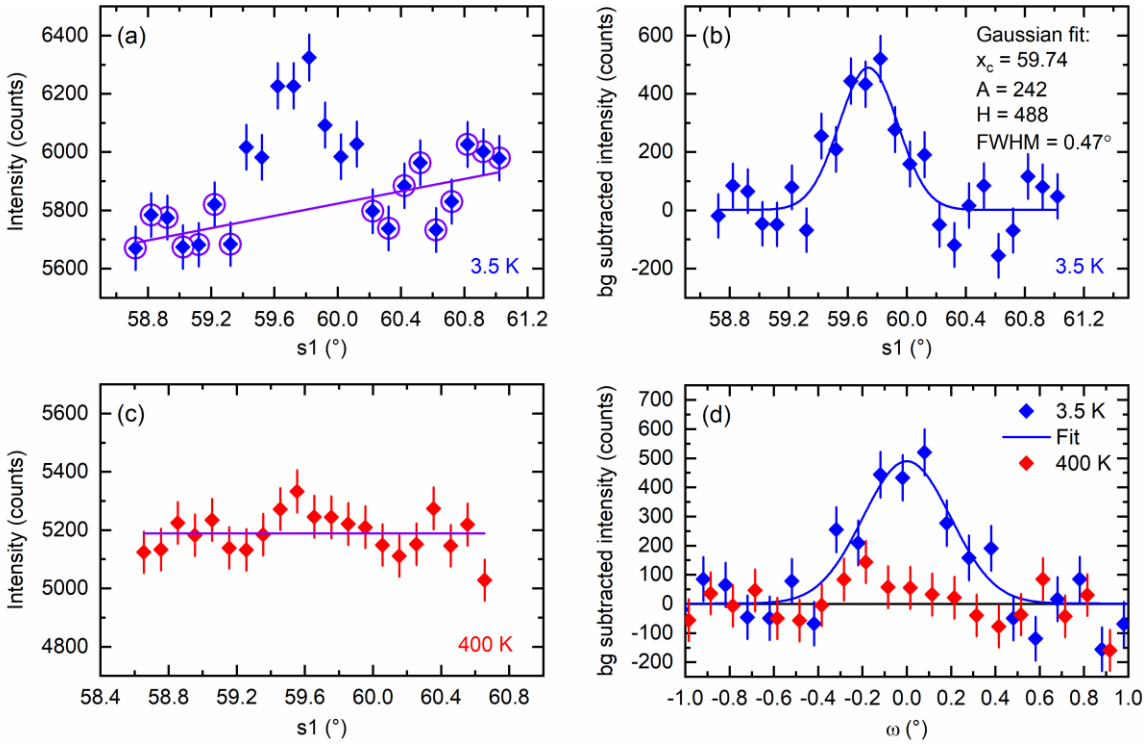

Figure E1: (a) Neutron diffraction rocking curve (RC) around the (201) peak position for a stack of six 50-nm-thick LSAT(001)/$SrCoO_{2.5}$ films at 3.5 K. The purple circled points and purple line represent the background and linear fit to the background. (b) The same peak as in (a) but after performing point-by-point subtraction of the purple fit line in (a). The blue solid line represents a Gaussian fit to the data. Note that the maximum peak height (~500) divided by the counting time per point (10 minutes) yields a count rate ~0.83 counts per second. (c) The same RC as in (a),(b), but taken at 400 K, showing the disappearance of any discernible . In this case, the entire scan is effectively treated as the background, and the purple line is used to perform another point-by-point subtraction, resulting in (d): the final (201) RC background (bg) subtracted intensity *vs*. ω (ω = s1 – 59.75°) for the two 'raw' scans in (a),(c). Note the error bars in all plots represent the value of $\sqrt{\text{counts}}$ before background subtraction.

II. Background subtraction for (201) peak $\theta/2\theta$ scans

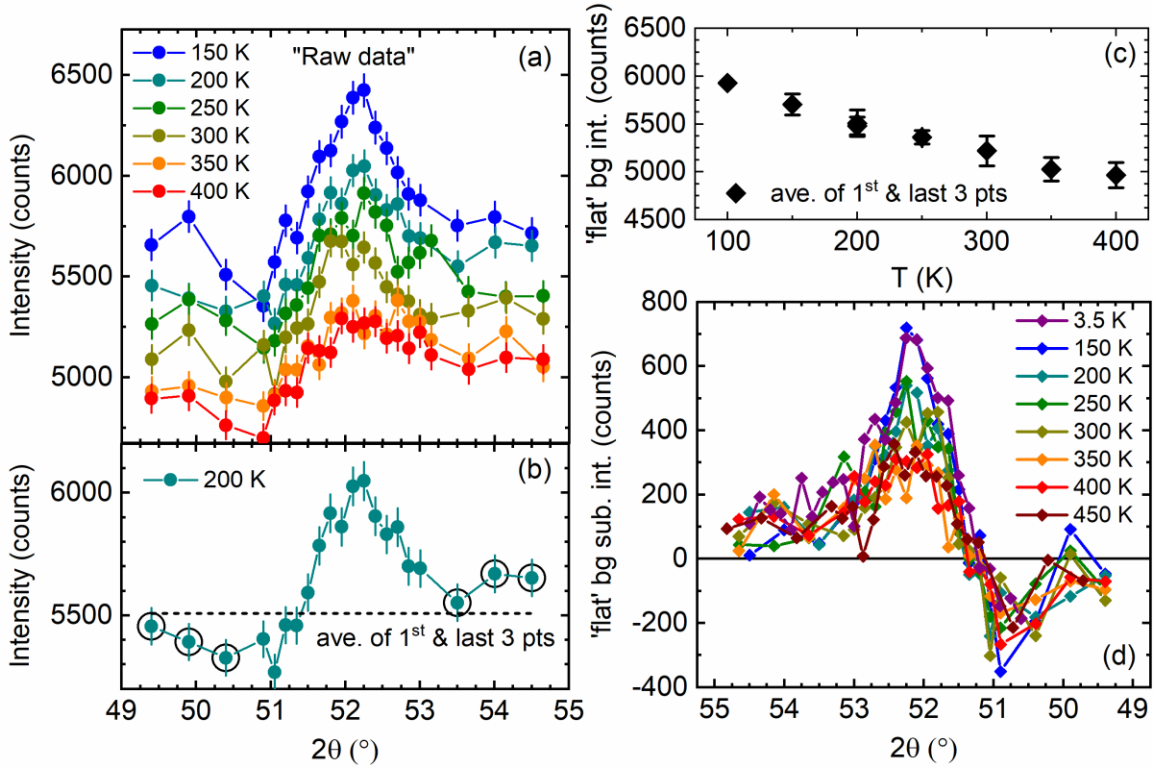

Figure E2: (a) Neutron diffraction $\theta/2\theta$ coupled scans around the (201) peak position for a stack of six 50-nm-thick LSAT(001)/$SrCoO_{2.5}$ films at selected temperatures (T) with 10 minute per point counting time. (b) Replot of the same data as in (a) but only for the 200 K data, to highlight the procedure of 'flat background' subtraction, where an average of the 1st and last 3 data points (circled points, and dashed line) was determined and subtracted point-by-point from the data. (c) "Flat" background intensity, as determined using the above procedure, as a function of T for the scans in (a). (d) Intensity after flat background subtraction ('flat' bg sub. int.) *vs.* 2θ for selected T scans, showing the tight grouping of all the scans away from the peak after subtraction of the T-dependent background.

The background subtraction procedure described above for the RCs of the (201) peak was relatively simplistic. However, we chose to probe the (201) peak intensity *vs.* T using $\theta/2\theta$ coupled scans instead of RCs, which required a more complicated background subtraction procedure (outlined below) due to the unusual shape of the background. Fig. E2(a) shows "raw data", *i.e.*, no background subtraction, for $\theta/2\theta$ coupled scans of the (201) peak for at various selected T's (again for the x = 1 BM-SCO sample). From these scans a clear T-dependent background can be seen. To account for this, we subtracted a 'flat', *i.e.*, constant, background intensity value from each scan: the average of the first and last 3 points of each scan, as shown in Fig. E2(b) specifically for the 200 K scan. Following the same procedure for the other T scans then yielded Fig. E2(c), which shows a near-linear

decrease of the background intensity with T, and Fig. E2(d), which shows the results of the point-by-point 'flat background' subtraction for selected T scans. From inspection of Fig. E2(d), a clear decrease in peak intensity can be seen at higher temperatures, indicating the reduction in magnetic diffracted intensity on approaching T_N. The results of the flat background subtraction also demonstrate how the various T scans all stack up relatively nicely, particularly away from the peak as intended. However, the shape of the background is still nontrivial. In addition, we noticed that the scans at 350 K, 400 K, and 450 K in Fig. E2(d) are nearly overlaid on one another. We took this to be a sign of the 'native' shape of the background in this region of 2θ, *i.e.*, a 2θ-dependent background, which we then attempted to account for below.

To attempt to remove the 2θ-dependent background from the data, we first fit the 350 K, 400 K, and 450 K scans (after the flat background subtraction shown in Fig. E2) to a single 6^{th}-order polynomial function. The results of this fitting are shown in Fig. E3(a). This fit-determined polynomial was then used to perform another point-by-point subtraction from the rest of the scans (i.e., from data such as that in Fig. E2(d)), yielding the results shown in Fig. E3(b). Finally, noting the significant scatter in Fig. E3(b), we performed adjacent averaging (over an 8-point bin range), resulting in the smoothed data plotted in Fig. E3(c) (the same data as in Fig. 6.2(c)). The quality of the adjacent-averaged scan data was then sufficient to fit to Gaussian peaks (solid lines in Fig. E3(c)), that then allowed us to plot the peak area (from the fits) as a function of T (Fig. E3(d)). To complete the dataset shown in Fig. 6.2(d), first the red data points were scaled up by a scaling factor to account for observed high T structural degradation (see Appendix C II), and second, the temperature values where two scans were taken (blue points at 3.5 K and 200 K) were averaged together (adding their standard errors in quadrature).

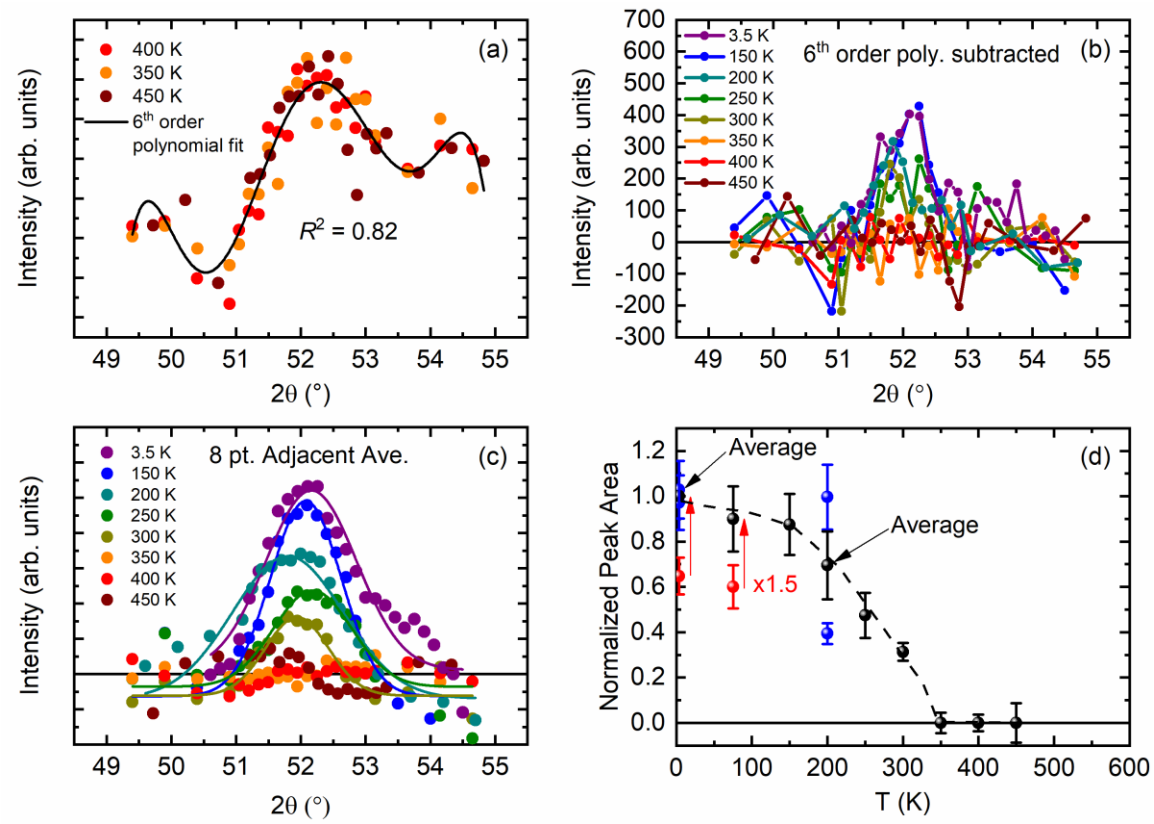

Figure E3: (a) 'Flat background' subtracted (see Fig. E2) ND $\theta/2\theta$ coupled scans around the (201) peak for a stack of six 50-nm-thick LSAT(001)/$SrCoO_{2.5}$ films at 350 K, 400 K, and 450 K (see legend). The data were fit together with a single 6th-order polynomial (black curve) (b) Background subtracted intensity (flat background, plus 6th-order polynomial background) *vs*. 2θ. [Explicitly, (b) shows the data in Fig. E2(d) after point-by-point subtraction of the polynomial fit function shown in (a).] (c) the same data as in (b) after adjacent averaging using an 8-data-point binning range. The solid lines represent Gaussian fits to the data. Note the data shown in (c) are the same as was shown earlier in Fig. 6.2(c). (d) Gaussian-fit peak area *vs*. temperature (*T*), normalized to the lowest *T* point. Note that the red data points were multiplied by a scaling factor of ~1.5 to account for film degradation at high *T* (see Appendix C II), and that the blue points were averaged together, resulting in the black point indicated by arrows. Error bars in (d), below 350 K, correspond to standard errors from the Gaussian fits, while above 350 K, they represent the absolute value of the total integrated intensity after background subtraction. The dashed line serves as a guide to the eye (see Section 6.3.1 and Fig. 6.2 caption for a fitting information and discussion).